Design and Synthesis of Rhodamine based Fluorescent Molecular Probes for Iron(III) Recognition

THESIS SUBMITTED FOR THE

DEGREE OF DOCTOR OF PHILOSOPHY (SCIENCE)

OF

JADAVPUR UNIVERSITY

By

HABIB ALI MOLLA

DEPARTMENT OF CHEMISTRY

JADAVPUR UNIVERSITY

JADAVPUR

K0LKATA-700032

INDIA

DECEMBER, 2024

Prof. Mahammad Ali,

Professor,

Department of Chemistry

JADAVPUR UNIVERSITY
KOLKATA - 7 0 0 0 3 2, I N D I A
E-mail: m_ali2062@yahoo.com
Mobile: +91-9433249716

CERTIFICATE FROM THE SUPERVISOR

This is to certify that the thesis entitled **"Design and Synthesis of Rhodamine based Fluorescent Molecular Probes for Iron(III) Recognition"** submitted by **Sri. Habib Ali Molla** who got his name registered on **06.12.2021 (Index No: 138/21/Chem./27)** for the award of **Ph.D. (Science) degree** of **Jadavpur University**, is absolutely based upon his own work under my direct supervision and that neither this thesis nor any part of it has been submitted for either any degree / diploma or any other academic award anywhere before.

Date: 16/12/2024

Mahammad Ali

(Prof. Mahammad Ali)
Signature of the Supervisor & date with seal
Department of Chemistry
Jadavpur University
Kolkata 700 032

Declaration

I hereby declare that the thesis entitled ***"Design and Synthesis of Rhodaminne based Fluorescent Molecular Probes for Iron (III) Recognition"*** *submitted for the degree of Doctor of Philosophy (Science) of Jadavpur University is based on the original work done by me under the guidance of Prof.Mahammad Ali, Department of Chemistry, Jadavpur University, Kolkata-700 032 and this work has not been included in any other thesis submitted previously for the award of any other degree.*

Habib Ali Molla 16/12/24

Jadavpur University

(Habib Ali Molla)
Department of Chemistry
Jadavpur University
Kolkata 700 032


DEDICATED TO MY
BELOVED PARENTS
who made all of this possible, with your endless loves, supports, and prayers.

Acknowledgements

This dissertation would not have been possible without the support and guidance of numerous individuals who contributed in various ways throughout my academic journey. I would like to take this opportunity to sincerely acknowledge and thank those who played a role, directly or indirectly, in the successful completion of my thesis.

First and foremost, I extend my heartfelt gratitude to my supervisor, **Prof. Mahammad Ali**, for welcoming me into his laboratory and entrusting me with such a challenging project. I am deeply appreciative of his unwavering support, encouragement, and belief in my abilities, which gave me the confidence to navigate the complexities of my research and Ph.D. studies. I am profoundly grateful for his invaluable advice, insightful guidance, and the rigorous training he provided, which have equipped me to face future challenges with confidence. Being a member of his research group has been an honor, and I take immense pride in the opportunity to work under his mentorship. I could not have imagined a better advisor and mentor for my Ph.D. journey.

I would also like to express my gratitude to the Inorganic Chemistry faculty members at Jadavpur University, particularly the present Dean of Science, **Prof. Chittaranjan Sinha**, the current Head of the Department of Chemistry, **Prof. Kajal Krishna Rajak**, and **Prof. Partha Roy**, Sectional In-Charge of Inorganic Chemistry, for their kind cooperation and encouragement throughout my research journey.

I am also deeply thankful to **Prof. S. Baitalik**, **Prof. J. P. Nasakar**, **Prof. S. Mukhopadhyay**, **Prof. T. K. Mandol**, and **Dr. B. B. Show** from the Department of Chemistry, Jadavpur University, for graciously providing access to their laboratory facilities whenever needed.

I sincerely appreciate the constant support and encouragement of all the faculty members and non-teaching staff, especially **Mr. Baidyanath Paul** and **Mr. Atikur Rahaman**, whose helpful attitude greatly contributed to my work.

Lastly, I extend my heartfelt thanks to the authorities at Jadavpur University for granting me access to the essential infrastructure and resources necessary for the successful completion of my research.

This journey would not have been possible without the unwavering support of my labmates: **Dr. Surajit Biswas**, **Dr. Ishita Banerjee**, **Dr. Arpan Dutta**, **Dr. Mainak Debnath**, **Dr. Tarun Mistri**, **Dr. Malay Dolai**, **Dr. Luna Paul**, **Dr. Rabiul Alam**, **Dr. Rahul Bhowmick**, **Dr. Arindam Giri**, **Dr. Abu Saleh Musha Islam**, **Dr. Dipankar Das**, **Dr. Hasan Mohammad**, **Dr. Mihir Sasmal**, **Dr. Debjani Maiti**, **Dr. Ananya Dutta**, **Dr. Rousunara Khatun**, **Miss Dolan Moni**, and **Mr. Mansur Habibullah**.

Their valuable discussions, constant support, general assistance, and most importantly, their friendship have been instrumental in making this journey both enriching and memorable. I deeply cherish the beautiful memories we created together, as well as the challenges and difficulties we overcame as a team. These shared experiences will remain etched in my heart forever.

It is a genuine pleasure to express my heartfelt gratitude to my close friends for their unwavering support and encouragement throughout this journey. In particular, I would like to extend my deepest thanks to **Dr. Tarak Nath Das** and **Dr. Pradip Kundu**. They stood by me through both joyful and challenging moments, consistently pushing and motivating me. Their support has been invaluable, making this journey much smoother and more enjoyable.

I would also like to sincerely thank all the teaching and non-teaching staff, as well as the managing committee members of my previous school, **Bargharia G.G.P.T High School** (Swarupnagar, North 24 Parganas), and my current school, **Jyangra Adarsha Vidyalaya** (Rajarhat-Newtown), for their encouragement and support, which contributed significantly to the successful completion of my thesis.

I extend my heartfelt thanks to my collaborators, **Prof. Keya Chowdhuri** and **Dr. Atul Katarkar**, from the CSIR-Indian Institute of Chemical Biology, Kolkata, for their invaluable cooperation and support during this journey.

Words cannot adequately express my gratitude to my family, who have been my unwavering pillars of strength. I am deeply thankful to my father, **Mr. Md. Younus Ali Molla**, my mother, **Mrs. Halima Begum**, my mother-in-law, **Mrs. Samsul Ara Begum**, and my father-in-law, **Mr. Sk Nasher Ali**, for their constant emotional and moral support throughout my life.

A special mention goes to my cherished wife, **Sk. Nafisa**, and my beloved daughter, **Kayanat Ara**, whose love and understanding have been my greatest sources of motivation. Their prayers and sacrifices have been instrumental in my success.

I am also deeply thankful to my sisters (**Firu, Tanu, Rubina, and Sebina**) and my brothers (**Sabir and Babar**) for their unconditional love, care, and support. Their priceless prayers and encouragement played a crucial role in helping me complete my thesis. I am forever indebted to each of them for their invaluable contributions to my journey.

I would like to extend my heartfelt thanks to everyone who contributed to the successful completion of this thesis. My sincere apologies for not being able to mention each individual personally; your support, in its various forms, has been deeply appreciated.

I am also profoundly grateful to **DST, West Bengal** and **CSIR, New Delhi** for providing the project funding that made this research possible.

Finally, I offer my deepest gratitude to **Allah Subhanahu Wa Ta'ala** for His countless blessings and guidance throughout this journey, enabling me to successfully complete my thesis.

Department of Chemistry
Jadavpur University
Kolkata– 700 032, India.

Habib Ali Molla

Preface

The work presented in this thesis entitled **''Design and Synthesis of Rhodamine based Fluorescent Molecular Probes for Iron(III) Recognition''** have been carried out in the Department of Chemistry, Jadavpur University.

The thesis consists of five chapters which are summarized below.

Chapter 1 contains a short review of previously reported rhodamine based fluorescent molecular probes for Fe(III) detection by fluorometric method. Additionally, a very brief overview of the present work is highlighted.

Chapter 2 describes a novel, highly sensitive and selective fluorescent chemosensor 'rhodamine-3,4-dihydro-2H-1,3 benzoxazine' [RH-BZN (3)], which has been characterized by single crystal X-ray diffraction and other physicochemical techniques. In 3:7 water: MeCN (v/v) at pH 7.2 (10 mM HEPES buffer, μ= 0.05 M LiCl) it selectively recognizes Fe^{3+} through 1:1 complex formation resulting in a 240-fold fluorescence enhancement and a binding constant (K_f) of 1.50 $\times 10^4$ M^{-1}. The otherwise non-fluorescent spirolactam form of the probe results in dual changes in absorbance and fluorescence arising out of opening of the spirolactam ring through coordination to Fe^{3+} ions. This probe could suitably be employed for cytoplasmic intracellular imaging of Fe^{3+} without notable cytotoxicity. The reversible binding of RH-BZN to Fe^{3+} was confirmed by reacting with tetra-n-butylammonium fluoride both in extra- and intra-cellular conditions.

Chapter 3 describes a novel highly sensitive and selective fluorescent chemosensor **L**, which has been synthesized and characterized by various physicochemical techniques. In 3:7 water: MeCN (v/v) at pH 7.2 (10 mM HEPES buffer, μ = 0.05 M LiCl), it selectively recognizes Fe^{3+} through 1:1 complexation resulting in a 106-fold fluorescence enhancement and a

binding constant of 8.10 $\times 10^4$ M^{-1}. The otherwise non-fluorescent spirolactam form of the probe results a dual-channel (absorbance and fluorescence) recognition of Fe^{3+} via CHEF through the opening of the spirolactam ring. Based on the dependence of FI (fluorescence intensity) and r (anisotropy) on [SDS] it was proposed that the probe is trapped between two SDS monolayers which again interact among themselves by π···π stacking. As a result, there is an increase in FI up to [SDS] ~ 7 mM– a phenomenon reminiscent of aggregation induced enhancement of emission (AIEE). Beyond this concentration of SDS (7 mM), micelle formation takes place and the π···π stacked polymer now becomes a monomer and is trapped inside the micellar cavity. As a result, there is a decrease in FI at [SDS] > 7 mM. $[L–Fe(NO_3)]^{2+}$ thin films on FTO (Fluorine-doped Tin Oxide) glass substrates have been designed with the help of the spin-coating deposition technique. The deposited film of thickness 1.6 × 10^{-5} cm is well characterized by optical band gap calculation with a direct band gap, $\mathcal{E}_g$ ~ 1.6 eV. Light-dependent exciton generation was carried out by taking the top and bottom contacts with graphite paste on FTO and on the $[L–Fe(NO_3)]^{2+}$ films for the measurement of switching behaviour. The light-induced frequency-switching behaviour and Schottky barrier diode characteristics of the material were established.

Chapter 4 describes a rhodamine-B based fluorescent molecular probe **L,** which can selectively recognizes Fe^{3+} ion calorimetrically as well as fluorometrically in the presence of various metal ions and anions. The structure of **L** was analysed by single crystal X-diffraction studies along with NMR, mass spectroscopy and FTIR studies. The dissociation constant values ((2.95 ± 0.06) x 10^{-5} M) and ((9.48 ± 0.06) x 10^{-5} M) were determined by UV-Vis and fluorescence titration, respectively, revealing a strong binding between **L** and Fe^{3+}. The limit of detection (LOD) of Fe^{3+} by **L** was 0.27 µM while quantum yields of **L** and [L–Fe] were 0.011 and 0.36, respectively. Fluorescence anisotropy measured in the presence of HSA indicates the rigidity of the local micro environment where [L–Fe] was trapped in the sub

domain IIA of HSA, as delineated by molecular docking studies. Furthermore, stone like microstructure of **L** formed in 8:2 HEPES buffer:MeCN, (v/v) medium changes to spherical shape in the presence of Fe^{3+} and when the complex interacts with HSA it gets agglomerated. All these are exhibited in SEM studies. All the forgoing discussion establishes that this probe (**L**) is useful for on-site Fe^{3+} recognition through a fast, simple and eco-friendly process.

Chaptero5 represents the highlights of the thesis.

List of Abbreviations

FAAS	Flame Furnance Atomic Absorption Spectroscopy
ICP-ES	Inductively Coupled Plasma Emission Spectroscopy
ICP-MS	Inductively Coupled Plasma Mass Spectrometry
TXRF	Total Reflection X-Ray Fluorimetry
τ	Fluorescence Lifetime
$\Delta\bar{\nu}$	Stokes shift
Φ	Quantum yield
CHEQ	Chelation Enhancement of Quenching
CHEF	Chelation Enhancement of Fluorescence
HSAB	Hard Soft Acid Base
MLCT	Metal Ligand Charge Transfer
ILCT	Intra Ligand Charge Transfer
PET	Photo induced Electron Transfer
ICT	Intramolecular Charge Transfer
PCT	Photo induced Charge Transfer
TICT	Twisted Intramolecular Charge Transfer

FRET	Fluorescence Resonance Energy Transfer
ESIPT	Excited State Intramolecular Proton Transfer
HOMO	Highest Occupied Molecular Orbital
LUMO	Lowest Unoccupied Molecular Orbital
HEPES	4-(2-Hydroxyethyl)piperazine-1-ethanesulfonic acid
DFT	Density functional theory
TDDFT	Time-dependent density functional theory
MeCN	Acetonitrile
MeOH	Methanol
NaOH	Sodium hydroxide
NaCl	Sodium chloride
DCM	Dichloromethane
DMF/dmf	Dimethyl formamide
H_2O	Water
DMSO/dmso	Dimethyl sulfoxide
mL	Milliliter
μM	Micro molar

μL	Micro litre
nM	Nano molar
mM	Mili Molar
K_a	Binding constant/Association constant
K_{ass}	Association constant
K_d	Dissociation constant
K_f /K_f'	Formations constant
ex	Excitation
em	Emission
λ	Wavelength
HeLa	Human epithelial carcinoma cell
HepG2	Human hepatocellular liver carcinoma cells
HCT116	Human colon cancer
PBS	Phosphate buffered saline
DMEM	Dulbecco's Modified Eagle's Medium
MTT	3-(4,5-di methylthiazol-2-yl)-2,5 diphenyltetrazolium bromide
%T	Percentage of Transmittance

FBS	Fetal Bovine Serum
EDTA	Ethylenediaminetetraacetic acid
Na_2H_2EDTA	Disodium EDTAdihydrate
LOD	Limit of detection
MS	Mass spectroscopy
NMR	Nuclear magnetic resonance
FT-IR	Fourier transform Infrared
Fig.	Figure
AIE	Aggregation induced emission
SMMC-7721	Hepatocellular carcinoma cell
FI /F.I	Fluorescence Intensity
GSH	Glutathione
Cys	Cysteine
Raw 264.7	Abelson leukemia virus transformed cell
NIR	Near-infrared
MCF7	Acronym of Michigan Cancer Foundation-7 cell
FE	Fluorescence Enhancement
Tris–HCl	Tris (hydroxymethyl) aminomethane

	hydrochloride
UV	Ultraviolet
Vis	Visible
h	Hours
HPLC	High-performance liquid chromatography
TMS	Tetramethylsilane
KBr	Potassium bromide
K_2CO_3	Potassium carbonate
ESI-MS^+	Electrospray ionization mass spectrometry
HRMS	High-resolution mass spectrometry
CH_2Cl_2	dichloromethane
$SOCl_2$	Thionyl chloride
$CDCl_3$	Chloroform-d
DMSO-d_6	Deuterated Dimethyl sulfoxide
LiCl	Lithium chloride
ATP	Adenosine triphosphate
Pi	Phosphate - Wikipedia
PPi	Pyrophosphate

CD_3OD	Methanol-d4
Et_3N	Triethylamine
MHz	Megahertz
f	Oscillator strength
°	degree
Å	Angstrom
eV	Electron volt
HSA	Human Serum Albumin
BSA	Bovine Serum Albumin
ROS	Reactive Oxygen Species
SDS	Sodium Dodecyl Sulphate
SEM	Scanning Electron Microscope
Trp	Tryptophan
Tyr	Tyrosine
Phe	Phenyl Alanine

Contents

Acknowledgements I-IV
Preface V-VII
List of Abbreviations VIII-XIII

Chapter 1 **Page**

Introduction: A Literature Survey

1.1 Introduction 2
1.2 General aspects of iron (III) 2
1.3 Conventional methods for the determination of iron ion 2
1.4 Background and introduction to fluorescence 3
1.4.1 Fluorescence lifetimes and Quantum yields 4
1.4.1.1 Excited state lifetimes 5
1.4.1.2 Fluorescence quantum yields 5
1.4.2 Applications of fluorescent chemosensors 6
1.4.3 Some conventional mechanisms for construction of fluorescent probes 7
1.4.3.1 Photoinduced Electron Transfer (PET) 7
1.4.3.2 Photo-induced charge transfer (PCT) 8
1.4.3.3 Chelation Enhanced Fluorescence (CHEF) 10
1.4.3.4 Excited state proton transfer (ESIPT) 10
1.4.3.5 Aggregation-based fluorescent sensing 11
1.4.3.6 Excimer / Exciplex Formation 13
1.5 Chemistry of Rhodamine 14
1.5.1 Mechanistic pathway 16
1.6 Brief literature survey on rhodamine based fluorescent sensors for Fe(III) 16
1.7 Present Work 30
1.8 Physical measurements 30
References 31-35

Chapter 2 **Page**

A novel *rhodamine-3,4-dihydro-2H-1,3-benzoxazine* conjugate as a highly sensitive and selective chemosensor for Fe^{3+} ion with cytoplasmic cell imaging possibilities

Abstract 37
2.1 Introduction 38
2.2 Experimental Section 39
2.2.1 Materials and methods 39
2.2.2 physical measurement 39
2.2.3 Synthesis 39
2.2.3.1 preparation of RH-BZN(3) 39
2.2.3.2 Synthesis of $[Fe(RH\text{-}BZN)(NO_3)_2(CH_3CN)$ 42
2.2.4 Cell culture 42
2.2.5 Cell cytotoxicity assay 44
2.2.6 Cell imaging study 44
2.2.7 Solution preparation for UV-Vis and fluorescence studies 45
2.2.8 Quantum yield determination 45

2.3 Results and Discussion 46
2.4 Conclusions 57
References 57-60

Chapter 3

Page

A turn-on fluorogenic chemosensor for Fe^{3+} and a Schottky barrier diode with frequency-switching device applications

Abstract 62
3.1 Introduction 63
3.2 Experimental Section 64
3.2.1 Materials and methods 64
3.2.2 Physical measurement 64
3.2.3 Synthesis 65
3.2.3.1 Preparation of L 65
3.2.3.2 Synthesis of $[L\text{-}Fe(NO_3)]^{2+}$ 65
3.2.4 Solution preparation for UV-Vis and fluorescence studies 67
3.2.5 Determination of fluorescence polarization anisotropy 67
3.2.6 Time -correlated single photon counting measurements 68
3.2 Results and discussion 69
3.3.1 Steady state fluorescence studies in the presence of SDS 72
3.3.2 Steady state fluorescence anisotropy 74
3.3.3 Analysis of surface topography of ligand,ligand- SDS,metal-ligand, and Metal-SDS 76
3.3.4 Thin film fabrication from the precursor of the $[L\text{-}Fe(NO_3)]^{2+}$ complex 77
3.3.5 Morphological characteristics of $[L\text{-}Fe(NO_3]^{2+}$ /FTO thin films 78
3.3.6 UV-Vis analysis 78
3.3.7 Electrical properties:current-votage(I-V) characteristics by the two-probe technique 79
3.3.8 Photon induced exciton generation 81
3.4 Conclusion 82
References 83-84

Chapter 4

Page

A Newly Synthesised Morphology Directing Highly Sensitive Rhodamine B based Fluorescent Fe^{3+} Complex Interaction with Human serum Albumin

Abstract 86
4.1 Introduction 87
4.2 Experimental Section 88
4.2.1 Materials and methods 88
4.2.2 Physical measurements 88
4.2.3 Synthesis 89
4.2.3.1 Preparation of RH-BZN(L) 89
4.2.3.2 Synthesis of $[Fe^{III}(L)(NO_3)_2]$ 91
4.2.4 Solution preparation for UV-Vis and fluorescence studies 91
4.2.5 Circular Dichroism(CD) Spectra 92
4.2.6 Molecular Docking Simulation Study 93
4.2.7 Determination of Fluorescence Polarization Anisotropy 93

	4.2.8 Preparation of sample for SEM studies	94
	4.2.9 Methods of Characterization	94
4.3	Results and Discussion	94
	4.3.1 UV-Vis Absorption Study	95
	4.3.2 Steady state fluorescence studies	96
	4.3.3 PH-stability	99
	4.3.4 Mechanism of L-Fe^{+3} interaction	99
	4.3.5 Spectro polarimetric studies	99
	4.3.6 Docking analysis	100
	4.3.7 Steady-State Fluorescence Anisotropy Measurements	101
	4.3.8 Scanning Electron Microscope (SEM) Studies	102
4.4	Conclusion	102
	References	103-106

Chapter 5	**Page**
Highlights of the Thesis	107-109

Appendix	**Page**
List of Publications	110

Chapter 1

Introduction: A Literature Survey

1.1 Introduction

Fluorescence technique is widely used by biologists, environmental scientists, and chemists for detecting metal ions at extremely low concentrations, ranging from nano- to picomolar levels. The technique allows for the efficient detection of cations, including biologically abundant metal ions such as Na^{+}, K^{+}, Cu^{2+} and Zn^{2+} as well as heavy metal ions like Cd^{2+}, Hg^{2+} and Pb^{2+}. Additionally, it can detect a variety of anions such as CN^{-}, SO_4^{2-}, $S_2O_4^{2-}$, $P_2O_7^{4-}$, HCO_3^{-}, NO_3^{-}, NO_2^{-}, Cl^{-}, F^{-}, PO_4^{3-}, S^{2-}, Br^{-}, $H_2AsO_4^{-}$, N_3^{-}, OAc^{-}, ClO_4^{-}, SCN^{-}, CO_3^{2-}, and others. Neutral molecules can also be detected with this technique. Some of these cations are biologically relevant, while others are highly toxic and hazardous. Transition metals like iron and heavy metals such as mercury are among the most commonly detected cations in these categories.

1.2 General aspects of iron (III)

Transition metals have a wide range of biological and environmental applications, including roles in metabolism, electron transport, and catalysis.[1] Iron(III) (Fe^{3+}), a significant trace element present in both plants and animals, is essential for cellular metabolism.[2] It plays a crucial role in enzyme catalysis, serving as a cofactor in numerous enzymatic processes and as an oxygen carrier in hemoglobin.[3,4] Fe^{3+} is one of the most critical trace elements in biological systems, vital for numerous cellular metabolic reactions.[5,6] However, an excess of Fe^{3+} in the body has been linked to an increased risk of certain cancers and organ dysfunction, including liver, heart, and pancreas.[7] Additionally, Fe^{3+} is implicated in the fundamental processes of various neurodegenerative diseases, such as Parkinson's and Alzheimer's.[8] Given these factors, it is crucial to develop fast and accurate techniques for analyzing Fe^{3+} in biological samples. Therefore, one of the primary objectives is to create methods for the rapid detection of Fe^{3+} in biological contexts.

1.3 Conventional methods for the determination of iron ion

Developing highly accurate and sensitive devices to measure metal ions at concentration levels prescribed by toxicity guidelines and standards is a challenging task. Numerous analytical techniques have been developed for detecting metal ions. For aqueous samples, photometric techniques like flame atomic absorption spectroscopy (FAAS), and graphite furnace atomic absorption spectroscopy (ETAAS) are the most commonly recommended methods.[9,10,11] Other techniques include mass spectrometry, inductively coupled plasma emission spectroscopy (ICP-ES), inductively coupled plasma mass spectrometry (ICP-MS),

and total reflection X-ray fluorescence (TXRF).[12] These techniques offer low detection limits and a wide linear range of sensitivity to metal ions. However, most of them involve labor-intensive and expensive pre-treatment steps, making them unsuitable for routine laboratory use. Therefore, a simple and cost-effective method for detecting and quantifying metal ions is needed for real-time monitoring of environmental, biological, and industrial samples. Among the various detection approaches, optical methods based on colorimetric and/or fluorescence changes are the most practical techniques due to their low detection limits, simplicity, and minimal time requirements.[13,14] Colorimetric sensors are suitable for both online and field monitoring, while fluorescence imaging spectroscopic methods based on fluorescent molecular sensors provide notable advantages in terms of sensitivity, selectivity, reaction time, and localized observation. Additionally, fluorescence assays are straightforward and highly sensitive, making it a valuable tool for detecting physiologically significant metal ions both *in vitro* and *in vivo*. As a result, significant efforts are being made to develop selective fluorescent chemical sensors for metal ion detection.[13-16]

1.4 Background and introduction to fluorescence

The first recorded observation of fluorescence dates back to 1565 when the Mexican wood *Lignum nephriticum*, loosely translated as "kidney wood," was infused into a liquid solution. Nicolás Monardes, a Spanish physician and botanist, noted this phenomenon as a blue tinge and attempted to use it to treat kidney and urinary diseases.[17-20] Over the following centuries, other scientists, including Kircher, Grimaldi, Boyle, Newton, Herschel, and others, became intrigued by the wood's unique optical properties.[17,18]

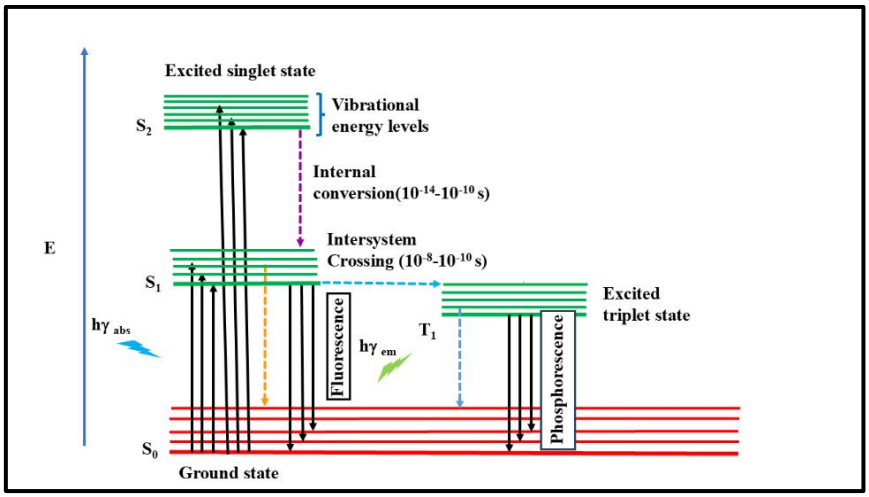

Figure 1.1 The Perrin-Jablonski diagram for different photophysical transitions.

Fluorescence in fluorites was first observed in 1819 by Edward D. Clarke and later in 1822 by René Just Haüy. David Brewster reported a similar phenomenon in chlorophyll in 1833. The first recorded observation of fluorescence from a quinine solution exposed to sunlight was made by John Frederick William Herschel in 1845.[21,22] George Gabriel Stokes later provided a formal definition of fluorescence as an emission mechanism and coined the term "fluorescence" in his paper in 1852,[23] which was celebrated as a significant breakthrough in fluorescence research. Stokes noted in the opening paragraph of his study that Herschel's earlier work on quinine solution inspired his investigation. In 1935, Alexander Jablonski introduced what is now known as the Jablonski diagram (**Figure 1.1**) to illustrate the processes involved in the absorption and emission of light. These diagrams are commonly used as a foundational tool for discussions on light absorption and emission, providing a theoretical basis for understanding the principles of fluorescence.

1.4.1 Fluorescence lifetimes and Quantum yields

The fluorescence lifetime and fluorescence quantum yields are the most crucial characteristics of a fluorophore, as they provide valuable information about the photophysical behavior of the molecule. The fluorescence lifetime, often denoted as τ, is the average time a molecule remains in its excited state before returning to the ground state by emitting a photon. This parameter is essential because it reflects how long a fluorophore can potentially emit light after being excited, influencing the brightness and duration of the fluorescence signal. In the absence of any deactivating perturbations, the rate constant for fluorescence emission, k_f, is inversely related to the natural radiative lifetime, τ_N, of the molecule. The natural radiative lifetime is defined as the time it would take for the excited state to decay solely by fluorescence emission, assuming no non-radiative processes are present. Mathematically, this relationship can be expressed as:

$$k_f = \frac{1}{\tau_N} = \frac{1}{\tau_f^0} \qquad (1)$$

This equation indicates that a shorter natural radiative lifetime corresponds to a higher rate of fluorescence emission. In the presence of other competitive deactivation processes, the average lifetime of the molecule is much reduced and the actual lifetime, τ_f, becomes

$$\tau_f = \frac{1}{k_f + \sum k_i} \qquad (2)$$

where, k_i is the rate constant for the i^{th} competitive process, assumed to be unimolecular.[25]

1.4.1.1 Excited state lifetimes

The average amount of time a molecule spends in the excited state before returning to the ground state is known as the excited state's life span. The triplet state always has a longer lifespan than the singlet state. If τ_s is the life span of the excited state S_1, then it could be expressed as in Eqn. (3).

$$\tau_S = \frac{1}{K_r^S + K_{nr}^S} \qquad (3)$$

Where k^s_{nr} is the rate constant for non-radiative deactivation, or the sum of the rate constants for internal conversion and intersystem crossover, and k^s_r is the rate constant for radiative deactivation for the transition from S_1 to S_0 with emission of fluorescence. The lifetime would be $1/k^s_r$, if the only way of de-excitation from S_1 to S_0 was fluorescence emission then it is called the radiative life time and denoted by k^S_r.[26]

1.4.1.2 Fluorescence quantum yields

The fluorescence quantum yield (Φ_F) is another critical parameter, representing the efficiency of the fluorescence process. It is defined as the ratio of the number of photons emitted to the number of photons absorbed by the fluorophore:

Φ = Number of photons emitted/Number of photons absorbed.

A quantum efficiency of approximately 0.9 indicates a highly efficient process, whereas Φ_F = 0 indicates a non-fluorescent molecule. Fluorescence quantum yield (Φ_F) is the fraction of excited molecules that return to the ground state. So, with emission of fluorescence photons ascertained by

$$\phi_F = \frac{K_r^{\ S}}{K_r^S + K_{nr}^S} = K_r^s . \tau_S \qquad (4)$$

Fluorescence quantum yield can be close to unity if the radiationless decay rate (k^S_{nr}) is much smaller than the rate of radiative decay (k^S_r).[26,27]

1.4.2 Applications of fluorescent chemosensors

Fluorescent chemosensors are versatile tools with various applications:

(i) Environmental Monitoring

- Pollutant Detection: Identify heavy metals and organic pollutants in water, air, and soil.
- Water Quality Testing: Monitor contaminants in drinking water and wastewater.

(ii) Biological and Medical Applications

- Cell Imaging: Visualize cellular components and monitor intracellular analytes.
- Disease Diagnosis: Detect biomarkers for diseases like cancer and cardiovascular disorders.
- Drug Development: Screen drug interactions and study pharmaceutical mechanisms.

(iii) Chemical Sensing

- Industrial Monitoring: Track chemical reactions and product quality in manufacturing.
- Quality Control: Ensure product safety in pharmaceuticals, food, and beverages.
- Environmental Remediation
- Pollutant Detection: Monitor the effectiveness of remediation techniques.

(iv) Forensic Science

- Crime Scene Investigation: Detect traces of substances like drugs or explosives.

(v) Educational and Research Applications

- Educational Tools: Demonstrate chemical principles in educational settings.
- Scientific Research: Explore new materials and develop novel sensing technologies.

(vi) Agriculture

- Soil Analysis: Optimize crop growth by analyzing soil composition and nutrient levels.
- Pesticide Detection: Detect chemical residues in crops and soil.

These sensors provide valuable information across various fields, enhancing safety, efficiency, and accuracy. It is used in *in vitro* or *in vivo* systems to monitor physiologically important species.

Furthermore, it is found that luminous chemosensors are clearly better than chemo dosimeters due to their reusability. Consequently, chemists are engaged in an exciting and dynamic field of research concerning the construction of fluorescent chemosensors. This is because these sensors may find use in cell physiology, analytical and environmental chemistry, and other

domains. Furthermore, these sensors may be used as a platform for engineering and/or manipulating different photophysical processes in order to eventually achieve sensitive and specific signalling of certain chemical or ionic species.[28]

1.4.3 Some conventional mechanisms for construction of fluorescent probes

Conventional methods have been devised for the fabrication of fluorescent probes, including photo-induced electron transfer (PET),[29-35] photo-induced charge transfer (PCT),[23] Intramolecular charge transfer (ICT),[30,32-35] twisted intramolecular charge transfer (TICT),[36] metal-ligand charge transfer (MLCT),[36,37] electronic energy transfer (EET),[32,33] Förster resonance energy transfer (FRET),[38] through bond energy transfer,[39] excited state intramolecular proton transfer (ESIPT),[40] aggregation-induced enhancement of emission (AIEE) and excimer/exciplex formation.[32-34,41,42]

1.4.3.1 Photoinduced Electron Transfer (PET)

In *fluorophore—spacer—receptor* systems, PET is the most prevalent method where only long-range electronic interactions are feasible. Photoinduced electron transfer (PET) is a widely used process in photosynthesis and artificial systems for solar energy conversion based on photoinduced charge separation. It is the electron transfer process that happens when specific photoactive materials interact with light signalling event resulting in emission quenching or enhancement (**Figure 1.2 and 1.3**).

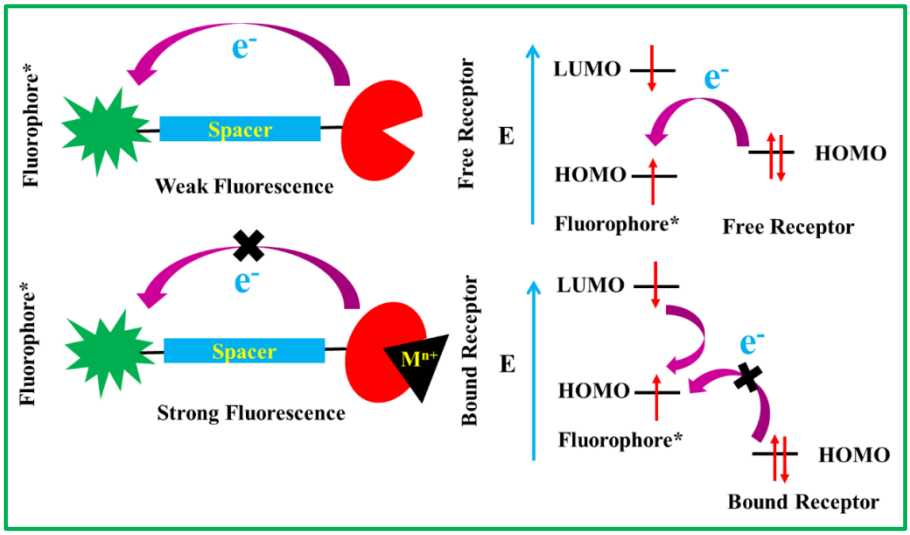

Figure 1.2 Mechanism of cation recognition by fluorescent PET sensors: reductive electron transfer.

As a result, it is highly useful for fluorescence sensing of neutral molecules, anions, or cations. Covalent linkage separates the fluorophore and receptor units, decreasing ground

state interactions, and is the primary component of covalently connected fluorescence probes, which are electrically independent. When the analyte is recognized by PET sensors, the *fluorophore—spacer—receptor* design modifies the quantum yield or fluorescence intensity.[43] In chemosensing Silva et. al. & Czamiket *et. al*[44] put forth this extensively applied design idea.

Fluorophores are electron acceptors whereas ionophores act as electron donors. The lowest unoccupied molecular orbital (LUMO) of the fluorophore can accept an electron from its highest occupied molecular orbital (HOMO) by absorbing an excitation photon. The electron from the ionophore's LUMO can travel through space to the LUMO of the excited fluorophore, blocking the emission transition of the excited electron from the fluorophore's LUMO to its HOMO, provided the energy of the ionophore's LUMO is slightly higher than that of the fluorophore's. This fluorescence quenching process is known as photo-induced electron transfer (PET). PET can occur in the bound complex when the energy level of the transition cation's LUMO lies between that of the fluorophore's HOMO and LUMO. An ON-OFF type chemosensor was constructed using a distinct PET process. This concept explains why a large number of fluoroionophores have been developed by altering either the binding motif or the fluorophore.[45-48]

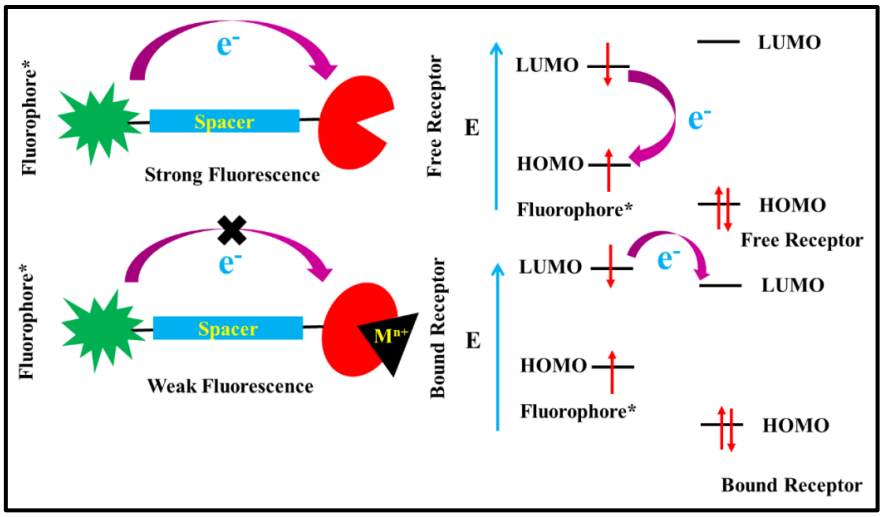

Figure 1.3 Fluorescent PET sensors: oxidative electron transfer.

1.4.3.2 Photo-induced charge transfer (PCT)

Photo-induced charge transfer (PCT) refers to a process in which the absorption of light (photons) causes the transfer of an electron from one part of a molecule (or molecular system) to another. This typically occurs in systems where there is a conjugation between an

electron-donating group (such as -NH_2, -NMe_2, or -OCH_3) and an electron-withdrawing group (such as >C=O or –CN). This movement of electrons from one orbital to another is accompanied by an instantaneous change in the dipole moment of the fluorophore. The process can significantly affect the photophysical properties of the molecule, such as its absorption and emission spectra, leading to phenomena like solvatochromism (where the color of the compound changes with the polarity of the solvent) and can be used in applications like sensing, where changes in the molecule's environment can be detected through shifts in its optical properties. Positive solvatochromism is a phenomenon that is associated with increased solvent polarity, lower relaxed state energy, and a stronger red shift of the emission spectrum (**Figure 1.4**). It is hypothesized that cation interaction with the donor or acceptor moiety will also alter the photophysical properties of the fluorophore by influencing the intramolecular charge transfer (ICT) efficiency, given the close relationship between the microenvironment and spectral features. The PCT type fluorophores can be used in cation sensing in two separate methods.[49]

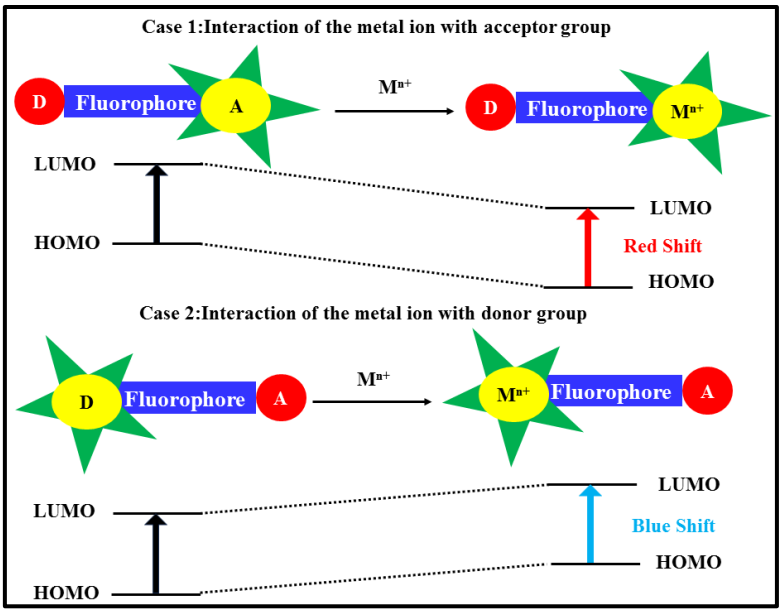

Figure 1.4 Sensing mechanisms of PCT fluorescent probes for metal cations.

When a cation binds to an accepter group, a red shift occurs. Complexation strengthens the acceptor's ability to extract electrons from the donor and raises the molar absorption coefficient. The stabilization of excited state of fluorophore on binding with cations is typically responsible for the red shift in emission spectra. On the other hand, the blue shift occurs when a donor group accommodates a cation resulting its lower electron-donating

activity. Upon excitation, a partial positive character is produced at the donor site due to charge transfer from the donor group to the acceptor, which reduces the donor group's capacity to connect with cations. The fluorescence spectrum frequently experiences a far smaller blue shift as compared to the absorption spectrum (**Figure 1.4**). All these indicate a photo disruption between the donor and acceptor groups due to coordination of a cation.[49,50] PCT chemosensors of this type are designed to detect metal ions selectively.[51,52]

1.4.3.3 Chelation Enhanced Fluorescence (CHEF)

When a guest molecule binds to the receptor site, the fluorophore-receptor connection disrupted. As a result, the fluorescence is either turned ON or OFF, resulting in either chelation enhanced fluorescence (CHEF) or chelation enhanced fluorescent quenching (CHEQ) (**Figure 1.5**).

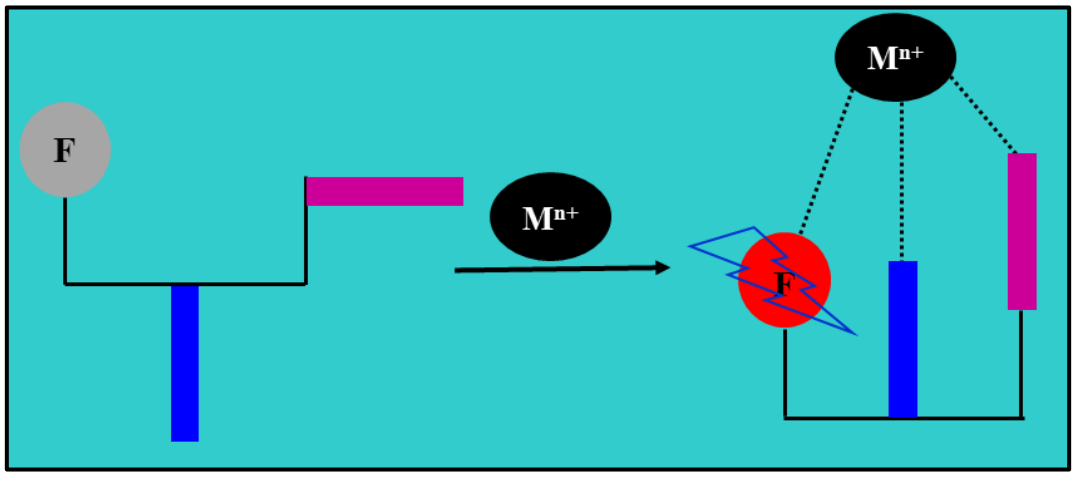

Figure 1.5 Pictorial representation of chelation enhanced fluorescence.

Particularly, metal ions show the CHEF effect. To see fluorescence variations on the metal ion binding, one must block the interaction between the fluorophore and the quenching metal ions while utilizing the fluorescent chemosensor, which is composed of a *fluorophore—spacer—receptor*.[30]

1.4.3.4 Excited state proton transfer (ESIPT)

Intramolecular hydrogen bond-containing fluorophores are susceptible to excited state proton transfer (ESPT), which produces aberrant fluorescence with a significant Stokes shift. A pre-existing six- or five-membered hydrogen bonded ring configuration causes the energy level of the excited state of these molecules to tend to drop when a hydroxyl (or amino) proton is

transferred to a nearby hydrogen-bonding atom (such as carbonyl oxygen or imine nitrogen). The ESIPT happens on a time scale of sub-picoseconds, making it a very quick process. Following the ground state relaxation of the keto-form, the energetically preferred enol-form is spontaneously regained by reversed proton transfer (**Figure 1.6**).[53] A significant Stokes shift of emission is produced during the ESIPT process as a result of the creation of a more stable excited molecule, called tautomer. If the acidity of the hydroxyl (or amino) proton is high enough, metal coordination will increase the acidity resulting its transfer from hydroxyl (or amino) group to a nearby hydrogen-bonded carbonyl oxygen or imine nitrogen there by disturbing the ESIPT process, and causing a substantial blue shift in the emission band. The pH, solvent polarity, and hydrogen bonding capacity of ESIPT fluorophores frequently have a significant impact on their total fluorescence emission spectra. The excitation wavelengths of most commonly reported ESIPT fluorophores lie in the UV-Vis range. Thus, the inhibition of ESIPT caused by metal coordination may provide a viable strategy for the creation of ratiometric probes for metal ions.[53]

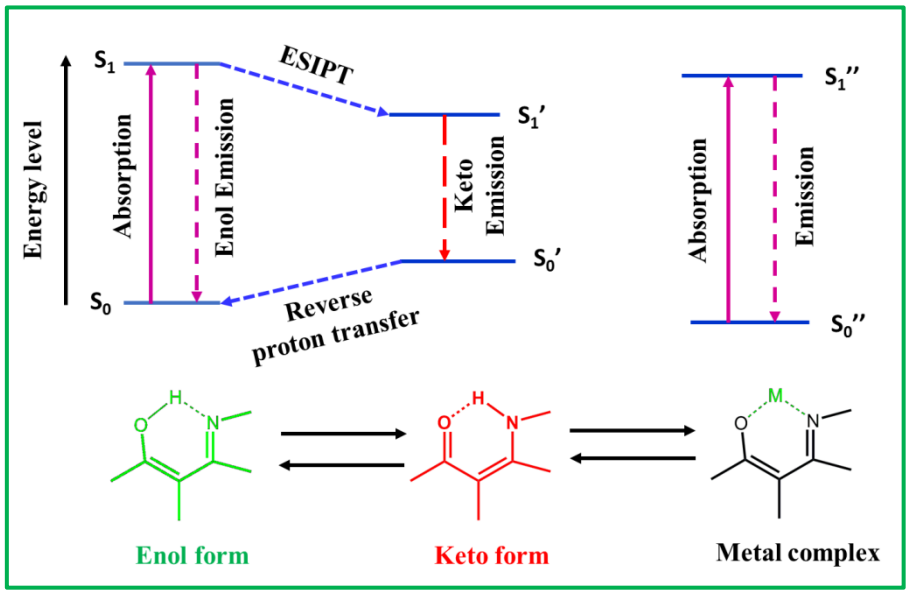

Figure 1.6 Schematic representation of ESIPT concept with respect to cation sensing.

1.4.3.5 Aggregation-based fluorescent sensing

Aggregation-based fluorescent sensing of metal ions helps to detect and quantify the presence of specific metal ions in a solution. Here, a change in the fluorescence properties of a probe occurs in the presence of a metal ion and gained significant attention due to its sensitivity, selectivity, and simplicity in detecting metal ions, which are essential in various fields like environmental monitoring, biochemistry, and clinical diagnostics. Aggregation-induced

emission enhancement (AIEE) has been seen in fluorescent probes recently, which is an uncommon phenomenon for organic luminophores providing superior photoemission efficiency in solution compared to solid states phenomenon (**Figure 1.7**).[54] Many of these probes are designed to be sensitive to the presence of metal ions.[55,56] When a metal ion binds to the probe it induces aggregation resulting a change in fluorescence properties (intensity, wavelength, or lifetime).

In the absence of metal ions, the fluorescent probe may exist as monomers, resulting in weak or negligible fluorescence due to free rotational and vibrational movement. When metal ions are introduced, they induce the aggregation of the probe molecules. This aggregation restricts molecular movement, reducing non-radiative decay processes and leading to enhanced fluorescence. It is also conceivable that the emission of an AIE-based system is likely to be responsive to an additional competing species that can modulate the probe–target interaction, thereby enabling the probe to render dual sensing. This sensor array might provide a fresh framework for creating cation detection sensors.[56,57]

In some cases, the probe is highly fluorescent in its monomeric form. However, a metal ion binding may induce aggregation resulting a significant fluorescence quenching. This phenomenon is often referred as Aggregation caused quenching (ACQ). This quenching is often due to π-π stacking interactions or energy transfer between the aggregated probes, facilitating non-radiative decay. Heavy metal ions like Hg^{2+} and Cu^{2+} are known to promote ACQ due to their strong coordination abilities, leading to fluorescence suppression.

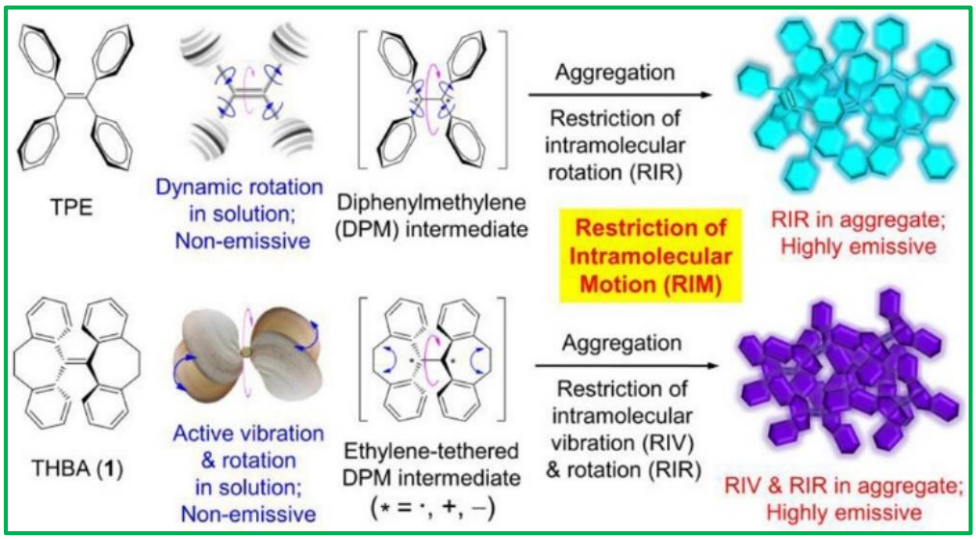

Figure 1.7 Representation of aggregation concept. Adapted with permission from ref. **54**. Copyright 2021 Wiley.

1.4.3.6 Excimer / Exciplex Formation

Excimers and **exciplexes** are excited-state molecular complexes that exist only in electronically excited states. They are important in photochemistry, photo physics, and certain laser technologies.

Excimers (Excited Dimers):

An *excimer* is a transient complex formed between two identical molecules, one in an excited electronic state and the other in the ground state and exist only in the excited state but dissociate when they return to the ground state. It is to be mentioned here that the two molecules do not bond in the ground state, and the binding interaction occurs only when one of them is in excited state. The most common example is the noble gas dimers like Xe_2, Kr_2, or Ar_2. For instance, xenon excimer lasers use xenon dimers (Xe_2) in an excited state to produce UV light. The broad, red-shifted emission, which has been interpreted as the experimental expression of excimer/exciplex[58-60] production, is caused by the difference in the equilibrium geometry of the excited state with respect to the ground state (**Figure 1.8**).

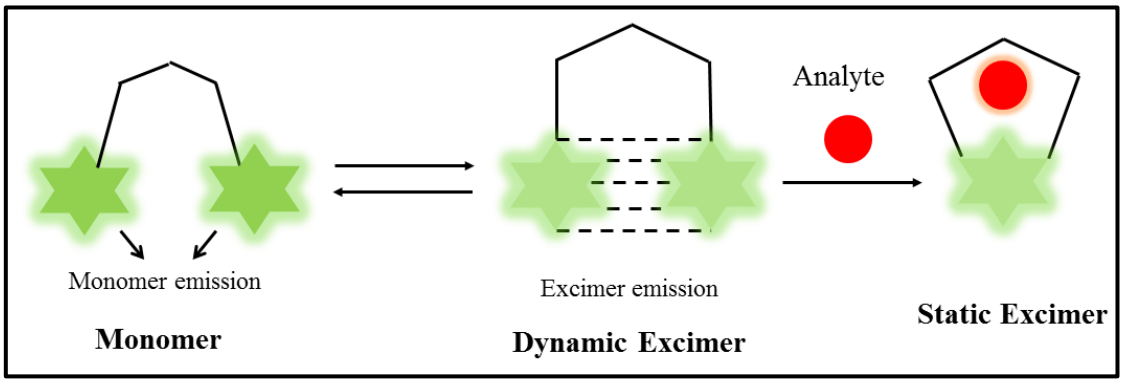

Figure 1.8 Excimer formation-based fluorescent sensing mechanism.

Intermolecular excited-state interactions have played a pivotal role in photochemistry and photo physics since the initial report of the pyrene excimer by Förster. If both chromophores are the same, the configuration interaction model can explain the stabilizing interaction between a ground state and an excited state molecule. In the event that the two chromophores differ, either an exciplex or a heteroexcimer may develop. The overlap of the two chromophores is critical for the stability of an excimer. Calculations suggest a picture of the excited-state complex in which the two chromophores, if they are planar, are at an optimum distance of 3.5 Å in a plane parallel orientation.

1.5 Chemistry of Rhodamine

Rhodamines belong to the xanthene's (**Figure 1.9**) family along with fluorescein and eosin dyes, and have been extensively used in multiple research fields after the discovery of the synthetic route by Noelting and Dziewonsky in 1905.

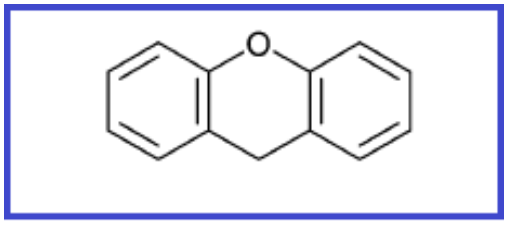

Figure 1.9 The general structure of xanthenes.

Rhodamine dyes, owing to their excellent photophysical properties along with photostability, high extinction coefficients for electronic spectral band at ≥475 nm, strong emission band at ≥ 550 nm and high quantum yield, find their application in various fields such as: (i) laser dyes, (ii) fluorescence standards for determining quantum yield and polarization; (iii) for characterizing the surface of polymer nanoparticles; (ii) to measure fluidity of lipid membranes, (iv) to detect polymer- bioconjugates; (v) to study adsorption of oligonucleotide-tides on latexes, (vi) to study the structure and dynamics of micelles; (viii) single-molecule imaging and (ix) imaging in living cells etc.[61,62]

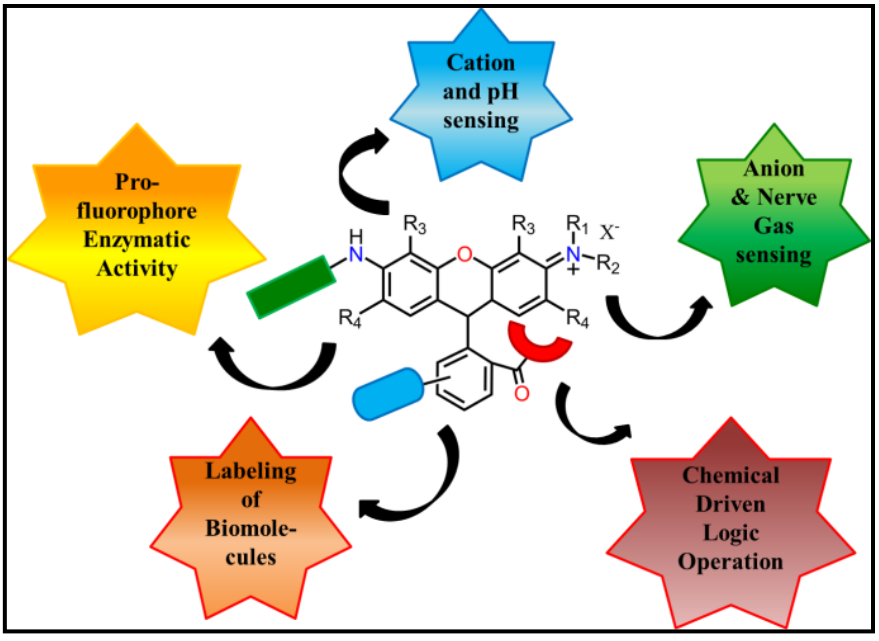

Figure 1.10 Representation of various upgraded applications of Rhodamine derivatives.

Spirolactam or spiro lactone derivatives of rhodamine are not luminous and are colourless, but when the spirolactam or lactone ring is opened, a bright pink fluorescence is generated. Rhodamine derivatives have also been used as molecular switches, a thermometer, to modify a virus's surface, and especially as chemosensors for *in vitro/ in vivo* selective detection of metal ions in the presence of other cations, anions and nerve gases. Rhodamine derivatives are crucial for this application, as recently been demonstrated by the fluorescent labelling of biomolecules and the development of chemically driven logic gate devices using rhodamine organic probes[61-64]. As a result, the above scheme (**Figure 1.10**) can be used to illustrate the different potential applications of Rhodamine derivatives.

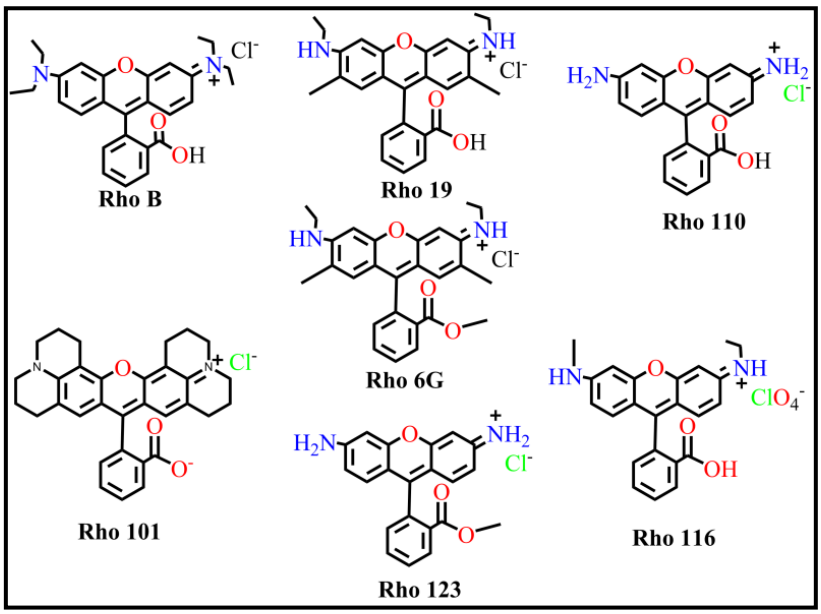

Figure 1.11 Commercially available various Rhodamine moieties.

Considering several advantages of Rhodamine dyes (**Figure 1.11**), Rhodamine 6G is chosen as the basic fluorophore unit for the design of suitable turn-on sensing platform for metal cations. Moreover, Rhodamine 6G is comparatively inexpensive among all the members of this family and straight-forward synthetic procedures can be adopted for metal ion recognition purpose. Usually, these changes are reversible in nature, with few exceptions, in the presence of a suitable metal ion. Nevertheless, the design of a reversible chemosensor based on rhodamine 6G is essential to ensure the re-usability of the probe providing an added advantage over the irreversible one.

Because rhodamine dyes have many benefits, we decided to use the rhodamine 6G moiety as the primary fluorophore unit in order to build an appropriate turn-on sensing platform for metal cations. Furthermore, Rhodamine 6G is the least expensive dye in this family among

the commercially available Rhodamine dyes, and it can be used for metal ion recognition by simple synthetic techniques.

1.5.1 Mechanistic pathway

The derivatives of the Rhodamine 6G moiety have a very diverse mechanistic pathway when it comes to cation sensing. The fact that the spirolactam ring containing the receptor unit is nearly colorless following metal-induced ring breakage is particularly intriguing.

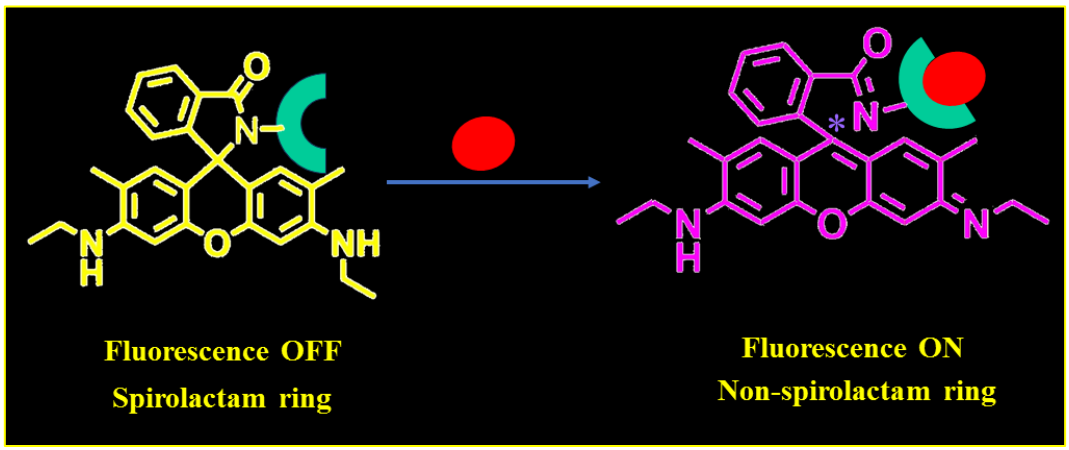

Figure 1.12 Schematic presentation of the change from cyclic lactam form to an acyclic xanthenes form of the rhodamine 6G derivatives on binding to a metal ion.

A noticeable shift in color from colourless to pink is linked with the transformation of the C atom from sp^3 (spirolactam-*C atom) to sp^2 (non-spirolactam-*C atom) hybridization. Specifically, these explain the observable shift in solution color from colorless to magenta and the corresponding "turn on" fluorescence response (**Figure 1.12**). Consequently, rhodamine 6G derivatives have been developed for the detection of iron because of their OFF-ON fluorescence characteristic, so that both reversible and irreversible reactions take place; nevertheless, a reversible chemosensor of a rhodamine 6G derivative is favoured because of the advantage of probe reusability.

1.6 Brief literature survey on rhodamine based fluorescent sensors for Fe(III)

Hava Ozay *et. al.*[65] developed a hexapodal ligand **1** (**Figure 1.13**), an excellent "'OFF-ON'" chemosensor that can selectively recognize Fe^{3+} in various samples over other cations and anions. This ligand was prepared from hexaazide-substituted phosphozene and rhodamine-6G derivative. Sensing characteristics of **1** was studied from UV-Vis and fluorescence spectroscopy. Stoichiometry in the complex between **1**-Fe^{3+} was found to be 1:3 from Job's

plot. The LOD of **1** for Fe^{3+} was calculated as 4.8 μM and formation constant was found to be 4.37 x 10^{14} in THF/H_2O medium. The reversible nature of this probe **1** was tested with ethylenediamine (EDA). According to this group fluorescence intensity of the complex quenched after the addition of EDA due to the exchange of ions from complex to EDA.

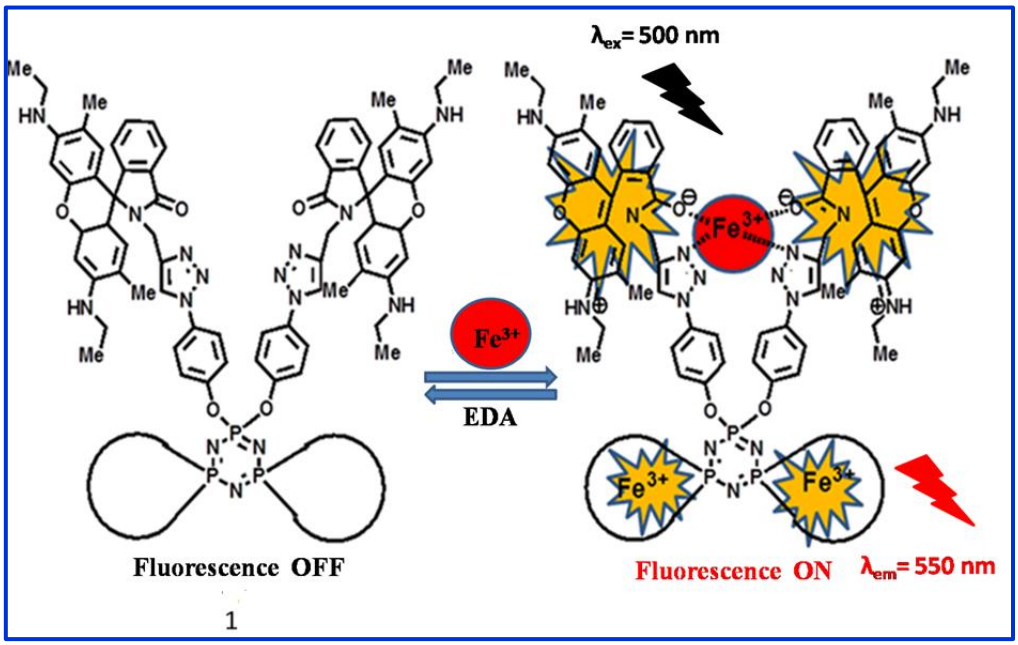

Figure 1.13 Structures of the chemosensor **1** for Fe^{3+} adopted from Ref 64.

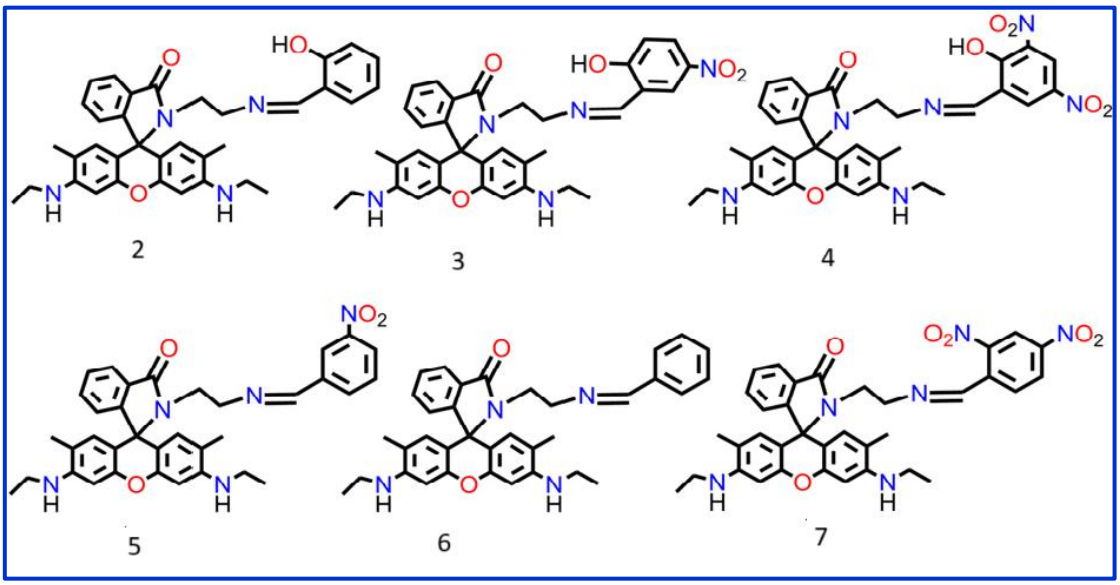

Figure 1.14 Structures of the chemosensors (**2-7**) for Fe^{3+}.

Lee, Kang and Kim's[66] group reported rhodamine-6G based fluorescent probes **2-7** (**Figure 1.14**) for the selective detection of Fe^{3+} in biological systems. Probes **2-7** showed a change in fluorescence in the presence of Fe^{3+} accompanied by the hydrolysis of the Schiff base.

Spectroscopic studies were performed with **2-7** in aqueous solution (CH_3CN: H_2O= 5:95). Absorption and emission band appeared at 526 nm and 551 nm for **7** and band became prominent with the increase in Fe^{3+} concentration, whereas in the presence of other biologically relevant metal ions fluorescence intensity remains almost unchanged. They observed usefulness of these probes for imaging Fe^{3+} in the HepG2 cell.

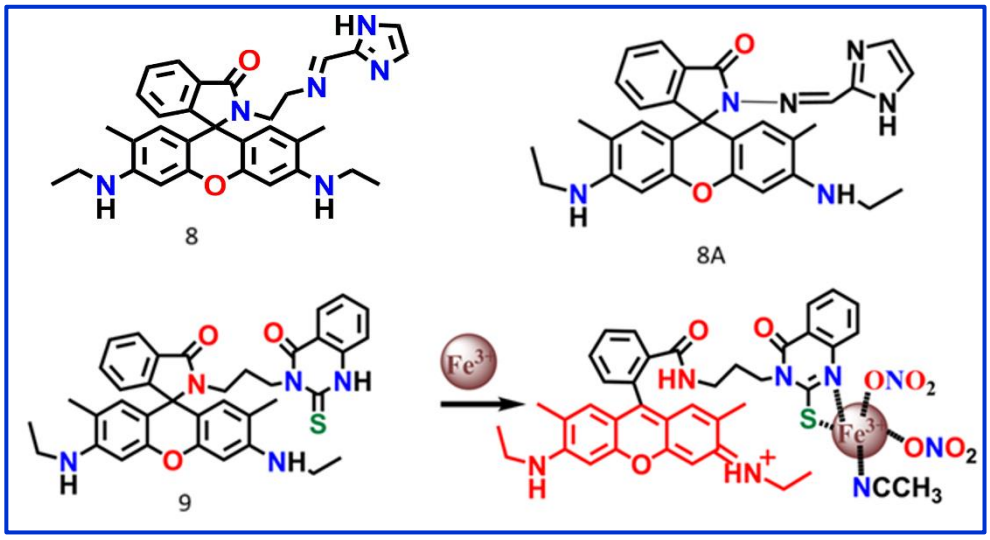

Figure 1.15 Structures of the chemosensors **(8** and **9)** for Fe^{3+}.

Chellappa et al.[67] prepared rhodamine 6G based probes **8** and **8A** (**Figure 1.15**) as chromo and fluorogenic sensor for the detection of Fe^{3+} in aqueous-PBS buffer (DMSO: H_2O, 2:8, pH=7.4) over other cations. In the presence of Fe^{3+} ion, the colour of the solution containing these probes changed from colourless to pink red. During fluorometric titration a strong emission band appeared at 553 nm and increase in intensity of the band continues till the saturation comes at 1.1 equivalent of metal ions. The LOD's of **8** and **8A** were evaluated as 0.66 nM and 0.45 nM respectively. The association constants of **8** and **8A** were calculated to be 6.74 x 10^4 M^{-1} and 3.964 x 10^4 M^{-1} respectively. This probe is almost non-fluorescent in the pH range 5 to 9 that makes the ligand useful under physiological conditions and for imaging of Fe^{3+} in living cells.

Wei-Na Wu and Qing Xu *et. al.*[68] reported **9** (**Figure 1.15**) that has been prepared from rhodamine-6G ethylenediamine and methyl -2-isothiocyanatobenzoate. It is extremely selective and sensitive chemosensor towards Fe^{3+} under biological condition. In the presence of Fe^{3+} ion, the ligand displayed a visual change in colour from colourless to yellow. A broad absorbance band at 380 nm and emission band at 555 nm with increase in Fe^{3+}concentration in 10 mM HEPES buffer (pH=7.4) was observed and intensity change was found to be linear.

Binding stoichiometry of **9** with Fe^{3+} was found to be 1:1 from job's plot. Quantum yield of **9** for five equivalents Fe^{3+} was found to be 0.69 in ethanol. LOD was found to be 4.11 µM. This probe was used successfully in monitoring Fe^{3+} in glioma cell line U251. This group also reported single crystal structures of **9** with Ag^{+} and Hg^{2+}.

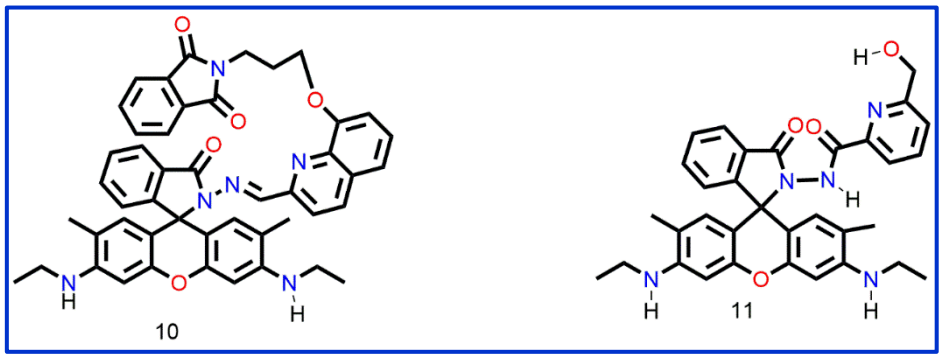

Figure 1.16 Structures of the chemosensors **(10** and **11)** for Fe^{3+}.

For the detection Fe^{3+} ion in aqueous medium, Xi and Zeng et al.[69] developed 'OFF-ON' fluorescent chemosensor **10** (**Figure 1.16**) that, in the presence other toxic metal ions and other metal ions in living organisms, showed selectivity towards Fe^{3+}. **10** showed a remarkable enhancement of absorption band intensity at 532 nm and emission band at 559 nm with 189-fold enhancement in an aqueous ethanol (7:3, v/v) solution. The formation constant for Fe^{3+} was calculated to be 1.1 x 10^{6} M^{-1} and stoichiometric ratio was observed to be 1:1 from job's plot. **10** could act as chemosensor in living cells. Goswami and Mondal[70] group developed CHEF induced colorimetric and fluorogenic sensor **11**, for the detection of Fe^{3+} and reported its crystal structure (**Figure 1.16**). It showed specificity over other transition metal ions and heavy metal ions having colorimetric change from colourless to pink in the presence of Fe^{3+} ion with a 23-fold enhancement of fluorescence intensity at 550 nm along with greenish yellow naked eye fluorescence at pH=7.2. The formation constant was calculated to be 5.55 × 10^{-7} M and 1:1 stoichiometric ratio was confirmed from job's plot. Reversibility and reusability of **11** was studied with EDTA fluorimetrically.

Ali et al.[71] reported rhodamine 6G based '**OFF-ON**' chemosensor **12** (**Figure 1.17**) for the selective detection of Fe^{3+} over other biologically important and toxic metal ions and this group showed interaction between **12**-Fe^{3+} complex and DNA. A gradual upgrade of the emission band at 556 nm was observed in presence of Fe^{3+} in HEPES buffer at pH=7.2. The binding constant was found to be 1.72 x 10^{4} M^{-1} with a detection limit of 0.17 µM. The

interaction between DNA and complex was monitored and a hypsochromic shift was observed in the presence of increasing concentration of DNA.

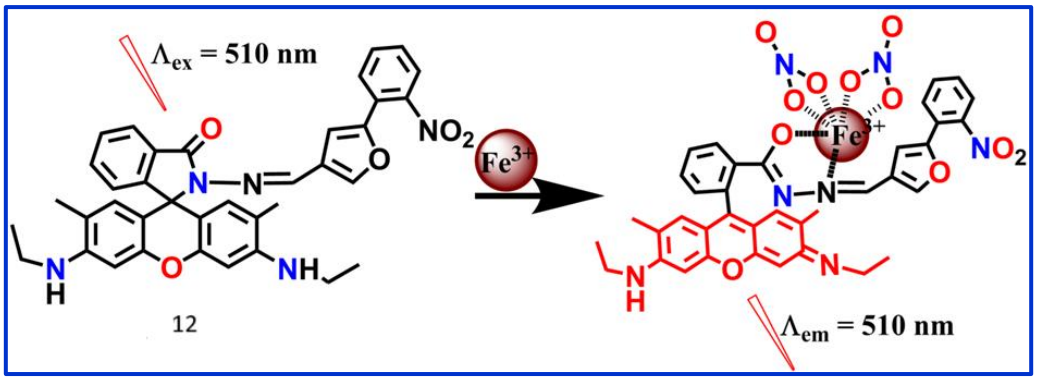

Figure 1.17 Structure of the chemosensor **12** for Fe^{3+}.

To discriminate Fe^{3+} from Fe^{2+}, Goswami et al.[72] reported a chemosensor **13** (**Figure 1.18**) that acted as a ratiometric and colorimetric sensor in MeOH/H_2O (1/4, v/v) upon excitation at 370 nm. A 1:1 complexation with $Fe^{3+}$was confirmed by HRMS and Job's plot. The structure of **13** was established by single crystal X-ray study. **13** acts as an efficient FRET-based single molecular switch for Fe^{3+} and also shows reversible nature with addition of Na_2EDTA solution in the **13**-Fe^{3+} complex (**Table 1.1**).

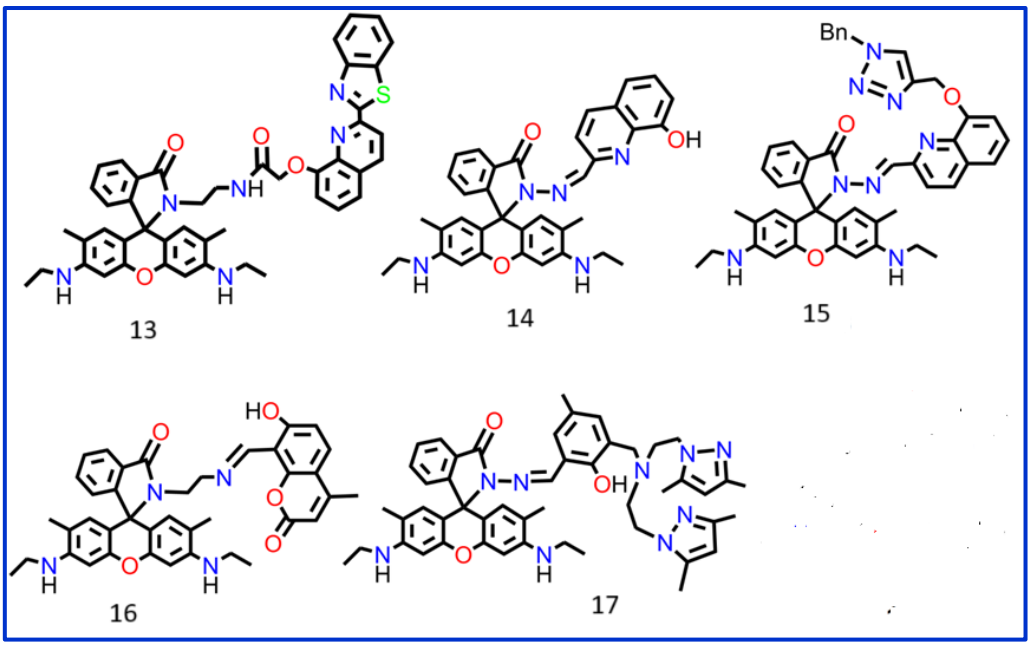

Figure 1.18 Structures of the chemosensors **(13-17)** for Fe^{3+}.

For the detection of Fe^{3+}, Thennarasu *et. al.*[73] developed two new rhodamine-based probes **14** and **15** (**Figure 1.18**) (in 1:1 v/v 0.01 M Tris HCl buffer–CH_3CN, pH 7.4 medium). **14**

displayed colorimetric as well as fluorometric response towards Fe^{3+} and Cu^{2+} ions whereas probe **14** displayed selectivity only towards Fe^{3+}. Job's plot indicates that **14** formed 1:1 complex with Fe^{3+} ion. The association constant for **15**-Fe^{3+} complex was found to be 4.5 × 10^4 M^{-1} with a detection limit of o.50 nM. The selectivity of **15** towards Fe^{3+} ions was also observed in the cell imaging of live fibroblast cells when treated with Fe^{3+} ions (**Table 1.1**).

Yan *et. al.*[74] reported a new fluorescent derivative **16** (**Figure 1.18**) which shows strong yellow-green fluorescence in ethanol medium in presence of Fe^{3+} with a 125-fold increase in emission. **16** acts as an 'OFF-ON' chemosensor that allows the detection of Fe^{3+} by monitoring changes in absorption and fluorescence spectra. 1:1 complexation between **16** and Fe^{3+} was confirmed by Job's plot. Fe^{3+} can potentially open the spirolactam ring and thus **16** shows a high selectivity and sensitivity towards Fe^{3+} over other metal ions. LOD was found to be in the range of 5.6 ppb (**Table 1.1**). The observed spectral response was supposed to originate due to photo-induced electron transfer coupled with intramolecular charge transfer.

To recognize Fe^{3+} in presence of biologically relevant as well as toxic metal ions, Ali and co-workers[75] reported a hexa-coordinating rhodamine-based chemosensor **17** (**Figure 1.18**) that selectively and rapidly recognizes Fe^{3+} upon excitation at 510 nm. Quenching in FI of [**17**-Fe^{3+}] was observed in the presence of I^- ion due to the heavy atom effect arising from spin-orbit coupling on coordination to metal centre of [**17**-Fe^{3+}] complex. **17** formed 1:1 complex with Fe^{3+} ion which was confirmed by Job's plot. Cytoplasmic *in vitro*/ *in vivo* cell imaging was studied for with Fe^{3+} ion (**Table 1.1**). Morphological studies were done for the probe **17** and its Fe^{3+} complex using SEM study, which shows spherical and hexagonal rod-like microstructures respectively. In the presence of SDS, the morphology for **17**-Fe^{3+} turned into cubic microstructures whereas in the presence of HSA both **17** and [**17**-Fe^{3+}] agglomerated severely.

For the detection of Fe^{3+} ions, Jadeja et al.[76] developed two novel Rhodamine–pyrazole-based colorimetric off–on fluorescent chemosensors **18** and **18A** (**Figure 1.19**) in which pyrazolone acts as the recognition moiety and Rhodamine 6G acts as the signalling moiety. Towards Fe^{3+}, both exhibit a remarkable 'turn-on' response. A 1:2 complex formation between Fe^{3+} and **18**/**18A** was observed. The fluorescent and colorimetric response of **18**/**18A** towards Fe^{3+} can be detected by the naked eye and their binding constants and LOD values are tabulated in **Table 1.1**.

A novel ratiometric fluorescence probe **19** (**Figure 1.19**) containing rhodamine and quinoline moiety was developed by Wang et al.[77] **19** displays a fluorescence emission at 425 nm in absence of Fe^{3+}, whereas a significant fluorescence enhancement at 550 nm in methanol was observed in the presence of Fe^{3+}. The association constant and LOD values are tabulated in **Table 1.1**. The observed spectral nature was suggested to occur due to FRET, coupled with PET. Job's plot suggests a 1:1 complexation between **19** and Fe^{3+}. By adding a Fe^{3+} bonding agent like Na_2EDTA, the reversibility of the recognition process by **19** was also observed.

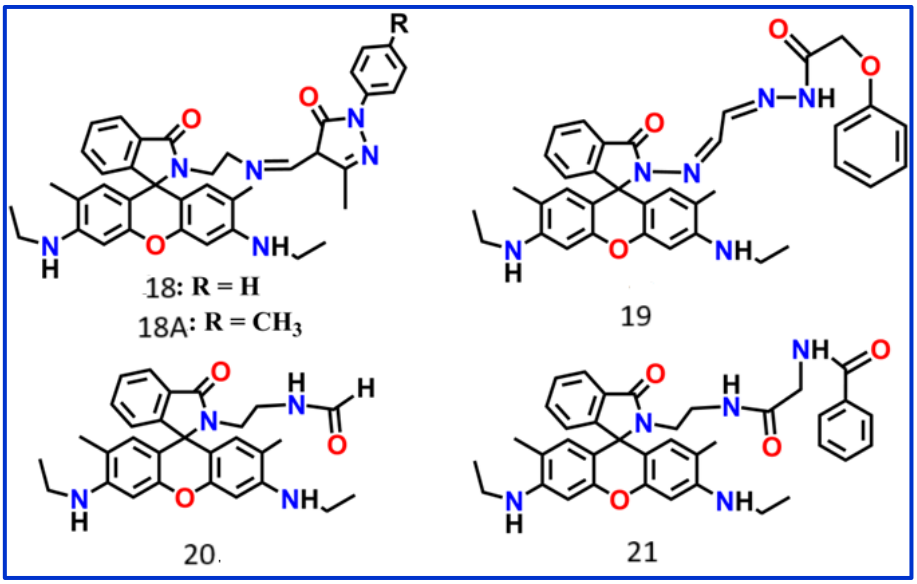

Figure 1.19 Structures of the chemosensors (**18-21**) for Fe^{3+}.

Weisheng Liu et al.[78] reported a reversible fluorescent probe **20** (**Figure 1.19**) for the optical detection of Fe^{3+} with a 1:1 stoichiometry in water upon excitation at 500 nm. A fluorescence turn-on response was displayed by **20** at 560 nm with increase in emission intensity, due to rhodamine ring-opening with Fe^{3+}, whereas a fluorescence turn-off response was observed on adding $Na_4P_2O_7$ to the **20**-Fe^{3+}complex. Furthermore, the cell permeability was detected by bioimaging investigations and its applicability to monitoring intracellular Fe^{3+} in living cells by confocal microscopy was concluded. The binding constant and LOD values related with the **20**-Fe^{3+}association are tabulated in **Table 1.1**.

Chang-Qing Qu et al.[79] developed a new fluorescent probe **21** (**Figure 1.19**), which upon addition of Fe^{3+} shows a distinct color change with a rapid emergence of fluorescence emission at 550 nm, thereby achieving 'naked eye' detection of Fe^{3+} upon excitation at 515 nm. Job's plot shows that the stoichiometric ratio between **21** and Fe^{3+} is 1:1. The probe **21** could be used to distinguish Fe^{3+} qualitatively and quantitatively on-site, as suggested by the

RGB experiment, test papers, and silica gel plates. Moreover, the probe **21** has also been successfully applied to have Fe^{3+} image in Caenorhabditis elegans, adult mice, and plant tissues. LOD was found to be 3.47 nM (**Table 1.1**).

Table 1.1 Some important parameters of recently reported fluorescent sensors for the selective detection of Fe^{3+}.

Probe	Analyte	Solvent system	Association constant	LOD	Applications	Ref.
13	Fe^{3+}	MeOH/H_2O (1/4, v/v)	6.12 x 10^5 M^{-1}	0.10 nM	-----	**71**
14	Fe^{3+} Cu^{2+}	0.01 M Tris HCl–CH_3CN (1: 1 v/v), pH 7.4	-----	-----	-----	**72**
15	Fe^{3+}	1: 1 v/v 0.01 M Tris HCl–CH_3CN, pH 7.4	4.5×10^4 M^{-1}	5×10^{-8} M	Cell imaging of live fibroblast cells	**72**
16	Fe^{3+}	Ethanol	1.1×10^7 M^{-1}	5.6 ppb	-----	**73**
17	Fe^{3+}	HEPES buffer	Dissociation constants K_d = (3.99 ± 0.09) x 10^{-5} M	110 nM	HepG2 cells	**74**
18	Fe^{3+}	Acetonitrile/water (1: 1 v/v)	6.08×10^5 M^{-2}	6.1×10^{-6} M	----	**75**
18A	Fe^{3+}	Acetonitrile/water (1: 1 v/v)	4.10×10^6 M^{-2}	4.2×10^{-6} M	----	**75**
19	Fe^{3+}	Methanol	1.67×10^4 M^{-1}	8.3×10^{-7} M	----	**76**
20	Fe^{3+}	H_2O	3.5×10^4 M^{-1}	1.9×10^{-8} M	Cell imaging in HBL-100 cells	**77**
21	Fe^{3+}	HEPES buffer (10 mM, pH = 7.4)/CH_3CN (2:3, v/v)	----	3.47×10^{-9} M	image in Caenorhabditis elegans, adult mice, and plant tissues	**78**

Hou et al.[80] reported a new fluorescent probe **22** (**Figure 1.20**) to detect Fe^{3+} in CH_3OH/H_2O mixture (1:9, v/v; PBS buffer 50 mmol/L; pH = 7.2) upon excitation at 525 nm. The binding of Fe^{3+} with **22** is irreversible and induces the ring opening and hydrolysing of spirolactam in the Rhodamine unit which gives emission intensity at 556 nm. **22** was applied to determine Fe^{3+} in drinking water samples and as a bioimaging reagent for Fe^{3+} detection in BEL-7402 cells. Job's plot and ESI-MS studies suggest that the stoichiometric ratio between **22** and Fe^{3+} in the complex is 1:1. LOD was found to be 0.030 μM/L (**Table 1.2**).

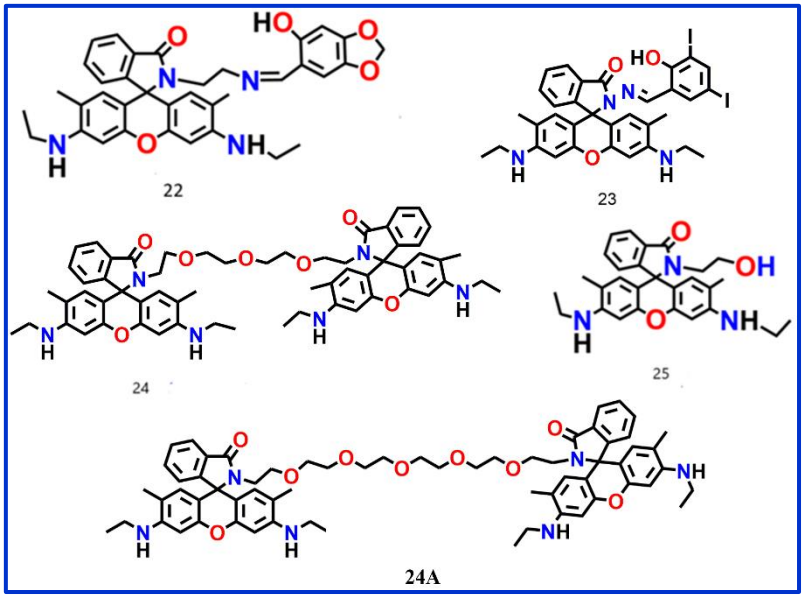

Figure 1.20 Structures of the chemosensors **(22-25)** for Fe^{3+}.

J. Annaraj et al.[81] synthesized a rhodamine based chemosensor **23** (**Figure 1.20**) which in the presence of Cu^{2+}/Fe^{3+} ion couple, enhances its absorbances at 521 and 529 nm for Cu^{2+} and Fe^{3+} ions respectively, by spirolactam bond cleavage. LOD was shown to be 263 pM (Cu^{2+}) and 2 nM (Fe^{3+}) (**Table 1.2**). It displays a fluorescence turn-on response with the increase in emission intensity at 554 nm for Fe^{3+} ions. The stoichiometric ratio of 1:1 between **23** and Fe^{3+}/ Cu^{2+} was obtained by Job's plot. Zebrafish bio-imaging and molecular logic circuits studied were also done.

K. Sung[82] developed chemo sensors **24, 24A** and **25** (**Figure 1.20**) for detection of Fe^{3+} and Cr^{3+} in 1:1 CH_3CN/H_2O medium. The probes are non-fluorescent and colorless but with addition of Fe^{3+} and Cr^{3+} strong emission and absorption intensity was observed at 550 nm and 530 nm. They also prepared another chemosensor **25** (**Figure 1.20**) for detection of Fe^{3+} and Cr^{3+} in 1:1 $DMSO/H_2O$ medium. The stoichiometric ratio of 1:1 between **24/24A/25** and Fe^{3+}/ Cr^{3+} was obtained by Job's plot. The detection limit and the linear range of **24** for

sensing Fe^{3+} are 33 µM and 35-104 µM, respectively (**Table 1.2**). The detection limit and the linear range of **24** for sensing Cr^{3+} are 38 µM and 39-154 µM, respectively. For **24A**, its detection limit and linear range for sensing Fe^{3+} are 10 µM and 14-69 µM, respectively, and its detection limit and linear range for sensing Cr^{3+} are 30 mM and 46-154 µM, respectively (**Table 1.2**). The detection limit and the linear range of **25** for sensing Fe^{3+} are 22 µM and 38-114 µM, respectively. The detection limit and the linear range of **25** for sensing Cr^{3+} are 43 µM and 85-212 µM, respectively (**Table 1.2**).

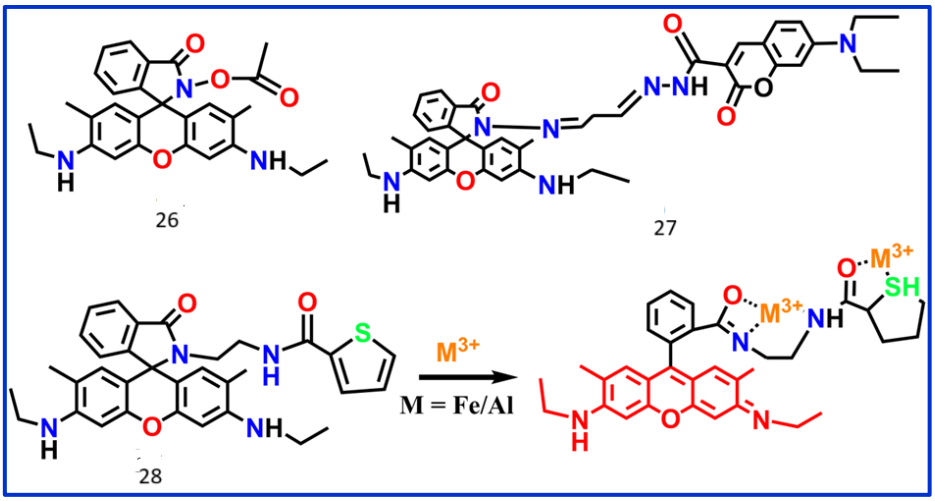

Figure 1.21 Structures of the chemosensors **(26-28)** for Fe^{3+}.

Yi Jiang and co-workers[83] reported rhodamine-based fluorescent and colorimetric reversible chemosensor **26** (**Figure 1.21**) for detecting Fe^{3+} that showed a significant enhancement of both fluorescence and absorbance intensity, with naked eye detection in CH_3CN. Job's plot showed the stoichiometric ratio of 1:1 between **26** and Fe^{3+}. The addition of CN^- could quench the fluorescence of the acetonitrile solution of **27**-Fe^{3+}, which indicates the reversible nature of the reaction between **26** and Fe^{3+}. The detection limit of **26** for Fe^{3+} was around 7.98 ppb (**Table 1.2**).

Li *et. al.*[84] developed a ratiometric fluorescent sensor **27** (**Figure 1.21**) based on the conjugation of rhodamine and coumarin for the detection of Fe^{3+}. Free **27** displays fluorescence emission at 475 nm, whereas upon addition of Fe^{3+} to its aqueous solution, a significant enhancement in fluorescence at 550 nm was recorded owing to an intramolecular fluorescence resonance energy transfer mechanism from coumarin to Rhodamine 6G. Job's plot showed a binding ratio of 1:1 in the Fe^{3+}-**27** complex. The binding constant for Fe^{3+}-**27** complexation was determined to be 5.2 x 10^4 M^{-1} and the detection limit of **27** for Fe^{3+} was around 4.05 µM (**Table 1.2**).

Table 1.2 Some important parameters of recently reported fluorescent sensors for the selective detection of Fe^{3+}.

Probe	Analyte	Solvent system	Association constant	LOD	Applications	Ref.
22	Fe^{3+}	CH_3OH/H_2O mixture (1:9, v/v)	-------	0.030 µM/L	Fluorescence images of BEL-7402 cells	79
23	Cu^{2+} Fe^{3+}	$CH_3CN:H_2O$ (9:1 v/v) mixture	1.1×10^{-2} M^{-1} 3.4×10^{-1} M^{-1}	263 pM 2 nM	Zebrafish bio-imaging and molecular logic circuits	80
24	Fe^{3+} Cr^{3+}	1:1 CH_3CN/H_2O	------	33 µM 38 µM	------	81
24A	Fe^{3+} Cr^{3+}	1:1 CH_3CN/H_2O	------	10 µM 30 µM	-----	81
25	Fe^{3+} Cr^{3+}	1:1 $DMSO/H_2O$	-------	22 µM 43 µM	-----	81
26	Fe^{3+}	CH_3CN	-----	7.98 ppb	-----	82
27	Fe^{3+}	$C_2H_5OH:H_2O$ (9:1,v/v)	5.2×10^{4} M^{-1}	4.05×10^{-6} M	-----	83
28	Fe^{3+} Al^{3+}	$C_2H_5OH:H_2O$ (1:1, v/v) mixture	3.91×10^{8} M^{-2} 5.26×10^{8} M^{-2}	5 µM 6 µM	Bioimaging of HeLa cells	84

Zhi-Qiang Hu et al.[85] reported a thiophene-modified rhodamine 6G chemosensor **28** (**Figure 1.21**), that shows a high degree of selectivity and sensitivity towards Fe^{3+} and Al^{3+} ions in fluorescence and ultraviolet spectroscopy, making it particularly suitable for cellular imaging applications. Fluorescence microscopy experiments demonstrated that **28** can be applied for the detection of Fe^{3+} and Al^{3+} in related cells and biological organs with satisfying resolution. Job's plot indicated a binding ratio of 2:1 in the Fe^{3+}/ Al^{3+}-**28** complex. The binding constant for Fe^{3+} was calculated to be 3.91×10^8 M^{-2} and the detection limit of **28** for Fe^{3+} was 5 μM (**Table 1.2**).

A highly sensitive and selective CHEF based sensor **29** (**Figure 1.22**) to recognize Al^{3+}, Fe^{3+} and Cr^{3+} in methanol/H_2O (1: 1, v/v, pH 7.2) was developed by Alam et al.[86] **29** showed the capability of naked eye detection with a considerable elevation in fluorescence intensities for Fe^{3+} (21-fold), Al^{3+} (14 -fold), and Cr^{3+} (10-fold) (λ_{ex} = 510 nm, λ_{em} = 555 nm). The K_f values were found to be 6.7 x 10^4 M^{-1}, 8.2 x 10^4 M^{-1}, and 6.0 x 10^4 M^{-1} for Fe^{3+}, Al^{3+}, and Cr^{3+} respectively. The limit of detection for Fe^{3+}, Al^{3+}, and Cr^{3+} were calculated and reported to be 0.29, 0.34, and 0.31 μM, respectively. In the Al^{3+}–**29** complex, arsenate ion quenches its fluorescence via its ring closed spirolactam form. The construction of advanced molecular logic and memory devices has been completed. Owing to the low cytotoxicity and high fluorescence intensity enhancement of the reported probe, it becomes a suitable candidate for imaging these metal ions in HepG2 cells and native cellular iron pools.

A rhodamine 6G-based chemo sensor **30** (**Figure 1.22**), for the selective and sensitive CHEF-based recognition of trivalent metal ions M^{3+} (M = Fe, Al and Cr) over mono, di and other trivalent metal ions, was reported by Ali and co-workers.[87] **30**, in presence of the mentioned metal ions showed significant enhancement in the absorption and fluorescence intensity viz. Fe^{3+} (669-fold), Al^{3+} (653-fold) and Cr^{3+} (667-fold) (λ_{ex} = 502 nm, λ_{em} = 558 nm) in H_2O/CH_3CN (7:3, v/v, pH 7.2). For the metal ions, the K_d values were calculated to be 1.94×10^{-5} (Fe^{3+}), 3.15×10^{-5} (Al^{3+}) and 2.26×10^{-5} M (Cr^{3+}). The LODs were calculated using 3σ methods and found to be 2.57, 0.78 and 0.47 μM for Fe^{3+}, Al^{3+} and Cr^{3+}, respectively. In case of [Fe^{3+}–**30**] complex, it was shown that cyanide ion can quench the fluorescence by grabbing the Fe^{3+}. Memory device and advanced molecular logic circuits with 2 and 4 inputs were also built.

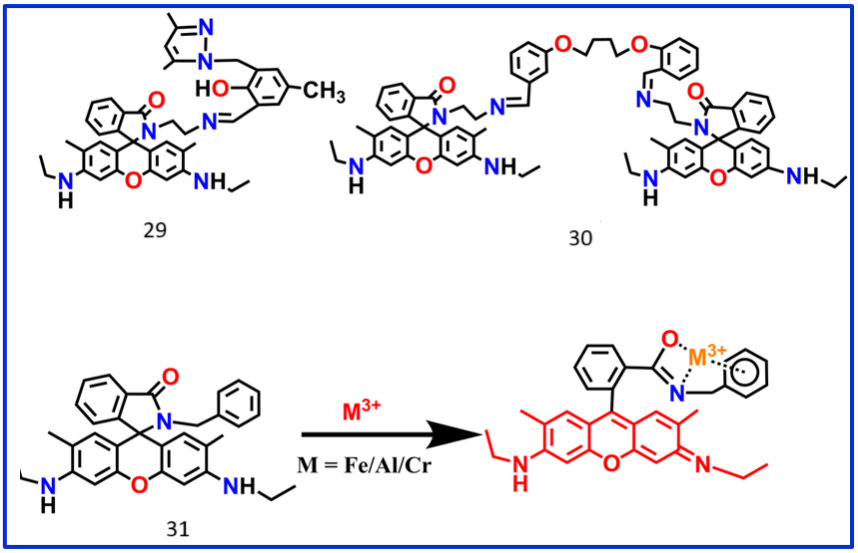

Figure 1.22 Chemical structures of some rhodamine 6G–based Fe^{3+}, Cr^{3+}, Al^{3+}sensors (**29-31**).

A new rhodamine 6G-benzylamine-based sensor **31** (**Figure 1.22**), with only hydrocarbon skeletons in the extended region, was developed and described using single-crystal X-ray crystallography by Ali and colleagues [88] that showed selective and sensitive recognition (even through naked eyes) of M^{3+} (M = Fe, Al, and Cr) over monovalent, divalent, and other trivalent metal ions. A considerable increase in fluorescence intensity for Fe^{3+} (41-fold), Al^{3+} (31-fold), and Cr^{3+} (26-fold) was detected (λ_{ex} = 502 nm, λ_{em} = 558 nm) when these metal ions were added to the probe in H_2O/CH_3CN (4:1, v/v, pH 7.2). K_f values were calculated and found to be 9.4 × 10^3 M^{-1}, 1.34 × 10^4 M^{-1} and 8.7 × 10^3 M^{-1} for Fe^{3+}, Al^{3+}, and Cr^{3+} respectively. LODs for Fe^{3+}, Al^{3+} and Cr^{3+} were calculated using 3σ methods and were found to be 1.28, 1.34, and 2.28 μM, respectively. Here, in case of Fe^{3+} again, it was found that cyanide ion muted the fluorescence enhancement by scavenging Fe^{3+} from the [Fe^{3+}–**31**] through formation of its ring-closed spirolactam form. Advanced molecular logic and memory devices have also been built. Due to the significant increase in fluorescence emission of **31** when complexed with M^{3+} metal ions, it was suggested that **31** can be an excellent candidate for bio-imaging of M^{3+} (M = Fe, Al, and Cr) in living HepG2 cells.

For the detection of Al^{3+}, Cr^{3+} and Fe^{3+} ions calorimetrically as well as fluorimetrically, a rhodamine-6G based probe **32** (**Figure 1.23**) was developed by P. Roy et al.[89] in which the fluorescence intensity at 550 nm was found to enhance by 1465, 588 and 800-fold in the presence of Al^{3+}, Cr^{3+} and Fe^{3+} ions respectively [methanol: water (9: 1, v/v), HEPES buffer at pH 7.4]. In the absence of these metal ions, due to the existence of a spirolactam ring, the

probe does not show any color and exhibits weak fluorescence, but trivalent cations form 1:1 complex with **32** (confirmed by Job's plot, elemental analysis, ESI mass spectral analysis), thereby inducing the opening of the spirolactam ring leading to change in color and the fluorescence intensity. For Al^{3+}, Cr^{3+}, Fe^{3+}, association constant values were found to be 1.47 x 10^5 M^{-1}, 6.24 x 10^4 M^{-1} and 8.74 x 10^4 M^{-1} respectively. LODs for Al^{3+}, Cr^{3+} and Fe^{3+} were calculated and found to be 6.97, 15.80 and 14.00 nM, respectively. **32** was also applied for living cell imaging (for Al^{3+}, Cr^{3+} and Fe^{3+} ions) with the human neuroblastoma SH-SY5Y cell line.

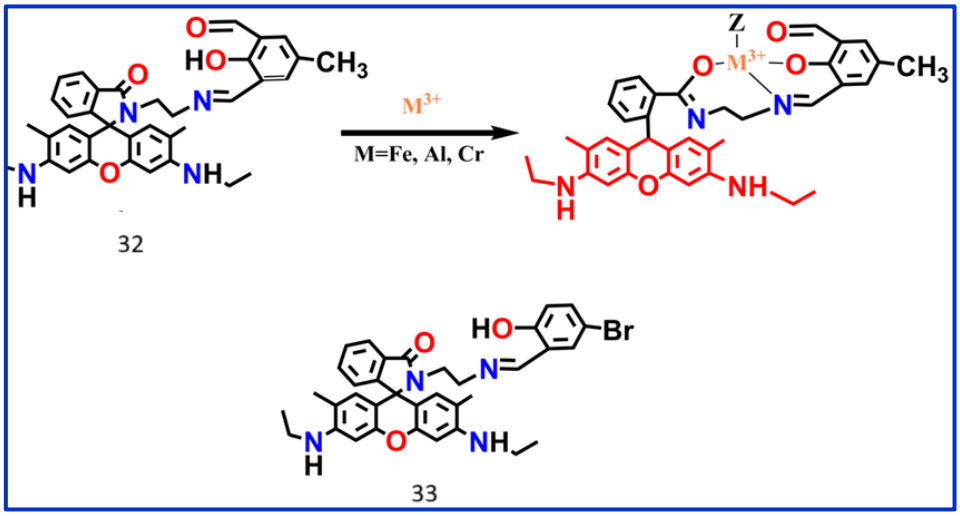

Figure 1.23 Chemical structures of some rhodamine 6G–based Fe^{3+}, Cr^{3+}, Al^{3+} sensors (**32-33**)

For the detection of trivalent cations, Al^{3+}, Fe^{3+} and Cr^{3+}, Roy et al.[90] developed a rhodamine-6G based probe **33** (**Figure 1.23**), that in the presence of these metal ions changes its colour from colorless to pink, enabling naked eye detection. It was reported that in the presence of Al^{3+}, Cr^{3+} and Fe^{3+} ions, the fluorescence intensity of **33** at 552 nm increases by 98, 50 and 38-fold, respectively [methanol: water (7:3, v/v) (pH 7.2)] upon excitation at 500 nm. **33**, due to its closed ring structure, is non-fluorescent, but the mentioned metal ions form complex with it and induce ring opening of spirolactam ring, leading to strong fluorescence. For Al^{3+}, Cr^{3+} and Fe^{3+}, LOD values were calculated and found to be 1.18, 1.80 and 4.04 nM, respectively. A 1:1 complex formation between **33** and metal ion was confirmed by Job's plot and mass spectral analysis. The K_d values were also determined using absorption spectral studies, and were found to be 5.20 ± 0.39, 4.07 ± 0.13 and 6.49 ± 0.21 µM for Al^{3+}, Fe^{3+} and Cr^{3+}, respectively. It was reported that quenching of emission intensity of **33**–Al^{3+} complex occurred in the presence of AsO_4^{3-} ion, because Al^{3+} was removed from its complex by

AsO_4^{3-} and non-fluorescent spirolactam unit was reproduced. Advanced level molecular logic devices e.g. molecular keypad lock, memory devices and different 3 and 5 input advanced level logic gates, have been constructed.

1.7 Present Work:

The main aim of our work is to synthesize some Rhodamine based fluorescent molecular probes for the recognition of Fe^{3+} ion in organo aqueous medium in very low concentration range, which have low toxicity to avail cell imaging study, protein binding study and the morphological change in the presence of metal ions. The ligands developed in this thesis are enlisted in **Scheme 1.1.**

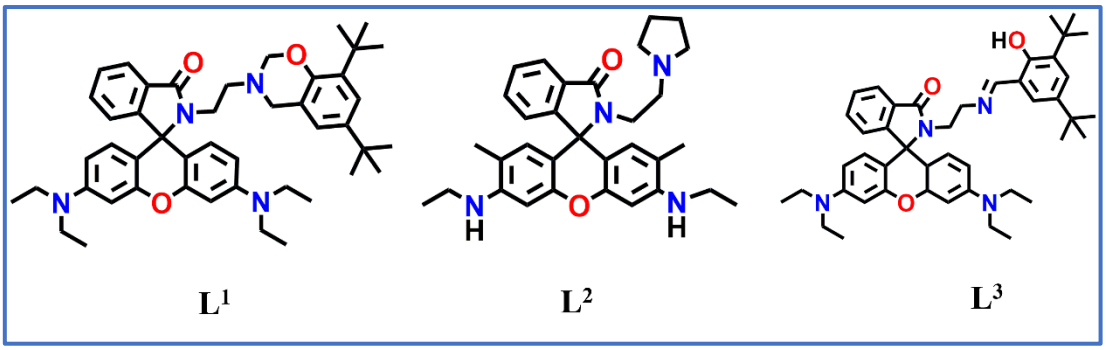

Scheme 1.1 Design of target molecules.

1.8 Physical measurements:

(i) Elemental analyses: Elemental analyses were carried out using a Perkin–Elmer 240 elemental analyzer.

(ii) FTIR spectra: Infrared spectra (400–4000 cm^{-1}) were recorded in liquid or solid states on a Nickolet Magna IR 750 series-II FTIR spectrometer.

(iii) ^{1}H NMR spectra: ^{1}H-NMR spectra were recorded in DMSO-d_6, $CDCl_3$, CD_3OD, CD_3CN on a Bruker 300 MHz NMR spectrometer using tetramethylsilane ($\delta = 0$) as an internal standard.

(iv) UV-vis spectra: UV-vis spectra were recorded on an Agilent diode-array spectrophotometer (Model, Agilent 8453).

(v) Mass spectra: ESI-MS^+ (m/z) of the ligands and complexes were recorded on a Waters' HRMS spectrometer (Model: QTOF Micro YA263).

(vi) Fluorescence spectra: Steady-state fluorescence measurements were performed with a PTI QM-40 spectrofluorimeter.

(vii) Life time measurements: Lifetimes were measured in Horiba–Jobin–Yvon on a Hamamatsu MCP photomultiplier (R3809) and analysed using IBH DAS6 software.

(viii) DFT calculations: Ground state electronic structure calculations of the ligand and complexes have been carried out using using Gaussian 09W software package, associated with the conductor-like polarizable continuum model (CPCM).

(ix) Cell imaging: Cell imaging studies has been performed under fluorescence microscope. Bright field and fluorescence images were taken using a fluorescence microscope (Leica DM3000, Germany) with an objective lens of 40x, 20 x magnifications.

(x) *p*H study: The pH of the solutions was recorded using a Systronics digital pH meter (Model 335, India) with the pH range 2–12. The pH meter was calibrated using standard buffer solutions (Acros Organics) of pH 4.0, 7.0 and 10.0.

(xi) XRD study: Single crystal X-ray diffraction studies were carried out on a Bruker SMART APEX-II CCD diffractometer.

(xii) SEM study: SEM studies were carried out on a ZEOL, JSM 8360 scanning electron microscope (SEM) operated at an accelerating voltage of 5 kV.

References

1) J. P. Sumner and R. Kopelman, *Analyst*, 2005, **130**, 528-533.
2) M. Ghaedi, A. Shokrollahi, R. Mehrnoosh, O. Hossaini and M. Soylak, *Cent. Eur. J. Chem.*, 2008, **6**, 488-496.
3) S. Bae and J. Tae, *Tetrahedron Lett.*, 2007, **48**, 5389-5392.
4) S. R. Lynch, *Nutr. Rev.*, 1997, **55**, 102-110.
5) P. Aisen, M. Wessling-Resnick and E. A. Leibold, *Curr. Opin. Chem. Biol.*, 1999, **3**, 200-206.
6) B. D. Autreaux, N. L. Tucker, R. Dixon and S. Spiro. *Nature*, 2005, **437**, 769-772.
7) D. Galaris, V. Skiada and A. Barbouti. *Cancer. Lett.*, 2008, **266**, 21-29.
8) A. S. Dornelles, V. A. Garcia, M. N. Lima, G. Vedana, L. A. Alcalde, M. R. Bogo and N. Schroeder, *Neurochem. Res.*, 2010, **35**, 564-571.
9) V. Iyengar and J. Wattles, *Clin. Chem.*, 1988, **34**, 474-481.

10) Diamond, D. *Principles of Chemical and Biological Sensors*. John Wiley & Sons, Inc; New York, NY: 1998.
11) A. T. Townsend, K. A. Miller, S. McLean and S. Aldous, *J. Anal. At. Spectrom.*, 1998, **13**, 1213-1219.
12) R. Klockenkämpfer, *Total-Reflection X-ray Fluorescence Analysis*, Wiley, New York, 1997.
13) A. P. de Silva, H. Q. Nimal Gunaratne, T. Gunnlaugsson, A. J. M. Huxley, C. P. McCoy, J. T. Rademacher and T. E. Rice, *Chem. Rev.*, 1997, **97**, 1515-1566.
14) J. F. Zhang, Y. Zhou, J. Yoon and J. S. Kim, *Chem. Soc. Rev.*, 2011, **40**, 3416-3429.
15) M. Formica, V. Fusi, L. Giorgi and M. Micheloni, *Coord. Chem. Rev.*, 2012, **256**, 170-192.
16) L. Xin, Y. Z. Chen, L. Y. Niu, L. Z. Wu, C. H. Tung, Q. X. Tong and Q. Z. Yang, *Org. Biomol. Chem.*, 2013, **11**, 3014-3019.
17) M. Gorur, F. Yilmaz, A. Kilic, Z. M. Sahin and A. J. Demirci, *Polym. Sci. Part A: Polym. Chem.*, 2011, **49**, 3193−3206.
18) M. Gorur, F. Yımaz, A. Kilic, A. Demirci, Y. Ozdemir, A. Kosemen and E. A. J. San, *Polym. Sci., Part A: Polym. Chem.* 2010, **48**, 3668-3682.
19) Z. Tian, C. Chen and H. R. Allcock, *Macromolecules*, 2013, **46**, 2715-2724.
20) H. R. Allcock, *Appl. Organometal. Chem*., 2013, **27**, 620-629.
21) R. J. Davidson, E. W. Ainscough, A. M. Brodie, G. B. Jameson, M. Waterland, H. R. Allcock, M. D. Hindenlang, B. Moubaraki, K. S. Murray, K. C. Gordon, R. Horvath and G. N. L. Jameson, *Inorg. Chem.* 2012, **51**, 8307-8316.
22) H. A. Alidagi, O. M. Girgic, Y. Zorlu, F. Hacivelioglu, S. U. Celik, A. Bozkurt, A. Kilic, and S. Yesilot, *Polymer*, 2013, **54**, 2250-2256.
23) C. W. Allen, *Chem. Rev*. 1991, **91**, 119-135.
24) B. Cosut and S. Yesilot, *Polyhedron*, 2012, **35**, 101-107.
25) K.K. Rohatgi-Mukherjee, Fundamentals of Photochemistry, Wiley Eastern, New Delhi, 1992.
26) A. D. Skoog, J. F. Holler and D. M. West, *Fundamentals of Analytical Chemistry*, 7th *ed.*, *Thomsen learning*, 2007, 601.
27) B. Valeur, *"Molecular Fluorescence: Principles and Applications" Wiley-VCH Verlag GmbH*, 2001.
28) M. Suresh, A.K. Mandal, S. Saha, E. Suresh, A. Mandoli, R. D. Liddo, P. P. Parnigotto and A. Das, *Org. Lett.*, 2010, **12**, 5406-5409.

29) A. P. de Silva, T. S. Moody and G. D. Wright, *Analyst*, 2009, **134**, 2385-2393.
30) J. S. Kim and D. T. Quang, *Chem. Rev.*, 2007, **107**, 3780-3799.
31) T. Gunnlaugsson, H. D. P. Ali, M. Glynn, P. E. Kruger, G. M. Hussey, F. M. Pfeffer, C. M. D. Santos and J. Tierney, *J. Fluoresce.*, 2005, **15**, 287-299.
32) J. F. Callan, A. P. de Silva and D. C. Magri, *Tetrahedron*, 2005, **61**, 8551-8588.
33) R. Martinez-Manez and F. San Cenon, *Chem. Rev.*, 2003, **103**, 4419-4476.
34) B. Valeur and I. Leray, *Coord. Chem. Rev.*, 2000, **205**, 3-40.
35) Z. C. Xu, J. Yoon and D. R. Spring, *Chem. Soc. Rev.*, 2010, **39**, 1996-2006.
36) W. Rettig and R. Laboulaye, *Fluorescence probes based on twisted intramolecular charge transfer (TICT) states and other adiabatic photoreactions, in Topics in Fluorescence Spectroscopy, Probe Design and Chemical Sensing*, ed. J. R. Lewkowicz, Plenum Press, New York, 1994, **4**, 109-149.
37) Q. Zhao, F. Y. Li and C. H. Huang, *Chem. Soc. Rev.*, 2010, **39**, 3007-3030.
38) K. E. Sapsford, L. Berti and I. L. Medintz, *Angew. Chem., Int. Ed.*, 2006, **45**, 4562-4589.
39) Y. Zhao, Y. Zhang, X. Lv, Y. Liu, M. Chen, P. Wang, J. Liu and W. Guo, J. Mater. *Chem.*, 2011, **21**, 13168-13171.
40) Y. N. Hong, J. W. Y. Lam and B. Z. Tang, *Chem. Commun.*, 2009, **390**, 4332-4353.
41) J. R. Lakowicz, Principles of Fluorescence Spectroscopy, Kluwer Academic/Plenum, New York, 1999.
42) C. Lodeiro and F. Pina, *Coord. Chem. Rev.*, 2009, **253**, 1353-1383.
43) C. M. G. dos Santos, M. Glynn, T. McCabe, J. S. Seixas de Melo, H. D. Burrows and T. Gunnlaugsson, *Supramol. Chem.*, 2007, **20**, 407-418.
44) A. P. de Silva and S. A. de Silva, *J. Chem. Soc. Chem. Commun.*, 1986, 1709-1710.
45) L. Yang, Q. Song, K. Damit-Og and H. Cao, *Sens. Actuators B*: Chem., 2013, **176**, 181-185.
46) R. Métivier, I. Leray, B. Valeur, *Chem. Eur. J.*, 2004, **10**, 4480-4490.
47) G. Bergamini, L. Boselli, P. Ceroni, P. Manca, G. Sanna and M. Pilo, *Eur. J. Inorg. Chem.*, 2011, **2011**, 4590-4595.
48) H. J. Jeong, Y. Li, M. H. Hyun, *Bull. Korean Chem. Soc.*, 2011, **32**, 2809-2812.
49) I. Leray, B. Valeur, *Coord. Chem. Rev.*, 2000, **205**, 3-40.
50) J. Bourson, J. Pouget, B. Valeur, *J. Phys. Chem.*, 1993, **97**, 4552-4557.
51) W. Jiang, Q. Fu, H. Fan and W. Wang, *Chem. Commun.*, 2008, 259-261.
52) S. Wagner, K. Brodner, B. A. Coombs, U. H. F. Bunz, *Eur. J. Org. Chem.*, 2012, **2012**, 2237-2242.

53) J. Zhao, S. Ji, Y. Chen, H. Guo and P. Yang, *Phys. Chem. Chem. Phys.*, 2012, **14**, 8803-8017.

54) Y. Wang, B. Xia, Q. Huang, T. Luo, Y. Zhang, P. Timashev, W. Guo, F. Li and X. J. Liang, Adv. Healthcare Mater., 2021, 10, 2100945.

55) W. Chen, Z. Zhang, X. Li, H. Agren and J. Su, *RSC Adv.*, 2015, **5**, 12191-12201.

56) X. Chen, X. Y. Shen, E. Guan, Y. Liu, A. Qin, J. Z. Sun and B. Z. Tang, *Chem. Commun.*, 2013, **49**, 1503-1505.

57) S. Samanta, S. Goswami, Md. N. Hoque, A. Ramesh and G. Das, *Chem. Commun.*, 2014, **50**, 11833-11836

58) S. Sarkar, S. Roy, A. Sikdar, R. N. Saha and S. S. Panja, *Analyst*, 2013, **138**, 7119-7126.

59) Y. Suzuki, T. Morozumi, H. Nakamura, M. Shimomura, T. Hayashita and R. A. Bartsh, *J. Phys. Chem. B*, 1998, **102**, 7910-7917.

60) L. N. Neupane, J. Y. Park, J. H. Park and K. H. Lee, *Org. Lett.*, 2013, **15**, 254-257.

61) H. N. Kim, M. H. Lee, H. J. Kim, J. S. Kim and J. Yoon, *Chem. Soc. Rev.*, 2008, **37**, 1465-1472.

62) M. Beija, C. A. M. Afonso and J. M. G. Martinho, *Chem. Soc. Rev*., 2009, **38,** 2410-2433.

63) X. Chen, T. Pradhan, F. Wang, J. S. Kim and J. Yoon, *Chem. Rev*., 2012, **112**, 1910-1956.

64) A. K. Das, A. Manna, A. K. Maity, P. Saha, C. K. Quah, H.-K Fun, H. A. Abdel-Aziz, S. Goswami, *Anal. Chem., 2014,* **86**, 6315-6322.

65) R. Kagit, M. Yildirim, O. O. S. Yesilot and H. Ozay, *Inorg. Chem*., 2014, **53**, 2144−2151.

66) M. H. Lee, H. Lee, M. J. Chang, H. S. Kim, C. Kang and J. S. Kim, *Dyes Pigm.*, 2016, **130**, 245-250.

67) G. Sivaraman, V. Sathiyaraja and D. Chellappa, *J. Lumin.*, 2014, **145**, 480–485.

68) Y. Wang, H.Q. Chang, W. N. Wu, X. L. Zhao, Y. Yang, Z. Q. Xu, Z. H. Xu and L. Jia, *Sens. Actuators B*: Chem., 2017, **239**, 60–68.

69) L. Huang, F. Hou, J. Cheng, P. Xi, F. Chen, D. Bai and Z. Zeng, *Org. Biomol. Chem*., 2012, **10**, 9634–9638.

70) S. Goswami, S. Das, K. Aich, D. Sarkar, T. K. Mondal, C. K. Quah and H. K. Fun, *Dalton Trans*., 2013, **42**, 15113–15119.

71) R. Bhowmick, A. S. M. Islam, U. Saha, G. S. Kumar and M. Ali, *New J. Chem., 2018,* **42**, 3435-3443.

72) S. Das, K. Aich, S. Goswami, C. K. Quah, and H. K. Fun, *New J. Chem*., 2016, **40**, 6414-6420.

73) N. R. Chereddy, S. Thennarasu and A. B. Mandal, *Dalton Trans*., 2012, **41**, 11753-11759.

74) J. An, T. Li, B. Wang, Z. Yang and M. Yan, *J. Coord. Chem.*, 2014, **67**, 921–928.

75) R. Bhowmick, A. S. M. Islam, A. Giri, A. Katarkar and M. Ali, *New J. Chem.*, 2017, **41**, 11661-11671.

76) S. Parihar, V. P. Boricha and R. N. Jadeja, *Luminescence*, 2015, **30**, 168-174.

77) J. C. Qin, Z. Y. Yang and G. Q. Wang, *J. Photochem. Photobiol. A: Chem.*, 2015, **310**, 122-127.

78) Y. Liu, R. Shen, J. Ru, X. Yao, Y. Yang, H. Liu, X. Tang, D. Bai, G. Zhang and W. Liu, *RSC Adv.*, 2016, **6**, 111754-111759.

79) J. Zhang, C. B. Bai, M. Y. Chen, S. Y. Yue, Y. X. Qin, X. Y. Liu, M. Y. Xu, Q. J. Zheng, L. Zhang, R. Q. Li, R. Qiao and C. Q. Qu, *ACS Omega*, 2021, **6**, 8616−8624.

80) Q. Diao, H. Guo, Z. Yang, W. Luo, T. Li and D. Hou, *Anal. Methods.*, 2019, **11**, 794-799.

81) A. S. Murugan, M. Kiruthika, E. R. A. Noelson, P. Yogapandi, G. G. Kumar and J. Annaraj, *Arab. J. Chem*., 2021, **14**, 102910.

82) Y. L. Lin, R. Sung and K. Sung, *Tetrahedron*, 2016, **72**, 5744-5748.

83) Z. Q. Hu, Y. Y. Gu, W. Z. Hu, L. L. Sun, J. H. Zhu and Y. Jiang, *ChemistryOpen*, 2014, **3**, 264-268.

84) J. C. Qin, Z. Y. Yang, G. Q. Wang and C. R. Li, *Tetrahedron Lett*., 2015, **56**, 5024-5029.

85) K. P. Wang, J. P. Chen, S. J. Zhang, Y. Lei, H. Zhong, S. Chen, X. H. Zhou and Z. Q. Hu, *Anal. Bioanal. Chem.*, 2017, **409**, 5547-5554.

86) R. Alam, R Bhowmick, A. S. M. Islam, A. katarkar, Keya Chaudhuri and M. Ali, *New J. Chem.*, 2017, **41**, 8359-8369.

87) D. Das, R. Alam and M. Ali, *Analyst*, 2022, **147**, 471-479.

88) D. Das, R. Alam, A. Katarkar and M. Ali, *Photochem. Photobiol. Sci*., 2019, **18**, 242-252.

89) A. Roy, S. Das, S. Sacher, S. K. Mandal and P. Roy, *Dalton Trans.*, 2019, **48**, 17594-17604.

90) S. Dey, S. Sarkar, D. Maity and P. Roy, *Sens. Actuators B: Chem.*, 2017, **246**, 518-534.

Chapter 2

A novel rhodamine-3,4-dihydro-2H-1,3-benzoxazine conjugate as a highly sensitive and selective chemosensor for Fe^{3+} ion with cytoplasmic cell imaging possibilities

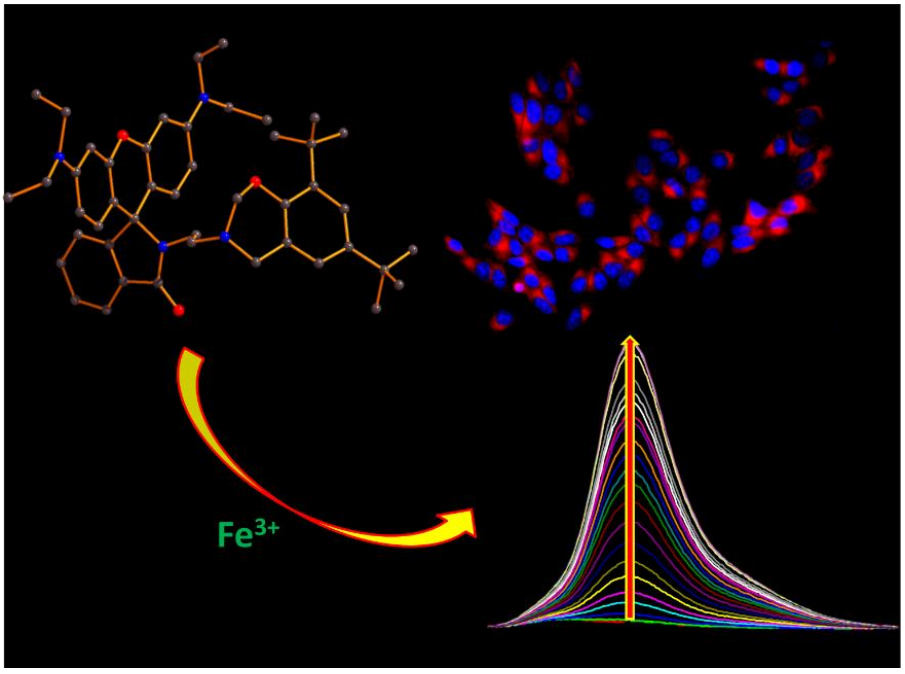

Abstract:

A novel, highly sensitive and selective fluorescent chemosensor 'rhodamine-3,4-dihydro-2H-1,3 benzoxazine' [RH-BZN (3)] has been synthesized and characterized by single crystal X-ray diffraction and other physicochemical techniques. In 3:7 water: MeCN (v/v) at pH 7.2 (10 mM HEPES buffer, μ= 0.05 M LiCl) it selectively recognizes Fe^{3+} through 1:1 complex formation resulting in a 240-fold fluorescence enhancement and a binding constant (K_f) of 1.50×10^4 M^{-1}. The otherwise non-fluorescent spirolactam form of the probe results in dual changes in absorbance and fluorescence arising out of opening of the spirolactam ring through coordination to Fe^{3+} ions. This probe could suitably be employed for cytoplasmic intracellular imaging of Fe^{3+} without notable cytotoxicity. The reversible binding of RH-BZN to Fe^{3+} was confirmed by reacting with tetra-n-butylammonium fluoride both in extra- and intra-cellular conditions.

2.1 Introduction

Transition-metal ions are involved in many biological and environmental processes, and there has been a great emergence of interest in recent years to generate metal ion selective and sensitive fluorescent probes.[1] Though numerous excellent studies focusing on the selective and sensitive detection of transition metal ions, e.g., Cu^{2+}, Pb^{2+}, Zn^{2+}, and Hg^{2+} have been reported,[2] examples of Fe^{3+}-selective fluorescent probes are still scarce,[3] despite the indispensable role of Fe^{3+} in many biochemical processes.[4,5]

Iron seems to be a versatile element involved in the proper functioning of numerous biological systems in all living organisms including bacteria and plants.[6,7] Both deficiency and excess of iron can induce a variety of diseases.[8] Iron being both useful and cytotoxic,[9] its deficiency throughout the developmental phases may lead to permanent loss of motor skills.[10] Iron over load in a living cell can lead to generation of reactive oxygen species (ROS) via the Fenton reaction, which can cause damage to lipids, nucleic acids, and proteins. Again, accumulation of iron in the central nervous system may lead to a number of diseases like Parkinson's, Huntington's and Alzheimer's.[9a] Keeping in view the roles played by iron in day-to-day life, the development of techniques for selective determination of iron is in great demand. It is necessary to design a simple, highly sensitive and selective chemosensor for Fe^{3+} detection and establish a method for the determination of trace amounts of Fe^{3+} ions. Most of the known Fe^{3+} sensors are based on fluorescence quenching mechanisms due to the paramagnetic nature of ferric ions.[11] In addition, most turn-on fluorescence sensors for Fe^{3+} are not selective over Cr^{3+} and Cu^{2+}.[12] Therefore, the development of a chemosensor that shows high selectivity for iron involving a fluorescence turn-on response is necessary for practical applications.

On the other hand, 3,4-dihydro-2H-1,3-benzoxazines are bicyclic heterocycles that are of significant interest in the polymeric and pharmacological fields. 1,3-Benzoxazines have long been recognized for their wide range of biological activities with uses as herbicides, agricultural microbicides, bactericides, fungicides, and antidepressive, anti-inflammatory, and anti-tumour agents.[13–16] Moreover, 1,3-benzoxazine monomers are recently used to develop a new type of phenolic resin, namely polybenzoxazines, by ring-opening polymerization.[17–20]

Rhodamine based conjugates with a spirolactam structure are, in general, non-fluorescent but act as colorimetric as well as fluorometric sensors with the enhancement of absorption and fluorescence emission intensity, respectively, on selective binding to metal ion(s).

In the present study, we are going to disclose, for the first time, a rhodamine-3,4-dihydro-2H-1,3-benzoxazine conjugate as a highly sensitive and selective fluorescent chemosensor for Fe^{3+} ions which further recognizes F^- ions by quenching the fluorescence of the Fe^{3+} – RH-BZN complex by abstracting the metal ion through the formation of a stable FeF_6^{3-} complex.

2.2 Experimental section

2.2.1 Materials and methods

The starting materials, such as, rhodamine B hydrochloride (Sigma-Aldrich), 2,4-di-tert-butyl phenol (Sigma-Aldrich), ethylene diamine (Sigma-Aldrich), formaldehyde (Sigma Aldrich), ferric nitrate (Sigma-Aldrich), and tetra-n-butyl ammonium fluoride (Sigma-Aldrich) were used for the preparation of RH-BZN and the Fe^{3+} complex. Other metal ions were obtained from previous studies. Solvents like EtOH, MeOH, MeCN, etc. (Merck, India) were of HPLC grade. MeCN and deionised water were used for spectroscopic studies**.**

2.2.2 Physical measurements

Infrared spectra (400–4000 cm^{-1}) were recorded from KBr pellets on a Nickolet Magna I750 series-II FTIR spectrophotometer. ^1H NMR and ^{13}C NMR were recorded in $CDCl_3$ Bruker 300 MHz NMR spectrometer using tetramethylsilane as an internal standard. UV vis spectra were recorded on an Agilent diode-array spectrophotometer (Model, Agilent 8453) steady-state fluorescence spectra were recorded on a PTI spectrofluorimeter (Model QM40.) and ESI-MS^+ (m/z) of the RH-BZN and Fe^{3+} complex were recorded HRMS spectrometer (Model: XeVG2 QTof).

2.2.3 Synthesis

2.2.3.1 Preparation of RH-BZN (3)

Rhodamine B hydrochloride (1) (5.0 mmol) and ethylenediamine (10.0 mmol) were dissolved in EtOH and refluxed for 6 hours with continuous stirring whereupon a white crystalline solid of rhodamine-amine (2) was deposited. The solid was filtered and washed with EtOH. The compound (2) (2 mmol), 2,4-di tertiary butyl phenol (4 mmol) and formaldehyde (4 mmol) were dissolved in MeCN and refluxed for 20 h with constant stirring whereupon a white solid was deposited, filtered and washed several times with ethanol and dried in air (68% yield) (**Scheme 2.1**). It was further recrystallized from MeOH to get single crystals suitable for X-ray diffraction studies. ^1H NMR (300 MHz, $CDCl_3$) ((δ, ppm): 1.20 (t, 12H, CH_3), 1.28 (t, 18H, CH_3), 2.48 (s, 2H, CH_2), 3.36 (s, 8H, CH_2), 3.83 (s, 2H, CH_2), 4.60 (s, 2H, CH_2), 6.28 (s, 2H, CH_2), 6.40–6.50 (m, 4H, ArH), 6.73 (1H, s, ArH), 7.09 (s, 2H, ArH), 7.29 (s, 1H,

ArH), 7.46 (s, 2H, ArH), 7.92 (s, 1H, ArH) (**Figure 2.1 and 2.2**). IR spectrum: 1692.15 cm^{-1} (spirolactam amide-keto), 1615.02 cm^{-1} (–CN) (**Figure 2.3**). ESI MS^{+} (m/z): 715.37 (RH-BZN + H^{+}) (**Figure 2.4**).

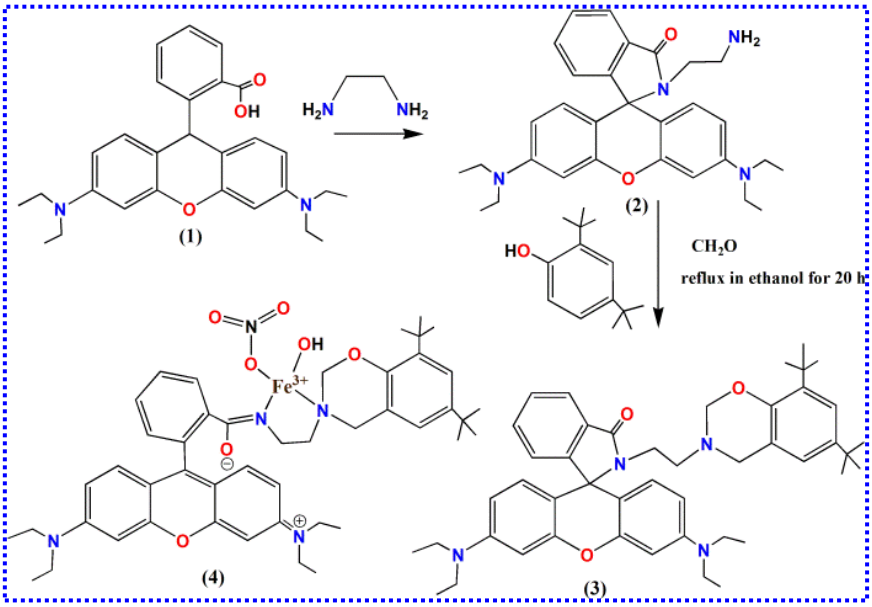

Scheme 2.1 Synthetic route for the preparation of probe 3 and its Fe^{3+} complex.

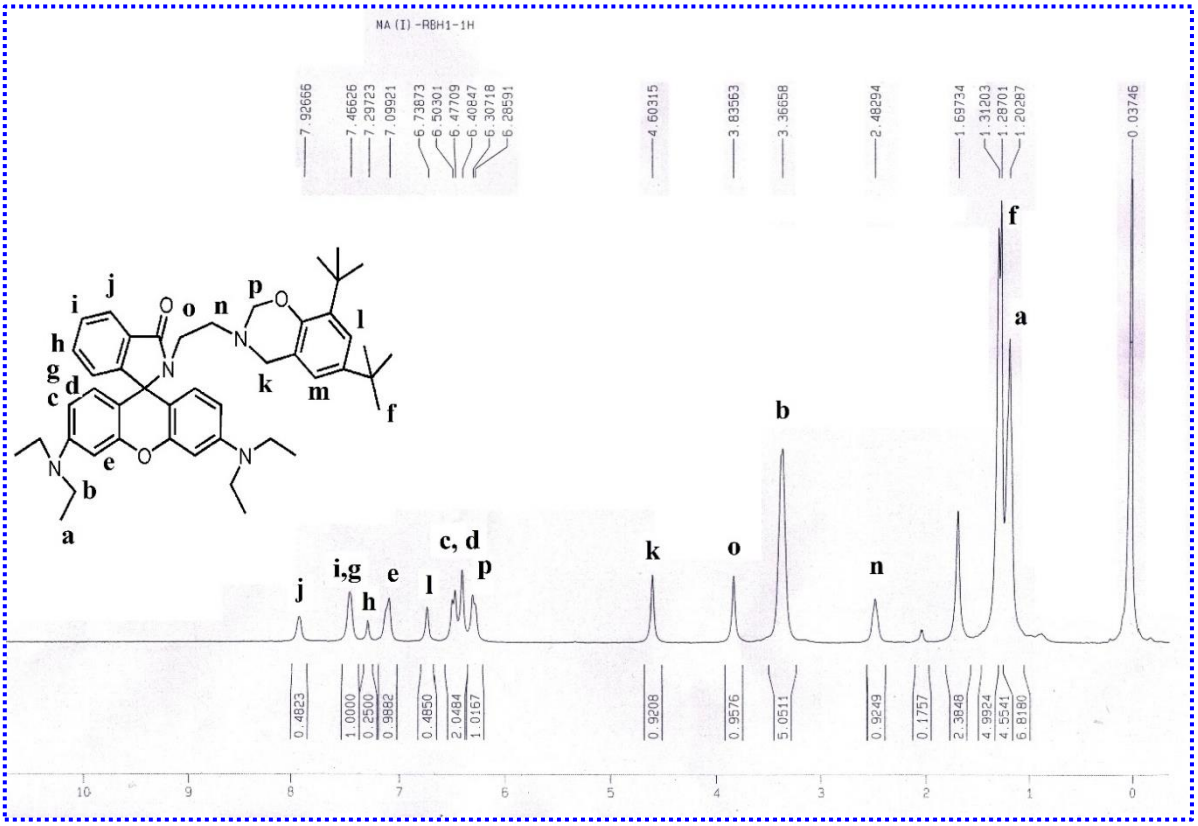

Figure 2.1 ^{1}H-NMR spectrum of RH-BZN.

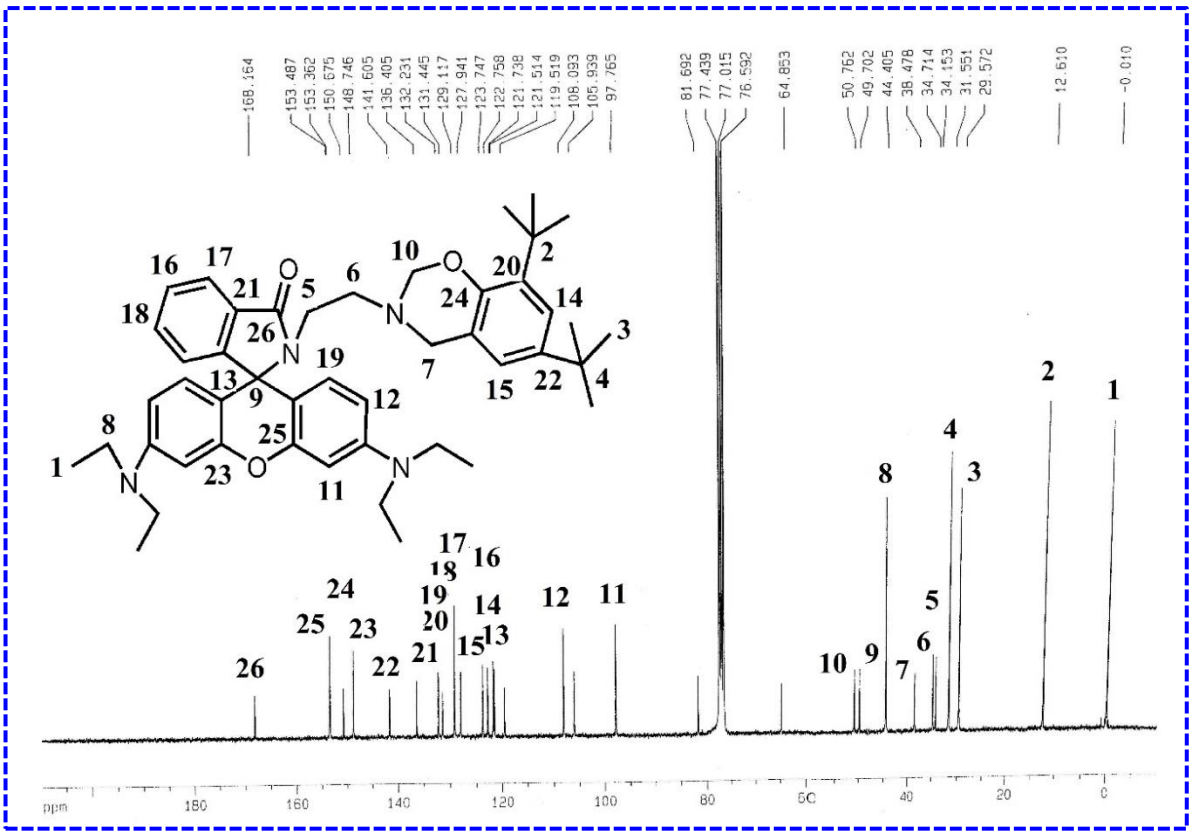

Figure 2.2 ^{13}C NMR spectrum of RH-BZN.

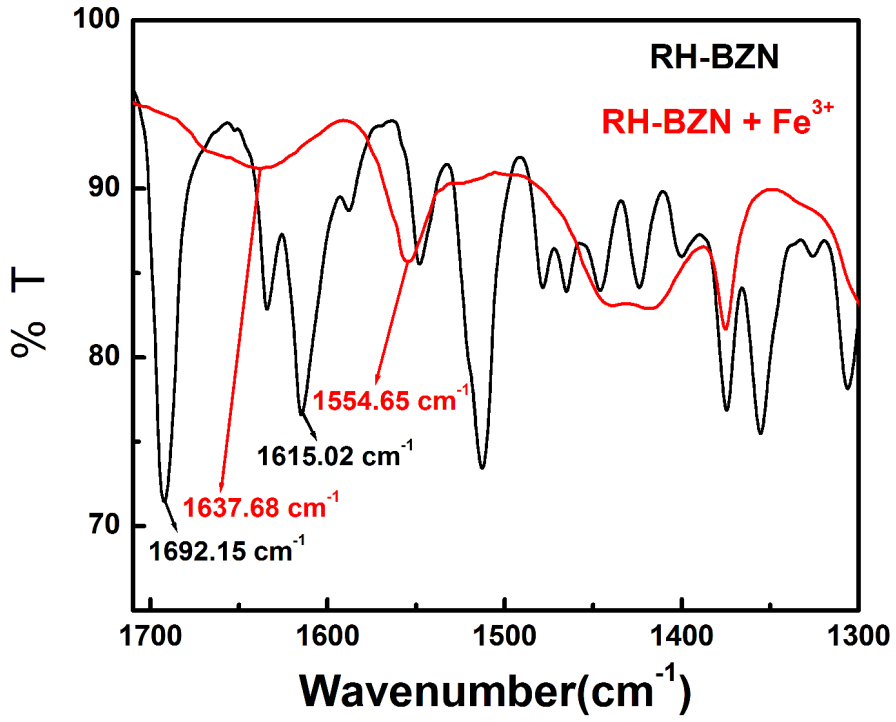

Figure 2. 3 IR Spectrum of **RH-BZN** and RH-BZN–Fe^{3+} complex.

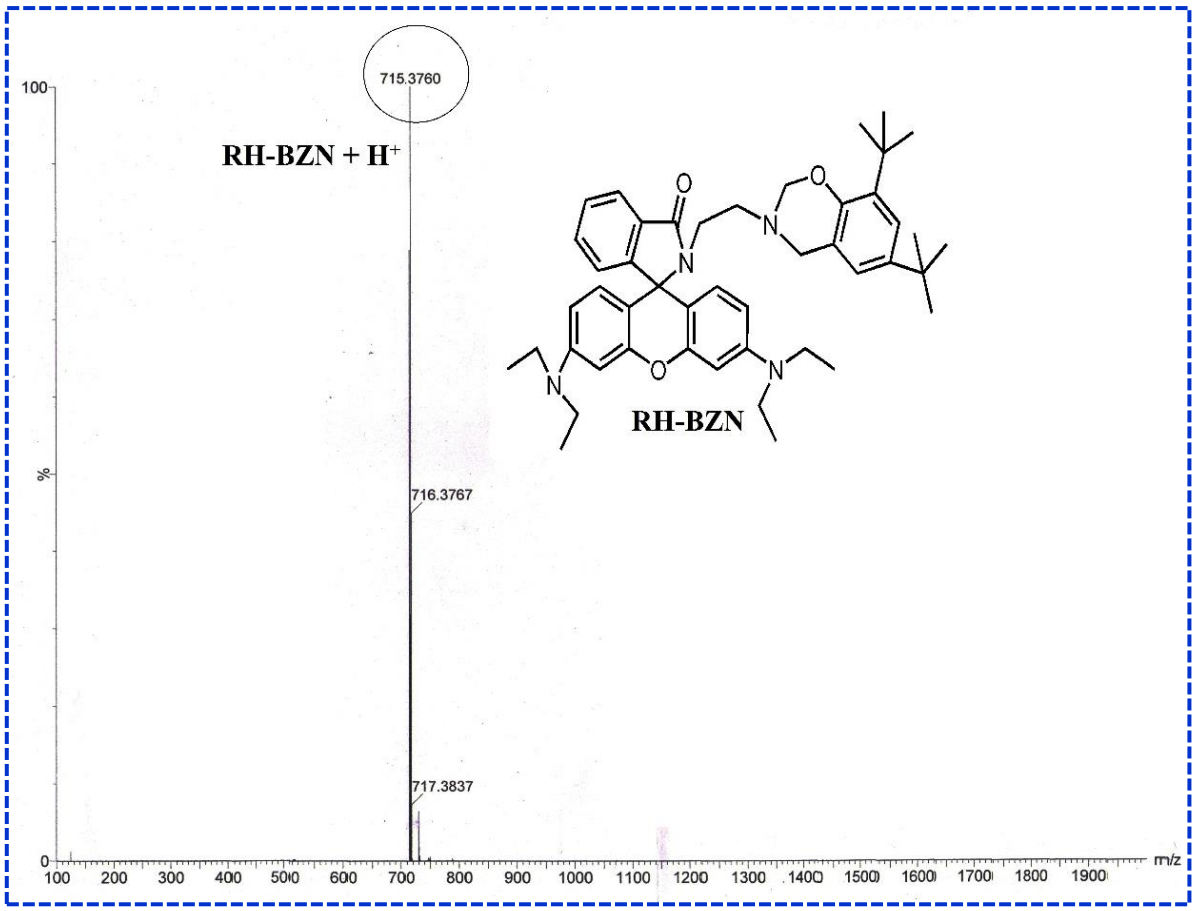

Figure 2. 4 Mass spectrum of RH-BZN in CH_3CN.

2.2.3.2 Synthesis of [Fe(RH-BZN)$(NO_3)_2(CH_3CN)$]

$Fe(NO_3)_3.9H_2O$ (2 mmol) in 5 ml MeCN was added drop wise to a solution of RH-BZN (2 mmol) in 20 ml MeCN with continuous stirring. After 1 hour the solution was filtered and kept aside undisturbed. After one day a crystalline complex was precipitated out. It was collected by filtration, washed several times with MeOH and dried in air. It was recrystallized from methanol. Several trials to grow single crystals failed. IR spectrum: $\bar{\nu}$ =1637.68 cm^{-1} (spirolactam amide-keto), 1554.65 cm^{-1} (–C=N) (**Figure 2.3**). ESI-MS^+ (m/z): 834.4961 [Fe (RH- BZN) (OCH_3) (CH_3OH)]; 934.5900 [Fe (RH-BZN) $(NO_3)_2(CH_3CN)$]; 948.6159 [Fe (RH-BZN) $(NO_3)_2(OCH_3)$] Na^+ (**Figure 2.5a and 2.5b**).

2.2.4 Cell culture

Human hepatocellular liver carcinoma (HepG2) cell lines (NCCS, Pune, India) were grown in DMEM supplemented with 10% FBS and antibiotics (penicillin, 10 µg ml^{-1}; streptomycin, 50µg ml^{-1}). Cells were cultured at 37 °C in a 95% air, 5% CO_2 incubator.

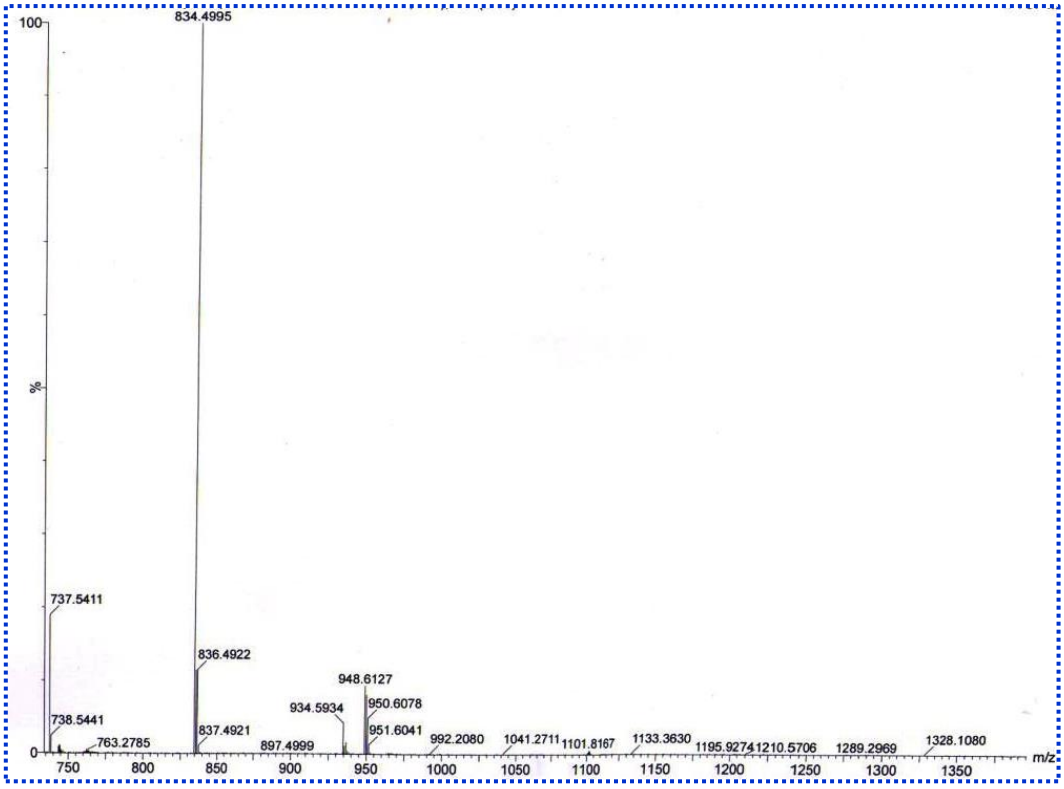

Figure 2.5a Mass spectrum of RH-BZN–Fe complex in CH_3CN and simulation spectra.

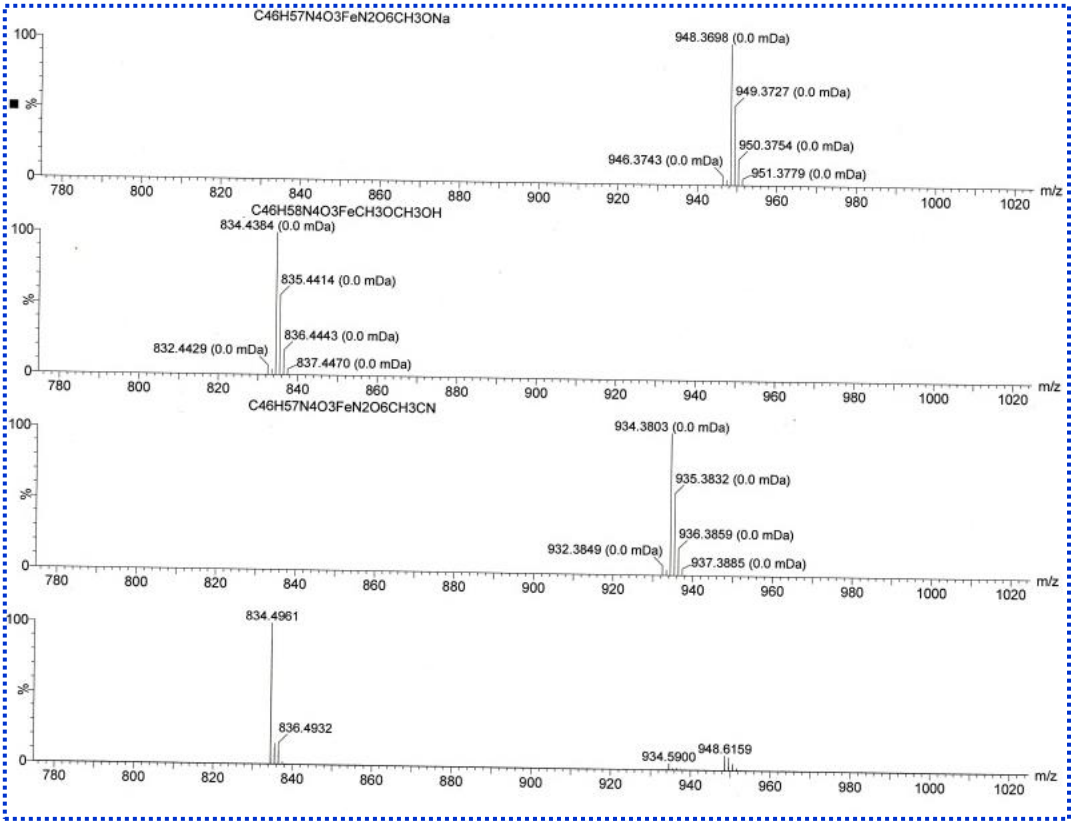

Figure 2.5b Mass spectrum of RH-BZN–Fe^{3+} complex in CH_3CN and simulation spectra.

2.2.5 Cell cytotoxicity assay

To determine the cell viability % of RH-BZN, MTT assay was performed. HepG2 cells (1× 10^5 cells per well) were cultured in a 96 well plate at 37 °C, and exposed to varying concentrations of RH-BZN, 1, 10, 20, 40, 60, 80 and 100 µM, respectively, for 12 h. 20 µl of MTT solution [5 mg ml $^{-1}$ 1× phosphate-buffered saline (PBS)] was added to each well of a 96-well culture plate and incubated again continuously at 37°C for a period of 4 h. All media were removed from wells and 100 µl of DMSO was added to each well and absorbance was measured at 550 nm (E_{Max} Precision Microplate Reader, Molecular Devices, USA). All experiments were performed in triplicate and the relative cell viability (%) was expressed as a percentage relative to the untreated control cells (**Figure 2.6**).

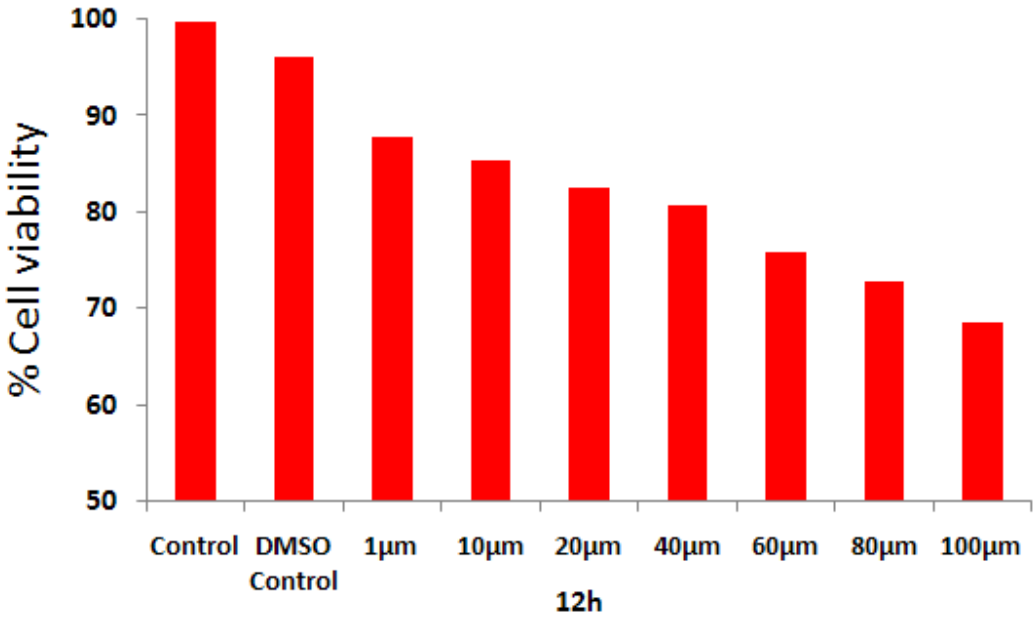

Figure 2.6 Cytotoxicity test of RH-BZN.

2.2.6 Cell imaging study

HepG2 cells were cultured and incubated in a 35× 10 mm culture dish over a cover slip for 24 h at 37 °C. The cells were allowed to incubate with 10 µm RH-BZN prepared by dissolving it in a mixed solvent (DMSO: water = 1: 9 (v/v)) in the culture medium for 30 min at 37 °C. After incubation, cells were washed twice with 1× PBS and allowed to be counterstained by DAPI (2-(4-amidinophenyl)-6-indolecarbamidine dihydrochloride-40, 6-diamidino-2-phenyl-indole, used for nuclear staining, Sigma). Fluorescence images of HepG2 cells were taken by using a fluorescence microscope (Leica DM3000, Germany) with an objective lens of 40x magnification. Fluorescence images of HepG2 cells were taken separately from another set of

experiment where cells were pre-incubated with 10 μM Fe^{3+} for 30 min at 37 °C followed by washing twice with 1x PBS and subsequent incubation with 10 μM RH-BZN for 30 min at 37 °C. Similarly, in another set of experiment, cells were incubated sequentially with 10 μm $Fe^{3+,}$ 10 μM RH-BZN and 100 μM F^- for 30 min at 37 °C with alternative washing with 1 x PBS two times. The live cell on the cover slip was allowed for fluorescence imaging. RH-BZN shows HepG2 intracellular cytoplasmic red fluorescence by forming a complex with Fe^{3+} and DAPI, used as the counter stain to localize the nucleus, showing blue color at the nucleus. Moreover, the concentration dependent capture of Fe^{3+} was preformed similarly as per described above at 1, 10 and 20 μM for RH-BZN. Furthermore, to confirm the cytoplasmic capturing of Fe^{3+} and cytoplasmic localization of RH-BZN after forming a complex with Fe^{3+} a cell imaging study was conducted by using DAPI as the nuclear counter stain and Lyso Tracker Green DND-26 (Invitrogen) for cytoplasm and, a live cell imaging study was carried out as described above. Likely, RH-BZN showed HepG2 intracellular cytoplasmic red fluorescence by forming a complex with Fe^{3+} confirmed against a nuclear and cytoplasmic tracker.

2.2.7 Solution preparation for UV-vis and fluorescence studies

For both UV-vis and fluorescence titrations, a stock solution of 1.0×10^{-3} M of the probe 3 was prepared by dissolving it in 0.5 ml MeCN and finally the volume is made up to 10 ml by MeCN. Similarly, 10 ml 1.0×10^{-3} M stock solutions of Fe^{3+} and tetra-n-butyl ammonium-fluoride were prepared separately in MeCN. 100 ml solution of 10 mM HEPES buffer was prepared and the pH was adjusted to 7.24 by using HCl and NaOH as required. 2.5 ml of this buffer solution was pipetted out into a cuvette to which 20 μM of the probe was added and Fe^{3+} ions were added incrementally starting from 0 to 25 μM in a regular interval of volume and UV-vis and fluorescence spectra were recorded for each solution. Similar is the case for tetra-n-butyl ammonium fluoride titration. Path length used of the cells for absorption and emission studies was 1 cm. Fluorescence measurements were performed using 2 nm × 2 nm slit width.

2.2.8. Quantum yield determination

Fluorescence quantum yields (Φ) were estimated by integrating the area under the fluorescence curves with the equation:

$$\Phi_{sample} = \frac{OD_{std}}{OD_{sample}} \text{ X } \frac{A_{sample}}{A_{std}} \text{ X } \Phi_{std}$$

where, A is the area under the fluorescence spectral curve and OD is optical density of the compound at the excitation wave length. The standard used for the measurement of fluorescence quantum yield was rhodamine 6G (Φ_{std} =0.94 in CH_3OH).

2.3 Result and discussion

As depicted in Scheme 2.1, receptor RH-BZN (3) was synthesized from the reaction of rhodamine-B with ethylenediamine followed by the Mannich reaction with 2,4-di-tert-butylphenol in the presence of formaldehyde in EtOH in refluxing conditions for 20 h with 68% yield. The final product (3) was well characterized by ^{1}H NMR (**Figure 2.1**), ^{13}C NMR (**Figure 2.2**), IR (**Figure 2.3**), HRMS (**Figure 2.4 and 2.5**) and a single crystal X-ray diffraction method (**Figure 2.7**). Details of the method of data collection and refinement are listed in **Table 2.1**.

Single crystal X-ray diffraction studies reveal that the compound RH-BZN crystallises in a monoclinic system of space group P21/c. The crystallographic details are depicted in **Table 2.1**. The receptor 3 was found to be a highly sensitive and selective colorimetric and fluorogenic dual sensor for Fe^{3+} while in the absence of Fe^{3+}; the solution of 3 is colourless and non-fluorescent.

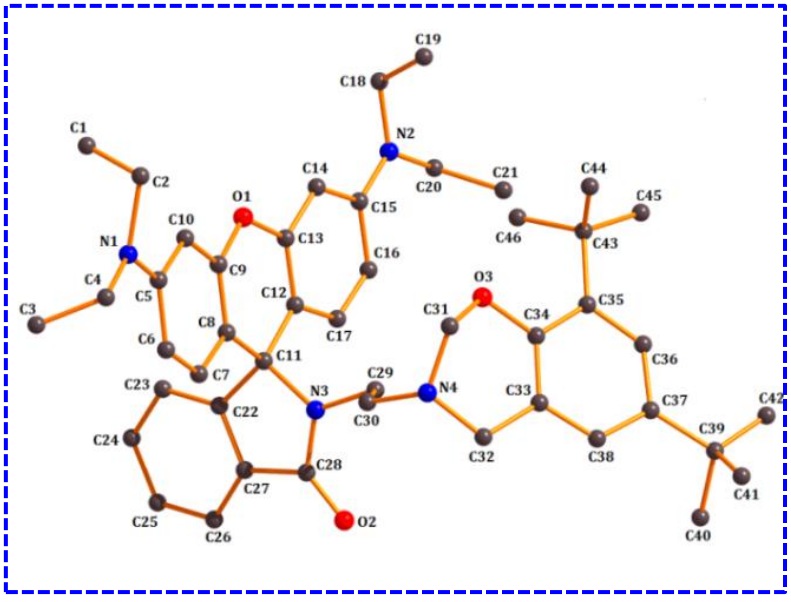

Figure 2.7 Molecular view of **3**, H atoms are removed to get better clarity.

Formula	$C_{46}\ H_{58}\ N_4\ O_3$
Formula Weight	714.96
Crystal System	Monoclinic
Space group	P21/c (no. 14)
a, b, c [Å]	17.313(3), 24.678(4), 9.5642(17)
α, β, γ [°]	90, 105.015(390), 90
V [$Å^3$]	3946.8(12)
Z	4
D (calc.) [g/cm^3]	1.203
μ(Mok_α) [mm^{-1}]	0.075
F(000)	1544
Crystal Size [mm]	0.05 x 0.18 x 0.23
Temperature (K)	296
Radiation [Å] Mok_α	0.71073
Θ Min-Max [°]	1.2, 27.6
Dataset	-22: 22; -32: 32; -12: 12
Tot., Uniq. Data, R(int)	32636, 9136, 0.094
Observed data [I > 2.0 σ(I)]	4317
N_{erf}, N_{ar}	9136, 492
R, wR_2, S	0.0861, 0.2329, 1.02
Max. and av. shift/error	0.02, 0.02
Min. and max. resd. dens. [e $Å^{-3}$]	-0.55, 0.86

[a]$w = 1/[s^2(F_o^2) + (0.2000P)^2]$, where $P = (F_o^2 + 2F_c^2)/3$

In order to determine the stability constant and composition of the RH-BZN–Fe^{3+} complex we have carried out UV-vis titration with a fixed concentration of 3 (20 μM) and variable concentrations of Fe^{3+} (0–35.0 μM) at 25 °C in aqueous MeCN (3: 7, v/v, 1.0 mM HEPES buffer, pH 7.2, μ = 0.05 M LiCl). It was revealed that there is a gradual development of a new absorption band at around 552 nm on addition of Fe^{3+} (**Figure. 2.8**). A plot of absorbance vs. [Fe^{3+}] showed a gradual increase in absorbance and tends to become almost constant at 1 : 1.75 ligand : metal mole ratio. The absorption titration data were fitted to a non-linear eqn (1),[21] where a and b are the absorbance fluorescence intensities in the absence and presence of excess metal ions, respectively, c (=K_f) is the formation constant and n is the stoichiometry of the reaction.

$$y = \frac{a + b \times c \times x^n}{1 + c \times x^n} \qquad (1)$$

The evaluated parameters are: K_f= (1.50 ± 0.18) x 10^4 M^{-1} and n = 1.04 ± 0.01.

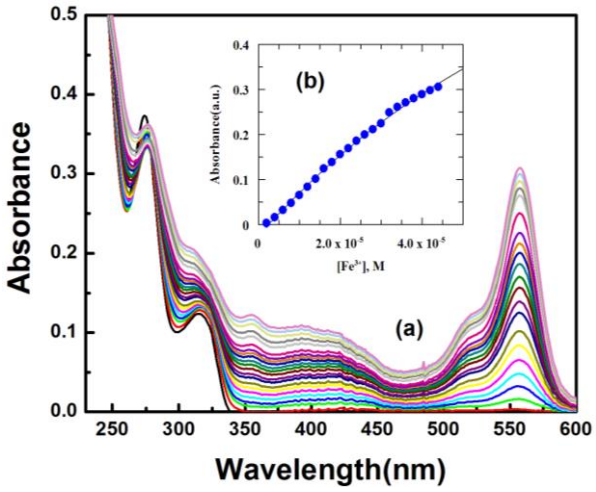

Figure 2.8 (a) Absorption titration of RH-BZN with Fe^{3+} in MeCN-H_2O (7:3, v/v) in HEPES buffer (1 mM) at pH 7.2; (b) non-linear fitting of data.

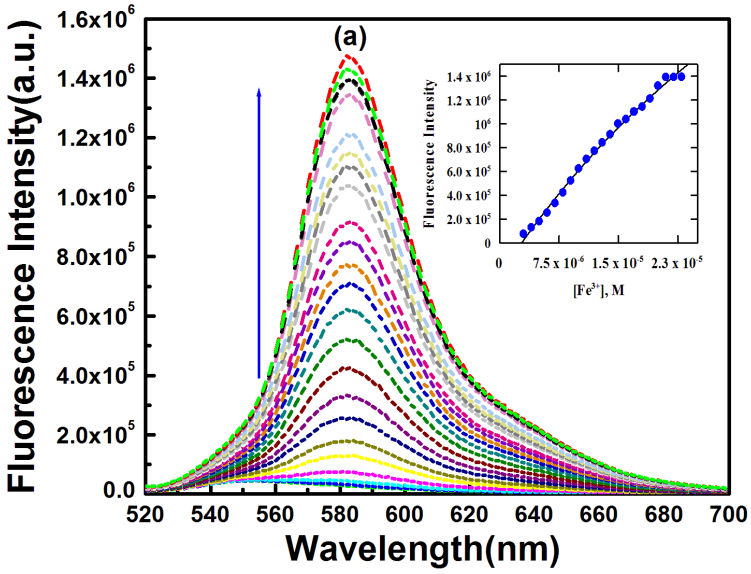

Figure. 2.9 (a) Fluorescence titration of (20.0 μM) in MeCN-H_2O (7:3, v/v) in HEPES buffer at pH 7.2 by the gradual addition Fe^{3+} with λ_{ex} = 510 nm, λ_{em} = 582 nm. Inset: non-linear curve-fit of F.I. vs. [Fe^{3+}] plot.

The fluorescence titration (**Figure 2.9a**) data were solved analogously as in the case of absorption titration data which gives a K_f of (1.50 ± 0.23) x 10^4 M^{-1}, n = 0.99 ± 0.02 (inset of **Figure 2.9a**). There is an excellent agreement between the K_f values extracted from absorption (K_f = (1.50 ± 0.18) × 10^4 M^{-1}, n = 1.04 ± 0.01) and fluorescence (K_f = (1.50 ±

0.23) × 10^4 M^{-1}, n = 0.99 ± 0.02) titration data manifesting the self-consistency of our results. The 1:1 composition of the complex was further confirmed by Job's experiment (**Figure 2.10**).

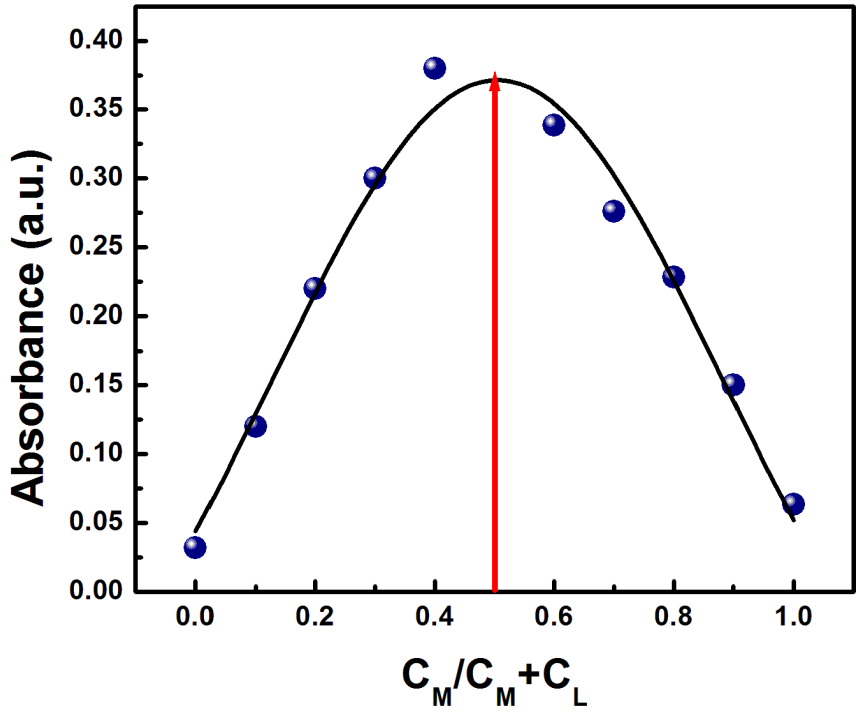

Figure 2.10 Jobs plot (M= Fe^{3+} and L= RH-BZN).

After performing all possible compositions of CH_3CN/H_2O for spectral (fluorescence) studies it was observed that $CH_3CN–H_2O$ (7: 3, v/v) is a good choice for this study. On increasing the water content beyond $CH_3CN–H_2O$ (7: 3, v/v) the fluorescence enhancement was found to decrease progressively and there is no visible change in F. I. when 100% water was used (**Figure 2.11**). The detection of Fe^{3+} was not perturbed by the presence of biologically abundant Na^+, K^+, Ca^{2+} and Mg^{2+} ions. Similarly, several transition-metal ions, namely Cr^{3+}, Mn^{2+}, Fe^{2+}, Co^{2+}, Cu^{2+}, Ni^{2+} and Zn^{2+}, and heavy-metal ions, like Cd^{2+}, Hg^{2+} and Pb^{2+} did not show any significant spectral change under identical reaction conditions (**Figure 2.12**) and the selectivity studies both for individual metal ions as well as in the presence of Fe^{3+} in each case were also carried out. These studies clearly suggest that all the tested metal ions have no interference in the selective detection of Fe^{3+} (**Figure 2.13**).

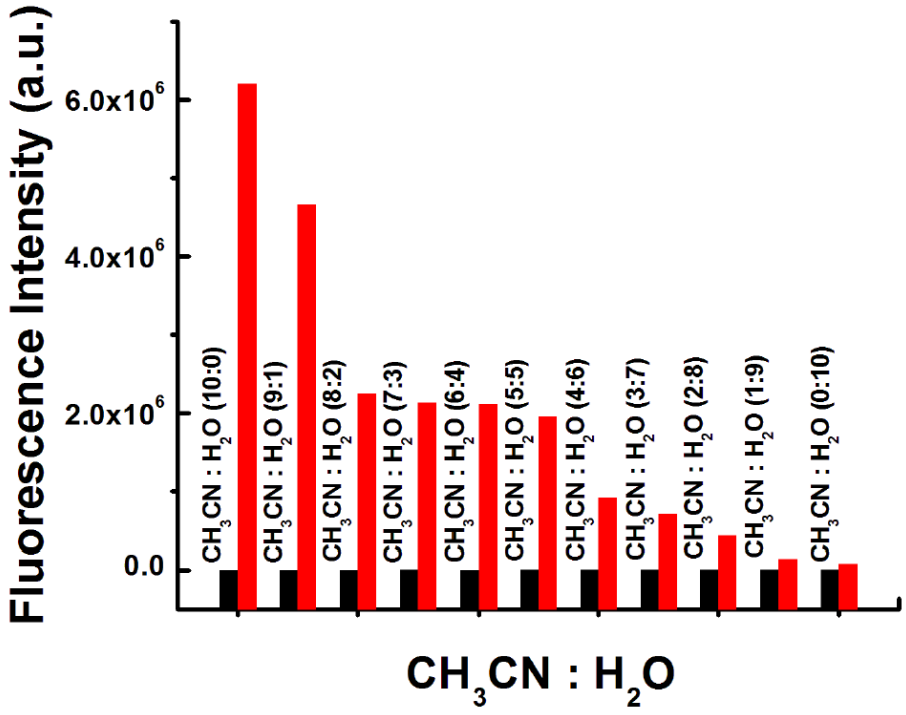

Figure 2.11 Fluorescence emissions with varying water contain.

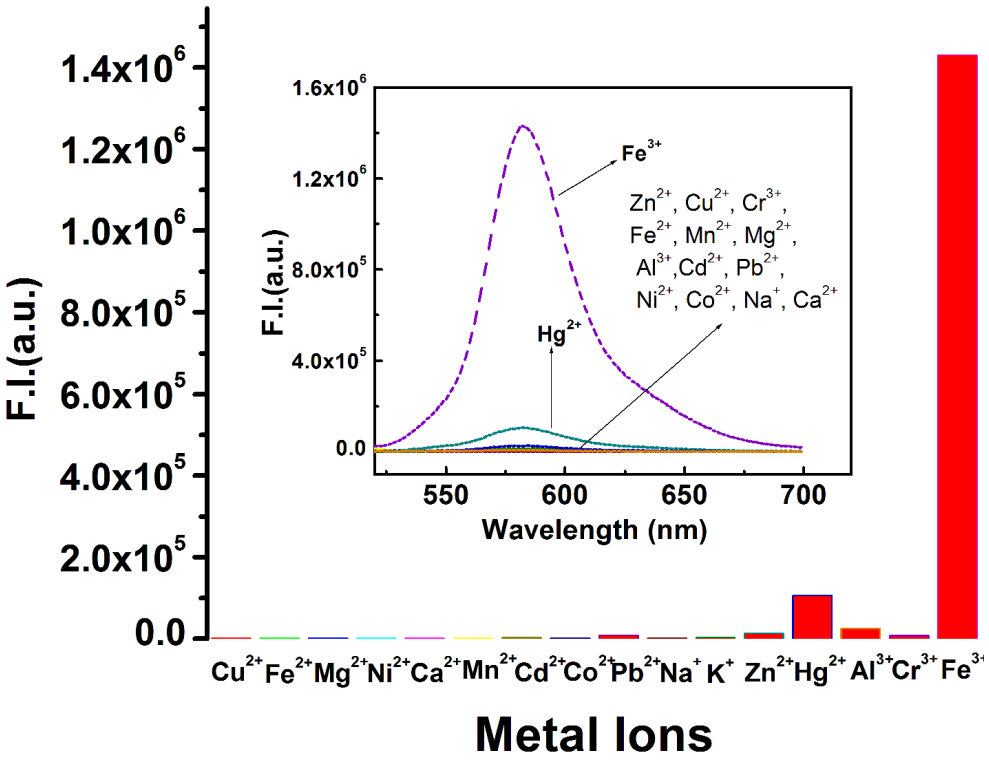

Figure 2.12 Fluorescence emission spectra of different metals.

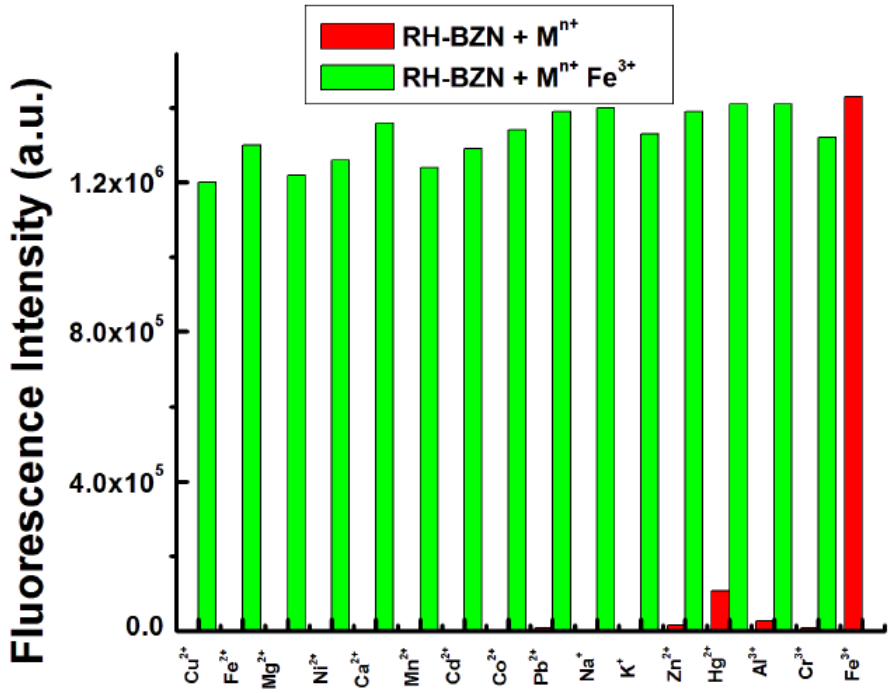

Figure 2.13 Over selectivity study of RH-BZN towards Fe^{3+} ion in presence of different metal ions.

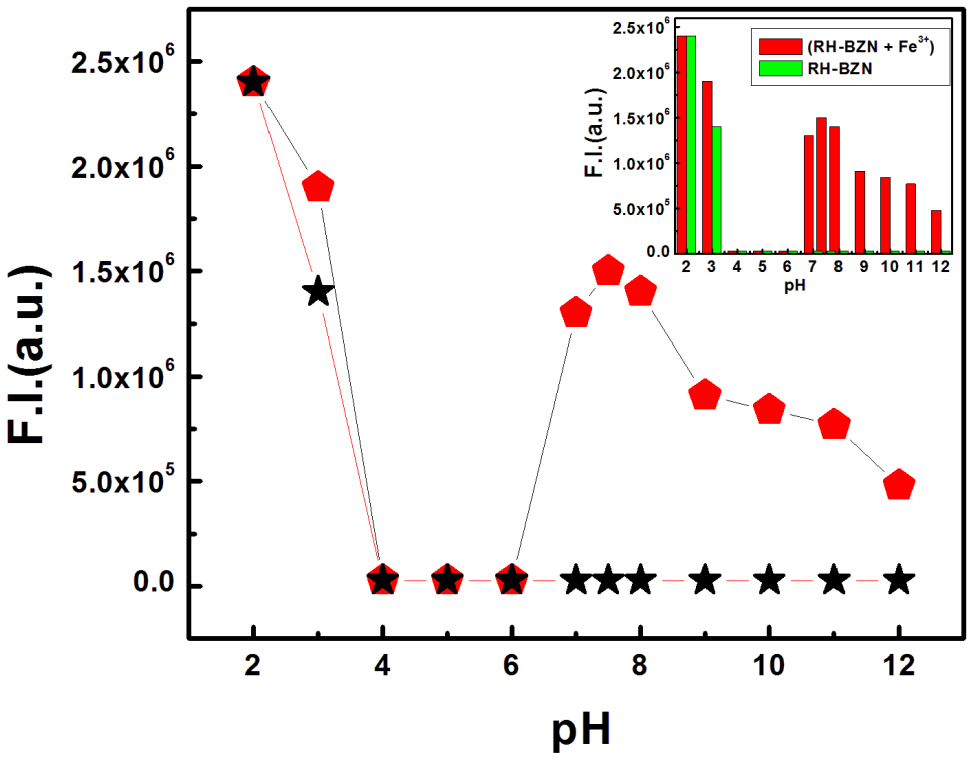

Figure 2.14 pH variation plot.

To check the suitability for the convenient biological application of this probe towards Fe^{3+} sensing under physiological conditions the pH-stability of the probe was investigated which showed no obvious fluorescence of RH-BZN between pH 6 and 12, suggesting the existence of a spirolactam form of RH-BZN over this wide range of pH (**Figure 2.14**). However, in the presence of a selective guest like Fe^{3+} ions its fluorescence effectively at pH ≥ 7.0 which clearly indicates the compatibility of the probe for biological applications under physiological conditions. The reversible binding of 3 to Fe^{3+} was investigated in the same solvent system as was used in the absorption and fluorescence titrations. Anions like SO_4^{-2}, NO_3^-, Cl^-, F^-, Br^-, I^-, OAc^- and N_3^- of 5 equivalents of 3 were introduced (**Figure 2.15**) into the solution of the RH-BZN–Fe^{3+} complex and subsequently the changes in their fluorescence intensities were monitored. The results showed that anions like F^- (tetra-n-butylammonium fluoride) have a strong affinity towards Fe^{3+} and their binding constants seem to be much higher than that of the RH-BZN–Fe^{3+} complex resulting in the abstraction of Fe^{3+} from the complex and bleaching of the emission band at 582 nm through there establishment of the spirolactam ring (**Figure 2.16**). The quantum yield of the RH-BZN–Fe^{3+}complex was determined to be Φ=0.57(with rhodamine 6G as a standard), whereas the free ligand is non-or very weakly fluorescent. The limit of detection (LOD) of $Fe^{3+}$was determined by the 3σ method[22] and found to be as low as 0.11μM (**Figure 2.17**). All these findings indicate that RH-BZN is a good example of an ideal chemosensor for Fe^{3+}.

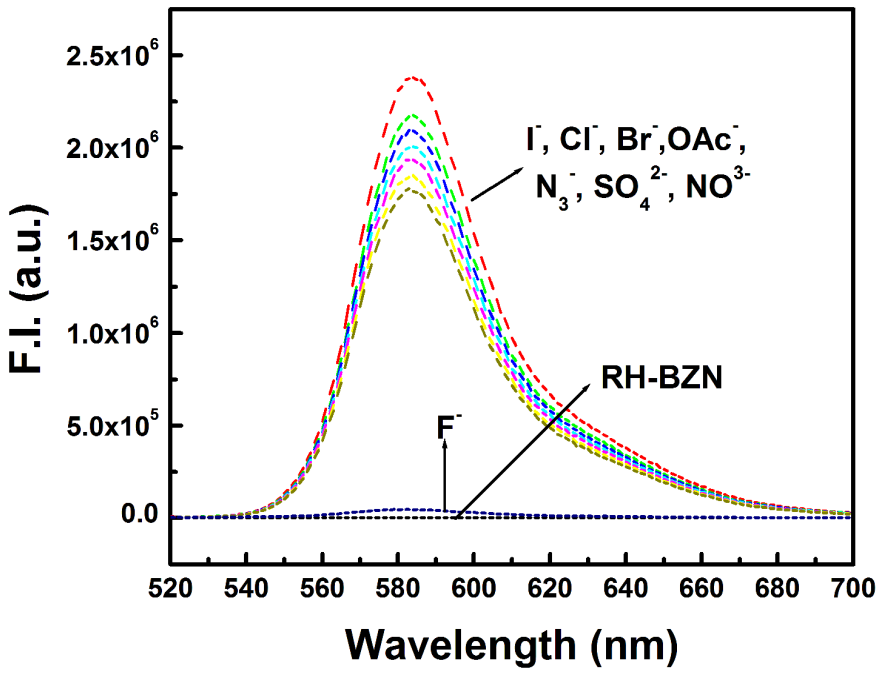

Figure 2.15 Fluorescence emission spectra of different anions.

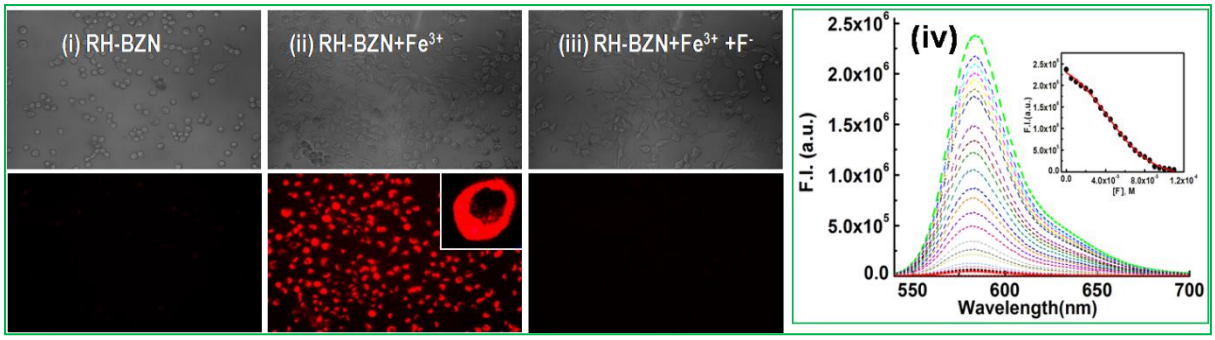

Figure 2.16 The phase contrast (upper panel) and fluorescence images (lower panel) of HepG2 cells were captured (40X) after incubation with (i) **RH-BZN** (10 μM), (ii) **RH-BZN** + Fe^{3+} (10 μM each) and (iii) **RH-BZN** + Fe^{3+} (10 μM each) followed by addition of 100 μM F^- for 30 min at 37°C. Inset shows the cytoplasmic response of RH-BZN towards Fe^{3+}. (iv) Fluorescence titration of **RH-BZN**–Fe^{3+} ensemble (20 μM) by gradual addition of F^- solution (5 μM at a time).

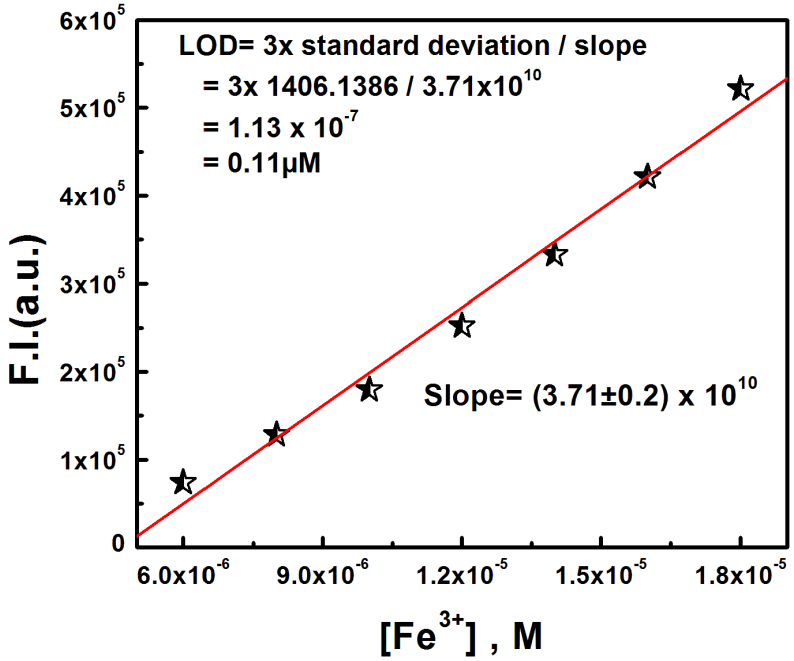

Figure 2.17 Limit of detection (LOD) calculation.

The formation of the RH-BZN–Fe^{3+} complex by opening of the spirolactam ring was established through IR studies. The IR study revealed that the characteristic stretching frequency of the amidic "C=O" of the rhodamine moiety at 1692.15 cm^{-1} is shifted to a lower wavenumber 1637.68 cm^{-1} in the presence of 1.2 equiv. of Fe^{3+} (**Figure 2.3**). This large shift signifies a strong polarization of the "C=O" bond upon efficient binding to the Fe^{3+} ion and infect indicates opening of the spirolactamring.[22]

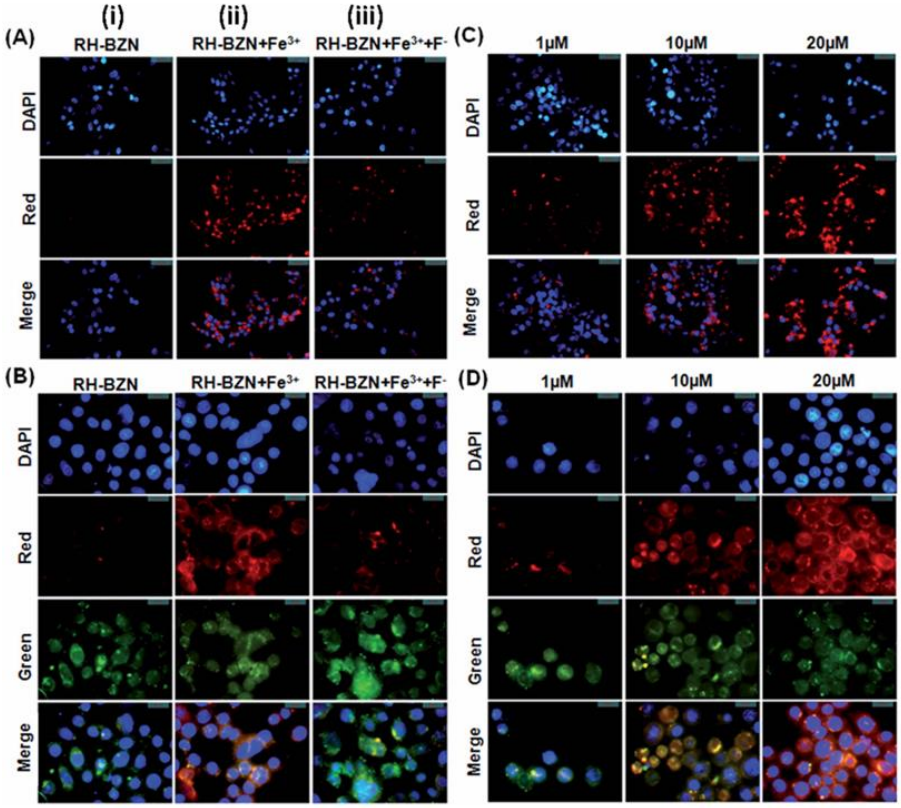

Figure. 2.18 HepG2 cells were incubated with (i) 10 μM of RH-BZN for 30 min at 37 °C, (ii) pre-incubated 10 μM of Fe^{3+} for 30 min at 37 °C followed by washing twice with 1× PBS and, subsequent incubation with 10 μM RH-BZN for 30 min at 37 °C and (iii) pre-incubated 10 μM of Fe^{3+} for 30 min at 37 °C followed by 10 μM RH-BZN and 100 μM F^- for 30 min at 37 °C with alternative washing with 1× PBS two times. (A) The fluorescence image (40×) shows the strong red fluorescence when RH-BZN complexes with Fe^{3+} (in green filter) and is subsequently quenched on the addition of F^- (in green filter). The merged image shows the cytoplasmic RH-BZN+Fe^{3+} fluorescence, suggesting no nuclear entry of RH-BZN fluorophore with DAPI as the nuclear counter stain (blue, in violet/blue filter). (B) The fluorescence image (100×) shows the strong red fluorescence when RHBZN complexes with Fe^{3+} and is subsequently quenched on the addition of F^-. The merged image shows the cytoplasmic RH-BZN + Fe^{3+} fluorescence, suggesting no nuclear entry of RH-BZN fluorophore with DAPI as the nuclear counter stain (blue) and LysoTracker (green, in blue filter) for cytoplasm. (C) The intracellular fluorescence image of RH-BZN in the complex with Fe^{3+} at 1, 10 and 20 μM concentrations of RH-BZN is shown (40×) by counterstaining using DAPI and (D) using DAPI as the nuclear counter stain and LysoTracker for cytoplasm (100×). The lowest concentration of RH-BZN (1 μm) shows excellent detection of Fe^{3+} in the cytoplasm of HepG2 cell.

Bio-imaging of Fe^{3+} by RH-BZN was performed in live cells (**Figure 2.16 and 2.18**) by using fluorescence microscopic techniques. To determine whether RH-BZN has any cytotoxic effect, MMT assay was performed on HepG2 cells which showed no significant cell cytotoxicity up to 80 µm [23] Hence further experiments were carried out at low dose (10 µm) of **RH-BZN**.

The intracellular imaging behaviour of RH-BZN (10 µM) on HepG2 cells displayed no obvious fluorescence (**Figure 2.16**). However, an excellent intracellular cytoplasmic fluorescence was observed inside the cells, when HepG2 cells were incubated with 10 µM RH-BZN followed by washing with 1x PBS and subsequent incubation with 10 µM Fe^{3+} and, also subsequent quenching of red fluorescence on treatment with tetra-n-butyl ammonium fluoride. Interestingly we have observed that the fluorophore RH-BZN shows the only cytoplasmic binding with Fe^{3+}, not the nuclear binding (**Figure 2.16, inset and Figure 2.18**). The specific binding of fluorophore **3** to the cytoplasm makes this fluorophore less toxic, as fluorophore **3** cannot cross the nuclear membrane to bind to the nucleus (DNA) which causes the more toxic effect oncells.[24] The cytotoxicity study by MMT assay shows 82% cell viability at 20 µM concentration and specially detects the cytoplasmic Fe^{3+}. Additionally, (**Figure 2.18**) displays the concentration dependent binding of RH-BZN to intracellular Fe^{3+} which clearly indicates that the present probe is capable of recognizing cytoplasmic Fe^{3+} as low as 1 µM concentration. As the dye is not water soluble, we performed all the extracellular experiments in the MeCN: H_2O) (7:3, v/v) mixture. However, when the probe is once solubilised in DMSO it did not give any precipitate on adding water up to 99%. So, there was no problem in performing the cell imaging experiment in the 1:9 DMSO : H_2O mixture.

Few of the recently investigated rhodamine-B based Fe^{3+} sensors are given in **Scheme 2.2** and some salient features are given in **Table 2.1**. A quick inspection of these studies reveal that all these are turn on Fe^{3+} ion sensors with moderate LOD values (0.32–5.0 µM) and formation constants (K_f = 5.1 × 10^3 – 4.52 × 10^5 M^{-1}) and applicable for monitoring intra cellular Fe^{3+}ions,[25] though in a few cases no cell imaging experiments were per formed. RH-BZN recognizes Fe^{3+} with 240-fold fluorescence enhancement with a binding constant of 1.50× 10^4 M^{-1} and a LOD of 0.11 µM through a 1:1 host–guest type interaction. Not only that the cytoplasmic binding makes this probe more appropriate for in vivo monitoring of Fe^{3+} without any genetic damage.

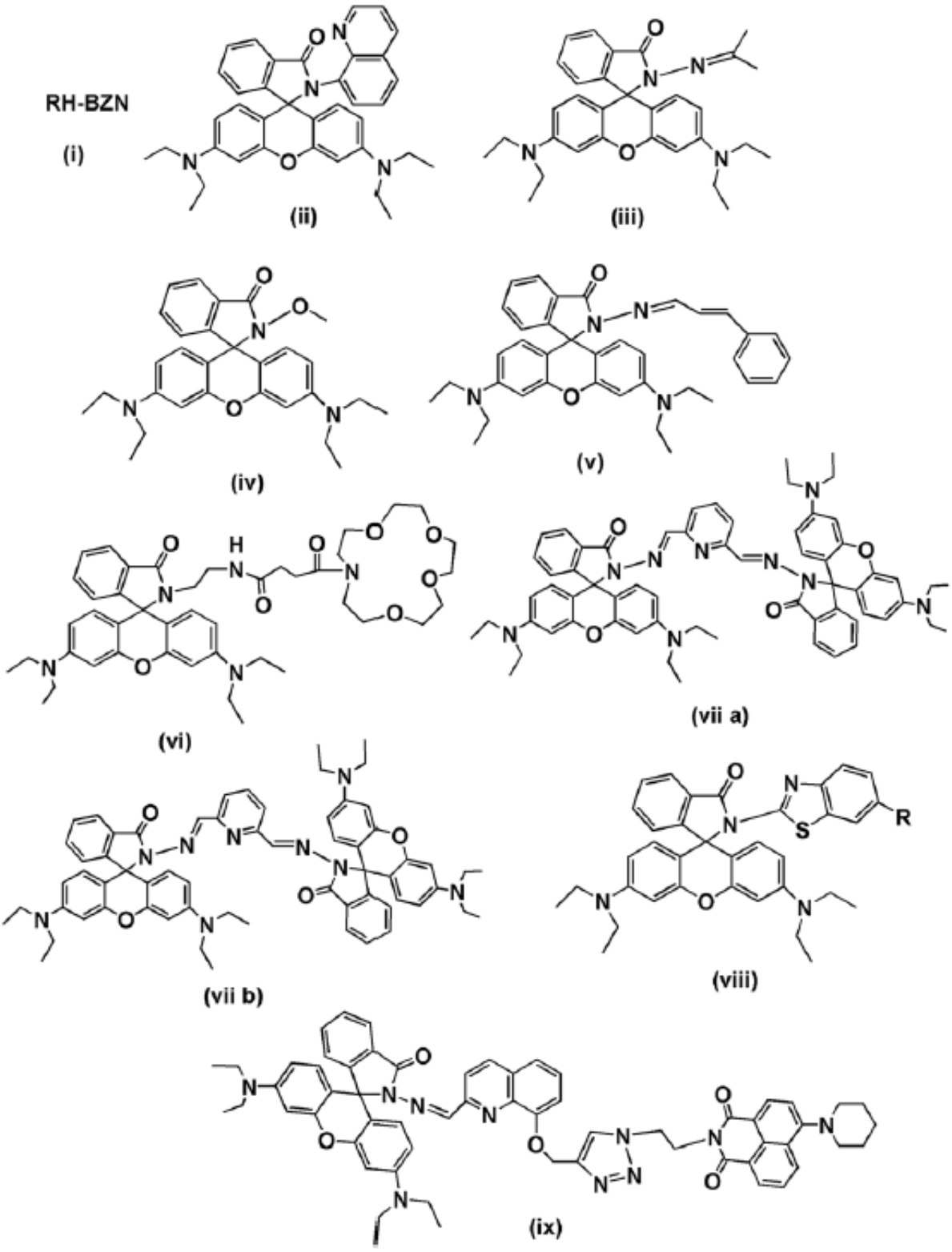

Scheme 2.2 Few of recently investigated rhodamine-B based Fe^{3+} sensors.

Table 2.1 Comparative results of selected rhodamine 6G based probes for recognizing Fe^{3+}.

Probe	Formation constant (M^{-1})	LOD (μM)	Cell
(i)RH-BZN	1.5×10^4	0.11	Done, cytoplasmic binding
(ii)	Not-determined	0.32	Done
(iii)	2.3×10^4	Not determined	Done
(iv)	1.58×10^5	Not determined	Not done
(v)	Not determined	1.8	Not done
(vi)	2.46×10^4	0.40	Done
(vii)(a)	7.5×10^3	Not determined	Not done
(vii)(b)	5.1×10^3	Not determined	Not done
(viii)	4.52×10^5	5	Done
(ix)	9.52×10^5	0.05	Done

2.4 Conclusions

In summary, a novel benzoxazine based dual sensor 'rhodamine-3,4-dihydro-2H-1,3-benzoxazine', RH-BZN (3) has been synthesized and structurally characterized. In 3: 7 waters: MeCN (v/v) and at physiological pH 7.2, it selectively recognizes Fe^{3+} giving 240-fold fluorescence enhancement and a binding constant of 1.50×10^4 M^{-1} through a 1: 1 host–guest type interaction, which could suitably be employed for cytoplasmic intracellular imaging of Fe^{3+} without notable cytotoxicity. Reversible binding of Fe^{3+} towards this probe was confirmed by reacting with tetra-n-butyl ammonium fluoride both in extra and intra-cellular conditions.

References

1) (a) M. Zhang, M. X. Yu, F. Y. Li, M. Zhu, M. Y. Li, Y. Gao, Z. Liu, J. Zhang, D. Zhang, T. Yi and C. H. Huang, *J. Am. Chem. Soc.,* 2007, **129**, 10322-10323; (b) J. H. Lee, C. S. Lim, Y. S. Tian, J. H. Han and B. R. Cho, *J. Am. Chem. Soc*., 2010, **132**, 1216-1217; (c) Y. Wei, Y. Zhang, Z. Liu and M. L. Guo, *Chem. Commun*., 2010, **46**, 4472-4474.

2) (a) Y. Zhou, F. Wang, Y. Kim, S.-J. Kim and J. Yoon, *Org. Lett.,* 2009, **11**, 4442-4445; (b) B. A. Smith, W. J. Akers, W. M. Leevy, A. J. Lampkins, S. Xiao, W. Wolter, M. A. Suckow, S. Achille and B. D. Smith, *J. Am. Chem. Soc*., 2010, **132**, 67-69; (c) H. S. Jung, P. S. Kwon, J. W. Lee, J. Kim, C. S. Hong, J. W. Kim, S. Yan, J. Y. Lee, J. H. Lee, T. Joo and J. S. Kim, J. Am. *Chem. Soc*., 2009, **131,** 2008-2012; (d) R. Bhowmick, R. Alam, T. Mistri, D.

Bhattacharya, P. Karmakar and M. Ali, *ACS Appl. Mater. Interfaces*, 2015, **7**, 7476-7485; (e) H. Y. Lee, K. M. K. Swamy, J. Y. Jung, G. Kim and J. Yoon, *Sens. Actuators*, B, 2013, **182**, 530-537; (f) F. Wang, S. W. Nam, Z. Guo, S. Park and J. Yoon, *Sens. Actuators, B,* 2012, **161**, 948-953; (g) X. Chen, T. Pradhan, F. Wang, J. S. Kim and J. Yoon, *Chem. Rev.,* 2012, **112**, 1910-1956; (h) P. Mahato, S. Saha, P. Das, H. Aggarwala and A. Das, *RSC Adv*., 2014, **4**, 36140-36174.

3) (a) S. Bae and J. Tae, *Tetrahedron Lett*., 2007, **48**, 5389-5392; (b) Y. Xiang and A. Tong, *Org. Lett.*, 2006, **8**, 1549-1552; (c) J. L. Bricks, A. Kovalchuk, C. Tri flinger, M. Nofz, M. Buschel, A. I. Tolmachev, J. Daub and K. Rurack, *J. Am. Chem. Soc*., 2005, **127**, 13522-13529; (d) M. Zhang, Y. Gao, M. Li, M. Yu, F. Li, L. Li, M. Zhu, J. Zhang, T. Yi and C. Huang, *Tetrahedron Lett.,* 2007, **48**, 3709-3712; (e) Y. Liu, Z. Xu, J. Wang, D. Zhang, Y. Ye and Y. Zhaoa, *Luminescence*, 2014, **29,** 945-951; (f) L. Zhang, J. Wang, J. Fan, K. Guo and X. Peng, *Bioorg. Med. Chem. Lett.,* 2011, **21**, 5413-5416; (g) J. Huang, Y. Xu and X. Qian, *Dalton Trans.,* 2014,**14**, 5983-5989.

4) M. Ghaedi, A. Shokrollahi, R. Mehrnoosh, O. Hossaini and M. Soylak, Cent. *Eur. J. Chem.,* 2008, **6**, 488-496.

5) S. Bae and J. Tae*, Tetrahedron Lett*., 2007, **48**, 5389-5392.

6) (a) R. Williams, *Pure Appl. Chem*., 1983, **55(1**), 35-46; (b) M. Ferrali, D. Donati, S. Bambagioni, M. Fontani, G. Giorgic and A. Pietrangelod, *Bioorg. Med. Chem.,* 2001, **9**, 3041-3047.

7) P. Aisen, M. Resnick and E. Leibold, *Curr. Opin. Chem. Biol.,* 1999**, 3**, 200-206.

8) D. Touati, *Arch. Biochem. Biophys*., 2000, **373**, 1-6.

9) (a) J. R. Burdo and J. R. Connor, *Biometals*, 2003, **16**, 63-75; (b) J. R. Connor, S. L. Menzies, S. M. S. Martin and E. J. Mufson, *J. Neurosci. Res.,* 1990, **27**, 595-611; (c) R. R. Crichton, S. Wilmet, R. Legssyer and R. J. Ward, *J. Inorg. Biochem*., 2002, **91**,9-18; (d) R. S. Eisenstein, *Annu. Rev. Nutr*., 2000, **20**, 627-662.

10) (a) B. T. Felt and B. Lozoff, *J. Nutr.,* 1996, **126**, 693-701; (b) C. J. Earley, J. R. Connor, J. L. Beard, E. A. Malecki, D. K. Epstein and R. P. Allen, *Neurology*, 2000**, 54**, 1698-1700.

11) (a) J. P. Sumner and R. Kopelman, *Analyst*, 2005, **130**, 528-533; (b) Y. Ma, W. Luo, P. J. Quinn, Z. Liu and R. C. Hider, *J. Med. Chem.,* 2004, **47**, 6349-6362; (c) G. E. Tumambac, C.

M. Rosencrance and C. Wolf, *Tetrahedron,* 2004**, 60,** 11293-11297; (d) A. Ali, Q. Zhang, J. Dai and X. Huang, *BioMetals*, 2003, **16**, 285-293.

12) (a) J. Mao, L. Wang, W. Dou, X. Tang, Y. Yan and W. Liu, *Org. Lett*., 2007, **9**, 4567-4570; (b) M. Xu, S. Wu, F. Zeng and C. Yu, *Langmuir,* 2010, **26**, 4529-4534; (c) X. Wu, B. Xu, H. Tong and L. Wang, *Macromolecules*, 2010, **43**, 8917-8923.

13) T. Besson, C. W. Rees, G. Cottenceau and A. Pons, *Bioorg. Med. Chem. Lett*., 1996, **6**, 2343-2348.

14) S. Ozden, A. Ozturk, H. Goker and N. Altanlar, *Il Farmaco*, 2000, **55**, 715-718.

15) R. Fringuelli, D. Pietrella, F. Schiaffella, A. Guarraci, S. Perito, F. Bistoni and A. Vecchiarilli, *Bioorg. Med. Chem*., 2002, **10**, 1681-1686.

16) S. Alper-Hayta, E. Aki-Sener, B. Tekiner-Gulbas, I. Yildiz, I. Yalcin and N. Alanlar, *Eur. J. Med. Chem.,* 2006, **41**, 1398-1404.

17) B. P. Mathew, A. Kumar, S. Sharma, P. K. Shukla and M. Nath, *Eur. J. Med. Chem.,* 2010, **45**, 1502-1507.

18) K. Waisser, J. Gregor, L. Kubicova, V. Klimesova, J. Kunes, M. Machacek and J. Kaustova, *Eur. J. Med. Chem*., 2000, **35**, 733-741.

19) P. Hsieh, F. Chong, C. Chang, F. Zheng and K. H. Lin*, Bioorg. Med. Chem. Lett*., 2004, **14**, 4751-4754.

20) K. M. Pritchard, J. A. Rawi and C. Bradley, *Eur. J. Med. Chem*., 2007, **42**, 1200-1210.

21) C. R. Lohani, J. M. Kim, S. Y. Chung, J. Yoon and K. H. Lee, *Analyst*, 2010, **135**, 2079-2084.

22) T. Mistri, R. Alam, M. Dolai, S. K. Mandal, P. Guha, A. R. KhudaBukhsh and M. Ali, *Eur. J. Inorg. Chem*., 2013,**34**, 5854-5861.

23) R. Bhowmick, M. Dolai, R. Alam, T. Mistri, A. Katarkar, K. Chaudhuri and M. Ali, *RSC Adv.*, 2014, **4**, 41784-41792.

24) F. Di Maria, I. E. Palamà, M. Baroncini, A. Barbieri, A. Bongini, R. Bizzarri, G. Gigli and G. Barbarella, *Org. Biomol. Chem*., 2014, **12**, 1603-1610.

25) (a) M. Zhang, Y. Gao, M. Li, M. Yu, F. Li, L. Li, M. Zhu, J. Zhang, T. Yia and C. Huang, *Tetrahedron Lett*., 2007, **48**, 3709-3712; (b) S. Bae and J. Tae, *Tetrahedron Lett*., 2007, **48**, 5389-5392; (c) Y. Liu, Z. Xu, J. Wang, D. Zhang, Y. Yea and Y. Zhaoa, *Luminescence*, 2014, **29**, 945-951; (d) X. Baoa, X. Caoa, X. Niec, Y. Xub, W. Guod, B. Zhouc, L. Zhangb, H. Liaob and T. Pang, *Sens. Actuators, B*, 2015, **208**, 54-66; (e) A. J. Weerasinghe, C. Schmiesing, S. Varaganti, G. Ramakrishna and E. Sinn, *J. Phys. Chem. B,* 2010, **114**, 9413-9419; (f) Z. Yang, M. She, B. Yin, J. Cui, Y. Zhang, W. Sun, J. Li and Z. Shi, *J. Org. Chem.,* 2012, **77**, 1143-1147; (g) N. R. Chereddy, S. Thennarasu and A. B. Mandal, *Analyst*, 2013, **138**, 1334-1337.

Chapter 3

A turn-on fluorogenic chemosensor for Fe^{3+} and a Schottky barrier diode with frequency-switching device applications

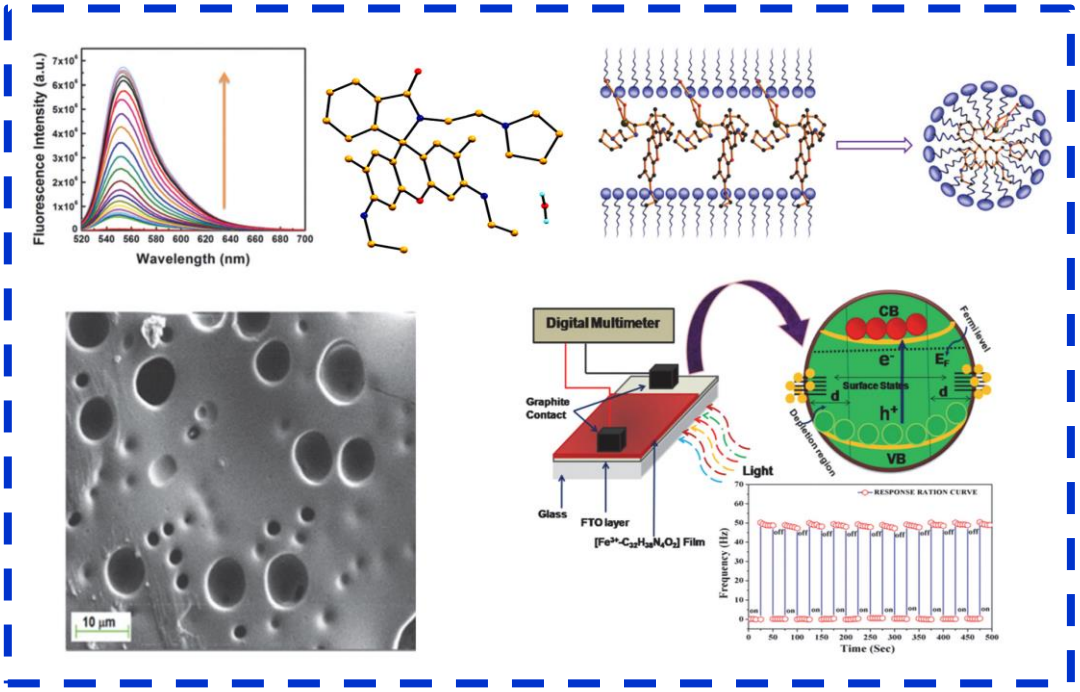

Abstract:

A novel highly sensitive and selective fluorescent chemosensor L has been synthesized and characterized by various physicochemical techniques. In 3:7 water: MeCN (v/v) at pH 7.2 (10 mM HEPES buffer, μ = 0.05 M LiCl), it selectively recognizes Fe^{3+} through 1:1complexation resulting in a 106-fold fluorescence enhancement and a binding constant of 8.10×10^4 M^{-1}. The otherwise non-fluorescent spirolactam form of the probe results a dual-channel (absorbance and fluorescence) recognition of Fe^{3+} via CHEF (chelation enhanced fluorescence) through the opening of the spirolactam ring. We have also carried out fluorescence titration and anisotropy (r) studies in pure water in the presence of SDS (sodium dodecyl sulphate). Based on the dependence of FI (fluorescence intensity) and r on [SDS] it was proposed that the probe is trapped between two SDS monolayers which again interact among themselves by π···π stacking. As a result, there is an increase in FI up to [SDS] ~ 7 mM– a phenomenon reminiscent of aggregation induced enhancement of emission (AIEE). Beyond this concentration of SDS (7 mM), micelle formation takes place and the π···π stacked polymer now becomes a monomer and is trapped inside the micellar cavity. As a result, there is a decrease in FI at [SDS] > 7 mM. But for anisotropy, it increases with [SDS] beyond 7 mM. Ligand, metal, and SDS interactions are well established through different optical and morphological studies. $[L–Fe(NO_3)]^{2+}$ thin films on FTO (Fluorine-doped Tin Oxide) glass substrates have been designed with the help of the spin-coating deposition technique. The deposited film of thickness 1.6×10^{-5} cm is well characterized by optical band gap calculation with a direct band gap, $\mathcal{E}_g$ ~ 1.6 eV. FESEM was also performed for the $[L–Fe(NO_3)]^{2+}$/FTO film. The current–voltage characteristics were measured by the two-probe technique. Light-dependent exciton generation was carried out by taking the top and bottom contacts with graphite paste on FTO and on the $[L–Fe(NO_3)]^{2+}$ films for the measurement of switching behaviour. The response ratio curve for the light-induced frequency-switching phenomena has been obtained. The frequency taped here is the oscillation frequency of the photo-generated electron and the hole in an exciton. Thus, the light-induced frequency-switching behaviour and Schottky barrier diode characteristics of the material were established.

3.1 Introduction

Iron is not only the most abundant transition metal in cellular systems, but also it is of outstanding biological importance given its presence in numerous enzymes and proteins. As to $Fe^{3+,}$ its vital roles in a variety of cell functions have been summarized in many reviews.[1–4] Haemoglobin, an iron-containing protein, is critically involved in both electron transfer reactions and oxygen transport processes in all tissues[5,6] and has suitable redox potential values and high affinity for oxygen. The deficiency or excess of Fe^{3+} can lead to a variety of diseases, such as Alzheimer's, Huntington's, Parkinson's etc.[7–10] Thus, there is an urgent need to develop chemical sensors that are capable of detecting and quantifying the presence of Fe^{3+} ions in biological samples. Due to its paramagnetic nature, Fe^{3+} is basically the most effective fluorescent quencher,[11–13] which makes it difficult to develop a desirable fluorescence turn-on sensor. For this reason, very few turn-on sensors of Fe^{3+} have been reported but many of them are interfered by few other metal ions.[14] Again, there are examples of rhodamine-based fluorescent sensors for $Fe^{3+,}$ but most of them are soluble either in organic solvents or mixed organo-aqueous media[15–24] with few exceptions which are soluble in purely aqueous medium.[25–27]

Consequently, the design of new probes bearing suitable multidentate chelating units, which can preferentially recognize $Fe^{3+,}$ is a timely important area of research. Given our interest in developing new chemo-sensing systems, we report, herein, a rhodamine-based dual channel probe for the detection of Fe^{3+}. Rhodamine-based conjugates with a spirolactam structure are, in general, non-fluorescent but act as colorimetric as well as fluorometric sensors with the enhancement of absorption and fluorescence emission intensity, respectively, on selectively binding to metal ion(s).

In the present article, we are going to disclose a rhodamine–1-(2-aminoethyl) pyrrolidine conjugate as a highly sensitive and selective fluorescent chemosensor for Fe^{3+} ions. Transition metal complexes are found to have huge potential to form an active layers which are important in the optical and electronic applications. Recently, considerable attention has been given to developing nanometre-scale materials due to their unique physical and chemical properties and potential applications in nanoscale devices.[28,29] Here, we will explore, for the first time, the feasibility of using a $[L–Fe(NO_3)]^{2+}$/FTO film as a Schottky barrier diode with frequency-switching device applications. With an indigenous design of a ligated chromophore, we believe that the luminescent Fe(III) complex may serve as a new

model for probing a variety of fundamental characteristics in view of the fabrication of optoelectronic devices.

3.2 Experimental section

3.2.1 Materials and methods

The starting materials, such as rhodamine-6G hydrochloride (Sigma Aldrich), 1-(2-aminoethyl) pyrrolidine (Sigma Aldrich), and ferric nitrate (Sigma Aldrich), were used for the preparation of L and the $[L–Fe(NO_3)]^{2+}$ complex. Solvents like EtOH, MeOH, MeCN, etc (Merck, India) were of HPLC grade. MeCN and de-ionized water were used for spectroscopic studies.

3.2.2 Physical measurements

Infrared spectra (400–4000 cm^{-1}) were recorded from KBr pellets on a Nickole Magna IR 750 series-II FTIR spectrophotometer. ^{1}H-NMR spectra were recorded in DMSO-d_6 on a Bruker 300 MHz NMR spectrometer using tetramethylsilane ($\delta = 0$) as an internal standard. UV-Vis spectra were recorded on an Agilent diode-array spectrophotometer (Model, Agilent 8453), steady-state fluorescence spectra were recorded on a PTI spectrofluorometer (Model QM-40), and ESI-MS^+ (m/z) of the receptor (L) and the $L–Fe^{3+}$ complex were recorded on a HRMS spectrometer (Model: XeVO G2 QTof). Morphological analyses of the films were carried out by field emission scanning electron microscopy (FESEM) (JEOL, JSM-6700F).

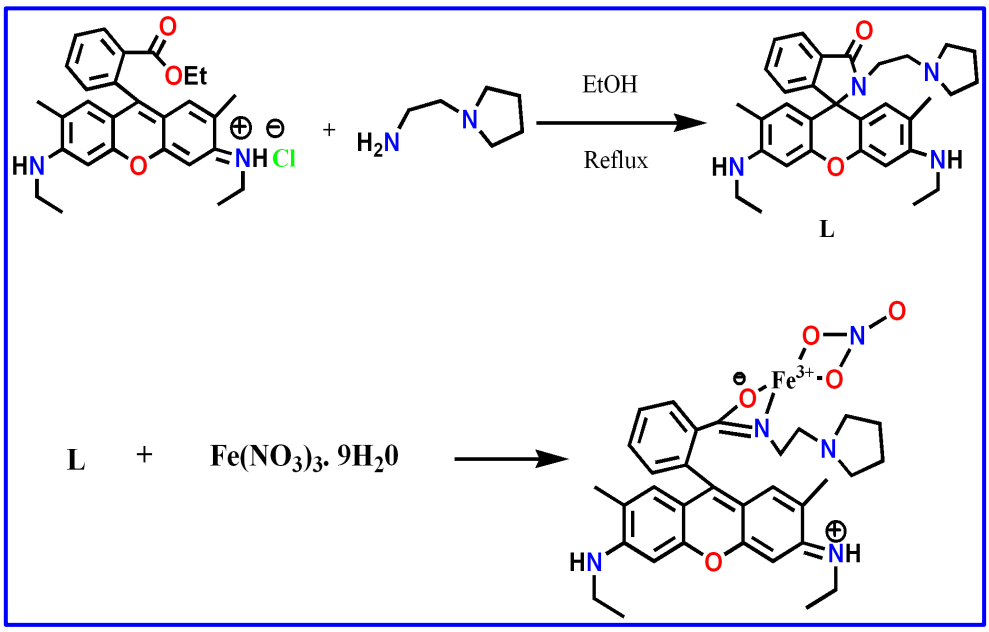

Scheme 3.1 Synthesis of probe L and its Fe^{3+} complex.

3.2.3 Synthesis

3.2.3.1 Preparation of L

Rhodamine-6G hydrochloride (1) (5.0 mmol) and 1-(2-aminoethyl) pyrrolidine (10.0 mmol) were dissolved in EtOH and refluxed for 6 h with continuous stirring whereupon a reddish crystalline solid of L (**Scheme 3.1**) was deposited. The solid was filtered and washed with EtOH and dried in air (68% yield). Recrystallization from EtOH afforded single crystals for X-ray diffraction studies. ^{1}HNMR (300 MHz, DMSO-d_6) (δ, ppm): 1.31 (t, 10H), 1.70 (s, 4H), 1.89 (s, 6H), 2.21 (d, 2H), 2.30 (s, 4H), 3.22 (t, 6H), 3.48 (s, 2H), 6.23 (s, 2H), 6.33(s, 2H), 7.03 (s, 1H), 7.42 (t, 2H), 7.90 (s, 1H) (**Figure 3.1**). IR spectrum: $\tilde{\nu}$ = 1692 cm^{-1} (spirolactam amide-keto), 1615 cm^{-1} (–C=N) (**Figure 3.2**). ESI-MS^{+} (m/z): 511.3624 (L + H^{+}) (**Figure 3.3**).

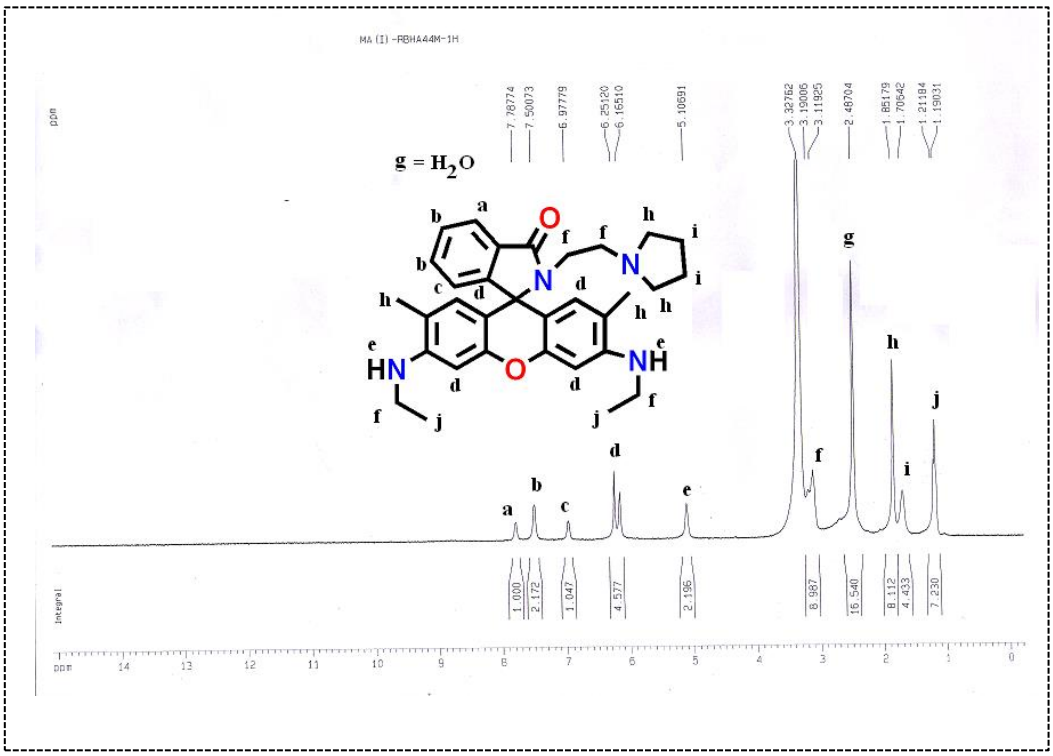

Figure 3.1 ^{1}H-NMR spectra of L in DMSO-d_6 in Bruker 300 MHz instrument.

3.2.3.2 Synthesis of [L–Fe(NO$_3$)]$^{2+}$

Fe $(NO_3)_3 \cdot 9H_2O$ (0.808 g, 2 mmol) in 5 ml MeCN was added dropwise to a solution of L (2 mmol) in 20 ml MeCN with continuous stirring. After 1 h, the solution was filtered and kept aside undisturbed. After one day, a crystalline compound of complex **[L–Fe(NO$_3$)]$^{2+}$** (**Scheme 3.1**) was precipitated out. It was collected by filtration, washed several times with MeOH and dried in air. It was recrystallized from methanol. Several trials to grow single

crystals were failed. IR spectrum: $\tilde{\nu}$ = 1637 cm^{-1} (spirolactam amide-keto), 1554 cm^{-1} (–C=N) (**Figure. 3.2**). ESI-MS^{+} (m/z): 628.4961 $[L–Fe(NO_3)]^{2+}$ (**Figure. 3.4**).

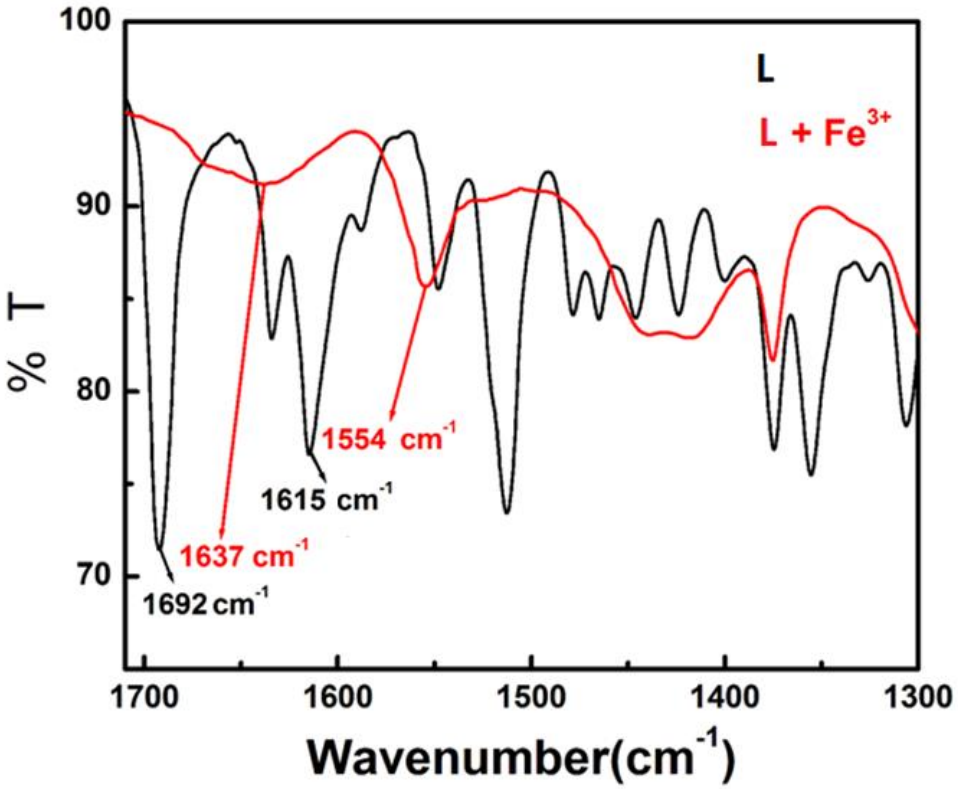

Figure 3.2 IR Spectrum of **L** and **L**-Fe^{3+} complex.

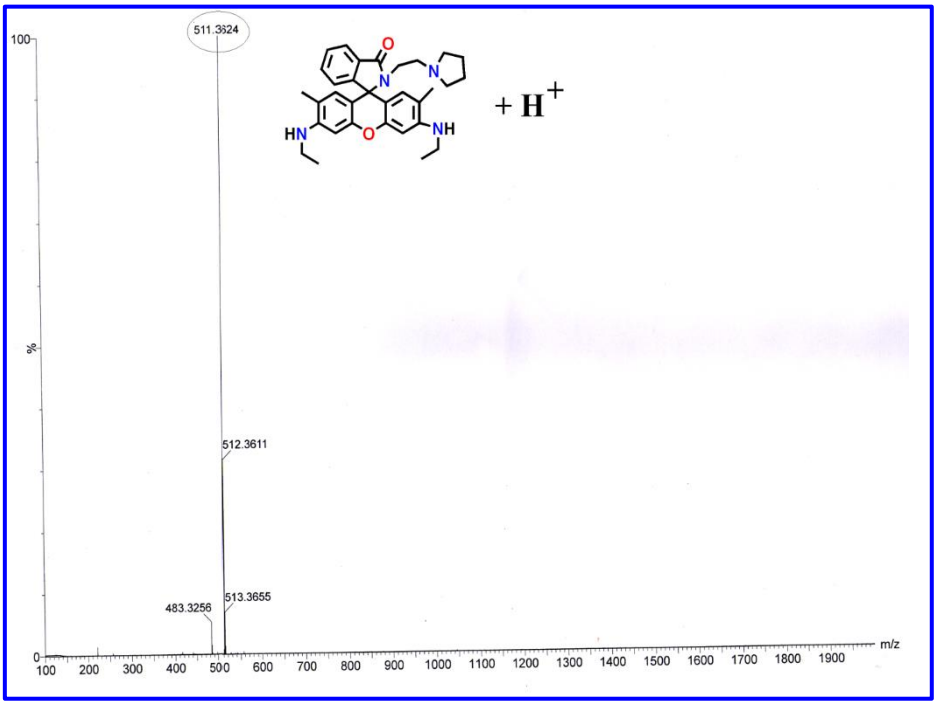

Figure 3.3 Mass spectra of L in MeCN.

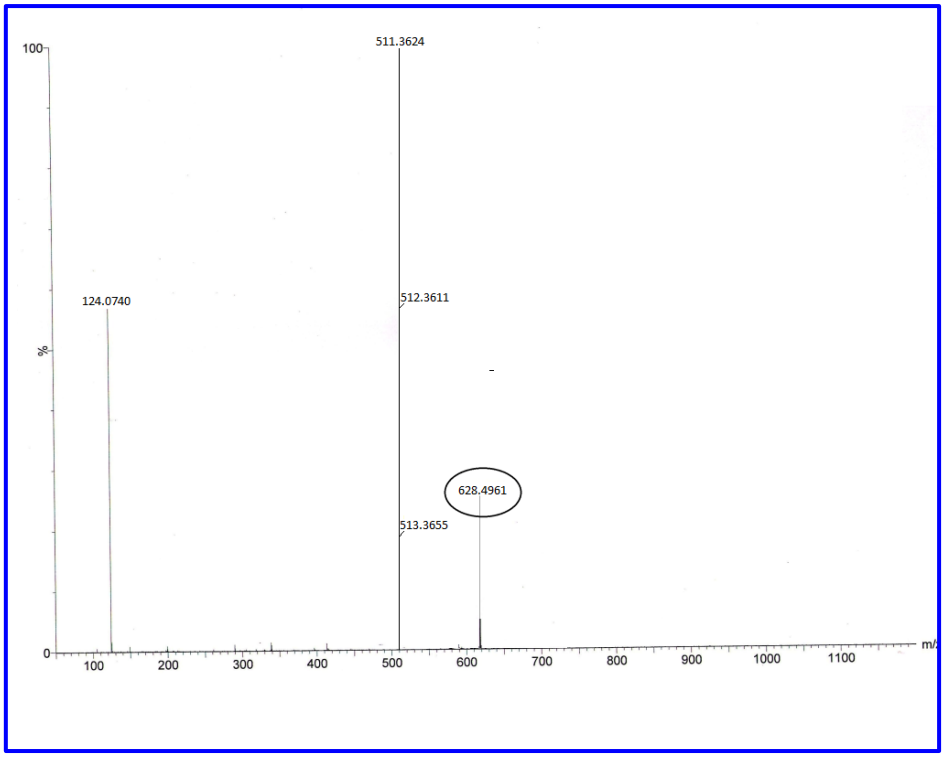

Figure 3.4 Mass spectra of L-Fe^{3+} complex in MeCN.

3.2.4 Solution preparation for UV-Vis and fluorescence studies

For both UV-Vis and fluorescence titrations, a 1.0 x 10^{-3} M stock solution of the probe L was prepared by dissolving it in 0.5 ml MeCN, the volume of which was finally adjusted to 10 ml by MeCN. Similarly, 10 ml 1.0 x 10^{-3} M stock solution of Fe^{3+} was prepared separately in MeCN. 100 ml 10 mM HEPES buffer was prepared in Milli-Q Millipore water and pH was adjusted to 7.24 by using HCl and NaOH. 2.5 ml of this buffer solution was pipetted out into a cuvette to which 50 µM of the probe was added and Fe^{3+} was added incrementally starting from 0 to 80 µM in a regular interval of volume and UV-Vis spectra were recorded for each solution. For fluorescence spectra 10 µM L was added to 2.5 ml buffer solution in a cuvette and Fe^{3+} was added incrementally starting from 0 to 25 µM in a regular interval of volume and fluorescence spectra were recorded for each solution. The 1 cm path lengths of the cells were used for absorption and emission studies. Fluorescence measurements were performed using 2 nm x 2 nm slit width.

3.2.5 Determination of fluorescence polarization anisotropy

A PTI QM-40 spectrofluorometer was used for the determination of fluorescence anisotropy (r) as defined by eqn. (1),

$$r = \frac{I_{VV} - G.I_{VH}}{I_{VV} + 2G.I_{VH}} \qquad (1)$$

where, I_{VV} and I_{VH} are the emission intensities obtained with the excitation polarizer oriented vertically and emission polarizer vertically and horizontally, respectively. The G factor is defined as [30]

$$G = \frac{I_{HV}}{I_{HH}} \qquad (2)$$

here, the intensities I_{HV} and I_{HH} refer to the vertical and horizontal positions of the emission polarizer, with the excitation polarizer being horizontal.

3.2.6 Time-correlated single photon counting measurements

Time-correlated single photon counting (TCSPC) measurements were performed in 10 mM HEPES buffer of pH 7.2 for the fluorescence decay of the free ligand, L and the $[L–Fe(NO_3)]^{2+}$ complex in the absence and presence of SDS at 25 °C. During the TCSPC measurements, photoexcitation was carried out at 510 nm for the $[L–Fe(NO_3)]^{2+}$ complex using a Hamamatsu MCP photomultiplier (R3809) and was analysed by using IBH DAS6 software using eqn (3),

$$F(t) = \sum_i \alpha_i \exp(-\frac{t}{\tau}) \qquad (3)$$

where a_i denotes the i th pre-exponential factor and τ represents the decay time. The decay time is referred to as the lifetime of the excited species.

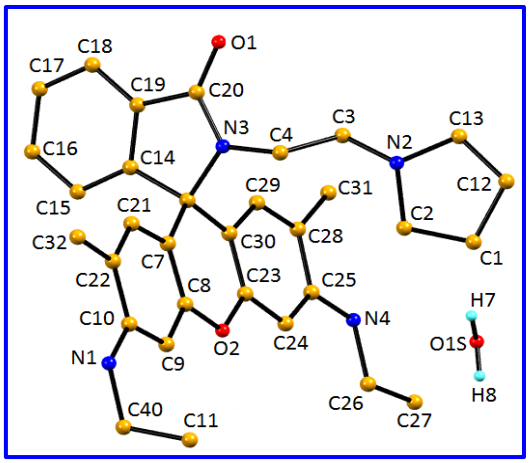

Figure 3.5 Molecular view of ligand (L). H-atoms are omitted for clarity.

3.3 Results and discussion

Scheme 3.1 describes the synthesis of receptor L from the reaction of rhodamine-6G with 1-(2-aminoethyl) pyrrolidine in EtOH under refluxing conditions for 20 h with 68% yield. The final product (L) was well characterized by ^{1}H-NMR (**Figure 3.1**), IR (**Figure 3.2**), HRMS (**Figures 3.3 and 3.4**) and single crystal X-ray diffraction techniques. **Figure 3.5** displays the molecular view of L which was found to crystallize in the P-1 space group of the triclinic system (**Table 3.1**)

Table 3.1 Details of crystallographic data collection and refinements.

Elemental formula	$C_{32}H_{40}N_4O_3$
Formula Weight	528.68
Crystal System	Triclinic
Space group	P-1
Temp/K	296(2)
a/Å	10.36(15)
b/Å	11.54(17)
c/Å	12.54(19)
V/A^3	1452.4(4)
Z	2
Cell angle alpha	81.87(5)
Cell angle beta	77.71(5)
Cell angle gamma	87.24(5)
Theta min	1.68
Theta max	27.16
Crystal description	Block shape
Crystal colour	Light brown
F000	568.0
F000′	568.22
h, k, l max	13,14,16
Tmin	0.991
Tmax	0.994

The solution of L is colorless and non-fluorescent because of its spirolactam form. However, it becomes dark red and highly fluorescent in the presence of Fe^{3+}. But many other metal ions do not produce such optical changes. So, it behaves as a highly sensitive and selective dual channel (colorimetric and fluorometric) sensor for Fe^{3+} in the presence of other metal ions. The apparent formation constant (*K*) was determined by UV-Vis titrations in MeCN-buffer solution (7 : 3 v/v, HEPES at pH 7.0) at 25 °C. A linear form of Benesi–Hildebrand equation (eqn 4) was used to evaluate the dissociation constant and stoichiometry of complexation, where, A_0 and A_{max} are the absorbances of the ligand in the absence and in the presence of

excess metal ion, respectively and n is the stoichiometry (L : $Fe^{3+)}$ of the reaction. A linear least square-fit of $(A_{max} - A_o)/ (A - A_o)$ against $1/[Fe^{3+]}$ clearly demonstrates a 1: 1 stoichiometry of the reaction (n = 1) which also gives an apparent dissociation constants K_d = (8.26 ± 0.03) × 10^{-5} M.

$$\frac{(A_{max} - A_0)}{(A - A_0)} = 1 + \frac{1}{K[Fe^{3+}]} \qquad (4)$$

Similarly, the fluorescence titration (**Figure 3.6**) of L (10 μM) against variable Fe^{3+} concentrations (0–50 μM) under identical reaction conditions gives K_d = (4.81 ± 0.12) × 10^{-5} M and n = 1. There is an excellent agreement between the K values for the $[L–Fe(NO_3)]^{2+}$ system obtained from the absorption and fluorescence titration data clearly manifesting the self-consistency of our results.

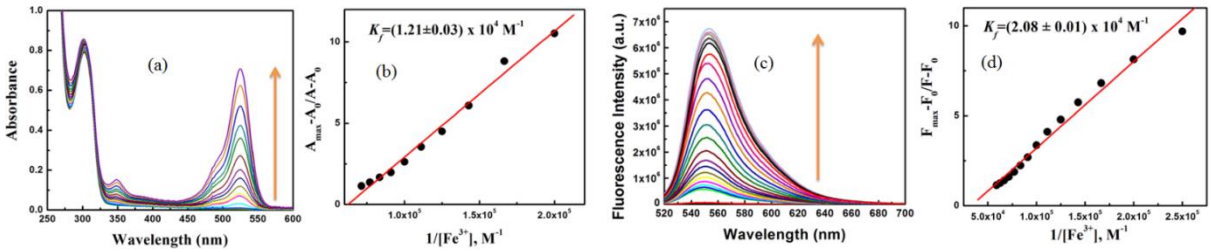

Figure 3.6 UV-Vis (20 μM of L) and florescence titration (10 μM of L) with $[Fe^{3+]}$ (0–25 μM) (a) absorbance vs. wavelength plots for various increasing concentrations of Fe^{3+} (0–20 μM) (b) Benesi–Hildebrand plot; (c) FI vs. wavelength plots for various increasing concentrations of Fe^{3+} (0–25 μM); (d) Benesi–Hildebrand plot.

The detection of Fe^{3+} was not interfered by the presence of different metal ions like Na^+, K^+, Ca^{2+}, Mg^{2+}, Cr^{3+}, Mn^{2+}, Fe^{2+}, Co^{2+}, Cu^{2+}, Ni^{2+}, Zn^{2+}, Cd^{2+}, Hg^{2+} and Pb^{2+} under identical reaction conditions. On addition of 1.5 equivalents of Fe^{3+} to the individual $L–M^{n+}$ solutions containing 5 equivalents of M^{n+} the fluorescence intensity corresponding to the $[L–Fe(NO_3)]^{2+}$ complex was obtained. This observation clearly indicates that Fe^{3+} forms a strong complex with L in the presence of the above-mentioned metal ions, which again suggests that all the tested metal ions do not interfere with the selective detection of Fe^{3+} (**Figure. 3.7**).

The pH-stability of the probe was investigated between pH 2 and 12, which showed no obvious fluorescence of L between pH 4 and 12 (**Figure 3.8**). However, in the presence of

selective guests like Fe^{3+} ions, it fluoresces effectively at pH ≥ 7.0, which clearly indicates the compatibility of the probe for biological applications under physiological conditions.

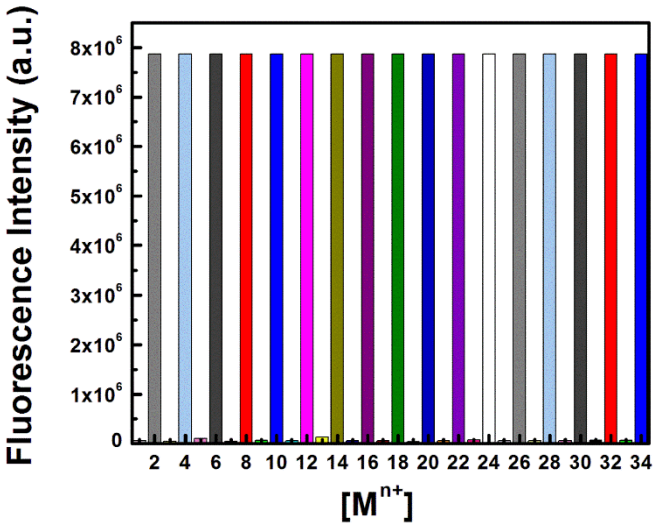

Figure 3.7 Fluorescence emission of L (20 μM) induced by different cations (100 μM) (1-34 are: L, L+Fe^{3+}, L+Na^{+}, L+Na^{+}+Fe^{3+}, L+Cr^{3+}, L+Cr^{3+}+Fe^{3+}, L+Ca^{2+}, L+Ca^{2+}+Fe^{3+}, L+Mg^{2+}, L+Mg^{2+}+Fe^{3+}, L+K^{+}, L+K^{+}+Fe^{3+}, L+Al^{3+}, L+Al^{3+}+Fe^{3+}, L+Mn^{2+}, L+Mn^{2+}+Fe^{3+}, L+ Fe^{2+}, L+ Fe^{2+}+Fe^{3+}, L+Co^{2+}, L+ Co^{2+}+Fe^{3+}, L+Cu^{2+}, L+Cu^{2+}+Fe^{3+}, L+Ni^{2+}, L+Ni^{2+}+Fe^{3+}, L+Zn^{2+}, L+Zn^{2+}+Fe^{3+}, L+Cd^{2+}, L+Cd^{2+}+Fe^{3+}, L+Hg^{2+}, L+Hg^{2+}+Fe^{3+}, L+Pb^{2+}, L+Pb^{2+}+Fe^{3+}, L+ Ag^{+}, L+ Ag^{+}+Fe^{3+}).

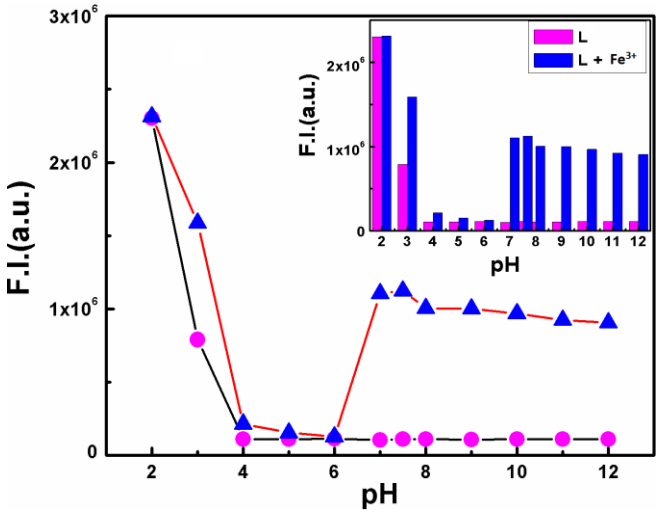

Figure 3.8 pH dependence of the FIs of the free ligand L (magenta) and the L –Fe^{3+} complex with L: Fe^{3+}= 1:1.05 (blue) in the MeCN/H_2O (3:7 v/v) solvent system with λ_{ex}= 510 nm. The inset shows the histogram plot.

The IR spectrum of the receptor reveals the presence of the characteristic stretching frequency of the amidic 'C=O' of the rhodamine moiety at 1692 cm^{-1}, which is shifted to a lower wavenumber of 1637 cm^{-1} in the presence of 1.2 equivalents of Fe^{3+} (**Figure 3.2**). This large shift ($\Delta\nu$ =54 cm^{-1}) signifies a strong polarization of the C=O bond upon efficient binding to the Fe^{3+} ion. In fact, it indicates the formation of the L–Fe^{3+} complex by opening of the spirolactam ring.

The 1: 1 (L: Fe^{3+}) complexation was determined by Job's method (**Figure 3.9**) and further supported by mass spectrometric analysis (m/z = 628.4961) $[L–Fe(NO_3)]^{2+}$.

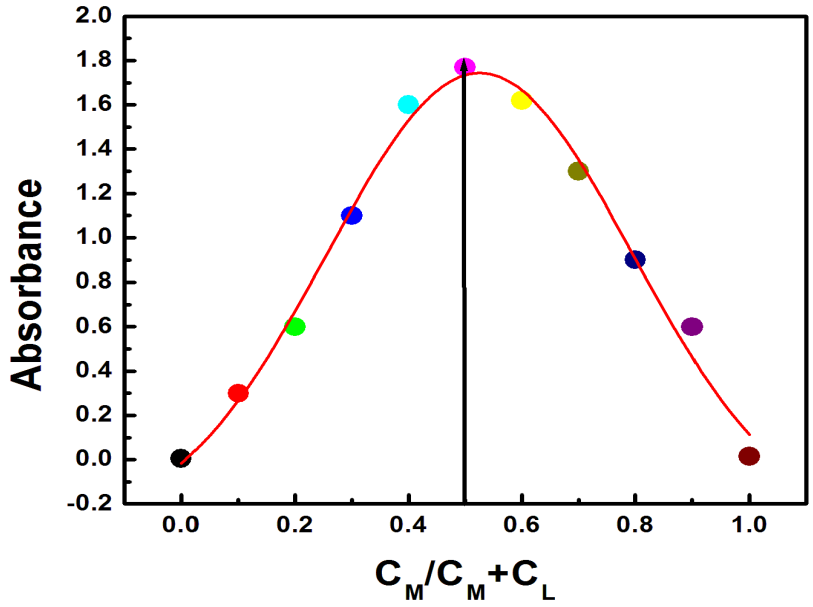

Figure 3.9. Job's plot for the determination of the composition of the L–Fe^{3+} complex.

3.3.1 Steady-state fluorescence studies in the presence of SDS

We have also carried out fluorescence titration in pure water in the presence of SDS under two conditions. (i) At a fixed concentration of L (10 μM) and SDS (10 mM) and a variable concentration of Fe^{3+} (ii) at a fixed concentration of L (10 μM) and Fe^{3+} (10 μM) and a variable concentration of SDS.

In case (i), there is a gradual increase in FI with the increase in Fe^{3+} concentration. It reaches a maximum at ~10 μM Fe^{3+} and then remains almost constant on a further increase in Fe^{3+} concentration. The major linear part of the plot was used to extract the association constant K_f by using the linear form of equation (5) under the condition $1 \gg c \times x^n$ with n = 1[31] and the value was evaluated to be $(1.27 \pm 0.10) \times 10^5$ M^{-1} (**Figure 3.10**). It is found to be

an order of magnitude higher than that obtained in MeCN– H_2O in the absence of SDS. This indicates a higher stability of the complex formed in the excited state in the presence of SDS.

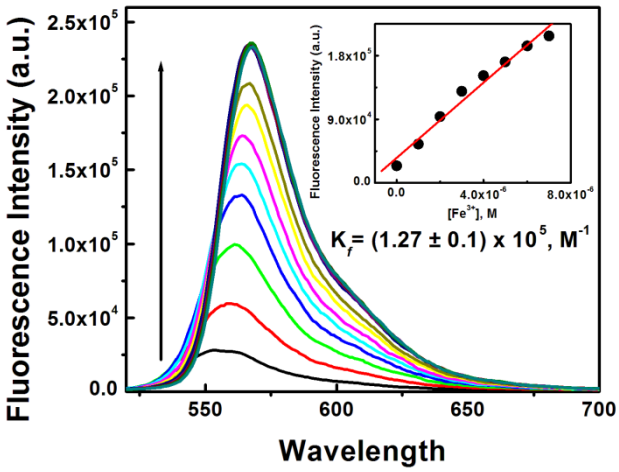

Figure 3.10 Florescence titration of L (10 µM) by Fe^{3+} in the presence of SDS (9 mM) with λ_{ex} = 510 nm; (b) plot of FI as a function of [SDS].

$$y = \frac{(a + b \times c \times x^n)}{1 + c \times x^n} \qquad (5)$$

This enhanced stability constant value may be due to the restricted movement of the doubly positively charged $[L–Fe(NO_3)]^{2+}$ complex by the strong electrostatic attraction with the negatively charged head group of SDS in the form of laminar aggregates.

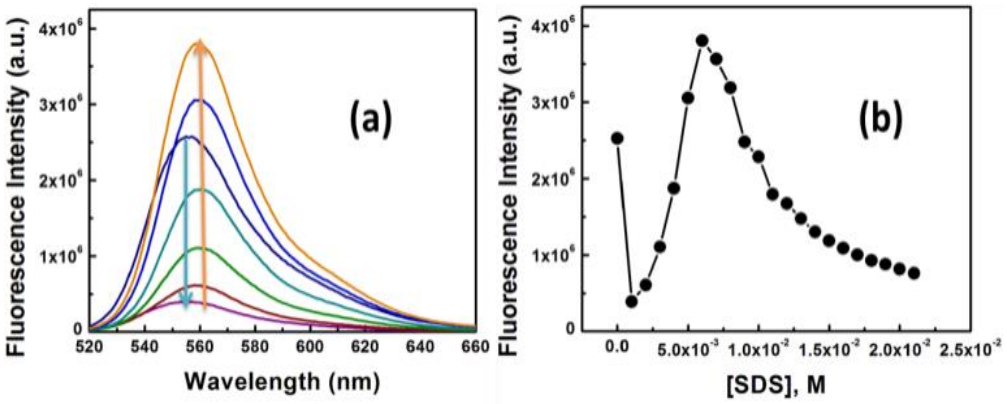

Figure 3.11 Florescence titration of L (10 µM) by SDS in the presence of $[Fe^{3+}]$ (10 µM) with λ_{ex} = 510 nm; (b) plot of FI as a function of [SDS].

In the second case, a plot of FI vs. [SDS] shows an initial sharp drop in FI of the $[L–Fe(NO_3)]^{2+}$ complex in water on adding 1 mM SDS and then it increases rapidly with the increase in SDS concentration, reaches a maximum at 7.0 mM, and then decreases with the

increase in SDS concentration, which is clearly demonstrated in (**Figure 3.11b**). The initial sharp drop in FI may arise due to the breakdown of the self-organized $[L–Fe(NO_3)]^{2+}$ complex (non-covalently attached polymer) in purely aqueous medium in the presence of 1 mM SDS.

This experiment clearly demonstrates the aggregation between $[L–Fe(NO_3)]^{2+}$ and SDS, which is favored with the increase in SDS concentration up to 7 mM SDS. With a further increase in [SDS], there is a gradual decrease in FI and it reaches almost a plateau at [SDS] ~ 18 mM (**Figure 3.11b**). The appearance of the fluorescence maximum at [SDS] ~ 7 mM clearly indicates that the critical micellar concentration (CMC) of SDS is 7 mM under the experimental conditions. The decrease in FI with [SDS] beyond 7 mM may be attributed to a change in the morphology of SDS surfactant from laminar to spherical micelles on increasing the [SDS], and at the same time the polymeric $[L–Fe(NO_3)]^{2+}$ becomes a monomer and gets trapped inside the micellar cavity. The formation of the monomer results in a decrease in FI. The increase in FI with [SDS] manifests the fact of aggregation-induced enhancement of emission (AIEE). It is interesting to note that in the presence of 9 mM SDS, no quenching of the fluorescence intensity of the $[L–Fe(NO_3)]^{2+}$ complex by HF_2^- was observed, which was otherwise observable in the absence of SDS. This clearly indicates the non-accessibility of the $[L–Fe(NO_3)]^{2+}$ complex to HF_2^- due to trapping inside the micellar cavity.

3.3.2 Steady-state fluorescence anisotropy

We have measured the steady-state fluorescence anisotropy to monitor the extent of restriction imposed by the micro heterogeneous environment on the dynamic properties of the probe. To check this, we have monitored the fluorescence anisotropy as a function of SDS concentration at a fixed concentration of L and Fe^{3+} (10 μM each) at 564 nm.

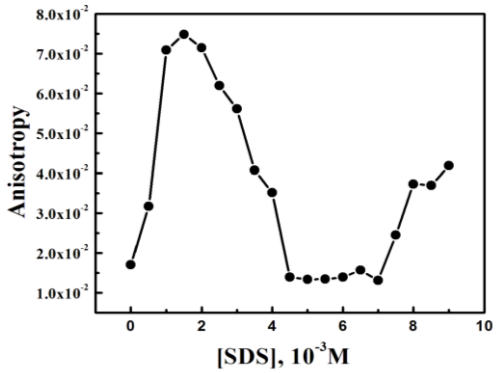

Figure 3.12 Plot of fluorescence anisotropy (r) as a function of [SDS] in purely aqueous medium at 25 °C and $[L] = [Fe^{3+}] = 10$ μM, $\lambda_{ex} = 510$ nm.

A steady increase in anisotropy on increasing the SDS concentration up to 1.5 mM occurs, followed by a gradual decrease with SDS concentration, reaching a plateau at ~4.2 mM, and then maintaining a steady value up to 7.0 mM. After that, it again slowly increases with the increase in [SDS] (**Figure. 3.12**).

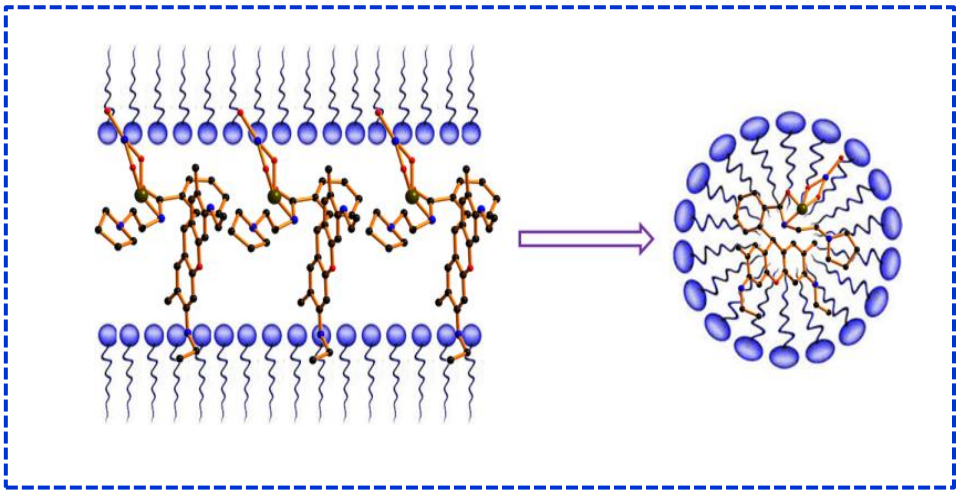

Scheme 3.2 Schematic presentation of the interactions of probe with the laminar microstructure and micellar microstructure of SDS (adopted from UC Davis Chewiki).

As discussed earlier, the initial sharp increase in anisotropy with [SDS] may be due to the layer arrangement of SDS. Between two such layers $[L–Fe(NO_3)]^{2+}$ complexes are trapped by electrostatic interaction with the negatively charged sulfonic acid head groups (**Scheme 3.2**). This regular arrangement of the $[L–Fe(NO_3)]^{2+}$ complex further interacted among themselves by π···π stacking interactions to form a polymer imposing a firm restriction to their free movement and hence resulting in an enhancement in anisotropy. On further increasing [SDS], the regular layer arrangement of SDS is broken down and $[L-Fe(NO_3)]^{2+}$ becomes free as a monomer. As a consequence, there value decreases and reaches a minimum at ~4.20 mM and remains constant up to 7 mM where no formation of micelle occurs. But above 7 mM of SDS, the micellization process dominates and this entraps the $[L–Fe(NO_3)]^{2+}$ complex inside the cavity as a monomer resulting in a slow but steady increase anisotropy with the increase in [SDS]. The encapsulation of $[L–Fe(NO_3)]^{2+}$ inside the cavity is supported by the failure of HF_2^- to quench the fluorescence of the complex, which otherwise is quenched in the absence of 9 mM SDS (**Figure 3.12**). It is well accepted that an increase in the rigidity of the fluorophore results in an increase in the fluorescence anisotropy.

3.3.3 Analyses of surface topography of ligand, ligand–SDS, metal–ligand and Metal- ligand –SDS composites

The change in surface topology has been noticed from the FESEM studies for ligand, ligand with SDS, metal–ligand, and metal–ligand with SDS, which indicates that SDS has a pronounced effect on the surface design. The synthesized materials are very different from each other**.** The morphology of the ligand is well dispersed throughout the phase having quasi cubical grains with an average size of ~30 nm, which is also indicated in the inset figure (**Figure 3.13(a)**). But in the case of ligand–SDS interactions a change in surface topology occurs, indicating that no free ligand molecules are present in the system [**Figure 3.13(a)** and **(b)**]. In the case of metal–ligand interactions, numerous microstructural defects with fibroid-like morphology are visible, but with SDS, the ternary interactions greatly influence the fibroid structure with densely occupied spherical uniform holes. This behaviour of the molecules enhances the optical properties as shown in **Figure 3.13(c)** and **(d)**, which is also clearly indicated in the respective inset figures. Due to the betterment of fibroid interactions between the metal and ligand, charge-transfer interactions take place. When fabricated on the conducting glass substrate (FTO), good electrical conductivity in the presence of photons is obtained, which performs as a photo-switching material. Thus, the FESEM analyses indicate that the surface structures as well as defects at the surface levels are important for device applications.

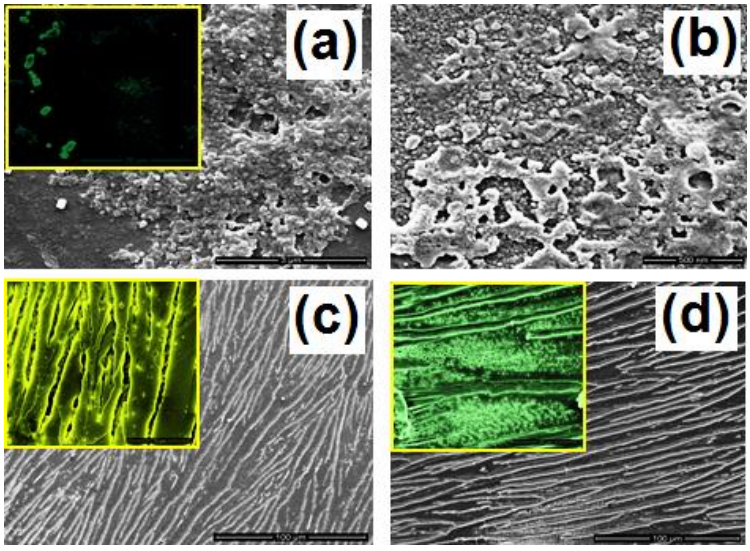

Figure 3.13 FESEM analyses of (a) Ligand with inset image, (b) Ligand-SDS (c) Metal-Ligand with inset image and (d) Metal-Ligand-SDS with inset image.

3.3.4 Thin film fabrication from the precursor complex $[L–Fe(NO_3)]^{2+}$

The thin films of hybrid materials have attracted both inorganic and organic chemists as they can be used to design various microelectronic and optoelectronic devices. For the preparation of inorganic–organic thin films, the spin-coating method has the merits of convenience, use of low-cost equipment, and a faster operating system. Spin coating is a convenient and reproducible method for applying highly uniform thin films to substrates of all kinds. Moreover, it requires smaller amounts of material and less processing time compared to other methods.

In our work, a $[L–Fe(NO_3)]^{2+}$ film is fabricated onto a FTO glass substrate having an area of 3.5 cm × 1.5 cm by spin coating of a sol precursor. For the preparation of $L–Fe^{3+}$ sol, the complex precursor $[L–Fe(NO_3)]^{2+}$ is mixed with acetonitrile in the ratio 1:10. The mixture solution was stirred for 20 minutes at room temperature and at a constant speed without any perturbation. The FTO glass substrates were cleaned from end to end ultrasonically in detergent, deionized water, acetone, and isopropanol sequentially before spin coating deposition under an ambient atmosphere. The nanostructure $[L–Fe(NO_3)]^{2+}$ complex sol was spin-coated at 2000 rpm for 1 min onto a FTO pre-cleaned glass. The spin coat consists of a variable rotating vacuum chuck powered by a motor. The substrate was held firmly in position by atmospheric pressure. In a clean environment, five drops of $[L–Fe(NO_3)]^{2+}$ complex precursor in acetonitrile were allowed to fall with the help of a clean syringe onto the centre of a stationary conducting glass substrate. The drop spreads outcross the substrate under the influence of the centrifugal force. As it moves, the solvent evaporates from the solution, leaving a smooth continuous film. The resulting hybrid film was annealed on a hot plate at ∼60 °C for 15 minutes to remove the residual solvent. This procedure was repeated several times to get crystalline, uniform, pinhole-free thin films of the inorganic–organic complex on the FTO substrate (sheet resistance ∼10 Ω sq^{-1}). The thicknesses of the films were determined by the gravimetric method using the formula[32] $t = (W_2 - W_1)/Ad$, where, t is the thickness of the film, A is the area covered by the film, d is the density of the $[L–Fe(NO_3)]^{2+}$ complex (1.18 g cm^{-3}), and W_1 and W_2 are the weight of the FTO glass substrate before and after deposition, respectively. The deposited film ($t = 1.6 \times 10^{-5}$ cm) was studied using a field emission scanning electron microscope for surface morphology, a UV-Vis spectrophotometer for optical measurement and a semiconductor characterization system for

electrical measurement. Therefore, iron complex modified TO thin films [L -Fe(NO_3)]$^{2+}$ / FTO/glass are used for diode characteristics and frequency-switching device application.

3.3.5 Morphological characteristics of [L–Fe(NO_3)]$^{2+}$/FTO thin films

The deposited [L–Fe(NO_3)]$^{2+}$/FTO film was investigated using FESEM as shown in **Figure 3.14**. From the surface morphology analysis, microstructural fractures in the film with numerous spherical grains with distinct grain boundaries have been observed at a low magnification of 1.30 K× (**Figure 3.14(a)**) due to drought of solvent molecules. At high magnification 20.00 K× (**Figure 3.14(b)**), small islands with several coarse wells are separated uniformly. Each island is composed of uniformly distributed spherical grains of the [L–Fe(NO_3)]$^{2+}$ complex having a diameter in the range of 80 to 100 nm on the FTO glass substrate at the magnification of 19.45 K×. The grains are distinct and the grain boundaries are prominent as shown in **Figure 3.14 (c)**.

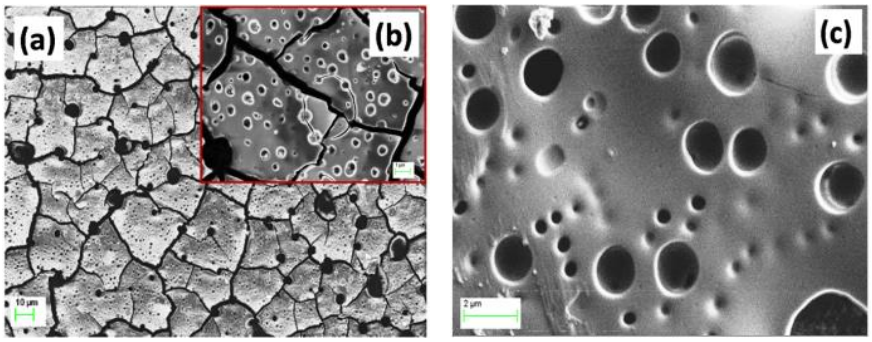

Figure 3.14 Field emission scanning electron micrograph of the [L–Fe(NO_3)]$^{2+}$/FTO thin film.

However, the formation of larger grains from smaller crystallites is essential for the spontaneous lowering of Gibb's free energy in the system to gain stability. Nanoparticles have a higher surface-to-volume ratio, so the surface energy of the system becomes significantly high. For this reason, every system has a tendency to lower down the free energy by forming larger grains from smaller crystallites by spontaneous agglomeration.

3.3.6 UV-Vis analysis

The absorption spectrum showed a moderately sharp onset in absorbance around 550 nm, which represents the typical band to band transition for the pure [L–Fe(NO_3)]$^{2+}$ complex (**Figure 3.15**).The band gap energy for the [L–Fe(NO_3)]$^{2+}$/FTO thin film was calculated using the Thuc's relation:[33] $[(\alpha h\nu)^{1/n} = A(h\nu - E_g)]$,where A is a constant related to the effective

masses of charge carriers, h is the Planck constant, E_g is the band gap energy, hν is the incident photon energy, and 1/n is the exponent that depends on the nature of the optical transition (n = 0.5 and 2 for direct and indirect transition, respectively). The Tauc's plot (inset **Figure 3.16**) indicates the direct band gap energy of 1.6 eV for the deposited films.

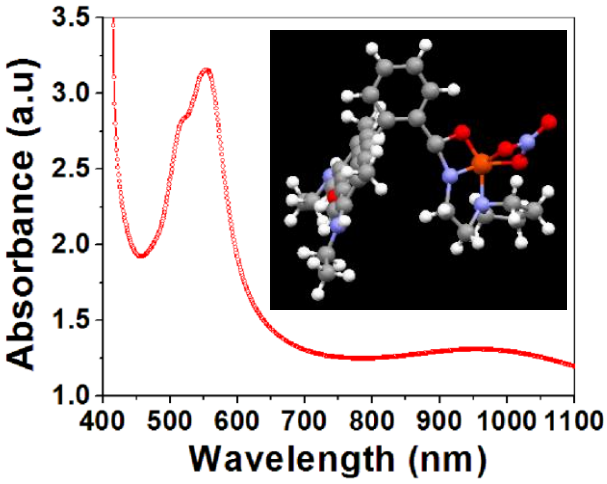

Figure 3.15 Absorption spectrum of the pure $[L–Fe(NO_3)]^{2+}$ complex.

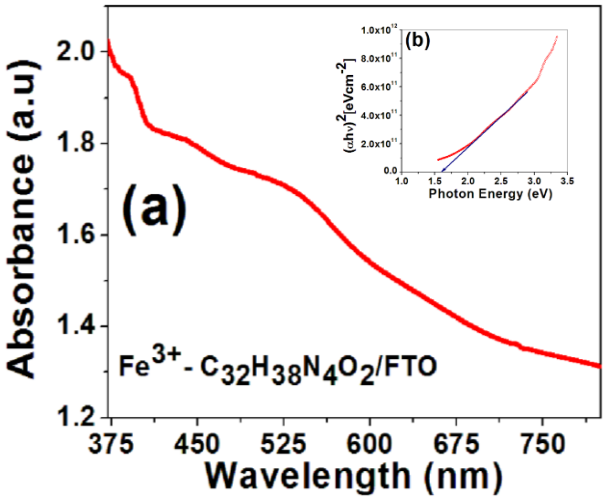

Figure 3.16 The absorption spectrum of $[L–Fe]^{2+}$ thin film (figure. a); inset (figure. b): plot of $(\alpha hv)^2$ vs. *hv*, Tauc's plot.

3.3.7 Electrical properties: current–voltage (I–V) characteristics by the two-probe technique

Two-probe I–V measurement was carried out by taking FTO coated glass substrates as the bottom contact and 2 mm ×2 mm graphite paste as the top contact as shown in **Figure 3.17**. The nanostructured thin film consists of surface defects which influence the intrinsic band nature from its bulk counterpart directly, which affects the electronic transition and phonon

transfer process.[34] The electronic defects at the grain boundaries of the nanoparticles generate traps which directly affect the current–voltage properties.

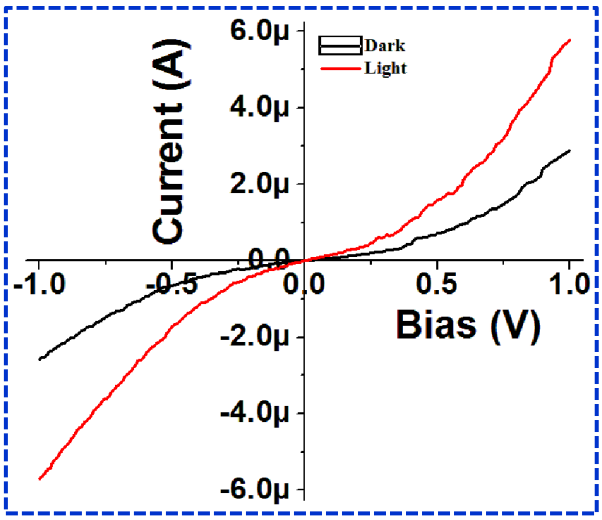

Figure 3.17 Representative two-probe *I-V* characteristics of the $[L–Fe(NO_3)]^{2+}$/FTO thin films under dark and light conditions.

Under a no-bias condition, the electron affinity for the traps at the surface of the grains is higher but upon changing the bias, the traps get filled. Therefore, the enrichment of current densities can be noticed when all the traps are filled; meanwhile, on irradiation of light, the generated charge carriers at the surface level influence the nature of the I–V curve with high current density and high steepness at forward bias. During the reverse bias, the opposite phenomenon is supposed to be taking place. The increase of reverse bias affects the electrostatic attraction of the trapped electronic environment with greater ease, and an increment in the negative current densities is observed both under dark and light conditions. Thus, trapping and de-trapping of charge carriers play an important role in the symmetrical nature of the I–V curve. As the FTO (n-type) modified $[L–Fe(NO_3)]^{2+}$ thin film showed anon-linear change in current–voltage, a possible formation of depletion region at the interface can be presumed. Non-linear symmetric I–V also supports the formation of a weak junction at the interface of p-type ($[L–Fe(NO_3)]^{2+}$) and n-type FTO glass substrate, through which electrons overcome the barrier in a restricted manner.[35] The current obtained in the reverse bias is mainly due to the loss of junction barrier properties which can increase the reverse saturation current due to the free minority carriers at the junction. On the other hand, from the FESEM image, it is evident that the deposited films have fewer micropores along

the c-axis, which is responsible for producing a leakage path, supporting the bias-assisted rectification.

3.3.8 Photon-induced exciton generation

Light-dependent exciton generation was carried out by taking the top and bottom contacts with graphite paste on FTO Andon the $[L–Fe(NO_3)]^{2+}$ film for the measurement of switching behaviour, a light with an intensity of 1 Sun was allowed to passthrough the FTO glass substrate and up to the film.[36] The response ratio curve for the light-induced frequency-switching phenomenon by which a 50-Hz pulse was generated as soon as the light was 'on' was found to be quite steady for a period of 25 s. A decay of only 1–2 Hz was noted during this period. A sudden drop of this pulse to the 'zero' state took place with the 'off' state of the incident light. This is due to the oscillation frequency of the photo-generated electrons and the holes in an exciton. On switching off the light, the photo-generated electrons and the holes will recombine, leading to no oscillation of the charged species, and hence no frequency was detected. Good consistency of this switching behaviour was found for more than 50 cycles; ten of them are represented here. This low magnitude light induced pulse generation might be the contribution of the confined exitonic transition that might be a very low free carrier concentration within the metal complex matrix.

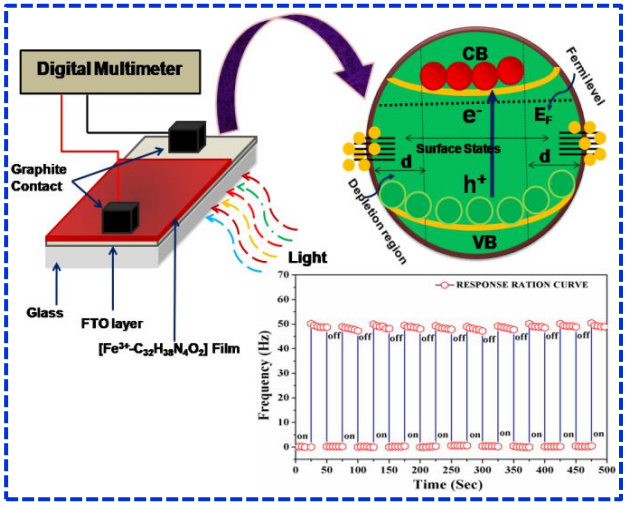

Figure 3.18 Schematic diagram of photo-switching behaviour of $[L–Fe(NO_3)]^{2+}$/FTO films and their response curves.

It is a fact that intrinsic defects like anion/cation vacancies within the metal ligand complex can adsorb gas molecules like oxygen or water vapor from the atmosphere. Trapping of such molecules will create some trap electrons/energy levels on the surface of the

semiconductor, leading to a space charge region and related band bending inside the semiconductor (**Figure 3.18**). So, the number of electrons–hole pairs increases, which significantly affect some unique physical properties like enhancement of photo-luminescence intensity, light-induced frequency-switching behaviour, etc.

3.4 Conclusion

In this article, we have successfully presented a highly selective fluorescent chemosensor of rhodamine-1-(2-aminoethyl) pyrrolidine(L) towards Fe^{3+} through 1: 1 complexation under the specified reaction conditions of 3 : 7 water : MeCN (v/v) at pH 7.2; 10 mM HEPES buffer, μ = 0.05 M LiCl; it shows an enhancement in the corresponding fluorescence intensity of 106-fold with an apparent binding constant (K_f) of 8.10 ×10^4 M^{-1}. We have also carried out fluorescence titration and anisotropy (r) studies in pure water in the presence of SDS. Based on the dependence of FI and r on [SDS], it was proposed that the probe is trapped between two SDS monolayers, which again interacted among themselves by π···π stacking. As a result, there is an increase in FI up to [SDS] ~ 7 mM – a phenomenon reminiscent of aggregation-induced enhancement of emission (AIEE). Beyond this concentration of SDS (7 mM), micelle formation takes place and the π···π stacked polymer now becomes a monomer and is trapped inside the micellar cavity, which is again confirmed by the failure of HF_2^- to quench the FI of the $[L–Fe(NO_3)]^{2+}$ complex trapped inside the micellar cavity, which otherwise quenches the FI of $[L–Fe(NO_3)]^{2+}$ in the absence of SDS. Due to the trapping of the$[L–Fe(NO_3)]^{2+}$ monomer complex, there is a decrease in FI at [SDS] > 7 mM. In the case of anisotropy, it increases on increasing [SDS] beyond 7 mM. Ligands, metals, and SDS interactions are well established through different optical and morphological studies. $[L–Fe(NO_3)]^{2+}$ thin films on an FTO glass substrate have been designed with the help of the spin coating deposition technique. The deposited film having a thickness of 1.6 × 10^{-5} cm is well characterized by optical band gap calculation with a direct band gap, ε_g ~ 1.6 eV. FESEM studies were also performed on the $[L–Fe(NO_3)]^{2+}$/FTO film. The electrical behaviour, i.e. current–voltage characteristics by the two-probe technique was also studied. Light dependent exciton generation was carried out by taking the top and bottom contacts with graphite paste on FTO and on the $[L–Fe(NO_3)]^{2+}$ films for the measurement of switching behaviour's response ratio curves for the light-induced frequency-switching phenomenon have been obtained. The frequency taped here is the oscillation frequency of the photogenerated

electron and the hole in an exciton. Thus, the light induced frequency-switching behaviour and Schottky barrier diode characteristics of the material were established.

References

1) J. R. Burdo and J. R. Connor, *Biometals*, 2003, **16**, 63–75.

2) J. R. Connor, S. L. Menzies, S. M. St. Martin and E. J. Mufson, *J. Neurosci. Res*., 1990, **27**, 595–611.

3) R. R. Crichton, S. Wilmet, R. Legssyer and R. J. Ward, *J. Inorg. Biochem.,* 2002, **91**, 9–18.

4) R. S. Eisenstein, Annu. *Rev. Nutr*., 2000, **20**, 627–662.

5) B. T. Felt and B. Lozoff*, J. Nutr*., 1996, **126**, 693–701.

6) C. J. Earley, J. R. Connor, J. L. Beard, E. A. Malecki, D. K. Epstein and R.P. Allen, *Neurology*, 2000, **54**, 1698–1700.

7) J. P. Sumner and R. Kopelman, *Analyst*, 2005, **130**, 528–533.

8) Y. Ma, W. Luo, P. J. Quinn, Z. Liu and R. C. Hider*, J. Med. Chem.*, 2004, **47**, 6349–6362.

9) G. E. Tumambac, C. M. Rosencrance and C. Wolf, *Tetrahedron*, 2004, **60**, 11293–11297.

10) A. Ali, Q. Zhang, J. Dai and X. Huang, *Biometals*, 2003, **16**, 285–293.

11) Y. Ma, W. Luo, P. J. Quinn, Z. Liu and R. C. Hider, *J. Med. Chem*., 2004, **47**, 6349–6362.

12) J. Mao, L. Wang, W. Dou, X. Tang, Y. Yan and W. Liu*, Org. Lett.*, 2007, **9**, 4567–4570.

13) M. Xu, S. Wu, F. Zeng and C. Yu, *Langmuir*, 2010, **26**, 4529–4534.

14) X. Wu, B. Xu, H. Tong and L. Wang, *Macromolecules*, 2010, **43**, 8917–8923.

15) S. Das, K. Aich, S. Goswami, C. K. Quah and H. K. Fun, *New J. Chem*., 2016, **40**, 6414–6420.

16) R. Kagit, M. Yildirim, O. Ozay, S. Yesilot and H. Ozay, *Inorg. Chem*., 2014, **53**, 2144–2151.

17) L. Zhanga, J. Fana and X. Penga, *Spectrochim. Acta, Part A*, 2009, **73**, 398–402.

18) L. Zhang, J. Wang, J. Fan, K. Guo and X. Peng, *Bioorg. Med. Chem. Lett*., 2011, **21**, 5413–5416.

19) N. R. Chereddy, S. Thennarasu and A. B. Mandal, *Dalton Trans*., 2012, **41**, 11753–11759.

20) S. Parihar, V. P. Boricha and R. N. Jadeja, *Luminescence*, 2015, **30**, 168–174.

21) J. An, T. Li, B. Wang, Z. Yang and M. Yan*, J. Coord. Chem.,* 2014, **67**, 921–928.

22) Y. Yu, X. Cheng, H. Liu, S. Gu, Z. Jiang, H. Huang and J. Lian, *J. Polym. Sci., Part A: Polym. Chem*., 2015, **53**, 615–621.

23) A. Sikdar, S. S. Panja, P. Biswas and S. Roy, *J. Fluoresc*., 2012, **22**, 443–450.

24) O. Ozay and H. Ozay, *J. Macromol. Sci., Part A: Pure Appl. Chem*., 2014, **51**, 308–317.

25) B. Wang, J. Hai, Z. Liu, Q. Wang, Z. Yang and S. Sun, *Angew. Chem., Int. Ed*., 2010, **49**, 4576–4579.

26) M. Deng, S. Wang, C. Liang, H. Shang and S. Jiang, *RSC Adv*., 2016, **6**, 26936–26940.

27) Y. Liu, R. Shen, J. Ru, X. Yao, Y. Yang, H. Liu, X. Tang, D. Bai, G. Zhang and W. Liu, *RSC Adv*., 2016, **6**, 111754–111759.

28) P. chabera, Y. Liu, O. Prakash, E. Thyrhaug, A. E. Nahhas, A. Honarfar, S. Essen, L. A. Fredin, T. C. B. Harlang, K. S. Kjaer, K. Handrup, F. Ericson, H. Tatsuno, K. Morgan, J. Schnadt, L. Haggstrom, T. Ericsson, A. Sobkowiak, S. Lidin, P. Huang, S. Styring, J. Uhlig, J. Bendix, R. Lomoth, V. Sundstrom, P. Persson and K. Warnmark, *Nature*, 2017, **543**, 695–699.

29) A. P. Alivisators, *J. Phys. Chem*., 1996, **100**, 13226–13239.

30) J. R. Lakowicz, *Principles of Fluorescence Spectroscopy, 3rdedn, Springer, New York*, 2006, p. 67.

31) C. R. Lohani, J. M. Kim, S. Y. Chung, J. Yoon and K. H. Lee, *Analyst*, 2010, **135**, 2079–2048.

32) B. Chakraborty, B. Show, S. Jana, B. C. Mitra, S. K. Maji, B. Adhikary, N. Mukherjee and A. Mondal*, Electrochim. Acta,* 2013, **94**, 7–15.

33) R. Bertoni, M. Lorenc, J. Laisney, A. Tissot, A. Moreac, S. F. Matar, M. L. Boillot and E. Collet, *J. Mater. Chem. C*, 2015, **3**, 7792–7801.

34) B. Show, N. Mukherjee and A. Mondal, *RSC Adv*., 2014, **4**, 58740–58751.

35) S. Jana, N. Mukherjee, B. Chakraborty, B. C. Mitra and A. Mondal, *Appl. Surf. Sci.,* 2014, **300**, 154–158.

36) K. W. Liu, R. Chen, G. Z. Xing, T. Wu and H. D. Sun, *Appl. Phys. Lett*., 2010, **96,** 023111.

Chapter 4

A Newly Synthesised Morphology Directing Highly Sensitive Rhodamine B based Fluorescent Fe^{3+} Complex: Interaction with Human serum Albumin

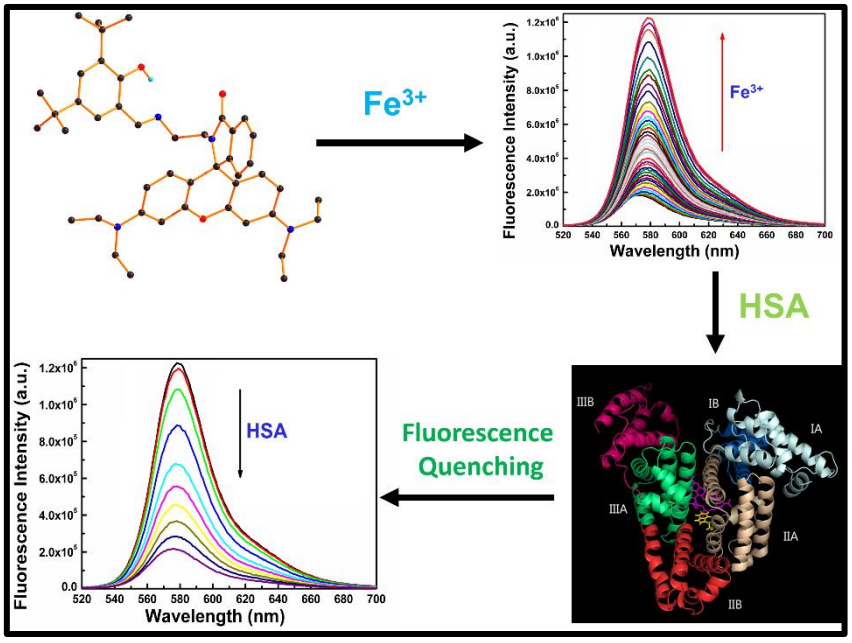

Abstract:

A rhodamine-B based fluorescent molecular probe **L** selectively recognizes Fe^{3+} ion calorimetrically as well as fluorometrically in the presence of various metal ions and anions. It forms [(L-Fe)] complex giving 1:1 binding stoichiometry in 8:2 (H_2O: MeCN, v/v) as delineated by **ESI-MS**$^+$ studies ($[Fe(L)(NO_3)_2(CH_3CN)(CH_3CN)] + Li^+$). The structure of **L** was analysed by single crystal X-diffraction studies along with NMR, mass spectroscopy and FTIR studies. The dissociation constant ($(2.95 \pm 0.06) \times 10^{-5}$ M) and ($(9.48 \pm 0.06) \times 10^{-5}$ M) were determined by UV-Vis and fluorescence titration respectively revealing a strong binding between **L** and Fe^{3+}. The limit of detection (LOD) of Fe^{3+} by **L** was 0.27 μM while quantum yields of **L** and [L–Fe] were 0.011 and 0.36, respectively. Fluorescence anisotropy measured in the presence of HSA indicates the rigidity of the local micro environment where [L–Fe] was trapped in the sub domain IIA of HSA, as delineated by molecular docking studies. Furthermore, stone like microstructure of **L** formed in 8:2 HEPES buffer:MeCN, (v/v) medium changes to spherical shape in the presence of Fe^{3+} and when the complex interacts with HSA it gets agglomerated. All these are exhibited in SEM studies. All the forgoing discussion establishes that this probe (**L**) is useful for on-site Fe^{3+} recognition through a fast, simple and eco-friendly process.

4.1 Introduction

Recently, chemosensors have become an important tool for environmental remediation as well as in medicinal chemistry.[1-3] They are particularly valuable for the recognition of metal ions such as Cu^{2+}, Fe^{2+}, Fe^{3+}, Zn^{2+}, Hg^{2+}, and Pb^{2+}. Over the last decade, the development of selective probes has enabled the detection of various species, including Cu^{2+}, Fe^{2+}, Fe^{3+}, Zn^{2+}, Hg^{2+}, Pb^{2+}, fluoride (F^-), cyanide (CN^-), and pyrophosphate, among others. [4-7]

Iron is one of the most crucial elements for all living organisms. It plays a vital role in haemoglobin formation and is also essential for several other biological processes.[8,9] A deficiency in iron can lead to conditions such as anaemia, hemochromatosis, liver damage, cancer, and diabetes due to reduced oxygen delivery. [10,11] Conversely, an excess of iron can trigger the Fenton reaction, which produces reactive oxygen species (ROS) that damage proteins, nucleic acids, and lipids.[12-17] This oxidative damage accelerates the development of serious diseases such as Parkinson's and Alzheimer's. [18-22]

Iron plays vital roles in various biochemical processes, but there are relatively few reports on selectively iron recognition probes.[23-30] So, it is very much desirable to design a simple, selective and sensitive iron sensor. As Fe^{3+} is paramagnetic in nature, so most of the sensors show fluorescence quenching.[31-34] Only in scarce cases turn-on fluorescence responses by Fe^{3+} were found, but few other metal ions like Cr^{3+} and Cu^{2+} have been found to interfere. [35-37] Mostly, rhodamine-6G based chemosensors response in non-aqueous media due to lack of solubility.[38-47] But for the biological study the complex must be soluble in pure aqueous media and there are only three reports where the study was carried out in pure aqueous buffer medium.[48-50] Thus, there is a strong need to develop a selective chemosensor for Fe^{3+} that is also soluble in aqueous media to facilitate biological study.

Human serum albumin (HSA) is a soluble protein consisting of 585 amino acids, making up approximately 60% of plasma, with a concentration of around 42 mg/mL, and contributing roughly 80% of the total colloid. HSA plays a key role in the circulatory system and is involved in numerous physiological activities, the most important of which is the transport and storage of various exogenous and endogenous compounds. These include ligands, metal ions, drugs, amino acids, fatty acids, and steroids.[51-53] In biomedical and pharmaceutical sciences, there is significant interest in studying drug-protein interactions due to the strong binding affinity between many drugs and albumin.[54] The hydrophobic binding regions of HSA are critical for drug deposition and efficacy, as they enhance the solubility of many drugs in plasma and modify their delivery to *in vivo* and *in vitro* cells. The fluorescence

emission of HSA is largely attributed to its tryptophan residue, which is highly sensitive to its local environment. This sensitivity depends on factors such as subunit association, conformational changes, and protein denaturation. Therefore, fluorescence measurements can be effectively used to determine the binding affinities/sites between HSA and various compounds.

The spirolactam ring structure of Rhodamine B is generally non-fluorescent, but it exhibits strong fluorescence upon binding with metal ions. In this study, we have developed a Rhodamine-B based selective fluorescent chemosensor for Fe^{3+} ion in an organo-aqueous medium. Additionally, we investigate the interaction of human serum albumin (HSA) with the iron complex, as well as the binding affinity, using various spectroscopic techniques. Circular dichroism (CD) spectroscopy was employed to assess the conformational changes in HSA upon binding with the iron complex. Furthermore, molecular docking study was also conducted to explore the possible binding location of iron complex within HSA. Scanning electron microscopy (SEM) study was also performed to confirm the binding of the probes to Fe^{3+}, as well as the morphological changes induced in the HSA-iron complex interaction.

4.2 Experimental section

4.2.1 Materials and methods

Rhodamine B, ethylenediamine, 3,5-di-tert-butyl-2-hydroxybenzaldehyde, and ferric nitrate, used as starting materials were purchased from Sigma-Aldrich, for the preparation of the ligand (L) and its iron complex [L−Fe]. Solvents such as ethanol and acetonitrile (Merck, India) were of HPLC grade. Metal perchlorate salts, including Na^+, K^+, Ca^{2+}, Fe^{2+}, Co^{2+}, Ni^{2+}, Zn^{2+}, Pb^{2+}, Cd^{2+}, Hg^{2+}, and Cu^{2+}, were also obtained from Sigma-Aldrich and used as received. Sodium salts of various anions, such as CN^-, SO_4^{2-}, NO_3^-, PO_4^{3-}, S^{2-}, Cl^-, F^-, Br^-, OAc^-, $H_2AsO_4^-$, N_3^-, ClO_4^-, $S_2O_4^{2-}$, HCO_3^-, SCN^-, CO_3^{2-}, $P_2O_7^{4-}$, and NO_2^-, were also used as received. For spectroscopic studies, HPLC-grade acetonitrile and Milli-Q ultrapure deionized water were used.

4.2.2 Physical measurements

A Bruker 300 MHz NMR spectrometer was employed to obtain ^{1}H-NMR spectra in DMSO-d_6. Infrared (IR) spectra within the 400–4000 cm^{-1} range were recorded using an IR 750 series-II FTIR (Nicolet Magna) spectrophotometer with KBr pellets. UV-Vis spectra were captured using an Agilent 8453 diode-array spectrophotometer. Steady-state fluorescence

spectra were measured on a PTI Spectro fluorimeter (Model QM-40). ESI-MS$^+$ (m/z) spectra for L and [L-Fe] complex were acquired using an HRMS spectrometer (Model: XeVO G2 QTof). Far UV Circular Dichroism (CD) spectra were analyzed on a JASCO J815 spectropolarimeter (Japan) equipped with a thermal programmer (Model: PFD-425L/15). The nano/microstructure was determined using a Hitachi S-530 scanning electron microscope (SEM).

4.2.3 Synthesis

4.2.3.1 Preparation of RH-BZN (L)

Preparation of Rhodamine B ethylenediamine (R)

Rhodamine B ethylenediamine was prepared by following the literature method.[55]

Preparation of desired Probe L

0.533 g (1.10 mmol) of **R** in EtOH (10 mL) was added dropwise to a 30 mL ethanolic solution of 3,5-di-*tert*-butyl-2-hydroxybenzaldehyde (1 mmol, 0.234 g) and stirred for 30 min under hot conditions (50 – 60 °C) and then at room temperature for about 6 h. The yellow crystalline precipitate thereupon formed was collected by filtration and thoroughly washed with cold methanol to get **L** in the pure form (yield 68%) (**Scheme 4.1**). We successfully grow yellow crystal for single crystal x-ray diffraction. ^{1}H-NMR (in DMSO d^6) (δ, ppm):1.11 (s, 12-H), 1.27 (s, 10-H), 1.39 (s, 10-H), 1.59 (s, 12-H); 6.47 (s, 4-H); 6.98 (s, 1-H), 7.09 (s, 1-H), 7.25 (s, 2-H), 7.32 (s, 1-H), 7.45 (s,1-H), 7.92 (m, 1-H), 8.14 (s, 1-H) (**Figure 4.1**). ESI-MS$^+$ (m/z): 701.48 (L+H$^+$) (**Figure 4.2**). IR spectrum: $\bar{\upsilon}$ = 1690 cm^{-1} (Spiro lactam amide-ketone), 1619 cm^{-1} (–C=N) (**Figure 4.3**).

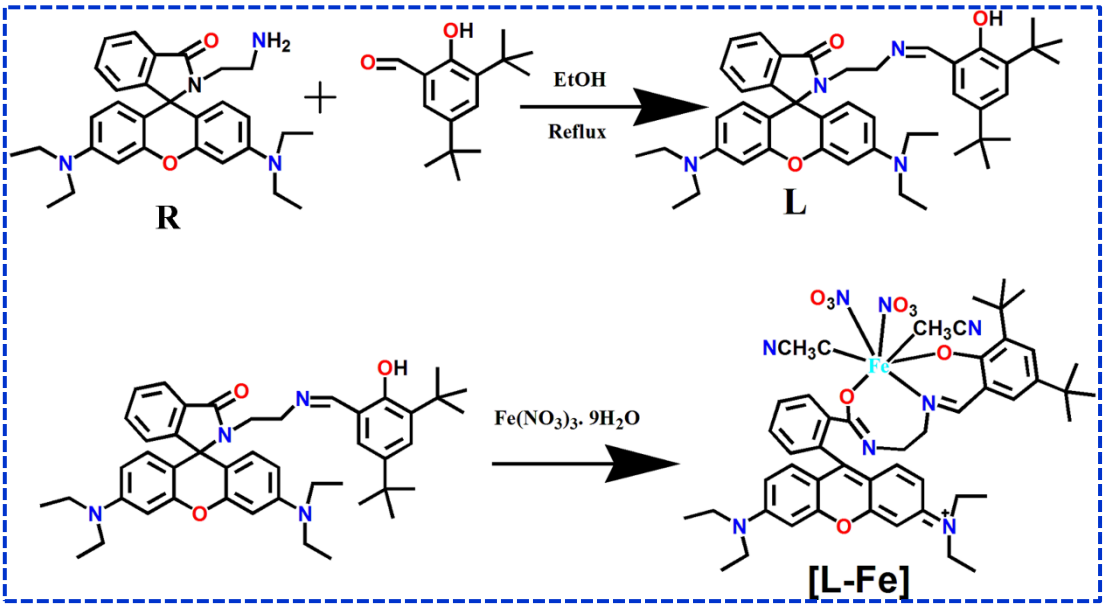

Scheme 4.1 Synthetic route for the preparation of probe **L** and its Fe^{3+} complex.

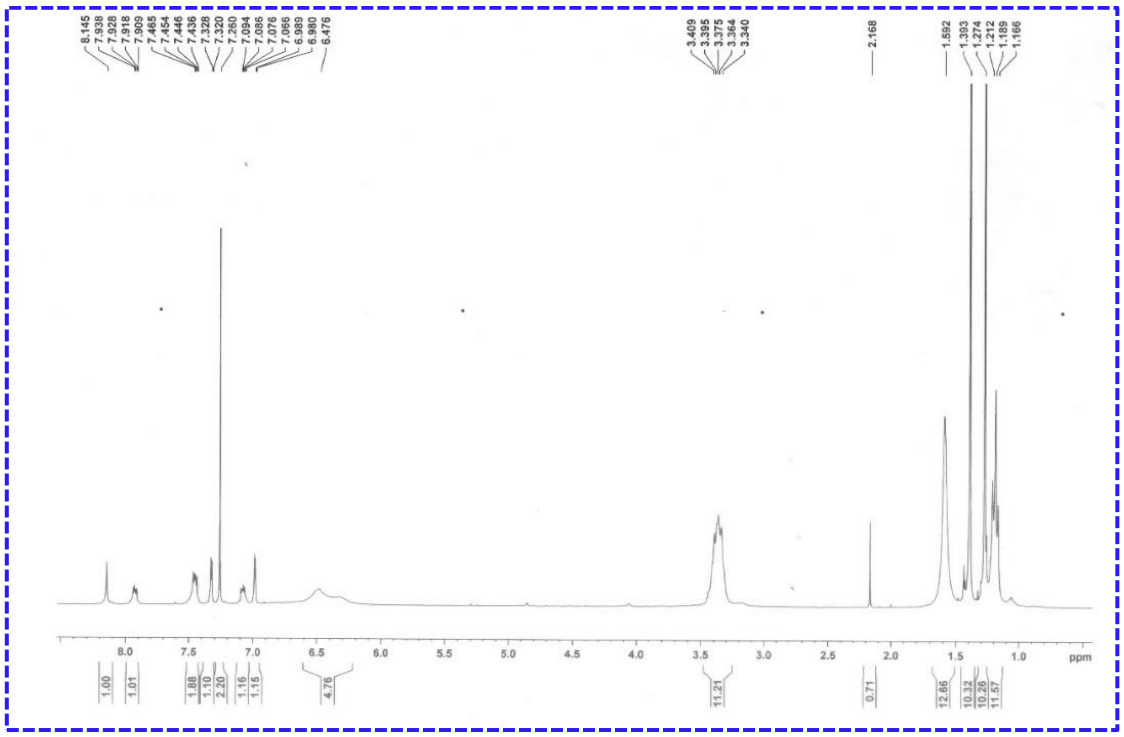

Figure 4.1 ^{1}H NMR of ligand **L** in DMSO-d_6.

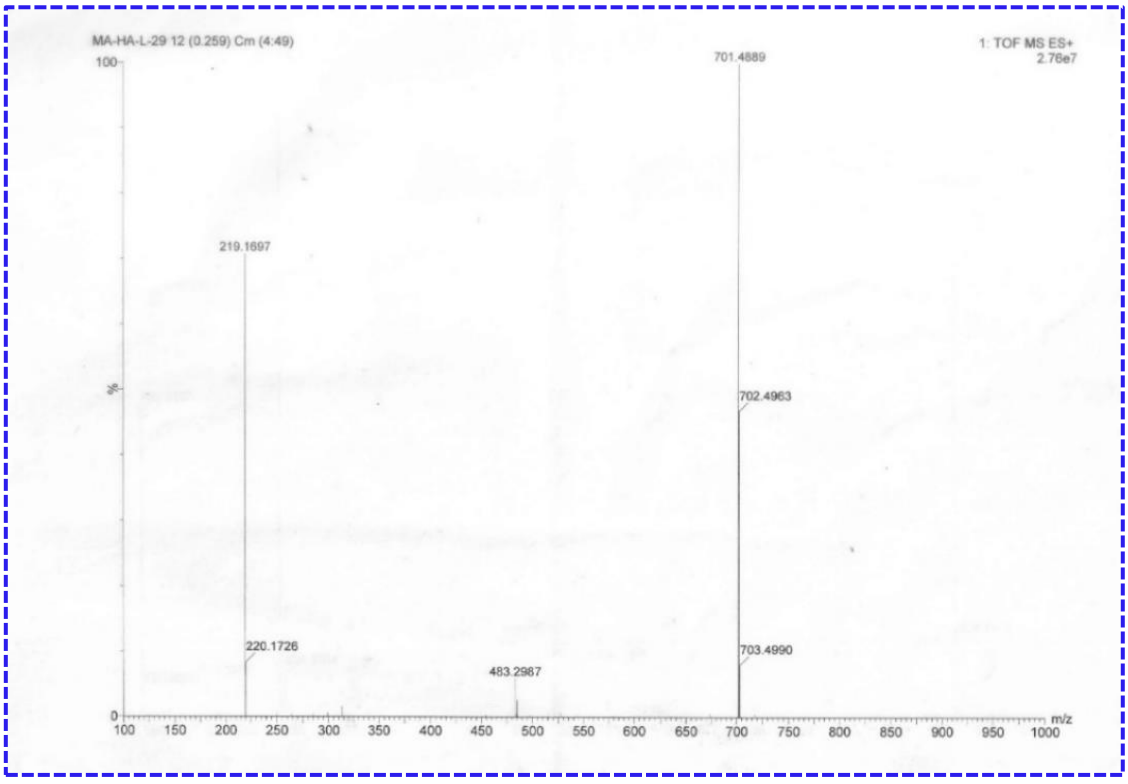

Figure 4.2 Mass spectra of ligand **L** in MeCN.

4.2.3.2 Synthesis of $[Fe^{III}(L)(NO_3)_2]$

A solution of L (0.700 g, 1 mmol) in 25 ml MeCN, $Fe(NO_3)_3.9H_2O$ (0.404 g, 1 mmol) in a small volume of MeCN (4 ml) was added drop wise with constant stirring for 1 h. The solid product thereupon formed was collected by filtration and washed with cold MeOH. Several attempts to grow single crystals for X-ray diffraction studies were failed. IR spectrum: $\tilde{\nu}$ = 1635 cm^{-1} (Spiro lactam amide-ketone), 1496 cm^{-1} (–C=N) (**Figure 4.3**). ESI-MS^+ (m/z): 969.55 $[Fe(L)(NO_3)_2(CH_3CN)(CH_3CN)] + Li^+$ (**Figure 4.4**).

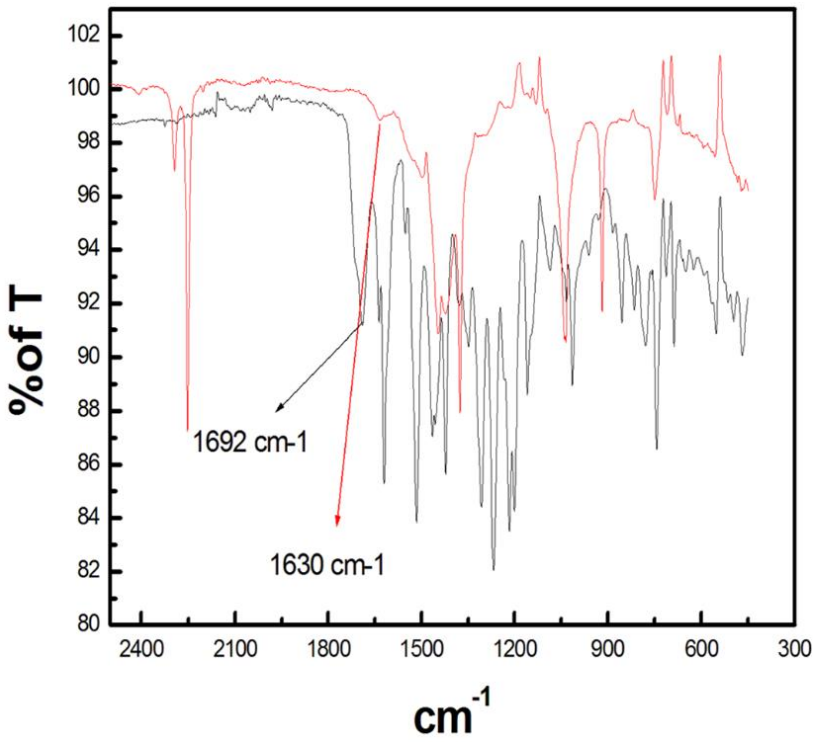

Figure 4.3 IR spectra of ligand **L** and [**L**-Fe].

4.2.4 Solution preparation for UV-Vis and fluorescence studies

10 ml 1.0 x 10^{-3} M solutions of the probe L and $Fe(NO_3)_3.9H_2O$ were prepared separately by dissolving appropriate amount of the materials in MeCN and used as stocks for all the UV-Vis and fluorescence studies. Similarly, 1.0 x 10^{-3} M 250 µL HSA solution was prepared freshly in 10 mM Tris buffer prepared by dissolving appropriate amount of HEPES in 100 ml water and pH was adjusted at 7.24 using HCl and NaOH as required. For UV-Vis spectral studies a 2.5 ml aliquot of the buffer solution was pipetted out into a cuvette to which 30 µM of the probe was added. Now, to this buffer solution Fe^{3+} was added starting from 0 to 40 µM at a regular interval of volume. UV-Vis spectra were recorded for each of these solutions. For

fluorescence studies, to 30 µM L was used keeping the same conditions and Fe^{3+} was added starting from 0 to 40 µM at a regular incremental volume and fluorescence studies were performed for each solution. Again, for protein binding studies, to 10 µM [L-Fe] complex solution (prepared by mixing equimolar concentration of **L** and Fe^{3+}) HSA solution was added incrementally between 0 and 20 µM. For both emission and absorption studies cuvettes of 1 cm path length were used. 2 nm x 2 nm slit widths were used for all fluorescence studies.

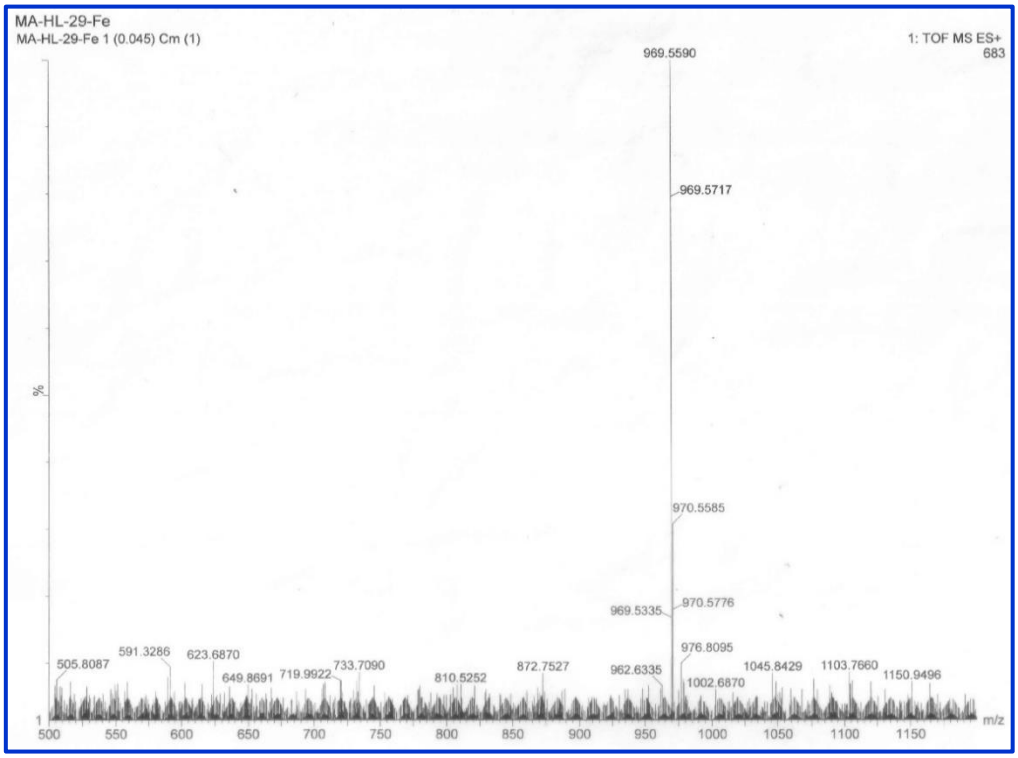

Figure 4.4 Mass spectra of ligand [**L**-Fe] in MeCN.

4.2.5 Circular Dichroism (CD) Spectra

Circular Dichroism (CD) spectroscopy was carried out on a PC-driven JASCO J815 (Japan) spectropolarimeter equipped with a thermal programmer (model PFD-425L/15) and temperature controller interfaced in a rectangular quartz cuvette of 1 cm path length. The scan rate of 100 nm/min was adopted in the range wavelength 195−300 nm. 99.9% pure nitrogen gas was sufficiently purged through the spectrophotometer before any measurements. Here, a variable concentration of [L-Fe] complex (0-6.0 µM) (1.0 x 10^{-3} M stock solution prepared by mixing equimolar concentration of **L** and Fe^{3+} in 10 mM Tris buffer, pH 7.2) was added to a fixed concentration of HSA (1.0 µM) and CD spectra were recorded for each solution at 25 °C. Baseline correction was performed for each spectrum

with Tris–HCl buffer. At least five scans were recorded for each spectrum, which were averaged and smoothened to minimized signal-to-noise ratio and expressed by concentration dependent molar ellipticity, [θ], deg cm^2dmol^{-1}.

4.2.6 Molecular Docking Simulation Study

Auto Dock program (version 4.2) [56] and Auto Dock Tools (ADT), using the Lamarckian Genetic Algorithm (LGA) based on the adaptive local method search were used for molecular docking, to get an idea about the mode of probable binding site and binding on HSA for the interaction between [L-Fe] and HSA.[57,58] X-ray crystal structure of HSA was adopted from RCS Protein Data Bank with PDB code 1AO6 was used for this purpose. ChemDraw (Ultra 8.0) was used to generate the 3D structure of complex, and also used for modification two well-known software packages Gaussian 09W and Auto Dock 4.2. The Gasteiger charges and polar hydrogen atoms were added to the protein and complex. For the identification of binding sites in HSA, docking was carried out with setting of grid box size 100 Å x 100 Å x 100 Å along x, y, z axes covering whole protein with a grid spacing 0.394 Å after assigning the protein and probe with Kollman charges. Other parameters are default as provided by the Auto Dock program. The grid maps of several atoms of the protein and the probe were considered using AutoGrid.[59]After grid mapping, we performed the flexible docking simulations with 200 runs and 2.5 × 10^6 energy evaluations, 50 GA population, 27,000 numbers of generations, and root mean square cluster tolerance of 2.0 Å[60] per run. According to ranking and scoring among 200 runs 10 minimum energy conformers were chosen.[60,61] Finally the best optimized model with the lowest energy was chosen for further docking simulations and best viewed in PyMOL software.

4.2.7 Determination of Fluorescence Polarization Anisotropy

For the determination of fluorescence anisotropy(r) PTI QM-40 spectrofluorometer was used as defined by eqn. (1)

$$r = \frac{I_{VV} - GI_{VH}}{I_{VV} + 2GI_{VH}} \qquad (1)$$

where, I_{VV} and I_{VH} are the emission intensities for the vertical orientation of excitation polarizer, and vertical and horizontal orientations of emission polarizer, respectively. The G factor is given as:[62]

$$G = \frac{I_{HV}}{I_{HH}} \qquad (2)$$

Here, the I_{HV} and I_{HH} are the intensities for the vertical and horizontal orientation of the emission polarizer, while the excitation polarizer is horizontal.

4.2.8 Preparation of sample for SEM studies

Three sets of solution were prepared for SEM studies, first one contains **L** (30 µL), second one contains [L-Fe] complex, third one contains containing complex and HSA, prepared by mixing equivalent amount of the reactants (30 µM) and HSA (30 µM). All these solutions were allowed to age overnight at room temperature before characterization.

4.2.9 Methods of Characterization

To study the morphologies of the synthesized microstructures a Hitachi S-530 scanning electron microscope (SEM) was used. The SEM instrument is operated at an accelerating voltage of 5 kV. For SEM studies, samples were dried under vacuum on a glass plate and then covered with a thin layer of gold.

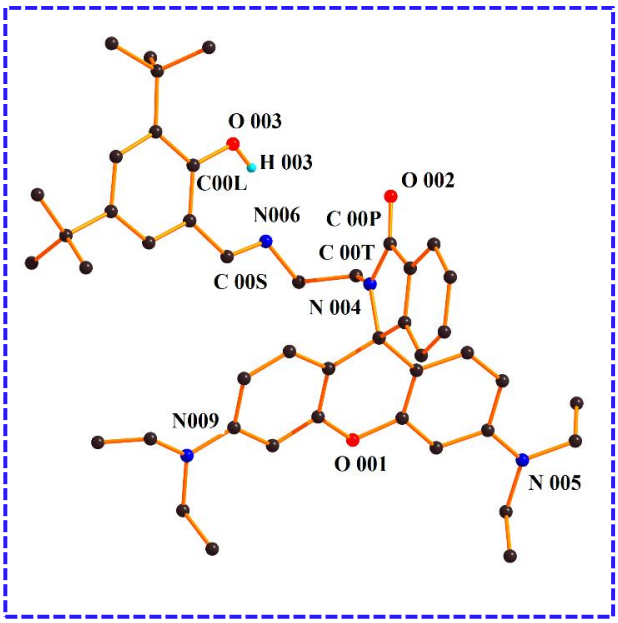

Figure 4.5 Single crystal X-ray structure of ligand **L**.

4.3 RESULTS AND DISCUSSION

The receptor **L** was synthesized by the reaction between 3,5-di-*tert*-butyl-2-hydroxybenzaldehyde and rhodamine-B hydrazide in ethanolic medium under stirring

conditions with 72% yield which is shown in **Scheme 4.1.** The ligand was well characterized by ^{1}H NMR (**Figure 4.1**), HRMS (**Figures 4.2 and 4.4**) and IR (**Figure 4.3**) and single crystal x-ray diffractometer (**Figure 4.5, Table 4.1 and 4.2)**, while the complex was characterized by HRMS (**Figure 4.4**) study.

Table 4.1 Details of crystallographic data collection and refinements

Parameters	1
Elemental formula	$C_{45}H_{56}N_4O_3$
Formula weight	700.44
Crystal system	Monoclinic
Space group	P 21/c
Temp/K	296
a/Å	11.91(7)
b/Å	22.09(15)
c/Å	15.56(10)
V/A^3	4080.6(5)
Z	4
Density(D/gcm^{-3})	1.129
μ/mm^{-1}	0.071
F(000)	1495.6
h, k, l	15, 28, 20
N_{ref}, N_{par}	9259, 473
R, wR2, S	0.0838, 0.2898, 1.026

Table 4.2 Some selected bond distances and bond angles

Bond lengths(Å)	
O 003-H 003	0.819
O 003-C 00L	1.348
C 00S-N 006	1.260
N 004-C 00T	1.457
C 00P- O 002	1.227

4.3.1 UV−Visible Absorption Study

The Uv-Vis absorption titration was carried out at a fixed (30 μM) **L** concentration and the concentration of Fe^{3+} was varied between 0 and 40 μM as shown in **Figure 4.6**. After that a gradual increase in absorbance at 527 nm with increasing the concentration of metal ion and

at ~ 1:1 metal to ligand concentration it reaches a maximum and get almost saturated. Utilization of Benesi-Hildebrand equation (eqn. 3) results a linear plot which was used to evaluate the dissociation constant and stoichiometry of complexation, where, A_0 and A_{max} are the absorbances of the ligand in the absence and presence of excess metal ion, respectively and n is the stoichiometry (L:Fe^{3+}) of the reaction. The plot of $(A_{max}\text{-}A_o)/(A\text{-}A_o)$ against 1/[M] clearly reveals that a 1:1 stoichiometry of the reaction (n= 1) which also gives dissociation constants K_d = (2.95 ± 0.06) x 10^{-5} M.

$$1/(A\text{-}A_o) = 1/\{K_d(A_{max}\text{–}A_o)\,[M^{x+}]^n\} + 1/[A_{max}\text{-}A_o] \qquad (3)$$

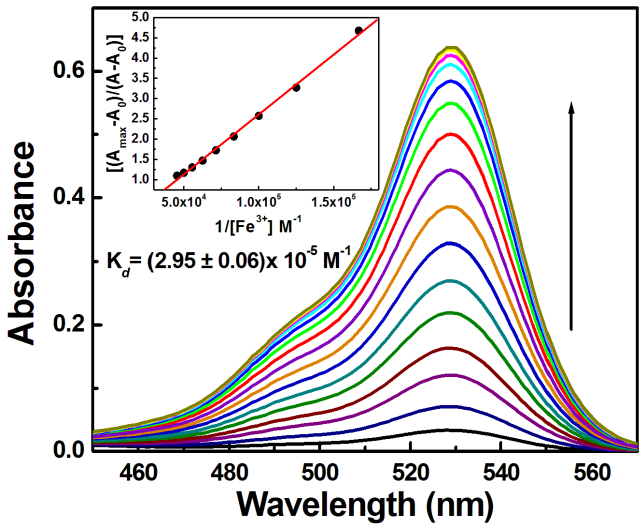

Figure 4.6 Absorption titration of **L** (30.0 μM) with Fe^{3+} (0-40 μM) in in HEPES buffer (10 mM) at pH 7.2 in 8:2 H_2O:MeCN (v/v); inset: Benesi-Hildebrand fitting of data.

4.3.2 Steady state fluorescence studies

Like UV-Vis absorption titration study, fluorescence titration of **L** (30 μM) with $Fe(NO_3)_3.9H_2O$ was also carried out in 10 mM HEPES buffer at physiological pH (7.2) (**Figure 4.7**). The weakly fluorescent ligand when interact with Fe^{3+}, the fluorescence intensity increases immensely at 574 nm and showing turn-on reaction. Again, from Benesi-Hildebrand equation we get a linear plot which was used to evaluate the dissociation constant K_d = (9.48 ± 0.06) x 10^{-5} M (**Figure 4.7**). In both cases the nearly same values of K_d from UV-Vis and fluorescence titration indicates the consistency of the experiments.

$$1/(F\text{-}F_o) = 1/\{K_d(F_{max}\text{–}F_o)\,[M^{x+}]^n\} + 1/[F_{max}\text{-}F_o] \qquad (4)$$

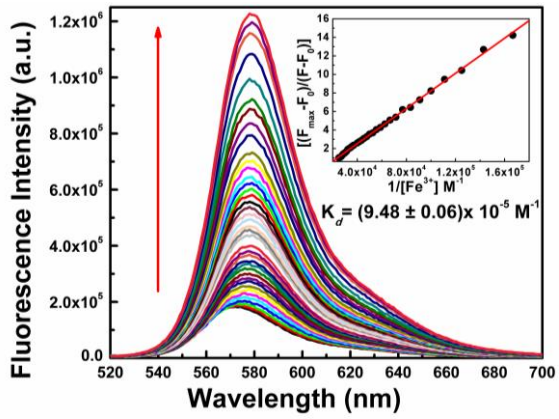

Figure 4.7 Fluorescence titration of **L** (30.0 μM) with Fe^{3+}(0-40 μM) in HEPES buffer (10 mM) at pH 7.2 in 8:2 H_2O:MeCN(v/v); inset: Benesi-Hildebrand fitting of data.

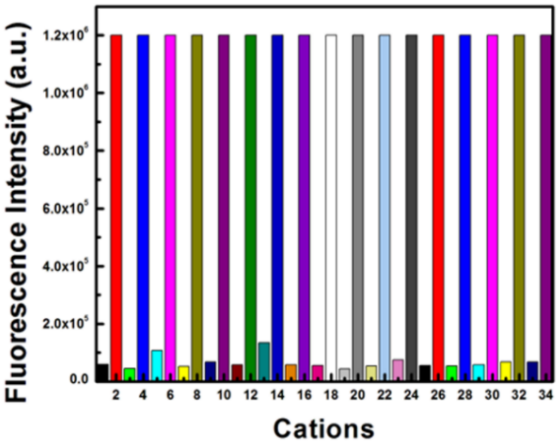

Figure 4.8 Fluorescence emission of **L** (30 μM) induced by different cations (300 μM). (1-34 are: 1. L, 2. L+Fe^{3+}, 3. L+Na^{+}, 4. L+Na^{+}+Fe^{3+}, 5. L+Cr^{3+}, 6. L+Cr^{3+}+Fe^{3+}, 7. L+Ca^{2+}, 8. L+Ca^{2+}+Fe^{3+}, 9. L+Mg^{2+}, 10. L+Mg^{2+}+Fe^{3+}, 11. L+K^{+}, 12. L+K^{+}+Fe^{3+}, 13. L+Al^{3+}, 14. L+Al^{3+}+Fe^{3+}, 15. L+Mn^{2+}, 16. L+Mn^{2+}+Fe^{3+}, 17. L+ Fe^{2+}, 18. L+ Fe^{2+}+Fe^{3+}, 19. L+ Co^{2+}, 20. L+Co^{2+}+Fe^{3+}, 21. L+Cu^{2+}, 22. L+Cu^{2+}+Fe^{3+}, 23. L+Ni^{2+}, 24. L+Ni^{2+}+Fe^{3+}, 25. L+Zn^{2+}, 26. L+Zn^{2+}+Fe^{3+}, 27. L+Cd^{2+}, 28. L+Cd^{2+}+Fe^{3+}, 29. L+Hg^{2+}, 30. L+Hg^{2+}+Fe^{3+}, 31. L+Pb^{2+}, 32. L+Pb^{2+}+Fe^{3+}, 33. L+Ag^{+}, 34. L+Ag^{+}+Fe^{3+}).

The selectivity studies of L towards Fe^{3+} detection was performed by fluorescence experiments where a fixed concentration of L (30 μM) and ten equivalents of different metal ions, both in the absence and presence of Fe^{3+} ion, were allowed to react. The recognition of Fe^{3+} ion was not affected in the presence of biologically favorable metal ions such as K^{+}, Na^{+}, $Mg^{2+}$and Ca^{2+} ions, transition-metal ions like Cr^{3+}, Fe^{2+}, Mn^{2+}, Cu^{2+}, Co^{2+}, Ni^{2+} and Zn^{2+}, and heavy-metal ions, like Hg^{2+}, Cd^{2+}, and Pb^{2+} (**Figure 4.8**). In similar fashion ten equivalent of

anions like SO_4^{2-},CN^-, PO_4^{3-}, NO_3^-, S^{2-}, F^-, Cl^-, OAc^-, $H_2AsO_4^-$, Br^-, N_3^-, $S_2O_4^{2-}$, ClO_4^-, HCO_3^-, CO_3^{2-}, SCN^-, $P_2O_7^{4-}$ and NO_2^- (**Figure 4.9**) were reacted separately with 30 μM of L which did not show interference with the recognition of Fe^{3+}. The limit of detection (LOD) of Fe^{3+} by **L** was found to be 0.27 μM (**Figure 4.10**). The quantum yields of the **L** and [L–Fe] are 0.011 and 0.36, respectively.

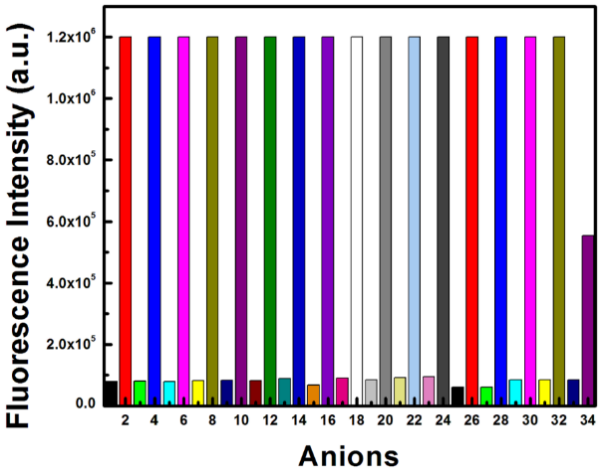

Figure 4.9 Fluorescence emission of **L** (30 μM) induced by different anions (300 μM). (1-34 are 1. L , 2. L+Fe^{3+}, 3. L+ CN^-, 4. L+ CN^-+Fe^{3+}, 5. L+ SO_4^{2-}, 6. L+ SO_4^{2-}+Fe^{3+}, 7. L+ NO_3^-, 8. L+ NO_3^- +Fe^{3+}, 9. L+ PO_4^{3-}, 10. L+ PO_4^{3-} +Fe^{3+}, 11. L+ S^{2-}, 12. L+ S^{2-}+Fe^{3+}, 13. L+ Cl^-, 14. L+ Cl^-+Fe^{3+}, 15. L+ Br^-, 16. L+ Br^-+Fe^{3+}, 17. L+ OAc^-, 18. L+ OAc^-+Fe^{3+}, 19. L+ $H_2AsO_4^-$, 20. L+ $H_2AsO_4^-$+Fe^{3+}, 21. L+ ClO_4^-, 22. L+ ClO_4^-+Fe^{3+}, 23. L+ $S_2O_4^{2-}$, 24. L+ $S_2O_4^{2-}$ + Fe^{3+}, 25. L+ HCO_3^-, 26. L+ HCO_3^-+ Fe^{3+}, 27. L+ SCN^-, 28. L+ SCN^-+ Fe^{3+}, 29. L+ $P_2O_7^{4-}$, 30. L+ $P_2O_7^{4-}$+ Fe^{3+}, 31. L+ F^-, 32. L+ F^-+ Fe^{3+}, 33. L+ I^-, 34. L+ I^-+ Fe^{3+}). Here ferric nitrate used.

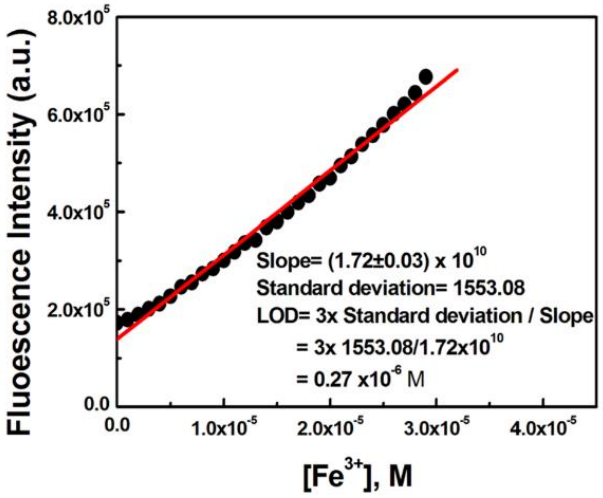

Figure 4.10 Limit of Detection calculation.

4.3.3 PH-stability

The *p*H studies were carried out to check the pH stability of the probe and its iron complex. The ligand **L** did not show any significant change in fluorescence intensity between pH 6 to 12 and in between pH 2 and 5 showing strong fluorescence emission due to opening of spirolactam ring in acidic *p*H (**Figure 4.11**). However, in the presence of Fe^{3+} ion the fluorescence emission intensity attains maximum at *p*H ~3.5, (where no *p*H effect on emission intensity of the free ligand is observable) and remains constant till pH 8.0 and then decreases with pH because the formation of $Fe(OH)_3$ under basic conditions. This observation undoubtedly shows that **L** is compatible for biological applications under physiological environment.

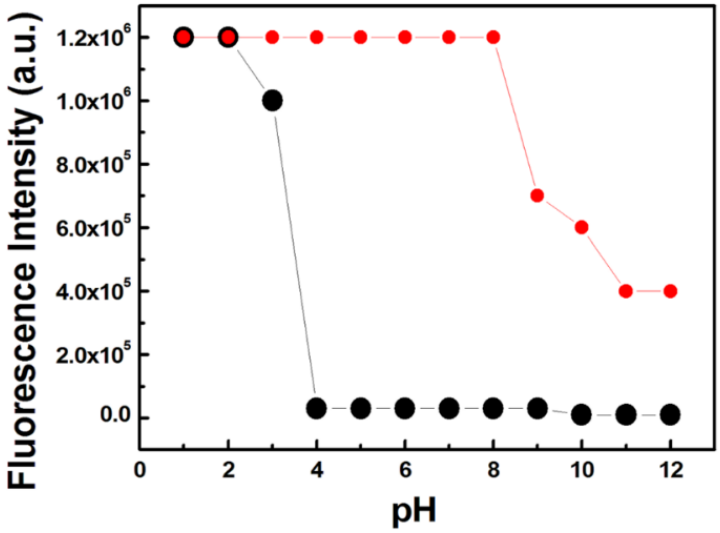

Figure 4.11 pH study of **L** (black) and [**L**-Fe] (red).

4.3.4 Mechanism of L–Fe^{3+} interaction

The probe **L** forms complex with Fe^{3+} concluding the spirolactam ring opening which was recognized through FTIR studies showing a shift in stretching frequency of the amidic 'C=O' of the rhodamine moiety at 1692 cm^{-1} to a lower wave number 1630 cm^{-1} in the presence of 1.1 equivalent of Fe^{3+} (**Figure 4.3**). This huge shift ($\Delta\nu$ = 62 cm^{-1}) suggests a strong polarization of the C=O bond and spirolactam ring opening upon effective binding to the Fe^{3+} ion.

4.3.5 Spectro polarimetric studies

A circular dichroism (CD) spectral study confirms the conformational changes in the secondary structure of HSA which was induced by complex [L–Fe]. In the CD spectra of

HSA at 7.2 pH, two negative bands at 207 and 220 nm clearly designates the existence of α-helix in the structure[63] arising mainly due to the charge transfer n→π* transition,[64] due to negative Cotton effect[65] in the peptide bond of α-helical structure of HSA. As the complex [L─Fe] is optically inactive, it is expected that it is also CD inactive in the whole range of UV−Vis region.[66] To determine the changes in the HSA conformation upon binding with [L─Fe], the CD spectra were recorded in the range 200−350 nm with varying concentration of [L─Fe] which is presented in **Figure 4.12**. It showed a fall in negative ellipticity value without any significant shift of the peak positions in the wavelength range of far-UV CD due to a partial unfolding of the helical structure and a decrease of the α-helix content in the protein in the presence of [L─Fe].

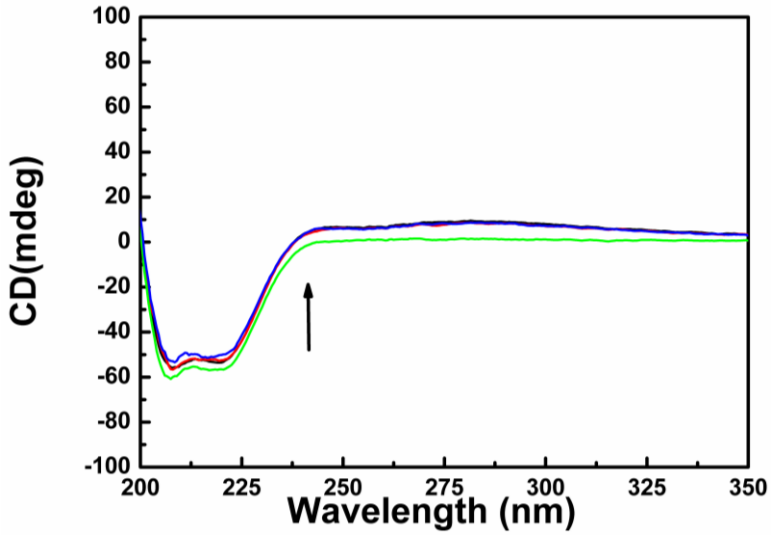

Figure 4.12 Effect of [**L**-Fe] on intrinsic circular dichroic (CD) spectrum of HSA; 2−6 denote CD spectrum of 1.0 μM HSA treated with 0, 2.0, 4.0 and 6.0 μM [**L**-Fe] (complex), at 25 °.

4.3.6 Docking analysis

There are three homologous domains, namely domain I (residue 1−183), domain II (residue 184−376), and domain III (residue 377−583) which were revealed from the crystal structure of HSA. Again, each contains two subdomains (A and B). Only one tryptophan residue (Trp 214) is present in HSA and when excited at 295 nm this protein's intrinsic fluorescence was shown due to this tryptophan residue. The two major binding sites of HSA were known as Sudlow site I and Sudlow site II and those are located in subdomains IIA and IIIA respectively.

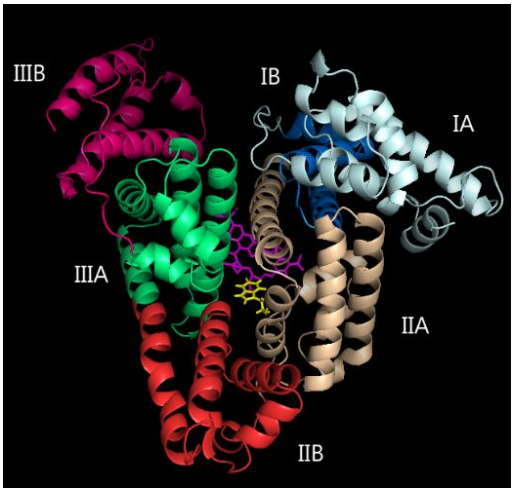

Figure 4.13 Stereo view of the docked conformations of [**L**-Fe] with HSA.

To identify the potential ligand binding sites and protein-ligand binding energy it was required to perform molecular docking calculation. **Figure 4.13** reveals that the most favorable binding site is subdomain IIA of HSA for complex [L─Fe] (purple colour). So, in the presence of [L─Fe] complex, the quenching of the HSA fluorescence occurs, arising from Trp 214 residue, which is shown in fluorescence titration (**Figure 4.14b**). Similar quenching of the fluorescence of [L─Fe] occurs in the presence of HSA (**Figure 4.14a**).

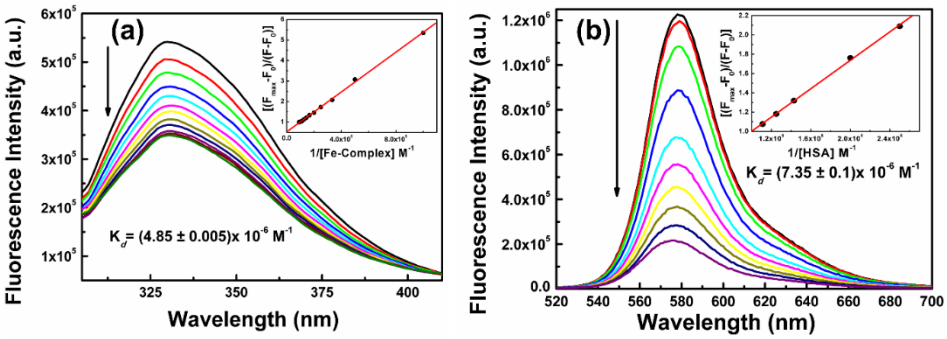

Figure 4.14 (a) Fluorescence quenching of [L-Fe] as a function of [HSA]; inset plot of FI vs. [HSA], λ_{ex} = 510 nm. (b)Fluorescence quenching of HSA as a function of [(L-Fe)]; inset plot of FI vs. $[(L^6\text{-Fe})^{2+}]$, λ_{ex} = 270 nm.

4.3.7 Steady-State Fluorescence Anisotropy Measurements

A steady state fluorescence anisotropy (r) studies were carried out for the motional information of the probe in micro heterogeneous environments. So, the fluorescence anisotropy was calculated as a function of [HSA] (0-30 µM) at a fix concentration **L** and Fe^{3+} (30 µM each) at 574 nm. A plot of r vs. [HSA] showed a gradual increase in r with [HSA]

(**Figure 4.15**) which arises due to localization of the complex in the hydrophobic pocket (Trp-214, IIA) which restricts the free movement of the fluorophore.

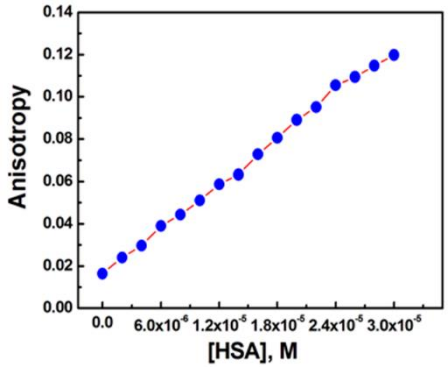

Figure 4.15 The plot of the fluorescence anisotropy (r) vs. HSA.

4.3.8 Scanning Electron Microscope (SEM) Studies

The solid ligand shows the stone like microstructures in SEM studies and in the presence of Fe^{3+} ion the structure changes to spherical because of π•••π stacking interaction. Moreover, when the complex interacts with HSA the structure gets agglomerated due to localization of the complex in the hydrophobic pocket. All these observations are shows in **Figure 4.16**.

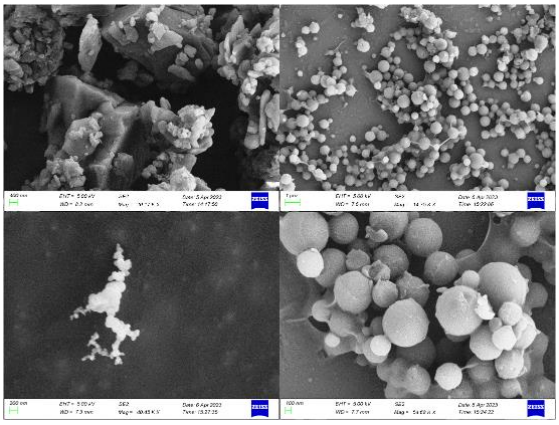

Figure 4.16 SEM images of (i) **L**, (ii) [**L**-Fe], (iii) zoom images of [**L**-Fe] and (iv) [**L**-Fe] in presence of HSA.

4.4 Conclusion

In summary, we have synthesized successfully a rhodamine-B based fluorescent molecular probe **L** which selectively recognizes Fe^{3+} calorimetrically as well as fluorimetrically in the presence of various metal ions and anions showing a 1:1 binding stoichiometry in 8:2 (H_2O: MeCN, v/v). The structure of **L** was confirmed by single crystal x-diffraction studies along

with NMR, mass spectroscopy and FTIR studies. The existence of [(L-Fe)] complex as ($[Fe(L)(NO_3)_2(CH_3CN)(CH_3CN)] + Li^+$) was confirmed by ESI-$MS^+$ studies. The dissociation constant determined from Uv-Vis ($(2.95 \pm 0.06) \times 10^{-5}$ M) and fluorescence ($(9.48 \pm 0.06) \times 10^{-5}$ M) titration were nearly the same revealing the strong binding towards Fe^{3+}. The limit of detection (LOD) of Fe^{3+} by L is 0.27 μM. The quantum yields of the **L** and [L–Fe] are 0.011 and 0.36, respectively. Fluorescence anisotropy also measured in the presence of HSA to know the rigidity of the local micro environment. Furthermore, SEM studies reveal the stone like microstructure of **L** which changes to spherical shape in the presence of Fe^{3+} and when the complex interacts with HSA it gets agglomerated. The experimental results dictates that this probe (**L**) is useful for on-site Fe^{3+} ions through a fast, simple and eco-friendly process.

REFERENCES

1) J. M. Lehn, (Ed.) Comprehensive Supramolecular Chemistry, Elsevier, Amsterdam, The Netherlands, 1996.
2) H. F. Lodish, Molecular Cell Biology, Freeman, W. H.; Company, New York, 5th edn. 2004.
3) Sensors Update, Wiley-VCH Verlag, Gmbh; Co KgaA, Weinheim 2003.
4) E. M. Nolan and S. J. Lippard, *Chem. Rev.*, 2008, **108**, 3443-3480.
5) H. N. Kim, W. X. Ren, J. S. Kim and J. Yoon, *Chem. Soc. Rev.*, 2012, **41**, 3210-3244.
6) X. Ou, Y. Jin, X. Chen, C. Gong, X. B. Ma, Y. Wang, C. Chow and Q. Tang, *Anal. Methods.*, 2015, **7**, 5239-5244.
7) J. T. Yeh, P. Venkatesan and S. P. Wu, *New. J. Chem*., 2014, **38**, 6198-6204.
8) P. Lipinski, A. Stys and R. R. Starzynski, *Cell. Mol. Life Sci.*, 2013, **70**, 23–38.
9) Crichton, R. Iron Metabolism: From Molecular Mechanisms to Clinical Consequences, Chapter 2, 3rd Edition, **2009**.
10) M. Ferrali, D. Donati, S. Bambagioni, M. Fontani, G. Giorgic and A. Pietrangelod, *Bioorg. Med. Chem.*, 2001, **9**, 3041-3047.
11) R. C. Hider and X. Kong, *Met Ions Life Sci.*, 2013, **13**, 229-94.
12) R. R. Crichton, S. Wilmet, R. Legssyer and R. J. Ward, *Inorg. J. Biochem.*, 2002, **91**, 9-18.
13) J. R. Burdo and J. R. Connor, *Biometals*, 2003, **16**, 63-75.
14) R. Evstatiev and C. Gasche, *Gut.*, 2012**, 61**, 933-952.
15) P. Aisen, M. Resnick and E. Leibold, *Curr. Opin. Chem. Biol.*, 1999, **3**, 200-206.

16) C. J. Earley, J. R. Connor, J. L. Beard, E. A. Malecki, D. K. Epstein and R. P. Allen, *Neurol.*, 2000, **54**, 1698-1700.
17) D. *Arch. Biochem. Biophys.*, 2000, **373,** 1-6.
18) D. J. Bonda, H. Lee, J. A. Blair, X. Zhu, G. Perry and M. A. Smith, *Metallomics*, 2011, **3,** 267-270.
19) R. R. Crichton, D. T. Dexter and R. J. Ward, *Coord. Chem. Rev.*, 2008, **252**, 1189-1199.
20) A. S. Pithadia and M. H. Lee, *Curr. Opin. Chem. Biol.*, 2012, **16**, 67-73.
21) H. Kozlowski, A. J. Klos, J. Brasun, E. Gaggelli, D. Valensin and G. Valensin, *Coord. Chem. Rev.*, 2009, **253**, 2665-2685.
22) F. B. E. Garah, C. Bijani, Y. Coppel, P. Faller and C. Hureau, *Inorg.Chem.*, 2011, ***50***, 9024-9030.
23) H. A. Molla, R. Bhowmick, A. Katarkar, K. Chaudhuri, S. Gangopadhyay and M. Ali, *Anal. Methods*., 2015**, 7,** 5149-5156.
24) S. Bae and J. Tae, *Tetrahedron Lett.*, 2007, **48**, 5389-5392.
25) Y. Xiang and A. Tong, *Org. Lett.*, 2006, **8**, 1549-1552.
26) J. L. Bricks, A. Kovalchuk, C. Trieflinger, M. Nofz, M. Buschel, A. I. Tolmachev, J. Daub and K. Rurack, *J. Am. Chem. Soc.*, 2005, **127**, 13522-13529.
27) M. Zhang, Y. Gao, M. Li, M. Yu, F. Li, L. Li, M. Zhu, J. Zhang, T. Yi and C. Huang, *Tetrahedron Lett.*, 2007, **48**, 3709-3712.
28) Chen X., Q. Zhao, W. Zou, Q. Qu and F. Wang, *Sens. Actuators, B: Chemical*, 2017, **244**, 891–896.
29) L. Zhang J. Wang, J. Fan, K. Guo and X. Peng, *Bioorg. Med. Chem. Letters.*, 2011, **21**, 5413-5416.
30) J. Huang, Y. Xu and X. Qian, *Dalton Trans*., 2014, **43**, 5983-5989.
31) J. P. Sumner and R. Kopelman, *Analyst*, 2005, **130,** 528-533.
32) Y. Ma, W. Luo, P. J. Quinn, Z. Liu and R. C. Hider, *J. Med. Chem*., 2004**, 47**, 6349-6362.
33) G. E. Tumambac, C. M. Rosencrance and C. Wolf, *Tetrahedron*, 2004, ***60***, 11293-11297.
34) A. Ali, Q. Zhang, J. Dai and X. Huang, *BioMetals*, 2003, ***16***, 285-293.
35) J. Mao, L. Wang, W. Dou, X.T ang, Y. Yan and W. Liu, *Org. Lett.*, 2007, **9**, 4567-4570.
36) M. Xu, S. Wu, F. Zeng and C. Yu, *Langmuir*, 2010, **26**, 4529-4534.
37) X. Wu, B. Xu, H. Tong and L. Wang, *Macromolecules*, 2010, **43,** 8917-8923.
38) S. Das, K. Aich, S. Goswami, C. K. Quah and H. K. Fun, *New J. Chem*., 2016, **40**, 6414-6420.

39) R. Kagit, M. Yildirim O. Ozay, S. Yesilot and H. Ozay, *Inorg. Chem.*, 2014, **53**, 2144−2151.

40) L. Zhanga, J. Fana and X. Penga, *Spectrochim. Acta A: Mol. Biomol. Spectrosc.*, 2009, **73,** 398–402.

41) L. Zhang, J. Wang, J. Fan, K. Guo and X. Peng, *Bioorg. Med. Chem. Lett.*, 2011, **21**, 5413–5416.

42) N. R. Chereddy, S. Thennarasu and A. B. Mandal, *Dalton Trans.*, 2012, **41,** 11753–11759.

43) S. Parihar, V. P. Boricha and R. N. Jadeja, *Luminescence*, 2015, **30**, 168–174.

44) J. An, T. Li, B. Wang, Z. Yang and M. Yan, *J. Coord. Chem.*, 2014, **67,** 921–928.

45) Y. Yu, X. Cheng, H. Liu, S. Gu, Z. Jiang, H. Huang and J. LianJ. *Polym. Sci. Part A: Polym. Chem.*, 2015, **53**, 615–621.

46) A. Sikdar, S. S. Panja, P. Biswas and S. Roy, *J. Fluoresc.*, 2012, **22**, 443–450.

47) O. Ozay and H. Ozay, *J. Macromol. Sci., Part A: Pure Appl. Chem.*, 2014, **51**, 308–317.

48) B. Wang, J. Hai, Z. Liu, Q. Wang, Z. Yang and S. Sun, *Angew. Chem. Int. Ed*., 2010, **49**, 4576 – 4579.

49) M. Deng, S. Wang, C. Liang, H. Shang and S. Jiang, *RSC Adv*., 2016, **6**, 26936–26940.

50) Y. Liu, R. Shen, J. Ru, X. Yao, Y. Yang, H. Liu, X. Tang, D. Bai, G. Zhang and W. Liu, *RSC Adv.*, 2016, **6**, 111754–111759.

51) G. Colmenarejo, *Med. Res. Rev.*, 2003, **23**, 275-301.

52) S. Sugio, A. Kashima, S. Mochizuki, M. Noda and K. Kobayashi, *Protein Eng.*, 1999, **12**, 439-446.

53) A. Molla, S. Vasavanonda, G. Kumar, H. L. Sham, M. Johnson, B. Grabowski, J. F. Denissen, W. Kohlbrenner, J. J. Plattner, J. M. Leonard, D. W. Norbeck and D. J. Kempf, *Virol.*, 1998, **250**, 255-262.

54) R. H. Vallejos and O. A. Roveri, *Biochem. Pharmacol.*, 1972, **21,** 3179−3182.

55) R. Bhowmick, A. S. M. Islam, A. Katarkar, K. Chaudhuri and M. Ali, *Analyst*, 2016, **141**, 225–235.

56) X. M. He and D. C. Carter, *Nature*,1992, **358**, 209−215.

57) G. M. Morris, D. S. Goodsell, R. Huey and A. J. Olson, *J. Comput. Aided Mol. Des.*, 1996, **10**, 293−304.

58) G. M. Morris, D. S. Goodsell, R. S. Halliday, R. Huey, W. E. Hart, R. K. Belew and A. J. Olson, *J. Comput. Chem.*, 1998, **19**, 1639−1662.

59) S. Bhuiya, A. B. Pradhan, L. Haque and S. Das, *J. Phys. Chem. B.*, 2016, **120**, 5–17.

60) T. Peters, Jr. All about Albumins: Biochemistry, Genetics and Medical Applications; Academic Press: San Diego, CA, 1996.
61) D. C. Carter and J. X. Ho, *Adv. Protein Chem.*, 1994, **45**, 153−203.
62) J. R. Lakowicz, *Principles of Fluorescence Spectroscopy*, *3rdedn*, *Springer*, *New York*, 2006, p. 67.
63) P. Serro, M. Bastos, J. C. Pesso and B. Saramago, *J. Biomed. Mater. Res.*, 2004, **70**, 420−427.
64) P. Yang and F. Gao, F. The Principle of Bioinorganic Chemistry; Science Press: Beijing, 2002.
65) H. Xu, N. Yao, H. Xu, T. Wang, G. Li and Z. Li, *Int. J. Mol. Sci.*, 2013, **14**, 14185−14203.
66) A. B. Pradhan, L. Haque, S. Bhuiya and S. Das, *RSC Adv*., 2014, **4**, 52815−52824.

Chapter 5

Highlights of the Thesis

After the elaborate description, here the overall view of this thesis has been briefly summarized chapterwise. This may be helpful to highlight the aim of our project and may provide an ultimate conclusion how far we have been able to fulfill our dream for the entitled project.

Chapter 1

This chapter contains a short review of previously reported rhodamine based fluorescent molecular probes for Fe(III) detection by fluorometric method. Additionally, a very brief overview of the present work is highlighted.

Chapter 2

In this chapter, we describe a novel, highly sensitive and selective fluorescent chemosensor 'rhodamine-3,4-dihydro-2H-1,3 benzoxazine' [RH-BZN (3)], which has been characterized by single crystal X-ray diffraction and other physicochemical techniques. In 3:7 water: MeCN (v/v) at pH 7.2 (10 mM HEPES buffer, μ= 0.05 M LiCl) it selectively recognizes Fe^{3+} through 1:1 complex formation resulting in a 240-fold fluorescence enhancement and a binding constant (K_f) of 1.50 $\times 10^4$ M^{-1}. The otherwise non-fluorescent spirolactam form of the probe results in dual changes in absorbance and fluorescence arising out of opening of the spirolactam ring through coordination to Fe^{3+} ions. This probe could suitably be employed for cytoplasmic intracellular imaging of Fe^{3+} without notable cytotoxicity. The reversible binding of RH-BZN to Fe^{3+} was confirmed by reacting with tetra-n-butylammonium fluoride both in extra- and intra-cellular conditions.

Chapter 3

This chapter describes a highly selective fluorescent chemosensor of rhodamine-1-(2-aminoethyl) pyrrolidine(L) towards Fe^{3+} through 1: 1 complexation under the specified reaction conditions of 3 : 7 water : MeCN (v/v) at pH 7.2; 10 mM HEPES buffer, μ = 0.05 M LiCl; it shows an enhancement in the corresponding fluorescence intensity of 106-fold with an apparent binding constant (K_f) of 8.10 $\times 10^4$ M^{-1}. We have also carried out fluorescence titration and anisotropy (r) studies in pure water in the presence of SDS. Based on the dependence of FI and r on [SDS], it was proposed that the probe is trapped between two SDS monolayers, which again interacted among themselves by π···π stacking. As a result, there is an increase in FI up to [SDS] ~ 7 mM – a phenomenon reminiscent of aggregation-induced enhancement of emission (AIEE). Beyond this concentration of SDS (7 mM), micelle formation takes place

and the π···π stacked polymer now becomes a monomer and is trapped inside the micellar cavity, which is again confirmed by the failure of HF_2^- to quench the FI of the $[L–Fe(NO_3)]^{2+}$ complex trapped inside the micellar cavity, which otherwise quenches the FI of $[L–Fe(NO_3)]^{2+}$ in the absence of SDS. Due to the trapping of the$[L–Fe(NO_3)]^{2+}$ monomer complex, there is a decrease in FI at [SDS] > 7 mM. In the case of anisotropy, it increases on increasing [SDS] beyond 7 mM. Ligands, metals, and SDS interactions are well established through different optical and morphological studies. $[L–Fe(NO_3)]^{2+}$ thin films on an FTO glass substrate have been designed with the help of the spin coating deposition technique. The deposited film having a thickness of 1.6×10^{-5} cm is well characterized by optical band gap calculation with a direct band gap, $\varepsilon_g \sim 1.6$ eV. FESEM studies were also performed on the $[L–Fe(NO_3)]^{2+}$/FTO film. The electrical behaviour, i.e. current–voltage characteristics by the two-probe technique was also studied. Light dependent exciton generation was carried out by taking the top and bottom contacts with graphite paste on FTO and on the $[L–Fe(NO_3)]^{2+}$ films for the measurement of switching behaviour's response ratio curves for the light-induced frequency-switching phenomenon have been obtained. The frequency taped here is the oscillation frequency of the photogenerated electron and the hole in an exciton. Thus, the light induced frequency-switching behaviour and Schottky barrier diode characteristics of the material were established.

Chapter 4

This chapter deals with a rhodamine-B based fluorescent molecular probe **L,** which can selectively recognizes Fe^{3+} ion calorimetrically as well as fluorometrically in the presence of various metal ions and anions. The structure of **L** was analysed by single crystal X-diffraction studies along with NMR, mass spectroscopy and FTIR studies. The dissociation constant values ($(2.95 \pm 0.06) \times 10^{-5}$ M) and ($(9.48 \pm 0.06) \times 10^{-5}$ M) were determined by UV-Vis and fluorescence titration, respectively, revealing a strong binding between **L** and Fe^{3+}. The limit of detection (LOD) of Fe^{3+} by **L** was 0.27 μM while quantum yields of **L** and [L–Fe] were 0.011 and 0.36, respectively. Fluorescence anisotropy measured in the presence of HSA indicates the rigidity of the local micro environment where [L–Fe] was trapped in the sub domain IIA of HSA, as delineated by molecular docking studies. Furthermore, stone like microstructure of **L** formed in 8:2 HEPES buffer:MeCN, (v/v) medium changes to spherical shape in the presence of Fe^{3+} and when the complex interacts with HSA it gets agglomerated. All these are exhibited in SEM studies. All the forgoing discussion establishes that this probe (**L**) is useful for on-site Fe^{3+} recognition through a fast, simple and eco-friendly process.

List of Publications

1. **H. A. Molla,** R. Bhowmick, A. Katarkar, K. Chaudhuri, S. Gangopadhyay and M. Ali, A novel rhodamine-3,4-dihydro-2H-1,3-benzoxazine conjugate as a highly sensitive and selective chemosensor for Fe^{3+} ions with cytoplasmic cell imaging possibilities, ***Anal. Methods***., 2015, **7**, 5149-5156.

2. M. Dolai, **H. A. Molla**, G. Rogez and M.Ali, Two $[Mn_3(\mu_3\text{-}O)]^{7+}$ based Single Chain Magnets with different solvent ligation, ***Polyhedron***, 2017, **127**, 248-256.

3. **H. A. Molla,** R. Bhowmik, A. S. M. Islam, B. Show, N. Mukherjee, A. Mondal and M. Ali, Turn-on fluorogenic chemosensor for Fe^{3+} and a Schottky barrier diode with frequency-switching device applications, ***Photochem. Photobiol. Sci.***, 2018, **17**, 465-473.

Analytical Methods

PAPER

View Article Online
View Journal | View Issue

Published on 11 May 2015. Downloaded by Indian Institute of Technology Roorkee on 9/11/2022 6:49:27 PM.

Cite this: *Anal. Methods*, 2015, 7, 5149

A novel rhodamine-3,4-dihydro-2*H*-1,3-benzoxazine conjugate as a highly sensitive and selective chemosensor for Fe^{3+} ions with cytoplasmic cell imaging possibilities†

Habib Ali Molla,[a] Rahul Bhowmick,[a] Atul Katarkar,[b] Keya Chaudhuri,[b] Sumana Gangopadhyay[c] and Mahammad Ali*[a]

Received 21st March 2015
Accepted 8th May 2015

DOI: 10.1039/c5ay00754b

www.rsc.org/methods

A novel, highly sensitive and selective fluorescent chemosensor 'rhodamine-3,4-dihydro-2*H*-1,3-benzoxazine' [RH-BZN (**1**)] has been synthesized and characterized by single crystal X-ray diffraction and other physicochemical techniques. In 3 : 7 water : MeCN (v/v) at pH 7.2 (10 mM HEPES buffer, $\mu = 0.05$ M LiCl) it selectively recognizes Fe^{3+} through 1 : 1 complex formation resulting in a 240-fold fluorescence enhancement and a binding constant (K_f) of 1.50×10^4 M^{-1}. The otherwise non-fluorescent spirolactam form of the probe results in dual changes in absorbance and fluorescence arising out of opening of the spirolactam ring through coordination to Fe^{3+} ions. This probe could suitably be employed for cytoplasmic intracellular imaging of Fe^{3+} without notable cytotoxicity. The reversible binding of RH-BZN to Fe^{3+} was confirmed by reacting with tetra-*n*-butylammonium fluoride both in extra- and intra-cellular conditions.

Transition-metal ions are involved in many biological and environmental processes, and there has been a great emergence of interest in recent years to generate metal ion selective and sensitive fluorescent probes.[1] Though numerous excellent studies focusing on the selective and sensitive detection of transition metal ions, *e.g.*, Cu^{2+}, Pb^{2+}, Zn^{2+}, and Hg^{2+}, have been reported,[2] examples of Fe^{3+}-selective fluorescent probes are still scarce,[3] despite the indispensable role of Fe^{3+} in many biochemical processes.[4,5]

Iron seems to be a versatile element involved in the proper functioning of numerous biological systems in all living organisms including bacteria and plants.[6,7] Both deficiency and excess of iron can induce a variety of diseases.[8] Iron being both useful and cytotoxic,[9] its deficiency throughout the developmental phases may lead to permanent loss of motor skills.[10] Iron overload in a living cell can lead to generation of reactive oxygen species (ROS) *via* the Fenton reaction, which can cause damage to lipids, nucleic acids, and proteins. Again, accumulation of iron in the central nervous system may lead to a number of diseases like Parkinson's, Huntington's and Alzheimer's.[9a] Keeping in view the roles played by iron in day-to-day life, the development of techniques for selective determination of iron is in great demand. It is necessary to design a simple, highly sensitive and selective chemosensor for Fe^{3+} detection and establish a method for the determination of trace amounts of Fe^{3+} ions. Most of the known Fe^{3+} sensors are based on fluorescence quenching mechanisms due to the paramagnetic nature of ferric ions.[11] In addition, most turn-on fluorescence sensors for Fe^{3+} are not selective over Cr^{3+} and Cu^{2+}.[12] Therefore, the development of a chemosensor that shows high selectivity for iron involving a fluorescence turn-on response is necessary for practical applications.

On the other hand, 3,4-dihydro-2*H*-1,3-benzoxazines are bicyclic heterocycles that are of significant interest in the polymeric and pharmacological fields. 1,3-Benzoxazines have long been recognized for their wide range of biological activities with uses as herbicides, agricultural microbiocides, bactericides, fungicides, and antidepressive, anti-inflammatory, and anti-tumor agents.[13–16] Moreover, 1,3-benzoxazine monomers are recently used to develop a new type of phenolic resin, namely polybenzoxazines, by ring-opening polymerization.[17–20]

Rhodamine based conjugates with a spirolactam structure are, in general, non-fluorescent but act as colorimetric as well as fluorometric sensors with the enhancement of absorption and fluorescence emission intensity, respectively, on selective binding to metal ion(s).

In the present study, we are going to disclose, for the first time, a rhodamine-3,4-dihydro-2*H*-1,3-benzoxazine conjugate

[a]*Department of Chemistry, Jadavpur University, 188, Raja S. C. Mullick Road, Kolkata 700 032, India. E-mail: m_ali2062@yahoo.com; mali@chemistry.jdvu.ac.in; Fax: +91-33-2414-6223*

[b]*Molecular & Human Genetics Division, CSIR-Indian Institute of Chemical Biology, 4 Raja S.C. Mallick Road, Kolkata 700 054, India*

[c]*Department of Chemistry, Gurudas College, Narkeldanga, Kolkata 700 043, India*

† Electronic supplementary information (ESI) available: X-ray crystallographic files in CIF format and experimental details regarding the synthesis and characterisation of the ligand and metal complex, including spectroscopic details. CCDC 1029259. For ESI and crystallographic data in CIF or other electronic format see DOI: 10.1039/c5ay00754b

Published on 11 May 2015. Downloaded by Indian Institute of Technology Roorkee on 9/11/2022 6:49:27 PM.

as a highly sensitive and selective fluorescent chemosensor for Fe^{3+} ions which further recognizes F^- ions by quenching the fluorescence of the Fe^{3+}–RH-BZN complex by abstracting the metal ion through the formation of a stable FeF_6^{3-} complex.

Experimental

Materials and methods

The starting materials, such as, rhodamine B hydrochloride (Sigma-Aldrich), 2,4-di-*tert*-butyl phenol (Sigma-Aldrich), ethylene diamine (Sigma-Aldrich), formaldehyde (Sigma-Aldrich), ferric nitrate (Sigma-Aldrich), and tetra-*n*-butylammonium fluoride (Sigma-Aldrich) were used for the preparation of RH-BZN and the Fe^{3+} complex. Other metal ions were obtained from previous studies. Solvents like EtOH, MeOH, MeCN, *etc.* (Merck, India) were of HPLC grade. MeCN and deionised water were used for spectroscopic studies.

Physical measurements

Infrared spectra (400–4000 cm^{-1}) were recorded from KBr pellets on a Nickolet Magna IR 750 series-II FTIR spectrophotometer. ^1H NMR and ^{13}C NMR were recorded in $CDCl_3$ on a Bruker 300 MHz NMR spectrometer using tetramethylsilane ($\delta = 0$) as an internal standard. UV-vis spectra were recorded on an Agilent diode-array spectrophotometer (Model, Agilent 8453), steady-state fluorescence spectra were recorded on a PTI spectrofluorimeter (Model QM-40.), and ESI-MS^+ (m/z) of the RH-BZN and Fe^{3+} complex were recorded on a HRMS spectrometer (Model: XeVO G2 QTof).

Syntheses

Preparation of RH-BZN (3)

Rhodamine B hydrochloride (**1**) (5.0 mmol) and ethylenediamine (10.0 mmol) were dissolved in EtOH and refluxed for 6 hours with continuous stirring whereupon a white crystalline solid of rhodamine-amine (**2**) was deposited. The solid was filtered and washed with EtOH. The compound (**2**) (2 mmol), 2,4-di tertiary butyl phenol (4 mmol) and formaldehyde (4 mmol) were dissolved in MeCN and refluxed for 20 h with constant stirring whereupon a white solid was deposited, filtered and washed several times with ethanol and dried in air (68% yield). It was further recrystallized from MeOH to get single crystals suitable for X-ray diffraction studies. ^1H NMR (300 MHz, $CDCl_3$) (δ, ppm): 1.20 (t, 12H, CH_3), 1.28 (t, 18H, CH_3), 2.48 (s, 2H, CH_2), 3.36 (s, 8H, CH_2), 3.83 (s, 2H, CH_2), 4.60 (s, 2H, CH_2), 6.28 (s, 2H, CH_2), 6.40–6.50 (m, 4H, ArH), 6.73 (1H, s, ArH), 7.09 (s, 2H, ArH), 7.29 (s, 1H, ArH), 7.46 (s, 2H, ArH), 7.92 (s, 1H, ArH) (Fig. S1–S2†). IR spectrum: $\tilde{\nu} = 1692.15$ cm^{-1} (spirolactam amide-keto), 1615.02 cm^{-1} (–C=N) (Fig. S3†). ESI-MS^+ (m/z): 715.37 (RH-BZN + H^+) (Fig. S4†).

Synthesis of [Fe (RH-BZN)$(NO_3)_2(CH_3CN)$]

$Fe(NO_3)_3 \cdot 9H_2O$ (2 mmol) in 5 ml MeCN was added drop wise to a solution of RH-BZN (2 mmol) in 20 ml MeCN with continuous stirring. After 1 hour the solution was filtered and kept aside undisturbed. After one day a crystalline complex was precipitated out. It was collected by filtration, washed several times with MeOH and dried in air. It was recrystallized from methanol. Several trials to grow single crystals failed. IR spectrum: $\tilde{\nu} = 1637.68$ cm^{-1} (spirolactam amide-keto), 1554.65 cm^{-1} (–C=N) (Fig. S3†). ESI-MS^+ (m/z): 834.4961 [Fe(RH-BZN)$(OCH_3)(CH_3OH)$]; 934.5900 [Fe(RH-BZN)$(NO_3)_2(CH_3CN)$]; 948.6159 [Fe(RH-BZN)$(NO_3)_2(OCH_3)]Na^+$ (Fig. S5†).

Cell culture

Human hepatocellular liver carcinoma (HepG2) cell lines (NCCS, Pune, India) were grown in DMEM supplemented with 10% FBS and antibiotics (penicillin, 100 μg ml^{-1}; streptomycin, 50 μg ml^{-1}). Cells were cultured at 37 °C in a 95% air, 5% CO_2 incubator.

Cell cytotoxicity assay

To determine the cell viability% of RH-BZN, MTT assay was performed. HepG2 cells (1×10^5 cells per well) were cultured in a 96 well plate at 37 °C, and exposed to varying concentrations of RH-BZN, 1, 10, 20, 40, 60, 80 and 100 μM, respectively, for 12 h. 20 μl of MTT solution [5 mg ml^{-1} 1× phosphate-buffered saline (PBS)] was added to each well of a 96-well culture plate and incubated again continuously at 37 °C for a period of 4 h. All media were removed from wells and 100 μl of DMSO was added to each well and absorbance was measured at 550 nm (E_{Max} Precision MicroPlate Reader, Molecular Devices, USA). All experiments were performed in triplicate and the relative cell viability (%) was expressed as a percentage relative to the untreated control cells (Fig. S6†).

Cell imaging study

HepG2 cells were cultured and incubated in a 35 × 10 mm culture dish over a cover slip for 24 h at 37 °C. The cells were allowed to incubate with 10 μm RH-BZN prepared by dissolving it in a mixed solvent (DMSO : water = 1 : 9 (v/v)) in the culture medium for 30 min at 37 °C. After incubation, cells were washed twice with 1× PBS and allowed to be counterstained by DAPI (2-(4-amidinophenyl)-6-indolecarbamidine dihydrochloride-4′,6-diamidino-2-phenyl-indole, used for nuclear staining, Sigma). Fluorescence images of HepG2 cells were taken by using a fluorescence microscope (Leica DM3000, Germany) with an objective lens of 40× magnification. Fluorescence images of HepG2 cells were taken separately from another set of experiment where cells were pre-incubated with 10 μM Fe^{3+} for 30 min at 37 °C followed by washing twice with 1× PBS and subsequent incubation with 10 μM RH-BZN for 30 min at 37 °C. Similarly, in another set of experiment, cells were incubated sequentially with 10 μm Fe^{3+}, 10 μM RH-BZN and 100 μM F^- for 30 min at 37 °C with alternative washing with 1× PBS two times. The live cell on the cover slip was allowed for fluorescence imaging. RH-BZN shows HepG2 intracellular cytoplasmic red fluorescence by forming a complex with Fe^{3+} and DAPI, used as the counter stain to localize the nucleus, showing blue color at the nucleus. Moreover, the concentration dependent capture of Fe^{3+} was

 This journal is © The Royal Society of Chemistry 2015

Published on 11 May 2015. Downloaded by Indian Institute of Technology Roorkee on 9/11/2022 6:49:27 PM.

preformed similarly as per described above at 1, 10 and 20 μM for RH-BZN. Furthermore, to confirm the cytoplasmic capturing of Fe^{3+} and cytoplasmic localization of RH-BZN after forming a complex with Fe^{3+}, a cell imaging study was conducted by using DAPI as the nuclear counter stain and Lyso-Tracker Green DND-26 (invitrogen) for cytoplasm and, a live cell imaging study was carried out as described above. Likely, RH-BZN showed HepG2 intracellular cytoplasmic red fluorescence by forming a complex with Fe^{3+}, confirmed against a nuclear and cytoplasmic tracker.

Solution preparation for UV-vis and fluorescence studies

For both UV-vis and fluorescence titrations, a stock solution of 1.0×10^{-3} M of the probe **3** was prepared by dissolving it in 0.5 ml MeCN and finally the volume is made up to 10 ml by MeCN. Similarly, 10 ml 1.0×10^{-3} M stock solutions of Fe^{3+} and tetra-*n*-butyl ammonium fluoride were prepared separately in MeCN. 100 ml solution of 10 mM HEPES buffer was prepared and the pH was adjusted to 7.24 by using HCl and NaOH as required. 2.5 ml of this buffer solution was pipetted out into a cuvette to which 20 μM of the probe was added and Fe^{3+} ions were added incrementally starting from 0 to 25 μM in a regular interval of volume and UV-vis and fluorescence spectra were recorded for each solution. Similar is the case for tetra-*n*-butyl ammonium fluoride titration. Path length used of the cells for absorption and emission studies was 1 cm. Fluorescence measurements were performed using 2 nm × 2 nm slit width.

Quantum yield determination

Fluorescence quantum yields (Φ) were estimated by integrating the area under the fluorescence curves with the equation:

$$\Phi_{sample} = \frac{OD_{std}}{OD_{sample}} \times \frac{A_{sample}}{A_{std}} \times \Phi_{std}$$

where, A is the area under the fluorescence spectral curve and OD is optical density of the compound at the excitation wavelength. The standard used for the measurement of fluorescence quantum yield was rhodamine 6G ($\Phi_{std} = 0.94$ in CH_3OH).

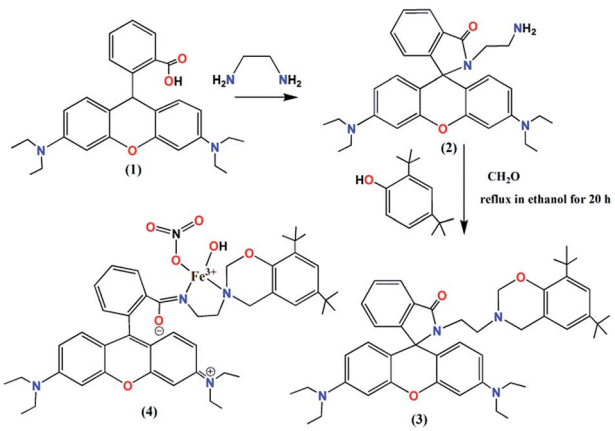

Scheme 1

Results and discussion

As depicted in Scheme 1, receptor RH-BZN (**3**) was synthesized from the reaction of rhodamine-B with ethylenediamine followed by the Mannich reaction with 2,4-di-*tert*-butylphenol in the presence of formaldehyde in EtOH in refluxing conditions for 20 h with 68% yield. The final product (**3**) was well characterized by ^{1}H NMR (Fig. S1†), ^{13}C NMR (Fig. S2†), IR (Fig. S3†), HRMS (Fig. S4 and S5†) and a single crystal X-ray diffraction method (Fig. 1). Details of the method of data collection and refinement are listed in Table 1.

Single crystal X-ray diffraction studies reveal that the compound RH-BZN crystallises in a monoclinic system of space group $P21/c$. The crystallographic details are depicted in Table 1.

The receptor **3** was found to be a highly sensitive and selective colorimetric and fluorogenic dual sensor for Fe^{3+} while in the absence of Fe^{3+}; the solution of **3** is colourless and non-fluorescent.

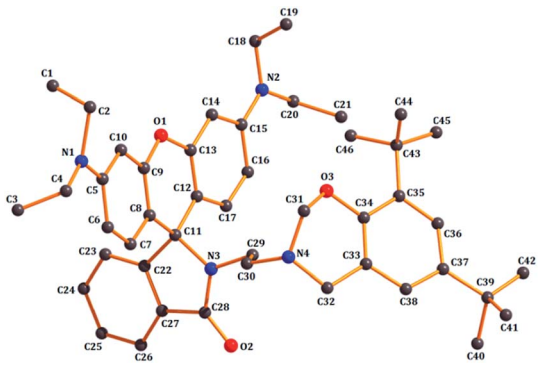

Fig. 1 Molecular view of **3**, H atoms are removed to get better clarity.

Table 1 Crystal data and details of the structure determination[a]

Formula	$C_{46}H_{58}N_4O_3$
Formula weight	714.96
Crystal system	Monoclinic
Space group	$P21/c$ (no. 14)
a, b, c [Å]	17.313(3), 24.678(4), 9.5642(17)
α, β, γ [°]	90, 105.015(390), 90
V [Å^3]	3946.8(12)
Z	4
D (calc.) [g cm^{-3}]	1.203
μ (MoK$_\alpha$) [mm^{-1}]	0.075
F (000)	1544
Crystal size [mm]	0.05 × 0.18 × 0.23
Temperature (K)	296
Radiation [Å] MoK$_\alpha$	0.71073
Θ min–max [°]	1.2, 27.6
Dataset	−22 : 22; −32 : 32; −12 : 12
Tot., uniq. data, R(int)	32636, 9136, 0.094
Observed data [$I > 2.0\ \sigma(I)$]	4317
N_{ref}, N_{par}	9136, 492
R, wR_2, S	0.0861, 0.2329, 1.02
Max. and av. shift/error	0.02, 0.02
Min. and max. resd. dens. [e Å^{-3}]	−0.55, 0.86

[a] $w = 1/[s^2(F_o^2) + (0.2000P)^2]$, where $P = (F_o^2 + 2F_c^2)/3$.

Published on 11 May 2015. Downloaded by Indian Institute of Technology Roorkee on 9/11/2022 6:49:27 PM.

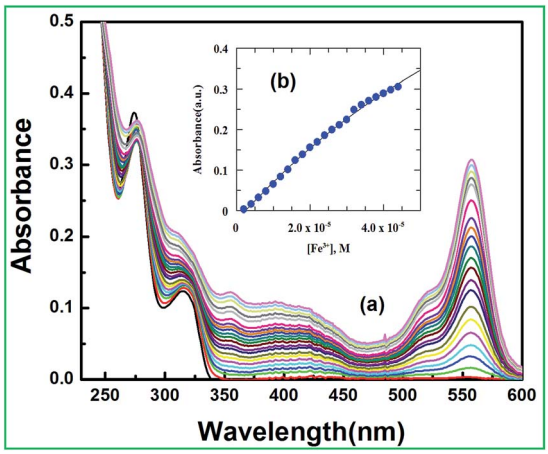

Fig. 2 (a) Absorption titration of RH-BZN with Fe^{3+} in MeCN–H_2O (7 : 3, v/v) in HEPES buffer (1 mM) at pH 7.2; (b) non-linear fitting of data.

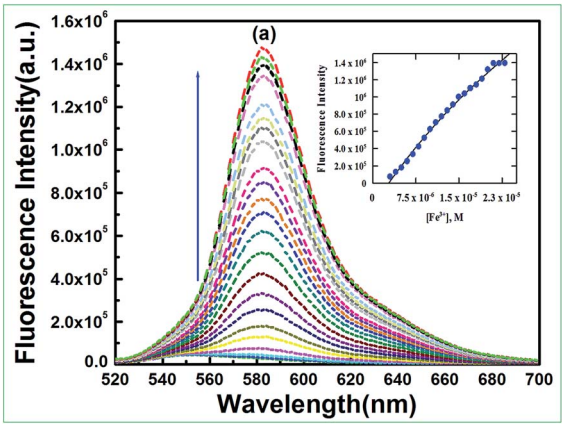

Fig. 3 (a) Fluorescence titration of (20.0 μM) in MeCN–H_2O (7 : 3, v/v) in HEPES buffer at pH 7.2 by the gradual addition Fe^{3+} with $\lambda_{ex} = 510$ nm, $\lambda_{em} = 582$ nm, inset (b) non-linear curve-fit of the FI *vs.* [Fe^{3+}] plot.

In order to determine the stability constant and composition of the RH-BZN–Fe^{3+} complex we have carried out UV-vis titration with a fixed concentration of **3** (20 μM) and variable concentrations of Fe^{3+} (0–35.0 μM) at 25 °C in aqueous MeCN (3 : 7, v/v, 1.0 mM HEPES buffer, pH 7.2, $\mu = 0.05$ M LiCl). It was revealed that there is a gradual development of a new absorption band at around 552 nm on addition of Fe^{3+} (Fig. 2a). A plot of absorbance *vs.* [Fe^{3+}] showed a gradual increase in absorbance and tends to become almost constant at ~1 : 1.75 ligand : metal mole ratio. The absorption titration data were fitted to a non-linear eqn (1),[21] where a and b are the absorbance/fluorescence intensities in the absence and presence of excess metal ions, respectively, c (=K_f) is the formation constant and n is the stoichiometry of the reaction.

$$y = \frac{a + b \times c \times x^n}{1 + c \times x^n} \quad (1)$$

The evaluated parameters are: $K_f = (1.50 \pm 0.18) \times 10^4\ M^{-1}$ and $n = 1.04 \pm 0.01$.

The fluorescence titration data were solved analogously as in the case of absorption titration data which gives a K_f of (1.50 ± 0.23) × $10^4\ M^{-1}$ and $n = 0.99 \pm 0.02$ (see Fig. 3B). There is an excellent agreement between the K_f values extracted from absorption ($K_f = (1.50 \pm 0.18) \times 10^4\ M^{-1}$, $n = 1.04 \pm 0.01$) and fluorescence (K_f of (1.50 ± 0.23) × $10^4\ M^{-1}$, $n = 0.99 \pm 0.02$) titration data manifesting the self-consistency of our results. The 1 : 1 composition of the complex was further confirmed by Job's experiment (Fig. S7†).

After performing all possible compositions of CH_3CN/H_2O for spectral (fluorescence) studies it was observed that CH_3CN–H_2O (7 : 3, v/v) is a good choice for this study. On increasing the water content beyond CH_3CN–H_2O (7 : 3, v/v) the fluorescence enhancement was found to decrease progressively and there is no visible change in FI when 100% water was used (Fig. S8†). The detection of Fe^{3+} was not perturbed by the presence of biologically abundant Na^+, K^+, Ca^{2+} and Mg^{2+} ions. Similarly, several transition-metal ions, namely Cr^{3+}, Mn^{2+}, Fe^{2+}, Co^{2+}, Cu^{2+}, Ni^{2+} and Zn^{2+}, and heavy-metal ions, like Cd^{2+}, Hg^{2+} and Pb^{2+} did not show any significant spectral change under identical reaction conditions and the selectivity studies both for individual metal ions as well as in the presence of Fe^{3+} in each case were also carried out. These studies clearly suggest that all the tested metal ions have no interference in the selective detection of Fe^{3+} (Fig. S9†).

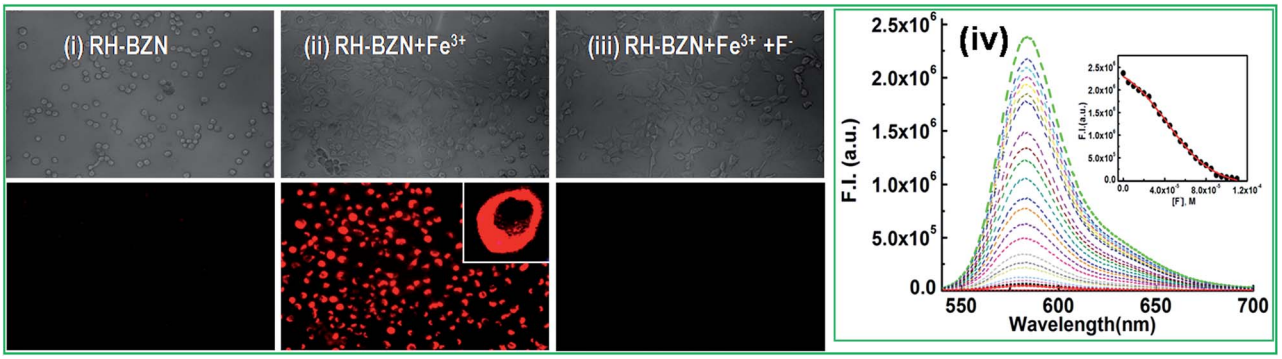

Fig. 4 The phase contrast (upper panel) and fluorescence images (lower panel) of HepG2 cells were captured (40×) after incubation with (i) RH-BZN (10 μM), (ii) RH-BZN + Fe^{3+} (10 μM each) and (iii) RH-BZN + Fe^{3+} (10 μM each) followed by the addition of 100 μM F^- for 30 min at 37 °C. Inset shows the cytoplasmic response of RH-BZN towards Fe^{3+}. (iv) Fluorescence titration of RH-BZN–Fe^{3+} ensemble (20 μM) by gradual addition of F^- solution (5 μM at a time).

 This journal is © The Royal Society of Chemistry 2015

Published on 11 May 2015. Downloaded by Indian Institute of Technology Roorkee on 9/11/2022 6:49:27 PM.

To check the suitability for the convenient biological application of this probe towards Fe^{3+} sensing under physiological conditions the pH-stability of the probe was investigated which showed no obvious fluorescence of RH-BZN between pH 6 and 12, suggesting the existence of a spirolactam form of RH-BZN over this wide range of pH (Fig. S10†). However, in the presence of a selective guest like Fe^{3+} ions it fluoresces effectively at pH ≥ 7.0 which clearly indicates the compatibility of the probe for biological applications under physiological conditions.

The reversible binding of **3** to Fe^{3+} was investigated in the same solvent system as was used in the absorption and fluorescence titrations. Anions like SO_4^{2-}, NO_3^-, Cl^-, F^-, Br^-, I^-, OAc^- and N_3^- of 5 equivalents of **3** were introduced (Fig. S11†) into the solution of the RH-BZN–Fe^{3+} complex and subsequently the changes in their fluorescence intensities were monitored. The results showed that anions like F^- (tetra-*n*-butylammonium fluoride) have a strong affinity towards Fe^{3+} and their binding constants seem to be much higher than that of the RH-BZN–Fe^{3+}

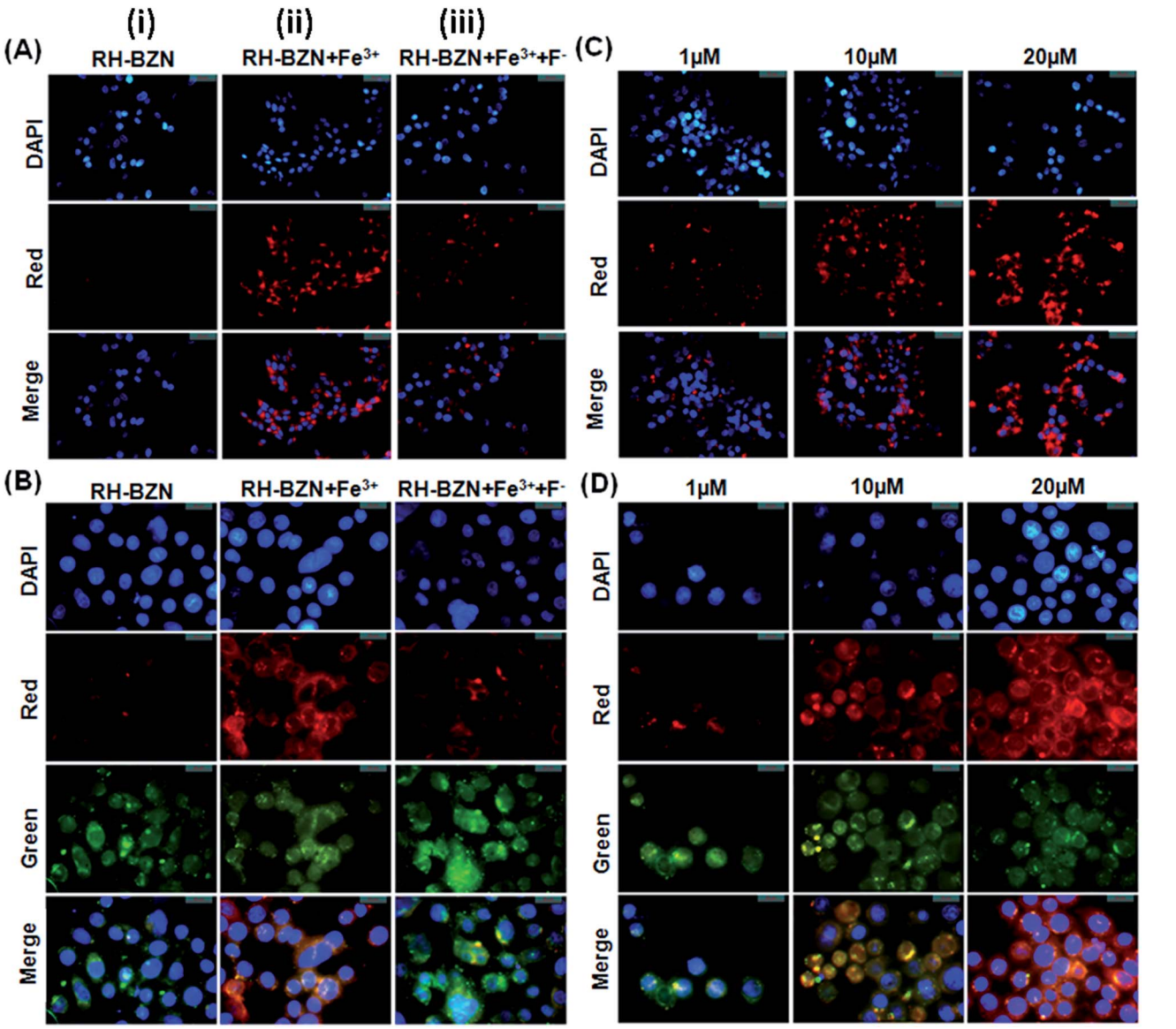

Fig. 5 HepG2 cells were incubated with (i) 10 μM of RH-BZN for 30 min at 37 °C, (ii) pre-incubated 10 μM of Fe^{3+} for 30 min at 37 °C followed by washing twice with 1× PBS and, subsequent incubation with 10 μM RH-BZN for 30 min at 37 °C and (iii) pre-incubated 10 μM of Fe^{3+} for 30 min at 37 °C followed by 10 μM RH-BZN and 100 μM F^- for 30 min at 37 °C with alternative washing with 1× PBS two times. (A) The fluorescence image (40×) shows the strong red fluorescence when RH-BZN complexes with Fe^{3+} (in green filter) and is subsequently quenched on the addition of F^- (in green filter). The merged image shows the cytoplasmic RH-BZN + Fe^{3+} fluorescence, suggesting no nuclear entry of RH-BZN fluorophore with DAPI as the nuclear counter stain (blue, in violet/blue filter). (B) The fluorescence image (100×) shows the strong red fluorescence when RH-BZN complexes with Fe^{3+} and is subsequently quenched on the addition of F^-. The merged image shows the cytoplasmic RH-BZN + Fe^{3+} fluorescence, suggesting no nuclear entry of RH-BZN fluorophore with DAPI as the nuclear counter stain (blue) and LysoTracker (green, in blue filter) for cytoplasm. (C) The intracellular fluorescence image of RH-BZN in the complex with Fe^{3+} at 1, 10 and 20 μM concentrations of RH-BZN is shown (40×) by counterstaining using DAPI and (D) using DAPI as the nuclear counter stain and LysoTracker for cytoplasm (100×). The lowest concentration of RH-BZN (1 μm) shows excellent detection of Fe^{3+} in the cytoplasm of HepG2 cell.

Published on 11 May 2015. Downloaded by Indian Institute of Technology Roorkee on 9/11/2022 6:49:27 PM.

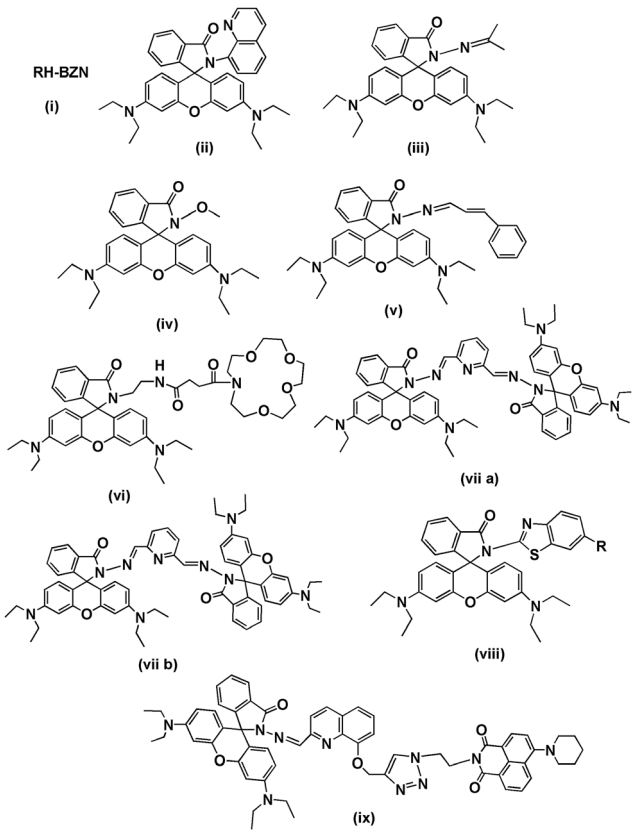

Scheme 2

complex resulting in the abstraction of Fe^{3+} from the complex and bleaching of the emission band at 582 nm through the re-establishment of the spirolactam ring (Fig. 4). The quantum yield of the RH-BZN–Fe^{3+} complex was determined to be Φ = 0.57 (with rhodamine 6G as a standard), whereas the free ligand is non- or very weakly fluorescent. The limit of detection (LOD) of Fe^{3+} was determined by the 3σ method[22] and found to be as low as 0.11 μM (Fig. S12†). All these findings indicate that RH-BZN is a good example of an ideal chemosensor for Fe^{3+}.

The formation of the RH-BZN–Fe^{3+} complex by opening of the spirolactam ring was established through IR studies. The IR study revealed that the characteristic stretching frequency of the amidic "C=O" of the rhodamine moiety at 1692.15 cm^{-1} is shifted to a lower wave number 1637.68 cm^{-1} in the presence of 1.2 equiv. of Fe^{3+} (Fig. S3†). This large shift signifies a strong polarization of the C=O bond upon efficient binding to the Fe^{3+} ion and in fact indicates opening of the spirolactam ring.[22]

Bio-imaging of Fe^{3+} by RH-BZN was performed in live cells (Fig. 4 and 5) by using fluorescence microscopic techniques. To determine whether RH-BZN has any cytotoxic effect, MMT assay was performed on HepG2 cells which showed no significant cell cytotoxicity up to 80 μm (<30% cytotoxicity) (Fig. S6†).[23] Hence further experiments were carried out at a low dose (10 μm) of RH-BZN.

The intracellular imaging behaviour of RH-BZN (10 μM) on HepG2 cells displayed no obvious fluorescence (Fig. 4). However, an excellent intracellular cytoplasmic fluorescence was observed inside the cells, when HepG2 cells were incubated with 10 μM RH-BZN followed by washing with 1× PBS and subsequent incubation with 10 μM Fe^{3+} and, also subsequent quenching of red fluorescence on treatment with tetra-*n*-butyl ammonium fluoride. Interestingly we have observed that the fluorophore RH-BZN shows the only cytoplasmic binding with Fe^{3+}, not the nuclear binding (Fig. 4, inset and Fig. 5). The specific binding of fluorophore **3** to the cytoplasm makes this fluorophore less toxic, as fluorophore **3** cannot cross the nuclear membrane to bind to the nucleus (DNA) which causes the more toxic effect on cells.[24] The cytotoxicity study by MMT assay shows 82% cell viability at 20 μM concentration and specifically detects the cytoplasmic Fe^{3+}. Additionally, Fig. 5 displays the concentration dependent binding of RH-BZN to intracellular Fe^{3+} which clearly indicates that the present probe is capable of recognizing cytoplasmic Fe^{3+} as low as 1 μm concentration. As the dye is not water soluble, we performed all the extracellular experiments in the MeCN : H_2O (7 : 3, v/v) mixture. However, when the probe is once solubilised in DMSO it did not give any precipitate on adding water up to 99%. So there was no problem in performing the cell imaging experiment in the 1 : 9 DMSO : H_2O mixture.

Few of the recently investigated rhodamine-B based Fe^{3+} sensors are given in Scheme 2 and some salient features are given in Table 2. A quick inspection of these studies reveal that all these are turn on Fe^{3+} ion sensors with moderate LOD values (0.32–5.0 μM) and formation constants (K_f = 5.1 × 10^3–4.52 × 10^5 M^{-1}) and applicable for monitoring intracellular Fe^{3+} ions,[25]

Table 2 Comparative results of selected rhodamine 6G based probes for recognizing Fe^{3+}

Probe	Formation constant (M^{-1})	LOD (μM)	Cell
(i) RH-BZN	1.5 × 10^4	0.11	Done, cytoplasmic binding
(ii)	Not-determined	0.32	Done
(iii)	2.3 × 10^4	Not determined	Done
(iv)	1.58 × 10^5	Not determined	Not done
(v)	Not determined	1.8	Not done
(vi)	2.46 × 10^4	0.40	Done
(vii) (a)	7.5 × 10^3	Not determined	Not done
(vii) (a)	5.1 × 10^3	Not determined	Not done
(viii)	4.52 × 10^5	5	Done
(ix)	9.62 × 10^5	0.05	Done

 This journal is © The Royal Society of Chemistry 2015

Published on 11 May 2015. Downloaded by Indian Institute of Technology Roorkee on 9/11/2022 6:49:27 PM.

though in a few cases no cell imaging experiments were performed. RH-BZN recognizes Fe^{3+} with 240-fold fluorescence enhancement with a binding constant of 1.50×10^4 M^{-1} and a LOD of 0.11 μM through a 1 : 1 host–guest type interaction. Not only that the cytoplasmic binding makes this probe more appropriate for *in vivo* monitoring of Fe^{3+} without any genetic damage.

Conclusions

In summary, a novel benzoxazine based dual sensor 'rhodamine-3,4-dihydro-2*H*-1,3-benzoxazine', RH-BZN (**3**) has been synthesized and structurally characterized. In 3 : 7 water : MeCN (v/v) and at physiological pH 7.2, it selectively recognizes Fe^{3+} giving 240-fold fluorescence enhancement and a binding constant of 1.50×10^4 M^{-1} through a 1 : 1 host–guest type interaction, which could suitably be employed for cytoplasmic intracellular imaging of Fe^{3+} without notable cytotoxicity. Reversible binding of Fe^{3+} towards this probe was confirmed by reacting with tetra-*n*-butyl ammonium fluoride both in extra- and intra-cellular conditions.

Acknowledgements

Financial support from the DST (Ref. SR/S1/IC-20/2012), New Delhi, is gratefully acknowledged.

References

1 (*a*) M. Zhang, M. X. Yu, F. Y. Li, M. Zhu, M. Y. Li, Y. Gao, Z. Liu, J. Zhang, D. Zhang, T. Yi and C. H. Huang, *J. Am. Chem. Soc.*, 2007, **129**, 10322; (*b*) J. H. Lee, C. S. Lim, Y. S. Tian, J. H. Han and B. R. Cho, *J. Am. Chem. Soc.*, 2010, **132**, 1216; (*c*) Y. Wei, Y. Zhang, Z. Liu and M. L. Guo, *Chem. Commun.*, 2010, **46**, 4472.

2 (*a*) Y. Zhou, F. Wang, Y. Kim, S.-J. Kim and J. Yoon, *Org. Lett.*, 2009, **11**, 4442; (*b*) B. A. Smith, W. J. Akers, W. M. Leevy, A. J. Lampkins, S. Xiao, W. Wolter, M. A. Suckow, S. Achilefu and B. D. Smith, *J. Am. Chem. Soc.*, 2010, **132**, 67; (*c*) H. S. Jung, P. S. Kwon, J. W. Lee, J. Kim, C. S. Hong, J. W. Kim, S. Yan, J. Y. Lee, J. H. Lee, T. Joo and J. S. Kim, *J. Am. Chem. Soc.*, 2009, **131**, 2008; (*d*) L. Huang, X. Wang, G. X. P. Xi, Z. Li, M. Xu, Y. J. Wu, D. C. Bai and Z. Z. Zeng, *Dalton Trans.*, 2010, 7894; (*e*) R. Bhowmick, R. Alam, T. Mistri, D. Bhattacharya, P. Karmakar and M. Ali, *ACS Appl. Mater. Interfaces*, 2015, **7**, 7476; (*f*) H. Y. Lee, K. M. K. Swamy, J. Y. Jung, G. Kim and J. Yoon, *Sens. Actuators, B*, 2013, **182**, 530; (*g*) F. Wang, S. W. Nam, Z. Guo, S. Park and J. Yoon, *Sens. Actuators, B*, 2012, **161**, 948; (*h*) X. Chen, T. Pradhan, F. Wang, J. S. Kim and J. Yoon, *Chem. Rev.*, 2012, **112**, 1910; (*i*) P. Mahato, S. Saha, P. Das, H. Agarwalla and A. Das, *RSC Adv.*, 2014, **4**, 36140.

3 (*a*) S. Bae and J. Tae, *Tetrahedron Lett.*, 2007, **48**, 5389; (*b*) Y. Xiang and A. Tong, *Org. Lett.*, 2006, **8**, 1549; (*c*) J. L. Bricks, A. Kovalchuk, C. Trieflinger, M. Nofz, M. Buschel, A. I. Tolmachev, J. Daub and K. Rurack, *J. Am. Chem. Soc.*, 2005, **127**, 13522; (*d*) M. Zhang, Y. Gao, M. Li, M. Yu, F. Li, L. Li, M. Zhu, J. Zhang, T. Yi and C. Huang, *Tetrahedron Lett.*, 2007, **48**, 3709; (*e*) Y. Liu, Z. Xu, J. Wang, D. Zhang, Y. Ye and Y. Zhaoa, *Luminescence*, 2014, **29**, 945; (*f*) L. Zhang, J. Wang, J. Fan, K. Guo and X. Peng, *Bioorg. Med. Chem. Lett.*, 2011, **21**, 5413; (*g*) J. Huang, Y. Xu and X. Qian, *Dalton Trans.*, 2014, 5983.

4 M. Ghaedi, A. Shokrollahi, R. Mehrnoosh, O. Hossaini and M. Soylak, *Cent. Eur. J. Chem.*, 2008, **6**, 488.

5 S. Bae and J. Tae, *Tetrahedron Lett.*, 2007, **48**, 5389.

6 (*a*) R. Williams, *Pure Appl. Chem.*, 1983, **55**(1), 35; (*b*) M. Ferrali, D. Donati, S. Bambagioni, M. Fontani, G. Giorgic and A. Pietrangelod, *Bioorg. Med. Chem.*, 2001, **9**, 3041.

7 P. Aisen, M. Resnick and E. Leibold, *Curr. Opin. Chem. Biol.*, 1999, **3**, 200.

8 D. Touati, *Arch. Biochem. Biophys.*, 2000, **373**, 1.

9 (*a*) J. R. Burdo and J. R. Connor, *Biometals*, 2003, **16**, 63; (*b*) J. R. Connor, S. L. Menzies, S. M. S. Martin and E. J. Mufson, *J. Neurosci. Res.*, 1990, **27**, 595; (*c*) R. R. Crichton, S. Wilmet, R. Legssyer and R. J. Ward, *J. Inorg. Biochem.*, 2002, **91**, 9; (*d*) R. S. Eisenstein, *Annu. Rev. Nutr.*, 2000, **20**, 627.

10 (*a*) B. T. Felt and B. Lozoff, *J. Nutr.*, 1996, **126**, 693; (*b*) C. J. Earley, J. R. Connor, J. L. Beard, E. A. Malecki, D. K. Epstein and R. P. Allen, *Neurology*, 2000, **54**, 1698.

11 (*a*) J. P. Sumner and R. Kopelman, *Analyst*, 2005, **130**, 528; (*b*) Y. Ma, W. Luo, P. J. Quinn, Z. Liu and R. C. Hider, *J. Med. Chem.*, 2004, **47**, 6349; (*c*) G. E. Tumambac, C. M. Rosencrance and C. Wolf, *Tetrahedron*, 2004, **60**, 11293; (*d*) A. Ali, Q. Zhang, J. Dai and X. Huang, *BioMetals*, 2003, **16**, 285.

12 (*a*) J. Mao, L. Wang, W. Dou, X. Tang, Y. Yan and W. Liu, *Org. Lett.*, 2007, **9**, 4567; (*b*) M. Xu, S. Wu, F. Zeng and C. Yu, *Langmuir*, 2010, **26**, 4529; (*c*) X. Wu, B. Xu, H. Tong and L. Wang, *Macromolecules*, 2010, **43**, 8917.

13 T. Besson, C. W. Rees, G. Cottenceau and A. Pons, *Bioorg. Med. Chem. Lett.*, 1996, **6**, 2343.

14 S. Ozden, A. Ozturk, H. Goker and N. Altanlar, *Il Farmaco*, 2000, **55**, 715.

15 R. Fringuelli, D. Pietrella, F. Schiaffella, A. Guarraci, S. Perito, F. Bistoni and A. Vecchiarilli, *Bioorg. Med. Chem.*, 2002, **10**, 1681.

16 S. Alper-Hayta, E. Aki-Sener, B. Tekiner-Gulbas, I. Yildiz, I. Yalcin and N. Alanlar, *Eur. J. Med. Chem.*, 2006, **41**, 1398.

17 B. P. Mathew, A. Kumar, S. Sharma, P. K. Shukla and M. Nath, *Eur. J. Med. Chem.*, 2010, **45**, 1502.

18 K. Waisser, J. Gregor, L. Kubicova, V. Klimesova, J. Kunes, M. Machacek and J. Kaustova, *Eur. J. Med. Chem.*, 2000, **35**, 733.

19 P. Hsieh, F. Chong, C. Chang, F. Zheng and K. H. Lin, *Bioorg. Med. Chem. Lett.*, 2004, **14**, 4751.

20 K. M. Pritchard, J. A. Rawi and C. Bradley, *Eur. J. Med. Chem.*, 2007, **42**, 1200.

21 C. R. Lohani, J. M. Kim, S. Y. Chung, J. Yoon and K. H. Lee, *Analyst*, 2010, **135**, 2079.

Published on 11 May 2015. Downloaded by Indian Institute of Technology Roorkee on 9/11/2022 6:49:27 PM.

22 T. Mistri, R. Alam, M. Dolai, S. K. Mandal, P. Guha, A. R. KhudaBukhsh and M. Ali, *Eur. J. Inorg. Chem.*, 2013, 5854.

23 R. Bhowmick, M. Dolai, R. Alam, T. Mistri, A. Katarkar, K. Chaudhuri and M. Ali, *RSC Adv.*, 2014, **4**, 41784.

24 F. Di Maria, I. E. Palamà, M. Baroncini, A. Barbieri, A. Bongini, R. Bizzarri, G. Gigli and G. Barbarella, *Org. Biomol. Chem.*, 2014, **12**, 1603.

25 (*a*) J. Huang, Y. Xua and X. Qia, *Dalton Trans.*, 2014, 5983; (*b*) M. Zhang, Y. Gao, M. Li, M. Yu, F. Li, L. Li, M. Zhu, J. Zhang, T. Yia and C. Huang, *Tetrahedron Lett.*, 2007, **48**, 3709; (*c*) S. Bae and J. Tae, *Tetrahedron Lett.*, 2007, **48**, 5389; (*d*) Y. Liu, Z. Xu, J. Wang, D. Zhang, Y. Yea and Y. Zhaoa, *Luminescence*, 2014, **29**, 945; (*e*) X. Baoa, X. Caoa, X. Niec, Y. Xub, W. Guod, B. Zhouc, L. Zhangb, H. Liaob and T. Pang, *Sens. Actuators, B*, 2015, **208**, 54; (*f*) A. J. Weerasinghe, C. Schmiesing, S. Varaganti, G. Ramakrishna and E. Sinn, *J. Phys. Chem. B*, 2010, **114**, 9413; (*g*) Z. Yang, M. She, B. Yin, J. Cui, Y. Zhang, W. Sun, J. Li and Z. Shi, *J. Org. Chem.*, 2012, **77**, 1143; (*h*) N. R. Chereddy, S. Thennarasu and A. B. Mandal, *Analyst*, 2013, **138**, 1334.

 This journal is © The Royal Society of Chemistry 2015

Published on 05 March 2018. Downloaded by Indian Institute of Technology Roorkee on 9/11/2022 6:51:01 PM.

Photochemical & Photobiological Sciences

PAPER

View Article Online
View Journal | View Issue

Check for updates

Cite this: *Photochem. Photobiol. Sci.*, 2018, **17**, 465

A turn-on fluorogenic chemosensor for Fe^{3+} and a Schottky barrier diode with frequency-switching device applications†

Habib Ali Molla,[a] Rahul Bhowmick,[a] Abu Saleh Musha Islam,[a] Bibhutibhushan Show,[a] Nillohit Mukherjee,[b] Anup Mondal[c] and Mahammad Ali *[a]

A novel highly sensitive and selective fluorescent chemosensor **L** has been synthesized and characterized by various physicochemical techniques. In 3 : 7 water : MeCN (v/v) at pH 7.2 (10 mM HEPES buffer, μ = 0.05 M LiCl), it selectively recognizes Fe^{3+} through 1 : 1 complexation resulting in a 106-fold fluorescence enhancement and a binding constant of 8.10×10^4 M^{-1}. The otherwise non-fluorescent spirolactam form of the probe results a dual-channel (absorbance and fluorescence) recognition of Fe^{3+} *via* CHEF (chelation enhanced fluorescence) through the opening of the spirolactam ring. We have also carried out fluorescence titration and anisotropy (*r*) studies in pure water in the presence of SDS (sodium dodecyl sulphate). Based on the dependence of FI (fluorescence intensity) and *r* on [SDS] it was proposed that the probe is trapped between two SDS monolayers which again interact among themselves by $\pi\cdots\pi$ stacking. As a result, there is an increase in FI up to [SDS] ~ 7 mM – a phenomenon reminiscent of aggregation-induced enhancement of emission (AIEE). Beyond this concentration of SDS (7 mM), micelle formation takes place and the $\pi\cdots\pi$ stacked polymer now becomes a monomer and is trapped inside the micellar cavity. As a result, there is a decrease in FI at [SDS] > 7 mM. But for anisotropy, it increases with [SDS] beyond 7 mM. Ligand, metal, and SDS interactions are well established through different optical and morphological studies. [**L**–Fe(NO_3)]$^{2+}$ thin films on FTO (Fluorine-doped Tin Oxide) glass substrates have been designed with the help of the spin-coating deposition technique. The deposited film of thickness 1.6×10^{-5} cm is well characterized by optical band gap calculation with a direct band gap, ε_g ~ 1.6 eV. FESEM was also performed for the [**L**–Fe(NO_3)]$^{2+}$/FTO film. The current–voltage characteristics were measured by the two-probe technique. Light-dependent exciton generation was carried out by taking the top and bottom contacts with graphite paste on FTO and on the [**L**–Fe(NO_3)]$^{2+}$ films for the measurement of switching behavior. The response ratio curve for the light-induced frequency-switching phenomena has been obtained. The frequency taped here is the oscillation frequency of the photo-generated electron and the hole in an exiton. Thus, the light-induced frequency-switching behavior and Schottky barrier diode characteristics of the material were established.

Received 25th August 2017,
Accepted 26th February 2018

DOI: 10.1039/c7pp00322f

rsc.li/pps

Introduction

Iron is not only the most abundant transition metal in cellular systems, but also it is of outstanding biological importance given its presence in numerous enzymes and proteins. As to Fe^{3+}, its vital roles in a variety of cell functions have been summarized in many reviews.[1–4] Haemoglobin, an iron-containing protein, is critically involved in both electron transfer reactions and oxygen transport processes in all tissues[5,6] and has suitable redox potential values and high affinity for oxygen. The deficiency or excess of Fe^{3+} can lead to a variety of diseases, such as Alzheimer's, Huntington's, Parkinson's *etc.*[7–10] Thus, there is an urgent need to develop chemical sensors that are capable of detecting and quantifying the presence of Fe^{3+} ions in biological samples.

Due to its paramagnetic nature, Fe^{3+} is basically the most effective fluorescent quencher,[11–13] which makes it difficult to develop a desirable fluorescence turn-on sensor. For this

[a]*Department of Chemistry, Jadavpur University, 188, Raja Subodh Chandra Mallick Rd, Kolkata, West Bengal 700032, India. E-mail: m_ali2062@yahoo.com*
[b]*Centre of Excellence for Green Energy and Sensor Systems, Indian Institute of Engineering Science and Technology, Shibpur, Howrah 711103, Botanic Garden, Howrah 711103, India*
[c]*Department of Chemistry, Indian Institute of Engineering, Science and Technology, Shibpur, Botanic Garden, Howrah 711103, India*

†Electronic supplementary information (ESI) available. CCDC 1563133. For ESI and crystallographic data in CIF or other electronic format see DOI: 10.1039/c7pp00322f

Published on 05 March 2018. Downloaded by Indian Institute of Technology Roorkee on 9/11/2022 6:51:01 PM.

reason, very few turn-on sensors of Fe^{3+} have been reported but many of them are interfered by few other metal ions.[14] Again, there are examples of rhodamine-based fluorescent sensors for Fe^{3+}, but most of them are soluble either in organic solvents or mixed organo-aqueous media[15–24] with few exceptions which are soluble in purely aqueous medium.[25–27]

Consequently, the design of new probes bearing suitable multidentate chelating units, which can preferentially recognize Fe^{3+}, is a timely area of research. Given our interest in developing new chemo-sensing systems, we report, herein, a rhodamine-based dual channel probe for the detection of Fe^{3+}. Rhodamine-based conjugates with a spirolactam structure are, in general, non-fluorescent but act as colorimetric as well as fluorometric sensors with the enhancement of absorption and fluorescence emission intensity, respectively, on selectively binding to metal ion(s).

In the present article, we are going to disclose a rhodamine–1-(2-aminoethyl)pyrrolidine conjugate as a highly sensitive and selective fluorescent chemosensor for Fe^{3+} ions. Transition metal complexes are found to have huge potential to form an active layer in the optical and electronic applications. Recently, considerable attention has been given to developing nanometer-scale materials due to their unique physical and chemical properties and potential applications in nanoscale devices.[28,29] Here, we will explore, for the first time, the feasibility of using a $[\mathbf{L}–Fe(NO_3)]^{2+}$/FTO film as a Schottky barrier diode with frequency-switching device applications. With an ingenious design of a ligated chromophore, we believe that the luminescent Fe(III) complex may serve as a new model for probing a variety of fundamental characteristics in view of the fabrication of optoelectronic devices.

Experimental section

Materials and methods

The starting materials, such as rhodamine-6G hydrochloride (Sigma Aldrich), 1-(2-aminoethyl)pyrrolidine (Sigma Aldrich), and ferric nitrate (Sigma Aldrich), were used for the preparation of **L** and the $[\mathbf{L}–Fe(NO_3)]^{2+}$ complex. Solvents like EtOH, MeOH, MeCN, *etc* (Merck, India) were of HPLC grade. MeCN and de-ionized water were used for spectroscopic studies.

Physical measurements

Infrared spectra (400–4000 cm^{-1}) were recorded from KBr pellets on a Nickolet Magna IR 750 series-II FTIR spectrophotometer. ^{1}H-NMR spectra were recorded in DMSO-d_6 on a Bruker 300 MHz NMR spectrometer using tetramethylsilane (δ = 0) as an internal standard. UV-Vis spectra were recorded on an Agilent diode-array spectrophotometer (Model, Agilent 8453), steady-state fluorescence spectra were recorded on a PTI spectrofluorimeter (Model QM-40), and ESI-MS$^+$ (m/z) of the receptor (**L**) and the **L**–Fe^{3+} complex were recorded on a HRMS spectrometer (Model: XeVO G2 QTof). Morphological analyses of the films were carried out by field emission scanning electron microscopy (FESEM) (JEOL, JSM-6700F).

Syntheses

Preparation of L. Rhodamine-6G hydrochloride (1) (5.0 mmol) and 1-(2-aminoethyl)pyrrolidine (10.0 mmol) were dissolved in EtOH and refluxed for 6 h with continuous stirring whereupon a reddish crystalline solid of **L** was deposited. The solid was filtered and washed with EtOH and dried in air (68% yield). Recrystallization from EtOH afforded single crystals for X-ray diffraction studies. ^{1}H NMR (300 MHz, $CDCl_3$) (δ, ppm): 1.31 (t, 10H), 1.70 (s, 4H), 1.89 (s, 6H), 2.21 (d, 2H), 2.30 (s, 4H), 3.22 (t, 6H), 3.48 (s, 2H), 6.23 (s, 2H), 6.33(s, 2H), 7.03 (s, 1H), 7.42 (t, 2H), 7.90 (s, 1H) (Fig. S1†). IR spectrum: $\tilde{\nu}$ = 1692 cm^{-1} (spirolactam amide-keto), 1615 cm^{-1} (–C=N) (Fig. S2†). ESI-MS$^+$ (m/z): 511.3624 (**L** + H^+) (Fig. S3†).

Synthesis of $[\mathbf{L}–Fe(NO_3)]^{2+}$. $Fe(NO_3)_3{\cdot}9H_2O$ (0.808 g, 2 mmol) in 5 ml MeCN was added dropwise to a solution of **L** (2 mmol) in 20 ml MeCN with continuous stirring. After 1 h, the solution was filtered and kept aside undisturbed. After one day, a crystalline compound precipitated out. It was collected by filtration, washed several times with MeOH and dried in air. It was recrystallized from methanol. Several trials to grow single crystals failed. IR spectrum: $\tilde{\nu}$ = 1637 cm^{-1} (spirolactam amide-keto), 1554 cm^{-1} (–C=N) (Fig. S2†). ESI-MS$^+$ (m/z): 628.4961 $[\mathbf{L}–Fe(NO_3)]^{2+}$ (Fig. S4†).

Solution preparation for UV-Vis and fluorescence studies

Solution preparation is described elaborately in the ESI.†

Determination of fluorescence polarization anisotropy

A PTI QM-40 spectrofluorimeter was used for the determination of fluorescence anisotropy (r) as defined by eqn (1),

$$r = \frac{I_{VV} - G \cdot I_{VH}}{I_{VV} + 2G \cdot I_{VH}} \quad (1)$$

where I_{VV} and I_{VH} are the emission intensities obtained with an excitation polarizer oriented vertically and an emission polarizer oriented vertically and horizontally, respectively. The G factor is defined as[30]

$$G = \frac{I_{HV}}{I_{HH}} \quad (2)$$

where the intensities I_{HV} and I_{HH} refer to the vertical and horizontal positions of the emission polarizer, respectively, with the excitation polarizer being horizontal.

Time-correlated single photon counting measurements

Time-correlated single photon counting (TCSPC) measurements were performed in 10 mM HEPES buffer of pH 7.2 for the fluorescence decay of the free ligand, **L** and the $[\mathbf{L}–Fe(NO_3)]^{2+}$ complex in the absence and presence of SDS at 25 °C. During the TCSPC measurements, photoexcitation was carried out at 510 nm for the $[\mathbf{L}–Fe(NO_3)]^{2+}$ complex using a Hamamatsu MCP photomultiplier (R3809) and was analyzed by using IBH DAS6 software using eqn (3),

$$F(t) = \sum_i a_i \exp\left(-\frac{t}{\tau}\right) \quad (3)$$

 This journal is © The Royal Society of Chemistry and Owner Societies 2018

Published on 05 March 2018. Downloaded by Indian Institute of Technology Roorkee on 9/11/2022 6:51:01 PM.

where α_i denotes the i^{th} pre-exponential factor and τ represents the decay time. The decay time is referred to as the lifetime of the excited species.

Results and discussion

Scheme 1 describes the synthesis of receptor **L** from the reaction of rhodamine-6G with 1-(2-aminoethyl)pyrrolidine in EtOH under refluxing conditions for 20 h with 68% yield. The final product (**L**) was well characterized by ^{1}H NMR (Fig. S1†), IR (Fig. S2†), HRMS (Fig. S3 and S4†) and single crystal X-ray diffraction techniques. Fig. 1 displays the molecular view of **L** which was found to crystallize in the $P\bar{1}$ space group of the triclinic system (please see Table S1 in the ESI†).

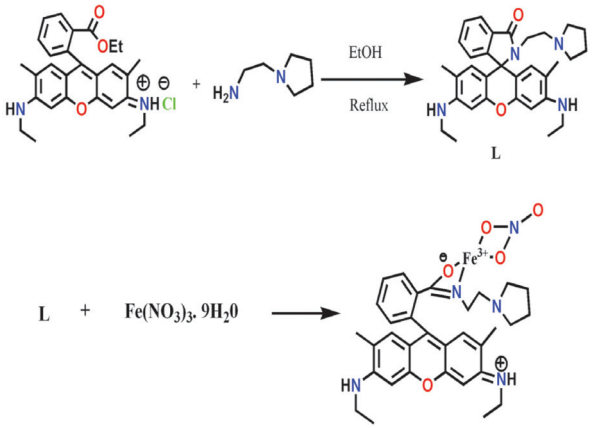

Scheme 1 Synthesis of probe L and its Fe^{3+} complex.

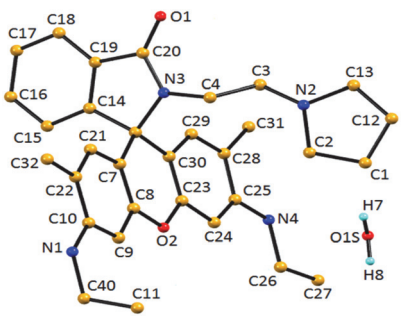

Fig. 1 Molecular view of ligand (**L**). H-Atoms are omitted for clarity.

The solution of **L** is colorless and non-fluorescent because of its spirolactam form. However, it becomes dark red and highly fluorescent in the presence of Fe^{3+}. But many other metal ions do not produce such optical changes. So it behaves as a highly sensitive and selective dual channel (colorimetric and fluorometric) sensor for Fe^{3+} in the presence of other metal ions. The apparent formation constant (K) was determined by UV-Vis titrations in MeCN-buffer solution (7 : 3 v/v, HEPES at pH 7.0) at 25 °C. A linear form of Benesi–Hilderbrand equation (eqn 4) was used to evaluate the dissociation constant and stoichiometry of complexation, where, A_0 and A_{max} are the absorbances of the ligand in the absence and in the presence of excess metal ion, respectively and n is the stoichiometry (**L** : Fe^{3+}) of the reaction. A linear least square-fit of $(A_{max} - A_o)/(A - A_o)$ against $1/[Fe^{3+}]$ clearly demonstrates a 1 : 1 stoichiometry of the reaction (n = 1) which also gives an apparent dissociation constants $K_d = (8.26 \pm 0.03) \times 10^{-5}$ M.

$$\frac{(A_{max} - A_0)}{(A - A_0)} = 1 + \frac{1}{K[Fe^{3+}]} \quad (4)$$

Similarly, the fluorescence titration (Fig. 2) of **L** (10 μM) against variable Fe^{3+} concentrations (0–50 μM) under identical reaction conditions gives $K_d = (4.81 \pm 0.12) \times 10^{-5}$ M and n = 1. There is an excellent agreement between the K values for the [**L**–Fe(NO$_3$)]$^{2+}$ system obtained from the absorption and fluorescence titration data clearly manifesting the self-consistency of our results.

The detection of Fe^{3+} was not interfered by the presence of different metal ions like Na^+, K^+, Ca^{2+}, Mg^{2+}, Cr^{3+}, Mn^{2+}, Fe^{2+}, Co^{2+}, Cu^{2+}, Ni^{2+}, Zn^{2+}, Cd^{2+}, Hg^{2+}, and Pb^{2+} under identical reaction conditions. On addition of 1.5 equivalents of Fe^{3+} to the individual **L**–M^{n+} solutions containing 5 equivalents of M^{n+} the fluorescence intensity corresponding to the [**L**–Fe(NO$_3$)]$^{2+}$ complex was obtained. This observation clearly indicates that Fe^{3+} forms a strong complex with **L** in the presence of the above-mentioned metal ions, which again suggests that all the tested metal ions do not interfere with the selective detection of Fe^{3+} (Fig. S5†).

The pH-stability of the probe was investigated between pH 2 and 12, which showed no obvious fluorescence of **L** between

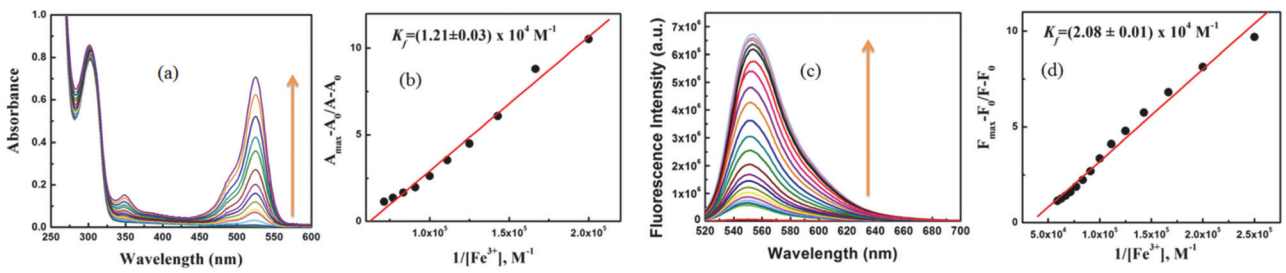

Fig. 2 UV-Vis (20 μM of L) and florescence titration (10 μM of L) of L [Fe^{3+}] (0–25 μM) (a) absorbance *vs.* wavelength plots for various increasing concentrations of Fe^{3+} (0–20 μM) (b) Benesi–Hilderbrand plot; (c) FI *vs.* wavelength plots for various increasing concentrations of Fe^{3+} (0–25 μM); (d) Benesi–Hilderbrand plot.

Published on 05 March 2018. Downloaded by Indian Institute of Technology Roorkee on 9/11/2022 6:51:01 PM.

pH 4 and 12 (Fig. S6†). However, in the presence of selective guests like Fe^{3+} ions, it fluoresces effectively at pH ≥ 7.0, which clearly indicates the compatibility of the probe for biological applications under physiological conditions.

The IR spectrum of the receptor reveals the presence of the characteristic stretching frequency of the amidic "C=O" of the rhodamine moiety at 1692 cm^{-1}, which is shifted to a lower wavenumber of 1637 cm^{-1} in the presence of 1.2 equivalents of Fe^{3+} (Fig. S2†). This large shift ($\Delta\nu$ = 54 cm^{-1}) signifies a strong polarization of the C=O bond upon efficient binding to the Fe^{3+} ion. In fact, it indicates the formation of the **L**–Fe^{3+} complex by the opening of the spirolactam ring.

The 1 : 1 (**L** : Fe^{3+}) complexation was determined by Job's method (Fig. S7†) and further supported by mass spectrometric analysis (m/z = 628.4961) $[\mathbf{L}\text{–Fe}(NO_3)]^{2+}$ (see Fig. S7 in the ESI†).

Steady-state fluorescence studies in the presence of SDS

We have also carried out fluorescence titration in pure water in the presence of SDS under two conditions. (i) At a fixed concentration of **L** (10 μM) and SDS (10 mM) and a variable concentration of Fe^{3+}; (ii) at a fixed concentration of **L** (10 μM) and Fe^{3+} (10 μM) and a variable concentration of SDS.

In case (i), there is a gradual increase in FI with the increase in Fe^{3+} concentration, it reaches a maximum at ~10 μM Fe^{3+} and then remains almost constant on a further increase in Fe^{3+} concentration. The major linear part of the plot was used to extract the association constant K_f by using the linear form of eqn (5) under the condition $1 \gg c \times x^n$ with n = 1 (ref. 31) and the value was evaluated to be (1.27 ± 0.10) × 10^5 M^{-1} (Fig. 3). It is found to be an order of magnitude higher than that obtained in MeCN–H_2O in the absence of SDS. This indicates a higher stability of the formed complex in the excited state in the presence of SDS.

$$y = \frac{(a + b \times c \times x^n)}{1 + c \times x^n} \quad (5)$$

This enhanced stability constant value may be due to the restricted movement of the doubly positively charged

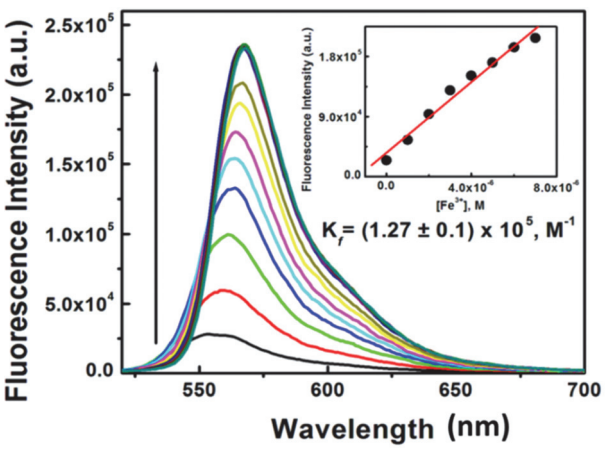

Fig. 3 (a) Florescence titration of L (10 μM) by Fe^{3+} in the presence of SDS (9 mM) with λ_{ex} = 510 nm; (b) plot of FI as a function of [SDS].

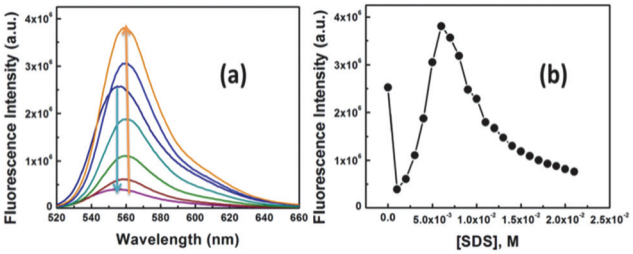

Fig. 4 (a) Florescence titration of L (10 μM) by SDS in the presence of [Fe^{3+}] (10 μM) with λ_{ex} = 510 nm; (b) plot of FI as a function of [SDS].

$[\mathbf{L}\text{–Fe}(NO_3)]^{2+}$ complex by the strong electrostatic attraction with the negatively charged head group of SDS in the form of laminar aggregates.

In the second case, a plot of FI *vs.* [SDS] shows an initial sharp drop in FI of the $[\mathbf{L}\text{–Fe}(NO_3)]^{2+}$ complex in water on adding 1 mM SDS and then it increases rapidly with the increase in SDS concentration, reaches a maximum at 7.0 mM, and then decreases with the increase in SDS concentration, which is clearly demonstrated in Fig. 4(b). The initial sharp drop in FI may arise due to the breakdown of the self-organized $[\mathbf{L}\text{–Fe}(NO_3)]^{2+}$ complex (non-covalently attached polymer) in purely aqueous medium in the presence of 1 mM SDS.

This experiment clearly demonstrates the aggregation between $[\mathbf{L}\text{–Fe}(NO_3)]^{2+}$ and SDS, which is favored with the increase in SDS concentration up to 7 mM SDS. With a further increase in [SDS], there is a gradual decrease in FI and it reaches almost a plateau at [SDS] ~ 18 mM (Fig. 4(b)). The appearance of the fluorescence maximum at [SDS] ~ 7 mM clearly indicates that the critical micellar concentration (CMC) of SDS is 7 mM under the experimental conditions. The decrease in FI with [SDS] beyond 7 mM may be attributed to a change in the morphology of SDS surfactant from laminar to spherical micelles on increasing the [SDS], and at the same time the polymeric $[\mathbf{L}\text{–Fe}(NO_3)]^{2+}$ becomes a monomer and gets trapped inside the micellar cavity. The formation of the monomer results in a decrease in FI. The increase in FI with [SDS] manifests the fact of aggregation-induced enhancement of emission (AIEE). It is interesting to note that in the presence of 9 mM SDS, no quenching of the fluorescence intensity of the $[\mathbf{L}\text{–Fe}(NO_3)]^{2+}$ complex by HF_2^- was observed, which was otherwise observable in the absence of SDS. This clearly indicates the non-accessibility of the $[\mathbf{L}\text{–Fe}(NO_3)]^{2+}$ complex to HF_2^- due to trapping inside the micellar cavity.

Steady-state fluorescence anisotropy

We have measured the steady-state fluorescence anisotropy to monitor the extent of restriction imposed by the micro-heterogeneous environment on the dynamic properties of the probe. To check this, we have monitored the fluorescence anisotropy as a function of SDS concentration at a fixed concentration of **L** and Fe^{3+} (10 μM each) at 564 nm. A steady increase in anisotropy on increasing the SDS concentration up to 1.5 mM occurs, followed by a gradual decrease with SDS concentration,

 This journal is © The Royal Society of Chemistry and Owner Societies 2018

Published on 05 March 2018. Downloaded by Indian Institute of Technology Roorkee on 9/11/2022 6:51:01 PM.

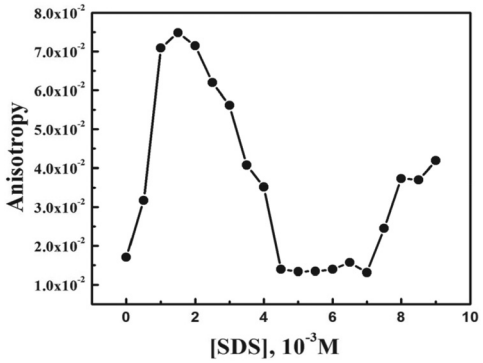

Fig. 5 Plot of fluorescence anisotropy (r) as a function of [SDS] in purely aqueous medium at 25 °C and [L] = [Fe^{3+}] = 10 μM, λ_{ex} = 510 nm.

reaching a plateau at ~4.2 mM, and then maintaining a steady value up to 7.0 mM. After that, it again slowly increases with the increase in [SDS] (Fig. 5).

As discussed earlier, the initial sharp increase in anisotropy with [SDS] may be due to the layer arrangement of SDS. Between two such layers [**L**–$Fe(NO_3)$]$^{2+}$ complexes are trapped by electrostatic interaction with the negatively charged sulfonic acid head groups (Scheme 2). This regular arrangement of the [**L**–$Fe(NO_3)$]$^{2+}$ complex further interacted among themselves by π···π stacking interactions to form a polymer imposing a firm restriction to their free movement and hence resulting in an enhancement in anisotropy. On further increasing [SDS], the regular layer arrangement of SDS is broken down and [**L**–$Fe(NO_3)$]$^{2+}$ becomes free as a monomer. As a consequence, the r value decreases and reaches a minimum at ~4.20 mM and remains constant up to 7 mM where no formation of micelle occurs. But above 7 mM of SDS, the micellization process dominates and this entraps the [**L**–$Fe(NO_3)$]$^{2+}$ complex inside the cavity as a monomer resulting in a slow but steady increase in r with the increase in [SDS]. The encapsulation of [**L**–$Fe(NO_3)$]$^{2+}$ inside the cavity is supported by the failure of HF_2^- to quench the fluorescence of the complex, which otherwise is quenched in the absence of 9 mM SDS (Fig. 5). It is well accepted that an increase in the rigidity of the fluorophore results in an increase in the fluorescence anisotropy.

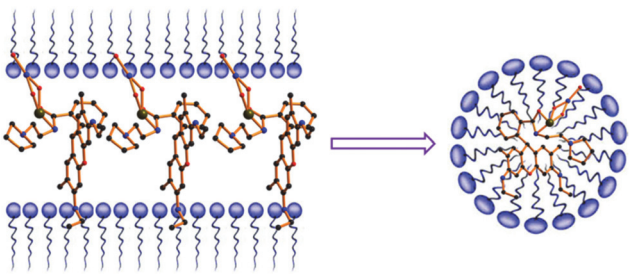

Scheme 2 Schematic presentation of the interactions of probe with the laminar microstructure and micellar microstructure of SDS (adopted from UC Davis ChemWiki).

Analyses of surface topography of ligand, ligand–SDS, metal–ligand, and metal–ligand–SDS

The change in surface topology has been noticed from the FESEM studies for ligand, ligand with SDS, metal–ligand, and metal–ligand with SDS, which indicates that SDS has a pronounced effect on the surface design. The synthesized materials are very different from each other. The morphology of the ligand is well dispersed throughout the phase having quasi cubical grains with an average size of ~30 nm, which is also indicated in the inset figure (Fig. 6(a)). But in the case of ligand–SDS interactions a change in surface topology occurs, indicating that no free ligand molecules are present in the system [Fig. 6(a) and (b)]. In the case of metal–ligand interactions, numerous microstructural defects with fibroid-like morphology are visible, but with SDS, the ternary interactions greatly influence the fibroid structure with densely occupied spherical uniform holes. This behavior of the molecules enhances the optical properties as shown in Fig. 6(c) and (d), which is also clearly indicated in the respective inset figures. Due to the betterment of fibroid interactions between the metal and ligand, charge-transfer interactions take place. When fabricated on the conducting glass substrate (FTO), good electrical conductivity in the presence of photons is obtained, which performs as a photo-switching material. Thus, the FESEM analyses indicate that the surface structures as well as defects at the surface levels are important for device applications.

Thin film fabrication from the precursor of the [L–$Fe(NO_3)$]$^{2+}$ complex

The thin films of hybrid materials have attracted both inorganic and organic chemists as they can be used to design various microelectronic and optoelectronic devices. For the preparation of inorganic–organic thin films, the spin-coating

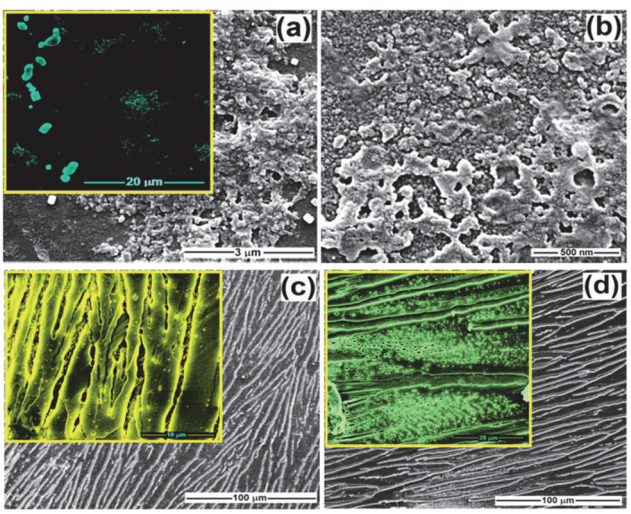

Fig. 6 FESEM analyses of (a) ligand with an inset image, (b) ligand–SDS, (c) metal–ligand with an inset image and (d) metal–ligand–SDS with an inset image.

Published on 05 March 2018. Downloaded by Indian Institute of Technology Roorkee on 9/11/2022 6:51:01 PM.

method has the merits of convenience, use of low cost equipment, and a faster operating system. Spin coating is a convenient and reproducible method for applying highly uniform thin films to substrates of all kinds. Moreover, it requires smaller amounts of material and less processing time compared to other methods.

In our work, a $[\mathbf{L}\text{–}Fe(NO_3)]^{2+}$ film is fabricated onto a FTO glass substrate having an area of 3.5 cm × 1.5 cm by spin-coating of a sol precursor. For the preparation of $\mathbf{L}\text{–}Fe^{3+}$ sol, the complex precursor $[\mathbf{L}\text{–}Fe(NO_3)]^{2+}$ is mixed with acetonitrile in the ratio 1 : 10. The mixture solution was stirred for 20 minutes at room temperature and at a constant speed without any perturbation. The FTO glass substrates were cleaned from end to end ultrasonically in detergent, deionized water, acetone, and isopropanol sequentially before spin-coating deposition under an ambient atmosphere. The nanostructure $[\mathbf{L}\text{–}Fe(NO_3)]^{2+}$ complex sol was spin-coated at 2000 rpm for 1 min onto a FTO pre-cleaned glass. The spin coater consists of a variable rotating vacuum chuck powered by a motor. The substrate was held firmly in position by atmospheric pressure. In a clean environment, five drops of $[\mathbf{L}\text{–}Fe(NO_3)]^{2+}$ complex precursor in acetonitrile were allowed to fall with the help of a clean syringe onto the center of a stationary conducting glass substrate. The drop spreads out across the substrate under the influence of the centrifugal force. As it moves, the solvent evaporates from the solution, leaving a smooth continuous film. The resulting hybrid film was annealed on a hot plate at ~60 °C for 15 minutes to remove the residual solvent. This procedure was repeated several times to get crystalline, uniform, pinhole-free thin films of the inorganic–organic complex on the FTO substrate (sheet resistance ~10 Ω sq^{-1}). The thicknesses of the films were determined by the gravimetric method using the formula[32] $t = (W_2 - W_1)/Ad$, where t is the thickness of the film, A is the area covered by the film, d is the density of the $[\mathbf{L}\text{–}Fe(NO_3)]^{2+}$ complex (1.18 g cm^{-3}), and W_1 and W_2 are the weight of the FTO glass substrate before and after deposition, respectively. The deposited film ($t = 1.6 \times 10^{-5}$ cm) was studied using a field emission scanning electron microscope for surface morphology, a UV-Vis spectrophotometer for optical measurement and a semiconductor characterization system for electrical measurement. Therefore, iron complex modified FTO thin films $[\mathbf{L}\text{–}Fe(NO_3)]^{2+}$/FTO/glass are used for diode characteristics and frequency-switching device applications.

Morphological characteristics of $[\mathbf{L}\text{–}Fe(NO_3)]^{2+}$/FTO thin films

The deposited $[\mathbf{L}\text{–}Fe(NO_3)]^{2+}$/FTO film was investigated using FESEM as shown in Fig. 7. From the surface morphology analysis, microstructural fractures in the film with numerous spherical grains with distinct grain boundaries have been observed at a low magnification of 1.30 K× (Fig. 7(a)) due to drought of solvent molecules. At high magnification 20.00 K× (Fig. 7(b)), small islands with several coarse wells are separated uniformly. Each island is composed of uniformly distributed spherical grains of the $[\mathbf{L}\text{–}Fe(NO_3)]^{2+}$ complex having a diameter in the range of 80 to 100 nm on the FTO glass substrate

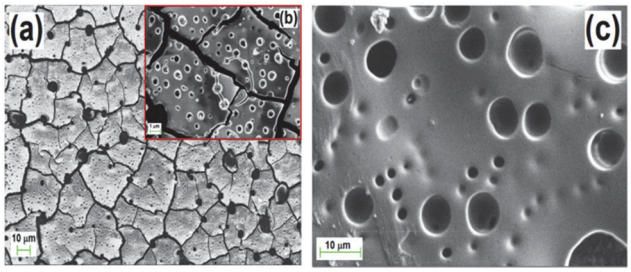

Fig. 7 Field emission scanning electron micrograph of the $[\mathbf{L}\text{–}Fe(NO_3)]^{2+}$/FTO thin film.

at the magnification of 19.45 K×. The grains are distinct and the grain boundaries are prominent as shown in Fig. 7c.

However, the formation of larger grains from smaller crystallites is essential for the spontaneous lowering of Gibb's free energy in the system to gain stability. Nanoparticles have a higher surface-to-volume ratio, so the surface energy of the system becomes significantly high. For this reason, every system has a tendency to lower down the free energy by forming larger grains from smaller crystallites by spontaneous agglomeration.

UV-Vis analysis

The absorption spectrum showed a moderately sharp onset in absorbance around 550 nm, which represents the typical band to band transition for the pure $[\mathbf{L}\text{–}Fe(NO_3)]^{2+}$ complex (Fig. 8). The band gap energy for the $[\mathbf{L}\text{–}Fe(NO_3)]^{2+}$/FTO thin film was calculated using the Tauc's relation:[33] $[(\alpha h\nu)^{1/n} = A(h\nu - E_g)]$, where A is a constant related to the effective masses of charge carriers, h is the Planck constant, E_g is the band gap energy, $h\nu$ is the incident photon energy, and $1/n$ is the exponent that depends on the nature of the optical transition (n = 0.5 and 2 for direct and indirect transition, respectively). The Tauc's plot (inset Fig. 9) indicates the direct band gap energy of 1.6 eV for the deposited films.

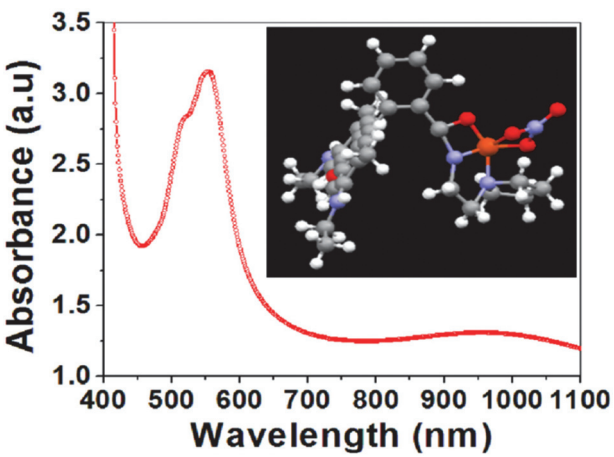

Fig. 8 Absorption spectrum of the pure $[\mathbf{L}\text{–}Fe(NO_3)]^{2+}$ complex.

This journal is © The Royal Society of Chemistry and Owner Societies 2018

Published on 05 March 2018. Downloaded by Indian Institute of Technology Roorkee on 9/11/2022 6:51:01 PM.

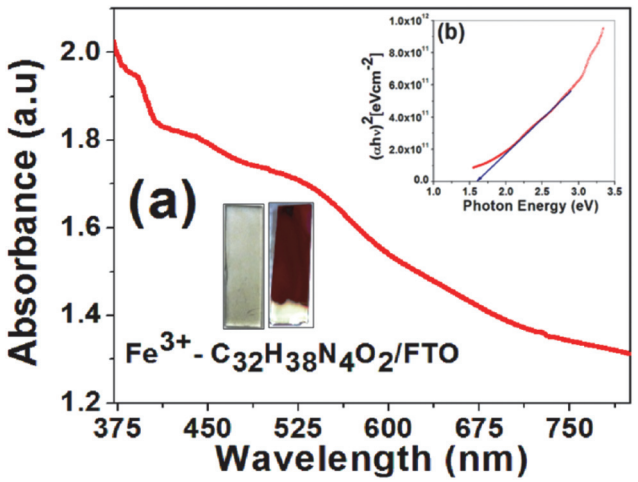

Fig. 9 The absorption spectrum of the $[L–Fe(NO_3)]^{2+}$ thin film (a); inset (b): plot of $(\alpha h\nu)^2$ *vs.* $h\nu$, Tauc's plot.

Electrical properties: current–voltage (*I–V*) characteristics by the two probe technique

Two-probe *I–V* measurement was carried out by taking FTO-coated glass substrates as the bottom contact and 2 mm × 2 mm graphite paste as the top contact as shown in Fig. 10. The nanostructured thin film consists of surface defects which influence the intrinsic band nature from its bulk counterpart directly, which affects the electronic transition and phonon transfer process.[34] The electronic defects at the grain boundaries of the nanoparticles generate traps which directly affect the current–voltage properties.

Under a no-bias condition, the electron affinity for the traps at the surface of the grains is higher but upon changing the bias, the traps get filled. Therefore, the enrichment of current densities can be noticed when all the traps are filled; meanwhile, on irradiation of light, the generated charge carriers at the surface level influence the nature of the *I–V* curve with high current density and high steepness at forward bias. During the reverse bias, the opposite phenomenon is supposed to be taking place. The increase of reverse bias affects the electrostatic attraction of the trapped electronic environment with greater ease, and an increment in the negative current densities is observed both under dark and light conditions. Thus, trapping and de-trapping of charge carriers play an important role in the symmetrical nature of the *I–V* curve. As the FTO (n-type) modified $[\mathbf{L}–Fe(NO_3)]^{2+}$ thin film showed a non-linear change in current–voltage, a possible formation of depletion region at the interface can be presumed. Non-linear symmetric *I–V* also supports the formation of a weak junction at the interface of p-type ($[\mathbf{L}–Fe(NO_3)]^{2+}$) and n-type FTO glass substrate, through which electrons overcome the barrier in a restricted manner.[35] The current obtained in the reverse bias is mainly due to the loss of junction barrier properties which can increase the reverse saturation current due to the free minority carriers at the junction. On the other hand, from the FESEM image, it is evident that the deposited films have fewer micropores along the *c*-axis, which is responsible for producing a leakage path, supporting the bias-assisted rectification.

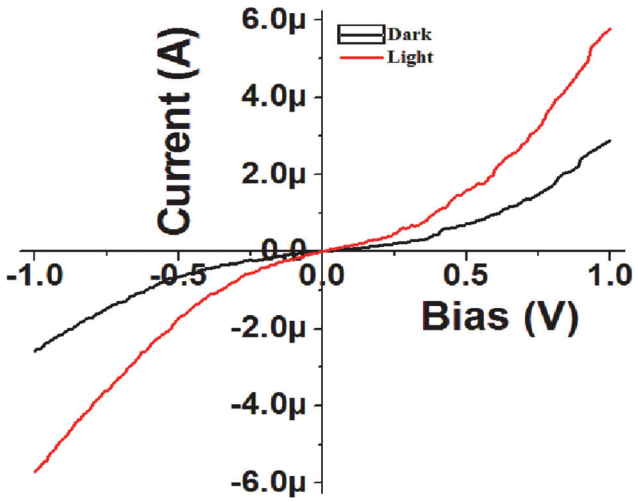

Fig. 10 Representative two-probe *I–V* characteristics of the $[L–Fe(NO_3)]^{2+}$/FTO thin films under dark and light conditions.

Photon-induced exciton generation

Light-dependent exciton generation was carried out by taking the top and bottom contacts with graphite paste on FTO and on the $[\mathbf{L}–Fe(NO_3)]^{2+}$ film for the measurement of switching behavior, a light with an intensity of 1 Sun was allowed to pass through the FTO glass substrate and up to the film.[36] The response ratio curve for the light-induced frequency-switching phenomenon by which a 50-Hz pulse was generated as soon as the light was 'on' was found to be quite steady for a period of 25 s. A decay of only 1–2 Hz was noted during this period. A sudden drop of this pulse to the 'zero' state took place with the 'off' state of the incident light. This is due to the oscillation frequency of the photo-generated electrons and the holes in an exciton. On switching off the light, the photo-generated electrons and the holes will recombine, leading to no oscillation of the charged species, and hence no frequency was detected. Good consistency of this switching behavior was found for more than 50 cycles; ten of them are represented here. This low magnitude light induced pulse generation might be the contribution of the confined exitonic transition that might be a very low free carrier concentration within the metal complex matrix.

It is a fact that intrinsic defects like anion/cation vacancies within the metal ligand complex can adsorb gas molecules like oxygen or water vapor from the atmosphere. Trapping of such molecules will create some trap electrons/energy levels on the surface of the semiconductor, leading to a space charge region and related band bending inside the semiconductor (Fig. 11). So the number of electron–hole pairs increases, which significantly affect some unique physical properties like enhancement of photo-luminescence intensity, light-induced frequency-switching behavior, *etc.*

Published on 05 March 2018. Downloaded by Indian Institute of Technology Roorkee on 9/11/2022 6:51:01 PM.

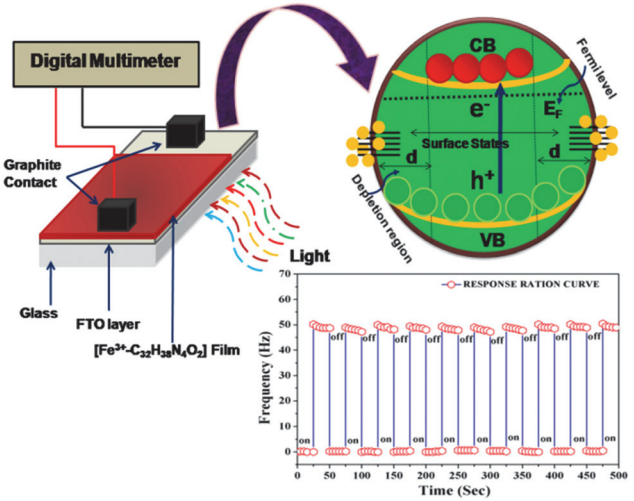

Fig. 11 Schematic diagram of the photo-switching behavior of [L–$Fe(NO_3)]^{2+}$/FTO films and their response curves.

Conclusion

In this article, we have successfully presented a highly selective fluorescent chemosensor of rhodamine-1-(2-aminoethyl)pyrrolidine (**L**) towards Fe^{3+} through 1 : 1 complexation under the specified reaction conditions of 3 : 7 water : MeCN (v/v) at pH 7.2; 10 mM HEPES buffer, μ = 0.05 M LiCl; it shows an enhancement in the corresponding fluorescence intensity of 106-fold with an apparent binding constant (K_f) of 8.10 × 10^4 M^{-1}. We have also carried out fluorescence titration and anisotropy (r) studies in pure water in the presence of SDS. Based on the dependence of FI and r on [SDS], it was proposed that the probe is trapped between two SDS monolayers, which again interacted among themselves by π···π stacking. As a result, there is an increase in FI up to [SDS] ~ 7 mM – a phenomenon reminiscent of aggregation-induced enhancement of emission (AIEE). Beyond this concentration of SDS (7 mM), micelle formation takes place and the π···π stacked polymer now becomes a monomer and is trapped inside the micellar cavity, which is again confirmed by the failure of HF_2^- to quench the FI of the $[\mathbf{L}\text{–}Fe(NO_3)]^{2+}$ complex trapped inside the micellar cavity, which otherwise quenches the FI of $[\mathbf{L}\text{–}Fe(NO_3)]^{2+}$ in the absence of SDS. Due to the trapping of the $[\mathbf{L}\text{–}Fe(NO_3)]^{2+}$ monomer complex, there is a decrease in FI at [SDS] > 7 mM. In the case of anisotropy, it increases on increasing [SDS] beyond 7 mM. Ligands, metals, and SDS interactions are well established through different optical and morphological studies. $[\mathbf{L}\text{–}Fe(NO_3)]^{2+}$ thin films on an FTO glass substrate have been designed with the help of the spin-coating deposition technique. The deposited film having a thickness of 1.6 × 10^{-5} cm is well characterized by optical band gap calculation with a direct band gap, ε_g ~ 1.6 eV. FESEM studies were also performed on the $[\mathbf{L}\text{–}Fe(NO_3)]^{2+}$/FTO film. The electrical behavior, *i.e.* current–voltage characteristics by the two probe technique was also studied. Light-dependent exciton generation was carried out by taking the top and bottom contacts with graphite paste on FTO and on the $[\mathbf{L}\text{–}Fe(NO_3)]^{2+}$ films for the measurement of switching behavior. The response ratio curves for the light-induced frequency-switching phenomenon have been obtained. The frequency taped here is the oscillation frequency of the photogenerated electron and the hole in an exciton. Thus, the light-induced frequency-switching behavior and Schottky barrier diode characteristics of the material were established.

Conflicts of interest

There are no conflicts to declare.

Acknowledgements

Financial support from the CSIR (Ref. No. 01(2896)/17/EMR-II), the DST (Ref. SR/S1/IC-20/2012), New Delhi and the DST (Ref. No. 809(Sanc)/ST/P/S&T/4G-9/2104) West Bengal is gratefully acknowledged. RB gratefully acknowledges the CSIR for a fellowship (SRF). The authors are thankful to Anupam Nandi, senior research scholar, CEGESS, IIEST, Shibpur for electrical measurements and technical discussion.

References

1 J. R. Burdo and J. R. Connor, *Biometals*, 2003, **16**, 63–75.
2 J. R. Connor, S. L. Menzies, S. M. St. Martin and E. J. Mufson, *J. Neurosci. Res.*, 1990, **27**, 595–611.
3 R. R. Crichton, S. Wilmet, R. Legssyer and R. J. Ward, *J. Inorg. Biochem.*, 2002, **91**, 9–18.
4 R. S. Eisenstein, *Annu. Rev. Nutr.*, 2000, **20**, 627–662.
5 B. T. Felt and B. Lozoff, *J. Nutr.*, 1996, **126**, 693–701.
6 C. J. Earley, J. R. Connor, J. L. Beard, E. A. Malecki, D. K. Epstein and R. P. Allen, *Neurology*, 2000, **54**, 1698–1700.
7 J. P. Sumner and R. Kopelman, *Analyst*, 2005, **130**, 528–533.
8 Y. Ma, W. Luo, P. J. Quinn, Z. Liu and R. C. Hider, *J. Med. Chem.*, 2004, **47**, 6349–6362.
9 G. E. Tumambac, C. M. Rosencrance and C. Wolf, *Tetrahedron*, 2004, **60**, 11293–11297.
10 A. Ali, Q. Zhang, J. Dai and X. Huang, *BioMetals*, 2003, **16**, 285–293.
11 Y. Ma, W. Luo, P. J. Quinn, Z. Liu and R. C. Hider, *J. Med. Chem.*, 2004, **47**, 6349–6362.
12 J. Mao, L. Wang, W. Dou, X. Tang, Y. Yan and W. Liu, *Org. Lett.*, 2007, **9**, 4567–4570.
13 M. Xu, S. Wu, F. Zeng and C. Yu, *Langmuir*, 2010, **26**, 4529–4534.
14 X. Wu, B. Xu, H. Tong and L. Wang, *Macromolecules*, 2010, **43**, 8917–8923.
15 S. Das, K. Aich, S. Goswami, C. K. Quah and H. K. Fun, *New J. Chem.*, 2016, **40**, 6414–6420.

This journal is © The Royal Society of Chemistry and Owner Societies 2018

Published on 05 March 2018. Downloaded by Indian Institute of Technology Roorkee on 9/11/2022 6:51:01 PM.

16 R. Kagit, M. Yildirim, O. Ozay, S. Yesilot and H. Ozay, *Inorg. Chem.*, 2014, **53**, 2144–2151.
17 L. Zhanga, J. Fana and X. Penga, *Spectrochim. Acta, Part A*, 2009, **73**, 398–402.
18 L. Zhang, J. Wang, J. Fan, K. Guo and X. Peng, *Bioorg. Med. Chem. Lett.*, 2011, **21**, 5413–5416.
19 N. R. Chereddy, S. Thennarasu and A. B. Mandal, *Dalton Trans.*, 2012, **41**, 11753–11759.
20 S. Parihar, V. P. Boricha and R. N. Jadeja, *Luminescence*, 2015, **30**, 168–174.
21 J. An, T. Li, B. Wang, Z. Yang and M. Yan, *J. Coord. Chem.*, 2014, **67**, 921–928.
22 Y. Yu, X. Cheng, H. Liu, S. Gu, Z. Jiang, H. Huang and J. Lian, *J. Polym. Sci., Part A: Polym. Chem.*, 2015, **53**, 615–621.
23 A. Sikdar, S. S. Panja, P. Biswas and S. Roy, *J. Fluoresc.*, 2012, **22**, 443–450.
24 O. Ozay and H. Ozay, *J. Macromol. Sci., Part A: Pure Appl. Chem.*, 2014, **51**, 308–317.
25 B. Wang, J. Hai, Z. Liu, Q. Wang, Z. Yang and S. Sun, *Angew. Chem., Int. Ed.*, 2010, **49**, 4576–4579.
26 M. Deng, S. Wang, C. Liang, H. Shang and S. Jiang, *RSC Adv.*, 2016, **6**, 26936–26940.
27 Y. Liu, R. Shen, J. Ru, X. Yao, Y. Yang, H. Liu, X. Tang, D. Bai, G. Zhang and W. Liu, *RSC Adv.*, 2016, **6**, 111754–111759.
28 P. chabera, Y. Liu, O. Prakash, E. Thyrhaug, A. E. Nahhas, A. Honarfar, S. Essen, L. A. Fredin, T. C. B. Harlang, K. S. Kjaer, K. Handrup, F. Ericson, H. Tatsuno, K. Morgan, J. Schnadt, L. Haggstrom, T. Ericsson, A. Sobkowiak, S. Lidin, P. Huang, S. Styring, J. Uhlig, J. Bendix, R. Lomoth, V. Sundstrom, P. Persson and K. Warnmark, *Nature*, 2017, **543**, 695–699.
29 A. P. Alivisators, *J. Phys. Chem.*, 1996, **100**, 13226–13239.
30 J. R. Lakowicz, *Principles of Fluorescence Spectroscopy*, 3rd edn, Springer, New York, 2006, p. 67.
31 C. R. Lohani, J. M. Kim, S. Y. Chung, J. Yoon and K. H. Lee, *Analyst*, 2010, **135**, 2079–2048.
32 B. Chakraborty, B. Show, S. Jana, B. C. Mitra, S. K. Maji, B. Adhikary, N. Mukherjee and A. Mondal, *Electrochim. Acta*, 2013, **94**, 7–15.
33 R. Bertoni, M. Lorenc, J. Laisney, A. Tissot, A. Moreac, S. F. Matar, M. L. Boillot and E. Collet, *J. Mater. Chem. C*, 2015, **3**, 7792–7801.
34 B. Show, N. Mukherjee and A. Mondal, *RSC Adv.*, 2014, **4**, 58740–58751.
35 S. Jana, N. Mukherjee, B. Chakraborty, B. C. Mitra and A. Mondal, *Appl. Surf. Sci.*, 2014, **300**, 154–158.
36 K. W. Liu, R. Chen, G. Z. Xing, T. Wu and H. D. Sun, *Appl. Phys. Lett.*, 2010, **96**, 023111.